FROM BINDER TO MIXTURE; EXPERIMENTAL PROGRAMME ON PERMANENT DEFORMATION BEHAVIOUR

By

Mahmoud Masoud Hamza Elnasri

Thesis submitted to the University of Nottingham

for the degree of Doctor of Philosophy

Department of Civil Engineering

December 2014

ABSTRACT

Asphalt mixture, the most common road construction material, comprises bitumen, filler, fine and coarse aggregates, and air voids. Traditionally and for simplification, the mixture is treated as a continuous and homogenous material confined in the domain of linear behaviour. The demand for more durable roads, particularly with the progressive growth in traffic volumes and loads, has raised the requirement for improved design methods. Wisely, before the complex adoption of the nonlinear behaviour, understanding the nature of the internal stress-strain relationships at different scales and determining their linearity limits is essentially required taking into consideration the time and temperature dependency.

So far, most experimental programs have been concerned with testing either asphalt mixture or bitumen in isolation. This thesis is intended to establish a systematic experimental investigation from binder to the asphalt mixture scale in terms of permanent deformation behaviour. Preliminary conclusions of the components contributions, their interactions, and the effect on the total macroscopic response are drawn from the experimental observations.

Investigation of the fillers influence on the viscoelastic property of the mastic (filler +bitumen) binder in the dynamic shear rheometer (DSR), results exhibited that binder behave nonlinearly at high shear stress levels and the linearity range reduces with increasing filler content and/or raising the temperature. Although filler inclusion increased the deformation resistance (stiffness) of the binder, its recoverability decreased. Consequently, a new binder rutting evaluation test was designed to distinguish between the two

rutting resistance mechanisms; stiffness and recovery. Results from the new test indicated that the linearity of the modified binders begins after an initial inherent nonlinearity stage and before a secondary nonlinearity stage triggered by the applied state of stresses in the DSR.

A new designed mortar type was developed from the mastic and originated from a standard asphalt mixture. The focus of this part in the research emphasised on measuring the stiffening effect of fine aggregates utilising a constitutive stress-strain relationship and determining the influence on the viscoelastic behaviour. Results indicated that the stiffening effect varies depending on the stress condition (uniaxial, triaxial, or shear), temperature, fine aggregate gradation, and binder with filler content. The stress linearity limit was also found to vary at different degrees with the previous parameters.

Uniaxial compression constant stress and strain rate tests were conducted on asphalt mixtures of different aggregate gradations at 30 and 50°C. X-ray CT was incorporated to characterise the coarse aggregates and air voids through advanced image analysis techniques. The test was shown to be insensitive to the asphalt mixture type in terms of air voids uniformity. Mixtures of coarse aggregates produced larger size and smaller number of air voids, opposite to the fine aggregate ones. Comparing the stiffening effect between fine and coarse aggregates, it was revealed that the air void content is a key factor. Finally, the radial strain as measured along the height followed the pattern of air void distribution in the specimen and exhibited both tensile and compressive forms.

ACKNOWLEDGEMENTS

DECLARATION

The research described in this thesis was conducted at the University of Nottingham, Department of Civil Engineering between December 2010 and December 2014. I declare that the work is my own and has not been submitted for a degree of another university.

<div align="right">

Mahmoud Masoud Hamza Elnasri

University of Nottingham

December, 2014

</div>

TABLE OF CONTENTS

LIST OF TABLES

LIST OF FIGURES

1. Introduction

1.1 Background

Roads are engineered to provide smooth and safe movements of traffic. Asphalt mixtures, the most common road surface construction material, consist of bitumen, filler, fine and coarse aggregates, and air voids. Bitumen is the binding agent stiffened by filler to adhere the aggregate skeleton. Different proportions of these components generate various types of asphalt mixtures of different behaviours.

Over time, asphalt pavement's efficiency and its riding quality degrades to the condition of failure. The most common forms of failure in flexible pavements are permanent deformation (rutting) and cracking. While rutting is caused mainly by shear deformation in the material due to repeated wheel loading, the generated tensile strain under traffic loading or variation in temperature results in cracking (Taherkhani, 2006). Cracking will not be considered here as it is outside the scope of the project.

In current design procedures, pavements are required to perform well against the distresses noted above and to reach a satisfactory stiffness (i.e. capacity to spread loading) (Read *et al.*, 2003). The mechanical properties of the asphalt mixture determine the ability to meet the performance requirements. The material composition that is sensitive to stresses and temperatures has primary influence on the mixture mechanical performance.

Therefore, it is essential to understand the relationship between the mix composition and the mechanical behaviour of the mixture over a wide range of conditions for the seek of better performance.

In addition, the design methods only consider part of the material behaviour (linearity) or neglect some influential factors that can cause differences from the expected performance. Therefore, proper mix design and reliable prediction of the performance are obtained by a detailed detection of the mix design effect on the mechanical properties combined with recognition of the complete behaviour.

1.2 Problem Definition

Flexible pavements can fail in several ways. Permanent deformation is one of the most common modes of failure that degrades flexible pavements. In permanent deformation, accumulated strains (deformation) due to repeated traffic loads manifest themselves as rutting in the wheel path (Figure 1.1) (Lundy *et al.*, 2004). Rutting can occur in the early life of the pavement due to inappropriate compaction, although it is more likely to develop during the life span of the road by the continuous shear displacement under wheel loading (Taherkhani, 2006). The susceptibility to permanent deformation is strongly dependent on the mechanical properties of the components of the asphalt mixture and their interactions.

Figure 1.1 Permanent deformation in asphalt pavement (Science, 2014)

Bitumen, the adhering agent of aggregates, is a viscoelastic material whose properties vary with time and temperature. It is the viscous part of bitumen's behaviour that is responsible for the irrecoverable and permanent deformations. However, bitumen does not occur in its pure form in an asphalt mixture but rather as a bitumen-filler mastic or 'effective binder'. Filler, with particle sizes less than 63 microns, is universally accepted as a stiffener to the bitumen. The degree of stiffening is determined by the type of filler, concentration, and its physiochemical properties.

The aggregate skeleton within an asphalt mixture contains both fine and coarse particles. Incorporating fine aggregates onto bitumen-filler mastic produces an asphalt 'mortar' that constitutes an intermediate level between mastic and an asphalt mixture. The influence of fine aggregates and their interactions with mastic on the behaviour of asphalt mixtures is poorly understood (Branco *et al.*, 2013).

In the asphalt mixture, the load carrying mechanism relies essentially on the aggregate interlocking and the stiffness of the binder. The extent to which the mechanism relies on aggregate skeleton and/or binder stiffness varies depending on the mix type and the working condition (Khanzada, 2000).

For design purposes, asphalt is traditionally treated as a continuous and linear material. When a continuum is assumed, the distribution of the components is considered uniform on a bulk scale. Nevertheless, at a microscopic scale asphalt is a highly complex heterogeneous material with a random distribution of components, that under loading creates a non-uniform field of stresses and strains (Wang, 2010). Binders may exist in thin films between aggregates with a considerable difference in modulus (Liao *et al.*, 2011). The variation in the binder strain can reach up to 500 times the mixture strain under loading, potentially shifting some of the binder into the nonlinear behaviour (Delgadillo *et al.*, 2010).

Accurate prediction of asphalt behaviour is still difficult due to the complex nature of the asphalt material. However, for more reliable design methods, defining the limits of linear viscoelastic theory is essential before the implications of the nonlinearity application. Therefore, there is a requirement to understand the detailed behaviour of the internal interactions between the components and the reflections on the viscoelsticity property.

1.3 Research Objectives

The overall aim of this project is to improve current understanding of the behaviour of asphalt mixtures in order to assist the pavement design. In order to achieve this, the performance of bituminous mixes in different scales was examined by laboratory testing. Bituminous materials were investigated in the laboratory using methods that would reveal details of interactions between the components and their roles in resistance to rutting. In order to achieve the aim of the research, the study sets out the following objectives:

- A survey of the literature on the permanent deformation of asphalt, mainly focusing on an assessment of methods for the evaluation of binder rutting behaviour. Bitumen-filler system role in asphalt mixture and mortars of the fine part of asphalt mixture are studied. Review of X-ray computed tomography (CT) principle and latest applications to asphalt mixtures.

- Experimental characterisation of the shear creep and recovery response of bitumen as well as bitumen-filler mastic with different filler contents.

- Experimental investigation of the stiffening effect of fine aggregates upon the mastic and the influence on the permanent deformation behaviour after developing a new fitting mortar type.

- Examine the internal microstructure of the asphalt mixture scale using the X-ray CT, before and after testing.

1.4 Research Methodology

To date, most experimental programs have been concerned with testing either asphalt mixtures or bitumen in isolation. This project was intended to establish the factors determining the mechanical behaviour of asphalt by examining its components and interactions at four different scales (Figure 1.2). The deformation behaviour of bitumen; mastic (investigation of bitumen-filler interactional system); mortar (investigation of fine aggregate contribution to the rutting resistance of the mastic); and the largest scale asphalt mixture (investigation of the overall behaviour of the asphalt to reveal the contribution of coarse aggregates and air voids to the rutting behaviour) will be determined. A 10mm DBM standard mixture was utilised in this study as it is widely used in the UK. Rutting will be addressed in the study by characterising the steady state and recovery behaviours of the bituminous materials.

Asphalt **Mastic** **Mortar** **Bitumen**
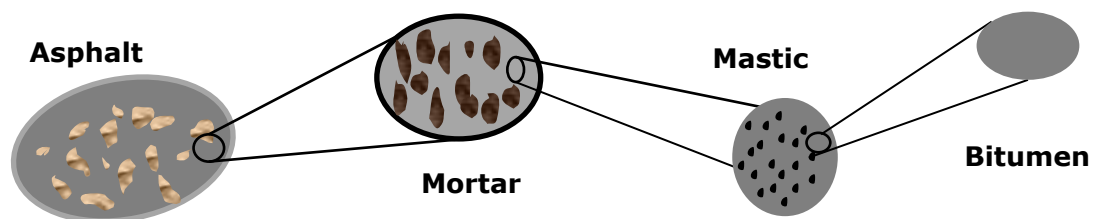
Figure 1.2 The four different scales of bituminous material investigated

Bitumen is the main element which, when mixed with filler (less than 63 μm) constitutes the 'effective binder' known as mastic. Testing mastic as well as pure bitumen enables the effect upon asphalt behaviour of interactions between constitutions to be assessed. Creep and creep-recovery tests that were carried out over a wide range of shear stresses and temperatures are

included in the work plan at this scale besides developing a new binder rutting evaluation test.

Mortar, defined as mastic containing aggregates less than 2 mm in diameter, represents the fine part of asphalt mixture that holds the coarse aggregate skeleton. Uniaxial compression, shear, and triaxial performances of mortars were examined. The degree at which fine aggregate stiffened the mastic was measured at different conditions. In the full asphalt mixture scale, tests of unconfined uniaxial compression under conditions of constant stress and constant strain rate were performed. Air voids and aggregates were characterised before and after testing. The contribution of coarse aggregates to the capacity of deformation resistance was quantified.

The aim of this experimental program was to build up comprehensive understanding of the components roles by establishing strong correlations between the four tested scales.

1.5 Organization of Thesis

The thesis is organized in 8 chapters. Previous literature research on the permanent deformation of bitumens and bituminous materials is reviewed in Chapter 2. In Chapter 3 the principles of operation of the X-ray CT is described and its recent applications to the study of asphalt mixtures is discussed. An extensive experimental investigation of the shear creep and recovery behaviour of pure bitumen and mastics (with different filler contents) is described in Chapter 4. Utilising the results described in Chapter 4, a new binder rutting evaluation test (Multiple stress-strain creep recovery)

was developed. The detailed design and validation of the tests is contained in Chapter 5.

The development of a new mix of a bituminous mortar type and the associated specimen manufacture procedure is described in Chapter 6. A full comparison between the shear, uniaxial compression, and triaxial steady state deformation behaviour is set out in this chapter.

Investigation of the asphalt mixture scale is addressed in Chapter 7, including account of specimen preparation and the testing program. The characterisation of air voids and of coarse aggregates before and after uniaxial compression is detailed. Finally, Chapter 8 outlines the major conclusions of the study and recommendations for future works.

2. Literature Review

2.1 Introduction

Asphalt mixtures comprise bitumen, filler, fine and coarse aggregate, and air voids. *Bitumen* is the main element governing the behaviour, and with filler constitutes the adhering agent '*mastic*' of the mixture. Incorporating fine aggregates with mastic constitutes the *mortar* scale; a material that exists between coarse aggregates (Izadi *et al.*, 2011) and mirrors the mechanical interactions between fine aggregates and mastic.

This chapter reviews permanent deformation investigation programs at *bitumen*, *mastic*, and *mortar* scales. The literature carefully tracks binder rutting tests after describing the deformation behaviour of bitumen, examines bitumen-filler systems, and assesses mortar production techniques, all under the umbrella of permanent deformation.

2.2 Permanent Deformation Characterisation

2.2.1 Definition and Mechanism

Permanent deformation is a common mode of failure that degrades flexible pavement and is a concern for the asphalt community. It manifests itself as rutting in the wheel path caused by accumulated strains (deformation) due to the repeated traffic loading (Figure 2.1) (Lundy *et al.*, 2004). The mechanism by which rutting occurs in pavement can be explained by two concepts:

densification (decrease in volume) and shear displacement (movement of the material without volume changing).
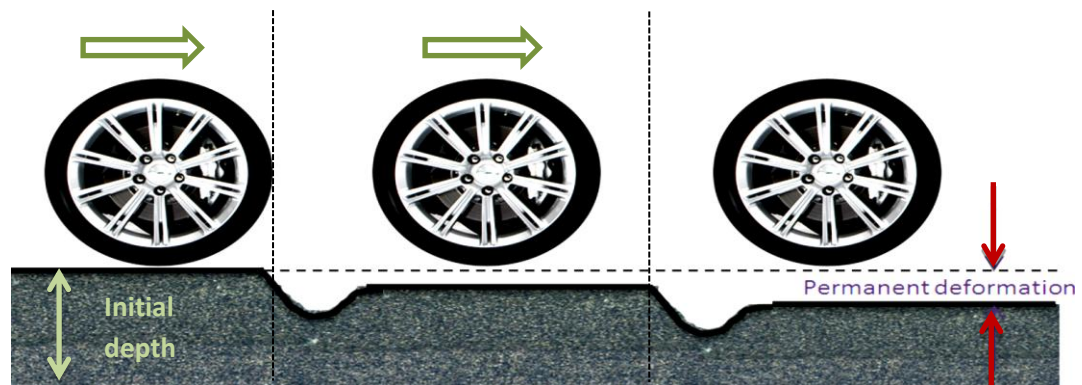
Figure 2.1 Accumulation of permanent strain due to repeated loading

Densification tends to appear in the early life of the pavement when the binder is still soft and fresh (un-aged), while shear displacement is a continuous process during the lifetime of the pavement (Khanzada, 2000). While densification can be minimised by proper compaction during construction, several laboratory studies support the primary reason for rutting is shear displacement (Hofstra *et al.*, 1972, Collop *et al.*, 1995). However, these are coupled mechanisms for a nonlinear behaving material such as asphalt. Yet, it is the material property that enables rutting to occur.

When the pavement is being passed by a wheel loading, there will be some irrecoverable strains generated in the material. It is the viscous property of the binder that is responsible for these permanent strains, and it dominates more at high temperatures and/or long loading times (Khanzada, 2000). Consequently, factors that affect permanent deformation can be classified into material properties and working condition.

2.2.2 Determination Factors

2.2.2.1 Material Properties

The structural strength of the asphalt mixtures relies primarily on the mechanical properties of bitumen and interlock between aggregate particles (Khanzada, 2000). Different proportions of the components produce various types of asphalt mixtures with different performances. In order to optimise the composition for maximum permanent deformation resistance, understanding the effect of each component and their influential properties is inevitable.

Bitumen is the main element in the asphalt mixture governing the behaviour. The amount of bitumen added to the aggregates is critical. An overfilled mixture has low air voids content and results in a thicker bitumen film between aggregate particles that raises the permanent deformation susceptibility. On the other hand, too little binder leads to aggregates separated by a very tight network of air voids. Therefore, optimum bitumen content in the mixture is required with no less than about 3% air voids content as recommended by (Khanzada, 2000, Suo *et al.*, 2009). In addition to the quantity, the grade of the bitumen plays a vital role in determining the deformation resistance.

Bitumen with higher stiffness considerably reduces the susceptibility to permanent deformation (Hofstra *et al.*, 1972, Lundy *et al.*, 2004). This is partially limited by the aggregate gradation type of the mixture. The effect is more significant in gap graded mixtures than when the resistance is

primarily dependent on aggregate interlocking as typically observed in continuously graded mixtures (Taherkhani, 2006).

Aggregates which occupy a large volume of the mixture, with their physical properties (type, shape, size, texture) have a great impact on the asphalt mixture performance. Aggregates resistance to sliding over each other and aggregates adhesion with the binder are the characteristics of aggregates to resist deformation. Rough surface aggregates allow more bond with bitumen and greater friction between particles than smoothed surface particles (Garba, 2002). In terms of physical properties, angular shape are more preferable due to the increased contact points between particles (Kim *et al.*, 1992). Mixtures with large aggregates have less rutting potential than mixture with small size aggregates because of better load transfer (Lundy and Sandoval-Gil, 2004).

Gradation or particle size distribution is a measurement of aggregate sizes and their proportions in the mixture, determined by sieve analysis. Superpave introduced the 'restricted zone' that lies between 2.36 and 0.3 mm in which aggregate gradation was recommended not to pass. In their study, Kandhal *et al.* (2001) reported significant difference in performance between asphalt mixtures that share similar mineralogical composition and had aggregate gradation below, above, and through the restricted zone, Figure 2.2. Test results in the Asphalt Pavement Analyser (APA) exhibited highest and intermediate rutting in mixes of gradation below and above the restriction zone respectively, whilst gradation through the intermediate zone generally had the lowest rutting.
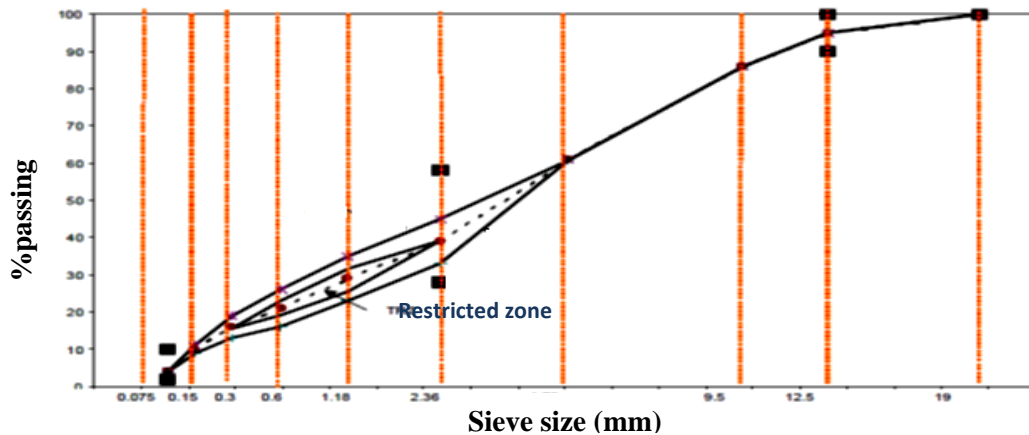
Figure 2.2 Aggregate gradation and restricted zone (Kandhal *et al.*, 2001)

Cross *et al.* (1992) argued that influence of the aggregates properties and gradation on rutting is limited when the air void content is low (<2.5%). Field samples were collected and tested in laboratory. They found that even for above 2.5% air void content, the fine aggregate angularity had more influence than aggregate gradation on rutting resistance.

2.2.2.2 Working Condition

Working conditions include mainly the environment (temperature, humidity, moisture content, etc.) (Qiao *et al.*, 2013) as well as wheel loading in terms of frequency, type and weight. Bitumen and bituminous materials behave in a more viscous manner at high temperature and low frequency loading. The more viscous the material is, the more severe is permanent deformation.

Increasing the temperature from 20 to 60ºC in the wheel tracking test, Collop *et al.* (2001) in their study revealed that the resistance to permanent deformation reduced by a factor of 1/250 to 1/350. Several researchers pointed out that heavy loading has a huge negative influence on deformation resistance resulting in higher rutting (Muraya, 2007). Paving process of

roads construction also has an influence as previously noted in which compaction is a crucial part for limiting early rutting.

Gaskins *et al.* (1960) stated that, during the paving operation, hardening of bitumen takes place substantially when the heated aggregate is mixed with the hot binder. During this time (short term ageing) the thin bitumen film is exposed to high temperatures which increase the viscosity. The hardening process continues till laying and compacting, and afterwards by 2 to 3 years and under the traffic loading the hardening (long term ageing) carries on at a lower rate. Yet, the structural linkages of the unaged bitumen molecules are less susceptible to strained rupture than an aged one (Cheung, 1995).

2.3 Bitumen Deformation Behaviour

2.3.1 Introduction

Central to evaluate the asphalt mixture performance is the identification of the deformation characteristics of bitumen. Early research programs on bitumen initiated by oil companies in the nineteenth century looked to understand the bitumen behaviour due to the extensive use in pavement construction. More details relating to bitumen progressing research history can be found in (Cheung, 1995).

Recently, tools and a wide range of testing techniques are being developed to investigate the correlation between the performance of bitumen and asphalt mixtures. This section reviews the deformation characteristics of bitumen and provides particular assessment on binder rutting evaluation tests.

2.3.2 Bitumen Viscoelastic Linear and Nonlinearity Behaviour, and the Steady State Condition

Asphalt mixture behaves in a viscoelastic manner because of bitumen. Bitumen response to a passing wheel load can be represented in the laboratory scale by the creep-recovery test where a constant load is applied for a time period (loading) followed by unloading as illustrated in Figure 2.3. Immediately after application of the load, the 'elastic' part of the material demonstrates an instantaneous strain that is time independent. After that, the strain gradually increases with time being controlled by the 'delayed elastic' (viscoelastic) property. Finally, the loading curve reaches a steady state condition where the strain rate is constant governed by the viscosity.
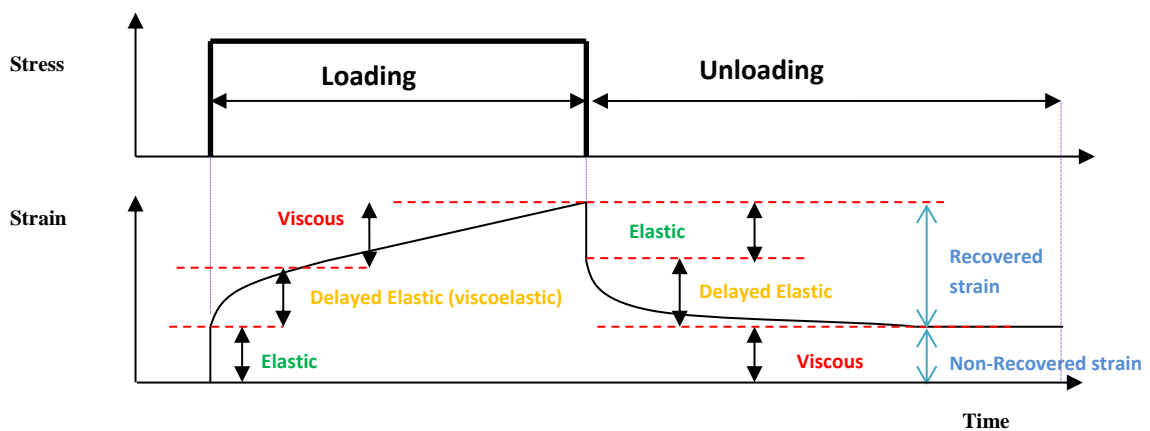
Figure 2.3 Viscoelastic response of bitumen under constant loading

When the load is removed the elastic component immediately recovers its part, while the delayed elastic takes time to recover. After a sufficient time, there will be irrecoverable (permanent) strain caused by the viscosity property. The degree to which the material is considered elastic or viscous is a function of temperature and loading. Bituminous material are more viscous at high temperature and/or low loading frequency, while dominated by

elastic response at low temperature and/or high loading frequency. In service, where the temperature and loading time is intermediate the performance is viscoelastic.

The elastic, delayed elastic, and viscous response described above is within the linear domain. Within this region the strain/stress ratio is by definition only a function of temperature and time but independent of stress level. Typically for a series of creep tests, the creep compliances (stress/strain) should coincide for different stress magnitudes at any given time (Rahimzadeh, 2002). Outside the linear domain that is reached by exceeding a certain stress limit (depending on the material), the stress independency criterion is no longer valid. Thus, the behaviour (strain/stress ratio) becomes a function of the stress magnitude. Because the nonlinear behaviour is very difficult to characterise, most laboratory experiments and models in practice are limited to the linear behaviour (Yusoff *et al.*, 2011).

Although rational pavement design customarily considers only the linearity domain, studies also emphasized the experience of bitumen exceeding the linear viscoelastic range under wheel loading (Masad *et al.*, 2002b, Delgadillo *et al.*, 2010, Rahmani *et al.*, 2013). For more accurate pavement design, the complete behaviour should be considered with the recognition of the limits between the linear and non-linear regions.

Cheung (1995) investigated the uniaxial deformation behaviour of 50 Pen bitumen over a wide range of stresses and temperatures. Different physical models were proposed based on the obtained results to quantify the behaviour at different conditions. The total deformation mechanisms were

constructed in a map form, shown in Figure 2.4. The map consists of six

regions where in each region a single mechanism is dominant and bounded

by specific stress and temperature ranges.
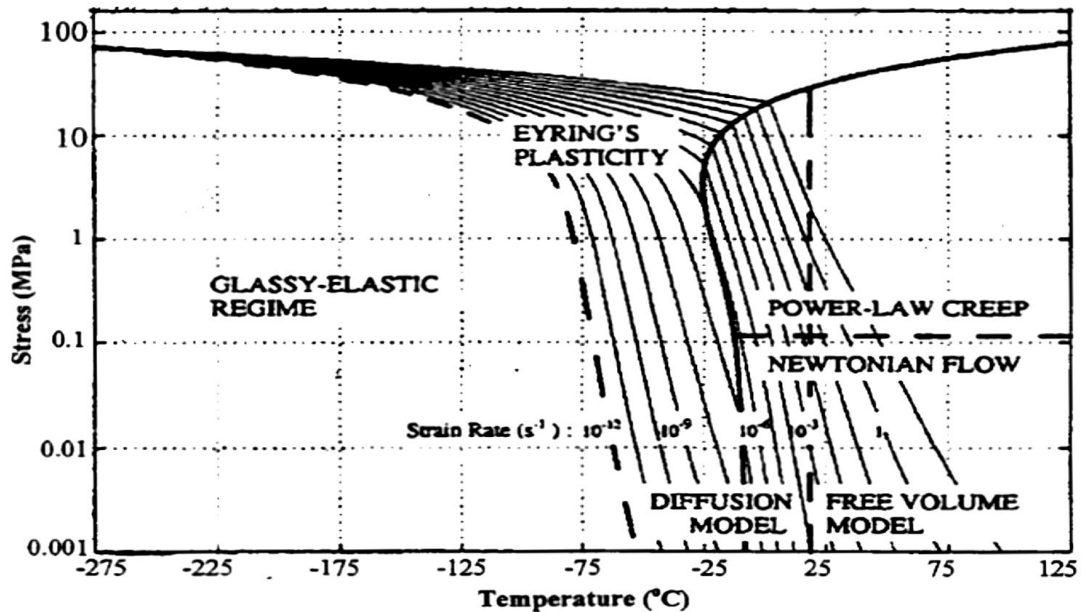
**Figure 2.4 Stress-Temperature deformation mechanism map of
50 Pen bitumen in tension (Cheung, 1995)**

The uniaxial behaviour of the 50 pen was found to be linear viscous at low

stresses and power-law creep at high stresses. The transition stress at which

the behaviour changed from linear to non-linear was found to be

independent of temperature. Above the glass transition temperature, the

steady state strain (SSSR) rate was successfully represented by the proposed

Modified Cross Model (MCM) as shown in Figure 2.5. The steady state

deformation behaviour as described by the MCM changes from linear to

nonlinear at low and high stress levels respectively, and transits from

diffusional as described by Arrhenius equation ($0^oC<T<20^oC$) to free-volume

dependent deformation at high temperature ($T>20^oC$).
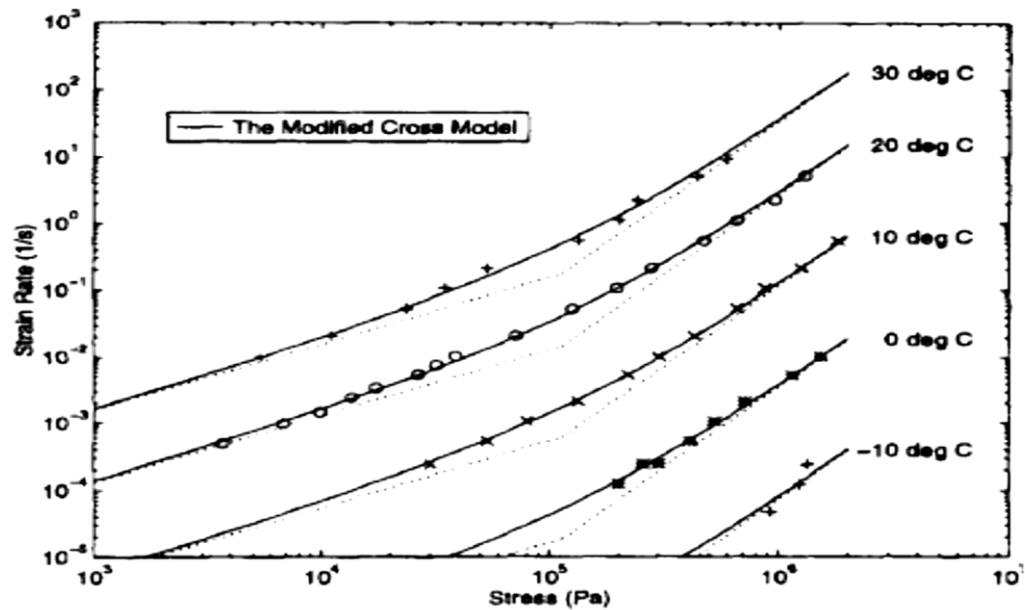
Figure 2.5 Steady State creep behaviour of 50 Pen Bitumen (Cheung *et al.*, 1997b)

Khanzada (2000) carried out shear creep tests using the dynamic shear rheometer (DSR) on 50 and 100 pen bitumen types at 20ºC. Test results showed for less than 70 kPa applied shear stress the SSSR laid in a straight line with a slope of approximately 1 in relation to the shear stress. However, at higher stresses a straight line was found with a slope of 2.4 indicating non-linear creep behaviour.

Taherkhani (2006) obtained similar results by testing 70/100 pen bitumen in the DSR at 10 and 20ºC. The stress limit at which linearity ends was found to be 100 kPa and the creep exponent in the nonlinear region was 2.6, see Figure 2.6. In conclusion, it had been proven that creep testing using parallel plates in DSR is applicable to investigate the bitumen steady state behaviour.
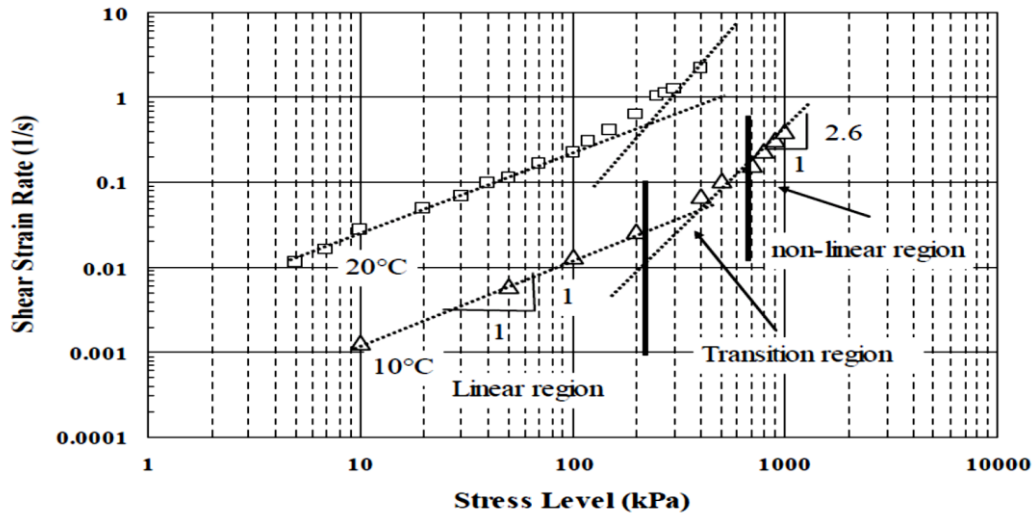
Figure 2.6 Steady state deformation behaviour of 70/100 pen bitumen (Taherkhani, 2006)

2.3.3 Binder Rutting Evaluation Tests

In a trial to rank binders in terms of rutting resistance and establish more correlation with asphalt mixture performance, several rheological studies suggested various testing techniques with different parameters. The first Superpave performance parameter in AASHTO M320-05 (|Complex modulus|/Sin Phase angle: $|G^*|/\sin \delta$) was previously utilised extensively to evaluate binders performances against rutting in the DSR. The parameter $|G^*|/\sin \delta = 1/(\text{loss modulus } J'')$ measures the dissipated energy per cycle in a sinusoidal approach. With larger deformation the more loss of energy will increase the value of J'' indicating more susceptibility to rutting as assumed (Wasage *et al.*, 2011).

Nevertheless $|G^*|/\sin\delta$ failed to effectively predict the performance with polymer modified binders (PMBs) as well as exhibited poor correlation with asphalt mixture (Bahia *et al.*, 2001, Shenoy, 2002, Biro *et al.*, 2009). This has raised the awareness to develop more representative tests and

appropriate parameters. Reasons behind the failure are detailed in (Delgadillo *et al.*, 2006b) and summarised as follows:

1- Test type of sinusoidal loading procedure doesn't simulate the actual rutting mechanism. The quantification of the recovery is not appropriate with cyclic loading applied in reversible directions in the DSR.

2- The parameter $|G^*|/\sin \delta$ evaluates binders based on the energy consumed at each cycle. Part of this energy is the 'delayed elastic' which is recoverable, doesn't contribute to permanent deformation, and its effect is more noticeable in PMBs.

3- The limiting number of cycles applied is insufficient to consider the variability obtained between cycles before reaching a steady condition.

To overcome this, Bahia *et al.* (2001) suggested a new testing method; repeated creep recovery (RCR). The test is easily performed using the DSR by applying 1 s of 300 Pa shear loading followed by 9 s unloading, repeated for 100 cycles. It simulates the rutting more where the load is repeated in one direction amid recovery periods. The number of cycles was selected to ensure a steady state condition is reached (the effect of delayed elasticity reduces with increasing the number of cycles). The derived parameter (G_v) is termed the viscous component of creep stiffness, and it is basically the inverse of the creep viscous compliance (J_v).

To validate the test protocol, Bahia *et al.* (2001) examined 9 modified binders and found a significantly better correlation than the $|G^*|/\sin \delta$ with the asphalt mixture. Nevertheless, the correlation was not good with individual aggregate type because the parameter was unable to identify the

interactions between binder and different aggregate types. Although the RCR testing is performed at a low stress level, there is an evidence of higher stress in the binder under traffic loading enough to shift the binder behaviour into the nonlinear region (Delgadillo *et al.*, 2006a).

Rather than limiting the stress into only 2 levels, D'Angelo *et al.* (2007a) examined four types of binders at different stress levels of 100 cycles. As shown in Table 2.1, the average unrecovered strain at 50 Pa of the Stylink had the least unrecovered strain, while at 1000 Pa it had the highest % of unrecovered strain. This indicates stress sensitivity of binders and therefore, a single stress level does not entirely account for the stress dependency.

Table 2.1 Average % unrecovered strain at different stress levels (D'Angelo *et al.*, 2007a)

Stress (Pa) at 70^{0}C	Air Blown	Control	Elvaloy	Stylink
50	7.41	13.95	7.45	5.79
100	15.02	29.88	19.42	16.50
150	23.71	45.35	30.20	21.00
300	46.60	75.48	58.43	57.02
1000	172.62	227.89	178.22	262.93

2.3.4 Zero Shear Viscosity

In Europe, attention had been paid on a parameter called Zero-Shear-Viscosity (ZSV) to evaluate rutting resistance of binders (Le Hir *et al.*, 2003). The concept of ZSV emerged based on the assumption that only linear viscoelastic behaviour occurs under wheel loading in rational pavement design. At this condition bitumen deforms slowly without any change in the structure maintaining an equilibrium state. The corresponding viscosity at this stage (ZSV) is independent on the shear rate (Liao, 2007).

In the DSR creep-recovery testing, the creep compliance ($J_{(t)} = \gamma_t/\sigma_o$) can be divided into three parts (Figure 2.7):

$$J_{(t)} = J_0 + J_1 + J_2 \qquad (2.1)$$

Where γ_t is the strain, and σ_o is the constant stress, J_0 is the elastic part, J_1 is the delayed elastic part, and J_2 is the viscous part.
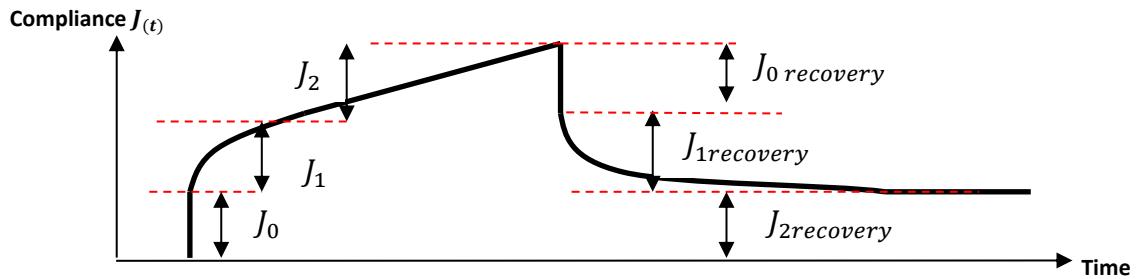
Figure 2.7 ZSV from creep and creep recovery

In the loading steady state region the ZSV is equal to the inverse of the slope, and in the recovery part the ZSV can be estimated from the residual compliance ($J_{2recovery}$), mathematically given by (Desmazes *et al.*, 2000):

$$ZSV_{creep} = \lim_{t.creep \to \infty} \frac{1}{J_2/t} \qquad (2.2)$$

$$ZSV_{recovery} = \lim_{t.recovery \to \infty} \frac{t_{creep}}{J_{2recovery}} = \frac{t_{creep}}{J_{2recovery}} \qquad (2.3)$$

There are other methods to estimate the ZSV using various test types (creep, creep-recovery, viscometry, and sinusoidal oscillation). The following section reviews important studies with different testing techniques to obtain ZSV.

Desmazes *et al.* (2000) suggested a protocol of long creep-recovery test to determine a consistent ZSV value. The test involved 4 successive cycles and the ZSV was measured in the creep and recovery parts. If the difference of

ZSV between sequential cycles was more than 20% then the number of cycles was increased up to a maximum of 8 cycles. A range of 30 to 300 Pa shear stresses was applied to two conventional grade bitumens and 20-50 Pa for two styrene butadiene styrene (SBS) PMBs at 40°C. For conventional bitumen, the same viscosity value (ZSV) was obtained at 30 and 300 Pa with less than 20% difference between cycles. However, for binder with high modified content it was difficult to decide on the right operational condition as steady state was not reached or the test consumed impractical waiting times.

To avoid this, De Visscher *et al.* (2004) proposed an alternative method to determine ZSV in a shorter time creep test. For pure 70/100 pen bitumen and for 1 hour loading followed by 1 hour recovery at 500 Pa and 40°C, the difference between the ZSVs determined from creep and recovery was found to be only 0.1%. In addition, the difference between ZSV measured within the last 15 minutes and 1 hour was less than 0.2%. For highly modified SBS binder 4 hours waiting time was not enough and the repeatability was poor. More importantly, the applied high shear stress may exceed the linearity region especially with PMBs.

Giuliani F. (2006) examined the effect of stress and loading time on estimating ZSV in a long creep test within the last 15 minutes. Pure 50/70 pen binder and crumb rubber modified (CRM) binder (16% and 20% concentrations by mass of bitumen) were tested at 60°C with loading times of 1 hour for pure binder and up to 8 hours for the CRM. For pure bitumen, increasing the stress from 10 to 100 Pa, the difference in ZSVs was less than

20% while a considerable variation was obtained with CRM. Additionally, the difference between the ZSVs calculated at different loading times didn't stabilise to less than 20% for CRM as shown in Figure 2.8.

ZSV [Pa s]	1 hour	2 hours	4 hours	8 hours
	94382	127273	126945	180723
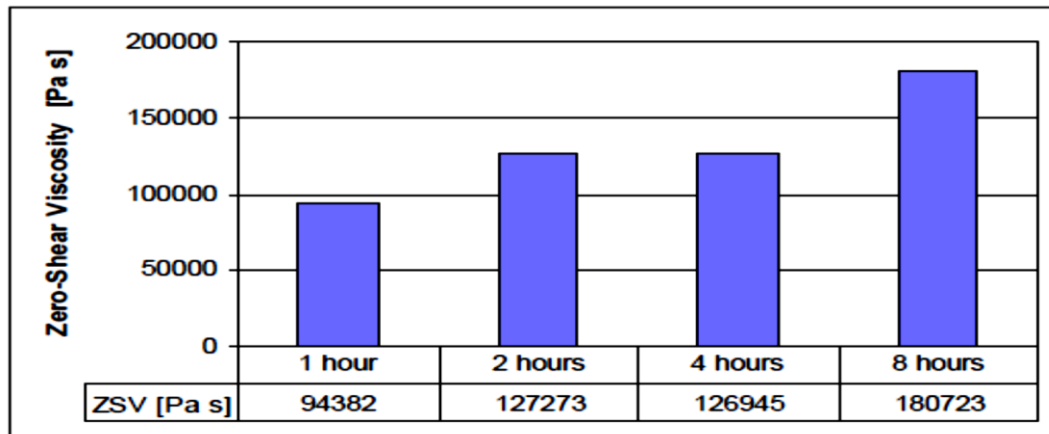
Figure 2.8 Comparison between ZSV of CRM at different loading times (Giuliani F., 2006)

Le Hir *et al.* (2003) compared ZSV values obtained in long creep and frequency sweep tests on different base, SBS, and ethylene vinyl acetate 'EVA' (with different contents) binders. The ZSV was measured in frequency sweep under the assumption of loss modulus over angular frequency equals to ZSV at a very low frequency ($\omega \to 0$, $G''/\omega \to$ ZSV). ZSV is then extrapolated as illustrated in Figure 2.9.
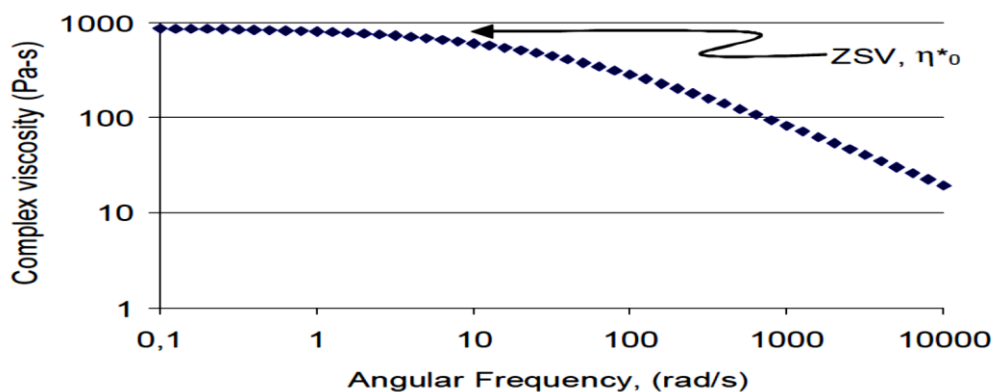
Figure 2.9 Extrapolation of ZSV from frequency sweep test results (Anderson *et al.*, 2002)

Comparison between the ZSVs using different test methods displayed a good correlation (less than 20% difference) except with the modified EVA binder as the properties of the binder changed due to the melting of some EVA crystalline parts during testing. However, at low temperature and for many modified binders the extrapolation is unreliable because occasionally the curve is curvilinear.

Anderson *et al.* (2002) utilised the Cross model to estimate ZSV from frequency sweep test. The Cross model is given by:

$$\eta^* = \frac{\eta_0^*}{1 + (K\omega)^m} \qquad (2.4)$$

Where η^* is the complex viscosity, η_0^* is the complex ZSV, K and m are constants calculated by nonlinear regression. Different models were suggested to estimate ZSV, details of these models can be found elsewhere (Liao *et al.*, 2011, Anwar Parvez *et al.*, 2014).

Comparison between different methods (Extrapolation, Cross model, and long creep tests) to estimate ZSV showed a good agreement of less than 20% difference except for some PMBs whose steady state was not reached in creep test.

However, when the same comparison was made by Biro *et al.* (2009) for highly modified binder with Sasobit and Asphamin the agreement was very poor and was attributed to the inability of the Cross model to predict ZSV as the curve didn't reach a plateau even at very low frequency levels (0.01 Hz). Also Vlachovicova *et al.* (2007) examined the ZSV values obtained from

different loading/unloading of creep/recovery times and the variation between ZSV values of SBS PMB was attributed to the time-dependent microstructure attitude.

Thus, although using ZSV concept has been widely utilised, different testing procedures were suggested with a lack of consistency. The fundamental problem with ZSV is associated with highly modified binders which behave as a solid struggling to reach a steady state condition. In addition, each testing technique was customised based on accommodating a specific type of binder rather than a standardised procedure. Therefore, the applicability of these tests is still narrow and limited (D'Angelo *et al.*, 2007a).

2.3.5 Multiple Stress Creep Recovery Test

Developing RCR test shifted the concept of binder rutting evaluation into a better representation, nevertheless, determining flow properties at a single stress level doesn't completely account for the actual condition where high strains are expected to be induced under wheel loading. On the other hand, there is a poor agreement on a generalised procedure to estimate ZSV.

In response to these needs, recent advancements in binder rutting evaluation tests introduced the multi-stress creep recovery 'MSCR' (AASHTO-TP70) test. It is recognised widely as a more accurate indicator to rank binder (pure or modified), simple and easy to perform, and well correlated to the asphalt mixture performance. It basically simulates the RCR by applying 1 s loading and 9 s recovery for 10 cycles, repeated at 2 different stress levels (0.1 and 3.2 kPa) continuously without any time lag using the DSR. It has the advantage of stress dependence recognition over the RCR.

100 Pa was selected as the lowest shear stress because below this level the accumulated strain doesn't vary much from one temperature to another, and based on the evaluation of many polymers and their compatibility with the base binder the upper limit 3.2 kPa was suited. A compatible PMB with good interactions of its entanglement chains with bitumen exhibits uniform behaviour at low and high stresses (D'Angelo *et al.*, 2007b).

Researchers later on started to realise the need to apply the same concept of MSCR test but with a range of stress levels. Following is the set of sequential stresses that was widely adopted: 25, 50, 100, 200, 400, 800, 1600, 3200, 6400, 12800, and 25600 Pa. The new parameter is termed the 'non-recoverable compliance' (J_{nr}). The compliance is calculated at each stress level through dividing the average non-recoverable strain by the applied stress. The following equation illustrates the calculation method:

$$J_{nr} = \sum_{i=1}^{10} \gamma_{unr}/(10\,\tau) \qquad\qquad (2.5)$$

Where γ_{unr} is the unrecovered strain at each cycle, τ is the specified stress in the group of 10 cycles.

Multiple stress levels has been used by Zoorob *et al.* (2012) to examine the stress sensitivity of pure bitumen and PMBs. Figure 2.10 compares J_{nr} over the stress increase. At low temperature the behaviour was stable but when the temperature increased the sensitivity appears with different performances. Although SBS showed the best performance at low stresses it diverged to the worst at high stresses.
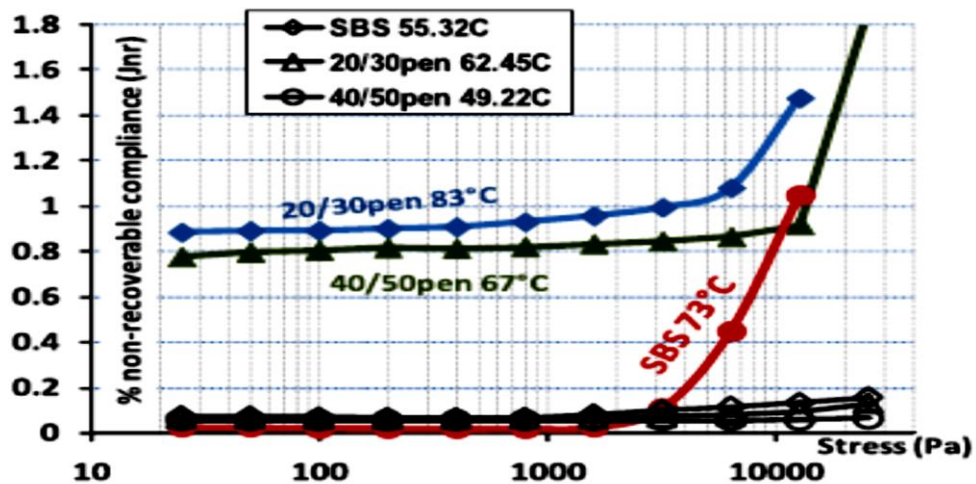
Figure 2.10 Comparison between J_{nr} values for binders in MSCR (Zoorob *et al.*, 2012)

Wasage *et al.* (2011) investigated the temperature dependency of J_{nr} for 85/100 pen bitumen, CRM, and SBS PMBs at 60°C. For pure bitumen, J_{nr} was found to be independent of stress level. On the other hand, for binders modified with SBS or Crumb rubber, there is an increased dependency with increasing the stress level as shown in Figure 2.11. It was also pointed out that increasing the temperature extended the region of stress dependency. Similar conclusions regarding the SBS higher sensitivity and J_{nr} temperature dependency were recorded by Zoorob *et al.* (2012).

Investigation of the correlation with the asphalt mixture performance, Wasage et al. (2011) revealed that only a good correlation was observed when the J_{nr} was calculated at the stress limit of non-linearity at 40°C. This indicates that the binder is exposed to higher stresses under wheel tracking more than in the MSCR. However, the correlation is not straightforward due to the intervention of several factors in the mixture.
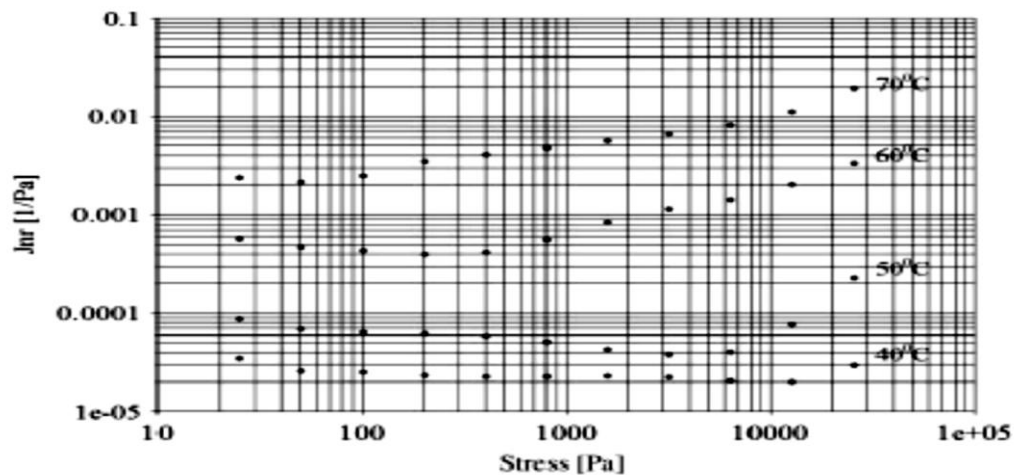
Figure 2.11 Non-recoverable compliance at different temperatures (Wasage *et al.*, 2011)

Although extensively utilised, there are still some concerns about the MSCR test. For the standard version, the two stress levels partially cover the condition under wheel loading. The recovery time is not satisfactory enough to complete the recovery. The number of cycles (10) may not allow the steady state condition where the delayed elasticity effect is removed to be reached (the rate of deformation per cycle tends to stabilize). The last point can be drawn by following Figure 2.12 where three different modifiers were blended with the same binder and tested by (1/9 s) loading for 100 cycles:
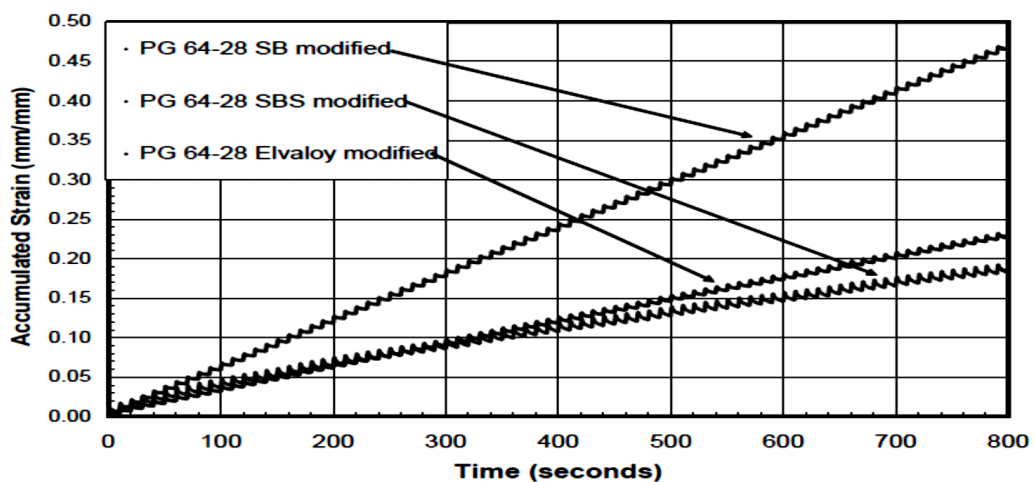
Figure 2.12 RCR of three different PMB (Delgadillo *et al.*, 2006b)

At the first cycles, the SBS shows a higher rate of permanent deformation than the Elvaloy modified binder. After about 30 cycles the SBS modified binder reverses the rate of permanent deformation to become the least in ranking. This indicates a better long term permanent deformation resistance for the SBS than Elvaloy modifier (Delgadillo *et al.*, 2006b). In addition, the delayed elastic effect generated from insufficient recovery (Masad *et al.*, 2009) may affect the following cycles in both loading and unloading phases.

2.3.6 Recovery Characterization of Bitumen

To investigate the recovery property of the bitumen, which plays a significant role in rutting characterisation, Ossa (2005) applied a series of single tension creep-recovery tests on 50 and 100 pen bitumen. In the creep-recovery test, a constant load was applied until reaching a predetermined total strain in a range of 0.02 to 0.2 at different stress levels at -5, 0, and 10°C. After reaching the predetermined strain the loading was removed immediately and the recovering strain was recorded until attaining approximately zero strain rate. The summary of the recovered strain against total strain is illustrated in Figure 2.13. It was concluded that there is a linear relationship with a slope φ, given by:

$$\varepsilon^r(\text{total strain}) = \varphi\varepsilon^t(recovered\ strain) \qquad (2.6)$$

The slope $0 \leq \varphi \leq 1$ was found to be independent of the stress level and temperature for a given bitumen type.
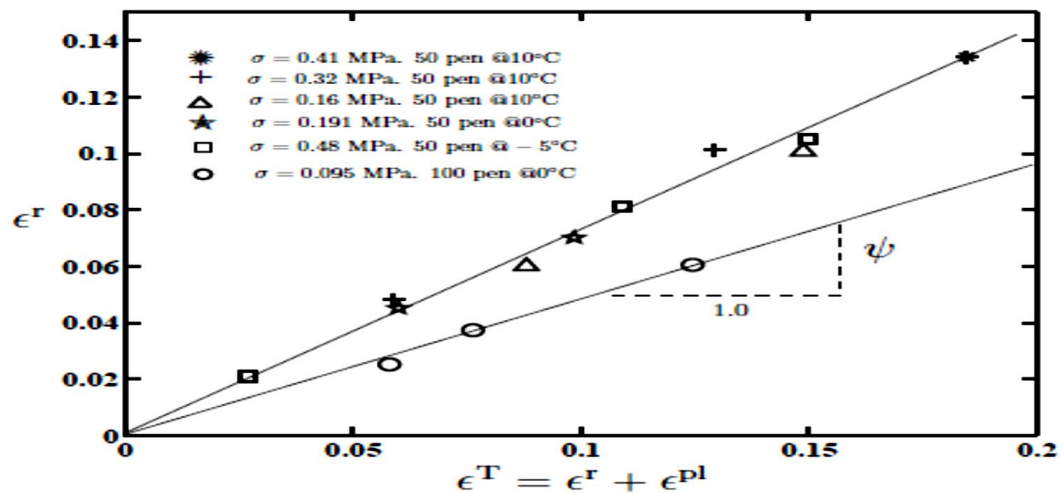
Figure 2.13 Summary of creep recovery tests (Ossa, 2005)

Similarly, a series of shear creep recovery tests was applied on 70/100 pen bitumen at 10oC and 20oC by Taherkhani (2006). The results confirmed the linear relationship but up to a certain total strain limit after which the recovered strain becomes constant, as presented in Figure 2.14. More importantly, this strain limit was found to be temperature independent but in contradiction with (Ossa, 2005) increased with increasing stress level. This was explained by the low strains operated by Ossa.
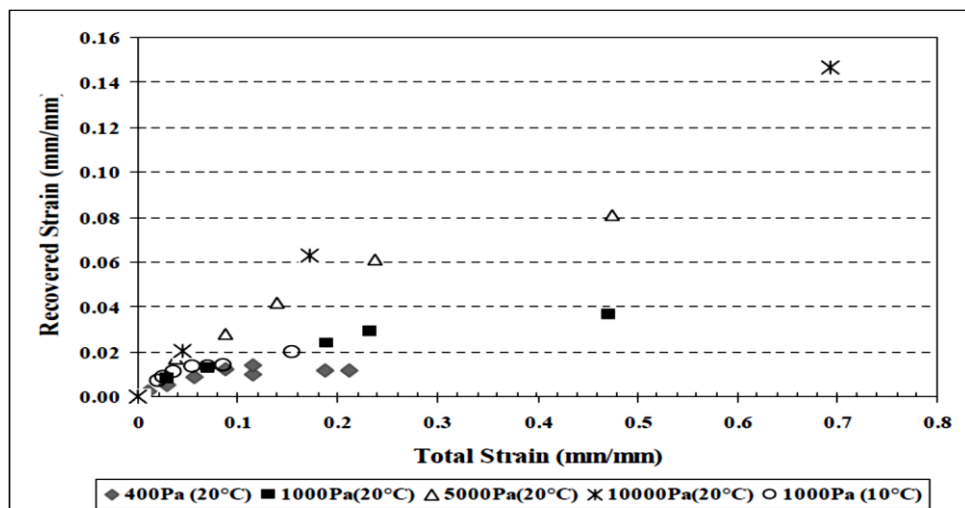
Figure 2.14 Summary of creep-recovery tests (Taherkhani, 2006)

2.4 Bitumen-Filler System

2.4.1 Introduction

Although a large number of rheological studies investigated the bitumen properties, pure or polymer modified, the fact remains that bitumen does not occur in its pure form in an asphalt mixture, but rather as bitumen-filler 'mastic'. Workability, compaction, voids in the mixture, and stiffness are among asphalt mixture properties affected by filler (Kavussi *et al.*, 1997, Hesami *et al.*, 2014). This section identifies fillers, their properties, and reviews bitumen-filler system (mastic) with a considerable emphasis on its rheological properties characterised utilising the DSR.

2.4.2 Mineral Filler; Definition and Properties

The fraction of aggregates passing sieve No.230 of size less than 63 μm is identified as filler. Different types of fillers are used in the asphalt mixture composition such as; limestone, Portland cement, hydrated lime, silt and volcanic ash (Osman, 2004). Filler particles serve as contact points between coarse aggregates and form with bitumen the 'effective binder' that keeps the aggregate skeleton adherent. The functionality of the binder is highly dependent on the filler properties and concentration (Kim *et al.*, 2003). Characterising fillers based on their properties is therefore crucial to understand their influence on the asphalt mixture performance.

Early research programs evaluated fillers based on soil mechanics tests such as liquid limit and plasticity index (Kavussi *et al.*, 1997). Later on, a wide range of tests have been established to deliver more associated properties

with the asphalt mixtures. Traxler (1936) classified filler characteristics into three groups:

- Primary characteristics: particle size, shape and size distribution.

- Secondary depend on primary characteristics: void content, surface area, average void diameter.

- Secondary mineralogical characteristics: texture, hardness, specific gravity, wettability.

Particle size distribution is a useful representation of the quantities available at each size of the total amount. The gradation of filler can be estimated through sieving or laser diffraction technique. Kavussi *et al.* (1997) found that large and angular fillers had more influence on penetration and softening point than fine and spherical shaped fillers. Chen *et al.* (1998) in their study concluded that the tensile strength of binder increases with the smaller size fillers because of their higher surface area. As the particle size increases the space distance between particles is shortened and the stress concentration area extends more, Figure 2.15.
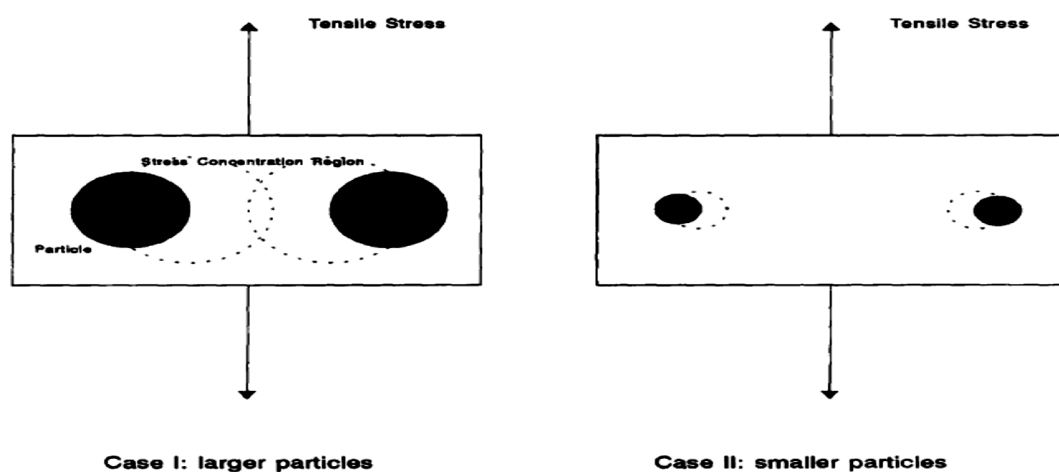
Figure 2.15 Stress concentration due to particle size (Chen *et al.*, 1998)

A number of studies emphasised the air void content in compacted filler as an important property that correlates well with the stiffening of binders (Shashidhar *et al.*, 1998, Faheem *et al.*, 2008, Kavussi *et al.*, 1997) and asphalt mixtures (Wang *et al.*, 2011). Void content is itself a function of particle size, size distribution, and shape. Consequently, this void content that represents the required bitumen amount in compacted filler is, at its least, an indirect measurement of these characteristics. To find this quantity, Rigden voids test was utilised (BS EN 1097-4:2008).

The test was developed by Rigden (1947) to investigate filler packing property in order to find the optimum bitumen content in mastic that maximize deformation resistance. The test apparatus (Figure 2.16) mainly consists of a dropping block with a cylindrical container filled with filler and a plunger. The test is performed by raising the whole block to a specific level and then leaving it to fall freely to the base for 100 times with approximately 1 s intervals. The void is then calculated based on the measured filler density, the measured weight, and the height difference before and after the test.

Key
1 Dropping block
2 Plunger
3 Base plate
4 Tare boring
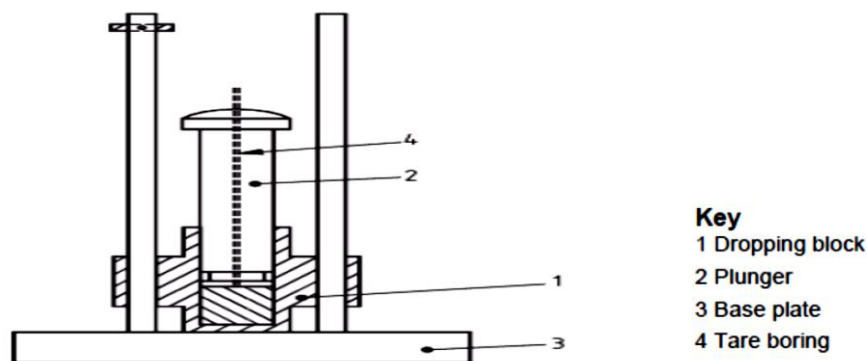
Figure 2.16 Typical compaction apparatus (Rigden, 1947)

Other properties like density, pH, specific surface area also provide good indications to the pavement performance against various distresses (Osman,

2004). However, as pointed out by Harris *et al.* (1995); one particular filler property may not be sufficient to fully characterise the filler and be used as a general performance indicator and the significance of the property varies with the purpose of the investigation.

2.4.3 Bitumen-Filler System

The investigation of the stiffening effect of filler on mastic started by measuring the change in properties of empirical tests (viscosity, softening point, and penetration) (Kavussi *et al.*, 1997). The mechanism at which filler interacts with bitumen and increases its stiffness is complex and extends beyond these simple tests estimations. Investigations progressed with a main focus on modified rheological properties of different mastics.

Soenen *et al.* (1999) blended four different bitumens with three filler types (quartz, Rhyolite, and Tuff) at three different volume concentrations (30%, 45%, and 55%). The three fillers were similar in their physical properties of density and specific area. Frequency sweep tests in the DSR were performed on mastics. The stiffening effect of mastic was evaluated through the stiffening ratio ($G^*_{mastic}/G^*_{binder}$).

Results from the test indicated that the relative stiffening is only dependent on the volume of filler concentration and independent on filler type and bitumen origin. In addition, at 45% and higher filler concentrations by volume, packing started to form and significantly influences the results.

Faheem *et al.* (2008) also studied the stiffening effects of filler type and content on binder performance against rutting and fatigue using DSR. Two

fillers (limestone and granite) were added at two different contents; 25% and 50% by volume of bitumen. For fatigue evaluation, the stiffening ratio was utilised. The stiffening effect on rutting was evaluated by comparing the terminal strain at the end of RCR test.

Results from fatigue tests exhibited a substantial improvement with limestone in comparison to granite. For rutting, adding filler enhanced the resistance and was significant when the content increased from 25% to 50%.

Liao (2007) tested bitumen with three filler types (limestone, cement, and gritstone) at different concentrations (0%, 15%, 35%, and 65% by mass) in the DSR at 40 and 60°C. ZSVs were measured by different tests; frequency sweep based on Cross model, stepped rotational viscometry (Figure 2.17), and RCR where ZSV was calculated at the last cycle.
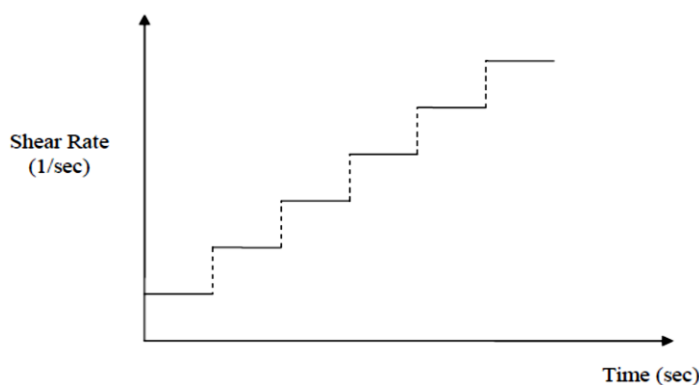
Figure 2.17 Stepped Shear rate mode (Liao, 2007)

Results revealed that the influence of filler type had a marginal effect on ZSVs values for 15% and 35% filler contents. With 65% filler, gritstone showed significantly higher ZSV values than limestone and cement. As concluded, at low (15%) and intermediate (35%) filler concentrations the behaviour is filler suspension system of mastic, while with 65% the filler skeleton is dominating the performance. A good correlation was found

between ZSV values measured from viscometry and RCR tests, while lower values were found from oscillation test due to the machine limitation of applying low frequency.

Taylor *et al.* (2010) studied the interaction of filler with binder in creep at different temperatures. The test consisted of 1 s loading of 2 kPa shear stress starting at 45°C up to 69°C at 4°C increment. Ten different fillers were mixed (0.3, 0.4, and 0.5 by volume) with three binder types. The stiffening of filler of each mastic type was evaluated through the creep compliance ratio of mastic over the pure bitumen.

The maximum packing fraction, $\emptyset_{max}$, at which mastic viscosity reaches infinity was introduced by Taylor *et al.* (2010). $\emptyset_{max}$ was determined by plotting the reciprocal of relative creep compliance ($1/J_{rel} = \frac{J_{mastic}}{J_{bitumen}}$) against different volume concentrations and then extrapolating to zero. At this point, the mastic creep compliance approaches zero and the volume reaches $\emptyset_{max}$. Different from Rigden voids, the measured $\emptyset_{max}$ via this technique contains the bitumen-filler interaction. No correlation was observed between $\emptyset_{max}$-Rigden measured in air and $\emptyset_{max}$ obtained from this method. A master curve of stiffening of each mastic type was plotted by normalizing the solid volume fraction by the maximum packing fraction ($\emptyset/\emptyset_{max}$) against the relative creep compliance, as shown in Figure 2.18. An exponential relationship was found between them where the stiffening increases considerably when $\emptyset/\emptyset_{max}$ exceeds approximately 0.7 ratio.
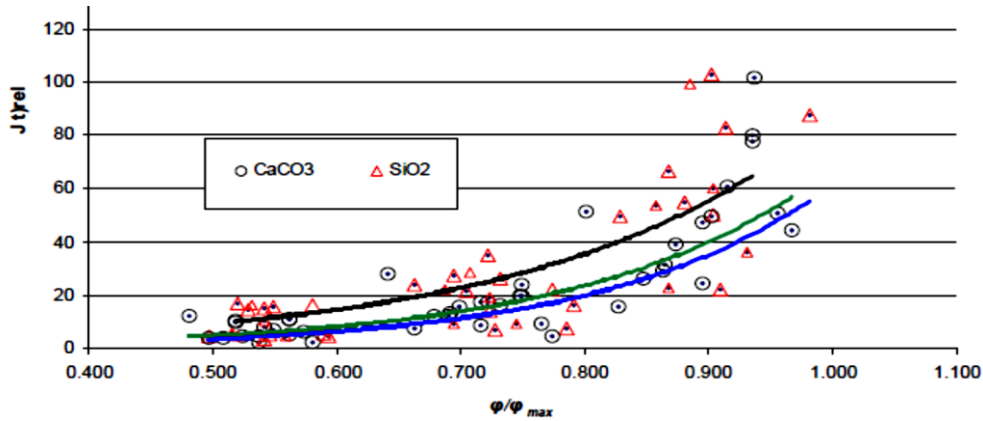
Figure 2.18 Stiffening of mastic in different bitumen types normalised for maximum packing fraction (Taylor *et al.*, 2010, Branco *et al.*, 2013)

There is a general agreement on filler stiffening the binder and enhancing its deformation resistance as mastic studies revealed. The significance of the stiffening was inclined to be dependent on the concentration more than the type of the filler. The mechanism by which filler stiffens binder based on the content can be speculated to follow two phases; diluted and concentrated (Faheem *et al.*, 2010).

In the dilution phase the interaction between filler and bitumen is minimal and the mastic/bitumen complex ratio follows a linear relationship with the filler concentration, Figure 2.19. When the concentrated region is reached the rate of the stiffening is in a higher degree indicating significant interactions. Between the two regions lies the 'critical filler concentration' at which the consumption of 'free bitumen' begins. The amount that fills the voids in compacted filler is termed 'fixed bitumen' and any amount that exceeds this limit is 'free' to coat aggregate or lubricate fillers and known as free bitumen (Harris *et al.*, 1995).
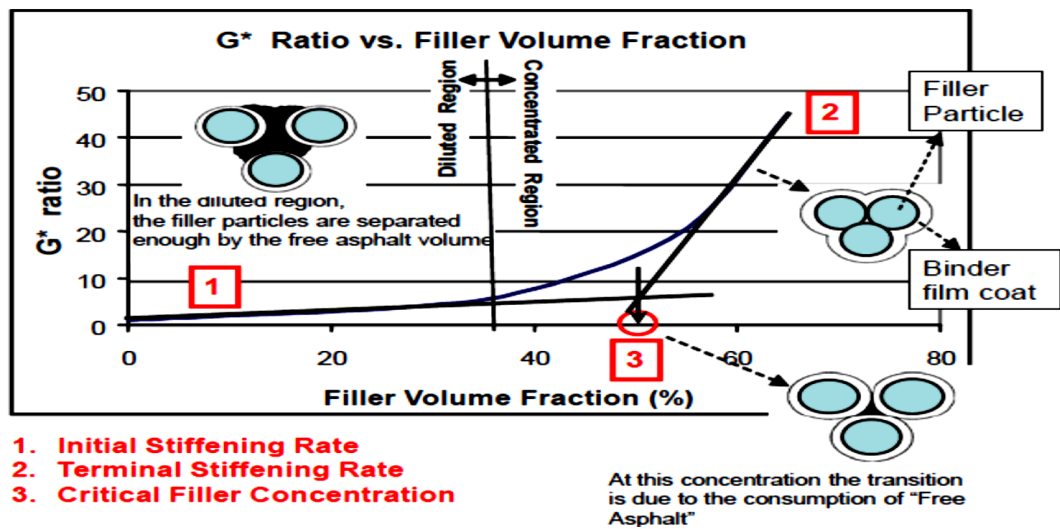
Figure 2.19 Mechanism of filler stiffening based on concentration (Faheem *et al.*, 2010)

Such a hypothesis can help in understanding and robustly modelling the stiffening effect of filler. One can assume two factors that control the stiffening effect; physical volume of which filler rigidity poses physical stiffening, and bitumen-filler interaction. The former can be seen to be more dominant at high temperature when bitumen is very soft and the effect on the interface can be considered negligible (Faheem *et al.*, 2010).

2.5 Mortar Mixtures

2.5.1 Definition

A second step after the mastic scale towards understanding the detailed asphalt mixture behaviour is to investigate the deformation behaviour at the mortar scale. Incorporating fine aggregates to the mastic provides an intermediate level between mastic and asphalt mixture; mortar mixtures. Representative mortars produced from a proper manufacturing procedure are required with the aim of accurate characterisation of interactions

between fine aggregate and mastic. This section reviews the development of different types of mortar mixtures and the properties of their steady state behaviour.

2.5.2 Single Sized Mortars and Steady State Behaviour

A simple recipe of a mortar mixture can be represented by idealised mixtures. Idealised mixture that contains fine aggregates of one size has been studied to simplify the complexity provoked by including various aggregate sizes in one mixture. Deshpande *et al.* (2000) prepared idealised mixtures of particle size from 2.36 to 1.18 mm, 600 to 300 μm, and 300 to 150 μm with 50 pen bitumen grade. Cylindrical specimens were manufactured by casting in prepared moulds through compaction in three layers by a mechanical plunger. Uniaxial constant stress and strain rate tests were performed at temperatures ranging from 0 to 40°C.

The SSSR against the steady state stress results were plotted as shown in Figure 2.20 with different volume fractions of aggregates. The figure also includes the MCM curve of the pure bitumen at 20°C. As can be seen, a similar trend to the bitumen is followed by the idealised mixture. The temperature dependency of the mortar steady state deformation was seen to be governed by the bitumen unconstrained by the aggregates. The stiffening effect of single sized aggregates was measured by a stiffening factor 'S' included in the MCM.
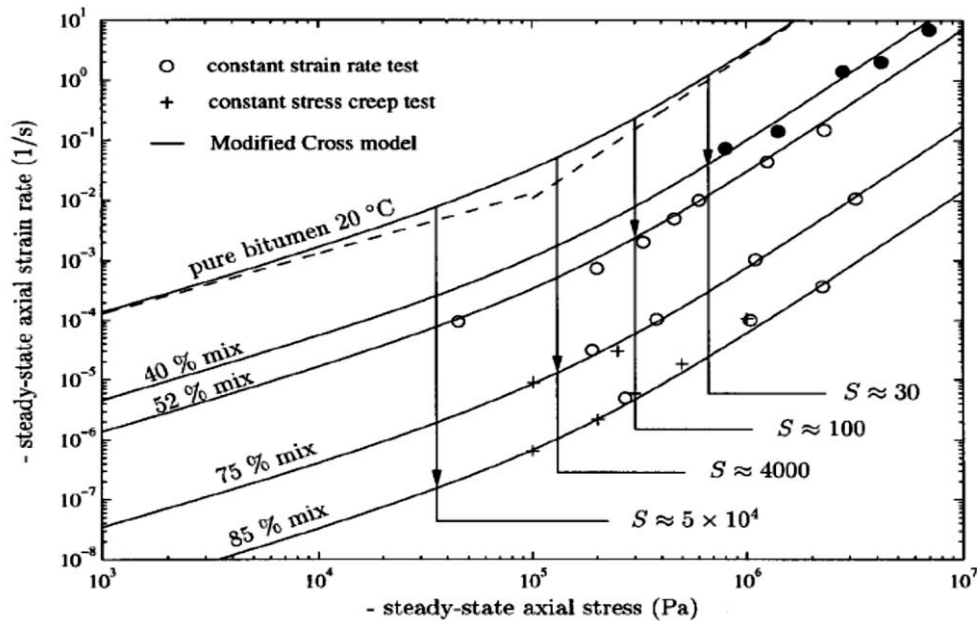
Figure 2.20 Summary of steady state deformation behaviour of idealised mixtures of different aggregate contents (Deshpande *et al.*, 2000)

Also two types of idealised mixtures of 64% aggregate volume (300 to 600 μm size) and 75% aggregate volume (37.5% of 150 to 300 μm, and 37.5% of 1.18 to 2.36 mm) were tested in triaxial by Deshpande et al. (1999) at 20°C. Again, the idealised mixes steady state had the same shape as the steady state of pure bitumen. The inclusion of fine aggregates increased the stiffness of the material and was found to increase with increasing the confinement pressure and the volume fraction of aggregates independent of the aggregate size. However, with larger fraction of aggregates the constitutive relationship may change from the pure bitumen as suggested.

Khanzada (2000) followed the work of Deshpande and studied the deformation behaviour relationships of idealised mixtures with the same volumetrics, applied in uniaxial static compression, repeated load axial (RLA) and simulative wheel tracking tests. Specimens were manufactured through vibratory compaction with variation in density between specimens

compacted in a single layer and compacted in three layers being less than 1%. The results from the uniaxial creep tests showed that above 500 kPa, the SSSR fitted a straight line with a slope of 2.4 indicating nonlinear behaviour. Less than 70 kPa, the experimental points fitted a straight line with a slope of approximately 1 by means of linear behaviour.

The RLA standard test applied stresses ranging from 50 to 100 kPa and the plot of the SSSR against the stress level showed a power law relationship with a slope varying from 1.1 to 1.5. These relatively lower slope values compared to the static creep test were due to the lower operating stresses in the equipment. Therefore, it was pointed out that the repeated loading technique could be utilised to rank rutting potential but with the inability to fully characterise the deformation behaviour.

Finally for laboratory scale wheel tracking tests on idealised mixtures over stresses ranging between 500 and 1500 kPa, the steady state rut rate after exceeding the linear region followed a nonlinear trend with a creep exponent that ranged from 1.9 to 2.4, similar to the creep exponent in the static creep test. It was therefore concluded that the static creep test proved to have the potential of characterising materials in terms of rutting resistance.

2.5.3 Mortars in DSR

Kim *et al.* (2003) produced another type of mortar (sand asphalt) and studied the material fatigue characteristics in the DSR. The driving force to study fatigue on mortar was under the assumption of crack initiation starts at a material level that exists between coarse aggregate particles. The mortar contained 8% bitumen by weight of the dry sand in mortar, arbitrary selected

to hypothetically represent an average value of 10 microns film thickness. Cylindrical samples were fabricated through compacting the mix in moulds by a static load. Samples were then glued to a holder in the DSR as shown in Figure 2.21. Amplitude sweeps as well as frequency sweep tests were performed to characterise the viscoelastic property. The efficiency of technique was proved by successfully establishing master curve diagrams and determining fatigue life.
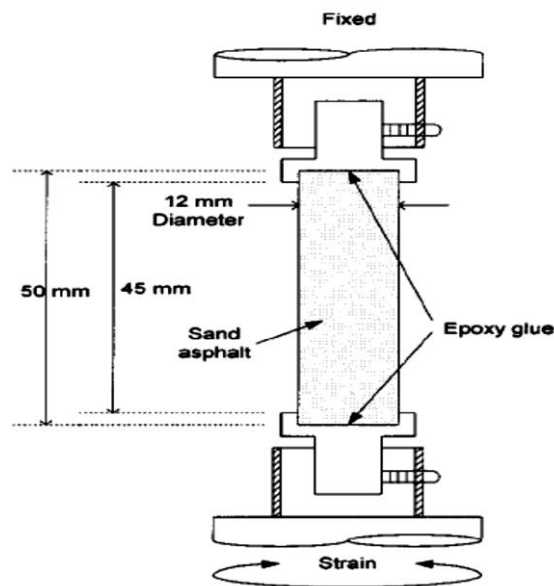
Figure 2.21 Cylindrical sample holding system in DSR (Kim *et al.*, 2003)

Zollinger (2005) followed the work of Kim and evaluated the moisture susceptibility of mortar samples of 1.18 mm maximum size fine aggregate using the DSR. The proportions of fine aggregates contents were the same as in the full asphalt mixture but normalised to the maximum sieve size. The mixture was produced by mixing filler (less than 75 μm) with pure bitumen by 10% of volume. 8% of the bitumen-filler by weight of the fine aggregate mass was then mixed and compacted with fine aggregates. It was found that using static load compaction method in moulds produced nonhomogeneous

samples with air voids concentrated more on top. Consequently, specimens were compacted using the Superpave gyratory compactor (SGC), trimmed to 50 mm height, and then cored to 12 mm diameter. A solid fixture system with glue was used to hold a sample in the DSR, Figure 2.22.
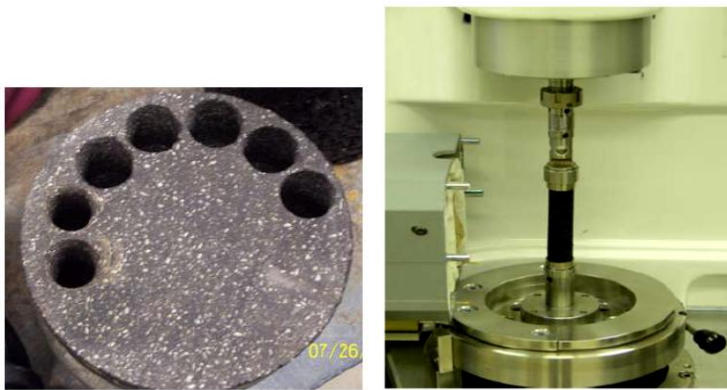
Figure 2.22 Cored specimen and sample mounted in the DSR (Zollinger, 2005)

Using x-ray scanning with imaging techniques, Izadi *et al.* (2011) confirmed that using SGC produced homogeneous air voids samples with microstructure that most closely resembles the mortar of asphalt mixture microstructure. In addition, two mounting setup procedures of mortar samples in DSR; gluing and steel-end clamps were compared by (Woldekidan, 2011) and revealed that the gluing method produced more repeatability.

Subsequent work on this type of mortar (fine aggregate mixture) followed the same fabrication protocol with SGC (Caro *et al.*, 2008, De Sousa, 2010, Cavalcanti De Sousa, 2013, Branco *et al.*, 2013) to characterise the moisture susceptibility and fatigue properties of the material. Others used different maximum size of fine aggregates to overcome the limitation of imaging technique and computational modelling (Underwood *et al.*, 2013).

2.6 Conclusions

The literature review introduced permanent deformation in flexible pavements and identified the influence of the composition on the performance. The following conclusions are drawn:

1- The steady state deformation behaviour of bituminous material was found to be linear at low stress levels and non-linear viscous at high stress levels. The recovered strain is independently proportional to the total strain before reaching a total strain limit after which it becomes constant.

2- While most published work from Europe has been concerned with evaluating binders to rutting based on their viscosity (ZSV for instance), work originated in the US has mainly concerned with ranking binders based on their recoveries in a multiple stress form (MSCR test). The former has not been standardised while the latter possesses some limitations.

3- To date, most rutting evaluation tests centred on assessing binder in a pure or polymer modified form. Binder in the asphalt mixtures contains filler. There is a lack of knowledge about the exact filler influence on the viscoelastic response in terms of permanent deformation. Ignoring filler in binder examination not only decreases the accuracy of the actual behaviour representation but also weakens the establishment of good correlations with asphalt mixtures.

4- Idealised mixtures follow the same pattern of the original bitumen steady state deformation behaviour in both uniaxial and triaxial conditions and is well represented through the MCM. Of the available techniques,

utilising the SGC produced advanced mortars that most resembles the asphalt mixture with homogeneity. Although utilised in fatigue, characterising fine aggregates mixtures in rutting through advanced mortar examination is poorly investigated.

3. X-Ray CT and Image Processing Techniques

3.1 Introduction

The spatial arrangements of the components in an asphalt mixture play a crucial part in its mechanical performance (Tashman *et al.*, 2007). The amount of research on the macroscopic behaviour is greater than the attention paid to the microscopic properties of asphalt mixtures. One primarily reason behind this is the difficulty involved in capturing the complex microstructure of the asphalt mixture (Hassan, 2012). Nevertheless, thanks to imaging technology and X-ray scanning, understanding the influence of the microstructural distribution on deformation is progressively improving.

In a number of earlier studies to capture images of some inner surfaces, specimens were cut into several sections to reveal some parts of the internal features (Hunter *et al.*, 2004, Abbas *et al.*, 2007, Coenen *et al.*, 2012). On the other hand, compared to other imaging methods, X-ray Computed tomography (CT) can reveal the entire internal microstructure of a material with the specimen still being intact for further testing. This makes the technique quite unique to provide images non-destructively that contain

valuable information on the spatial distribution not only of the surface but also deep inside at a micro scale.

This chapter seeks to briefly introduce the X-ray CT, imaging techniques, and the framework of the applications in the asphalt area.

3.2 X-ray System and Image Generation

The X-ray CT equipment consists of four main parts; an X-ray source, front and back filters, a manipulator, and a detector. The source emits an X-ray beam that is filtered before and after penetrating a specimen and finally received by the detector (Figure 3.1). When they penetrate a specimen, part of the X-ray energy will be absorbed (attenuation) depending on the material density. The difference between the intensity of the X-ray before and after penetration is used to distinguish between different materials. For each generated slice, the manipulator incrementally rotates the specimen to measure the attenuation at each orientation over 180°. By arranging and superimposing the orientation profiles according to their angles and positions, a 2D slice that displays the horizontal surface of the specimen is generated (Figure 3.2). Detailed explanations that address the fundamental principle of the X-ray CT can be found in the literature (Wang, 2001, Khan, 2010, Dhawan *et al.*, 2008, Synolakis *et al.*, 1996).

After completing the full rotation for generating a slice, the base systematically rises by a predefined distance before starting the scanning of the subsequent slice. The final set of slices depicted in 2D images visualises the internal microstructure of the specimen at a regular height and with

some applied image processing, measurements of various aspects can be obtained.
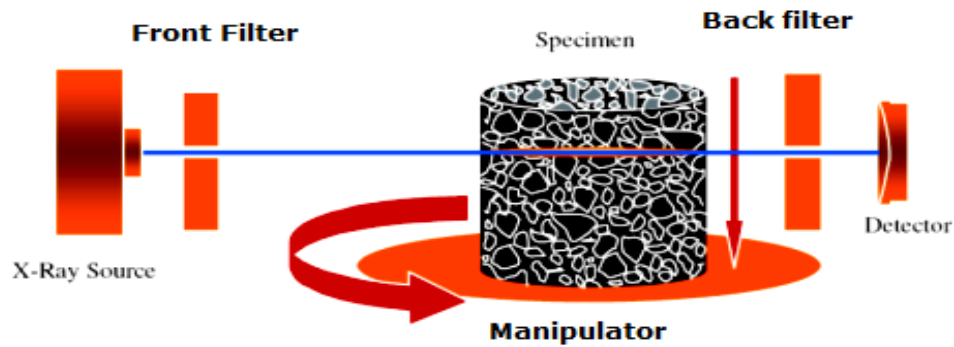
Figure 3.1 X-ray machine components (Tashman, 2003)
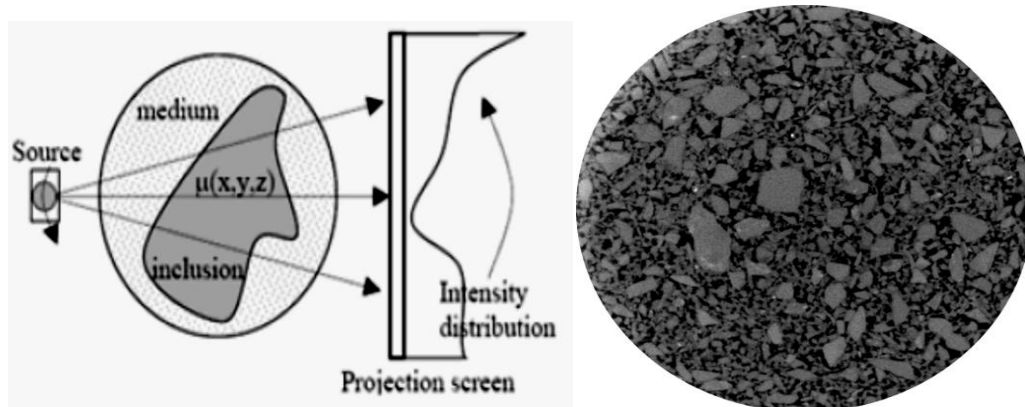
Figure 3.2 Intensity distribution in X-ray CT (Daigle *et al.*, 2005)

At the corresponding specimen altitude, the generated 2D image displays the spatial arrangement of the components in a pixel form. Pixel is the standard square unit in a 2D digital image, arranged as an array (Figure 3.3) and allocated a grey number (Romero *et al.*, 2001). For an 8-bit image there are 256 grey levels that each pixel in the image is painted conforming to the material density at that position. Typically, for an asphalt mixture; air voids are the darkest region, followed by the mastic (bitumen and fine aggregates) and then coarse aggregates as the brightest (Hassan, 2012). Before starting

any measurements, the image quality is improved by eliminating noise and artifacts.

Aggregate

Air void

Mastic
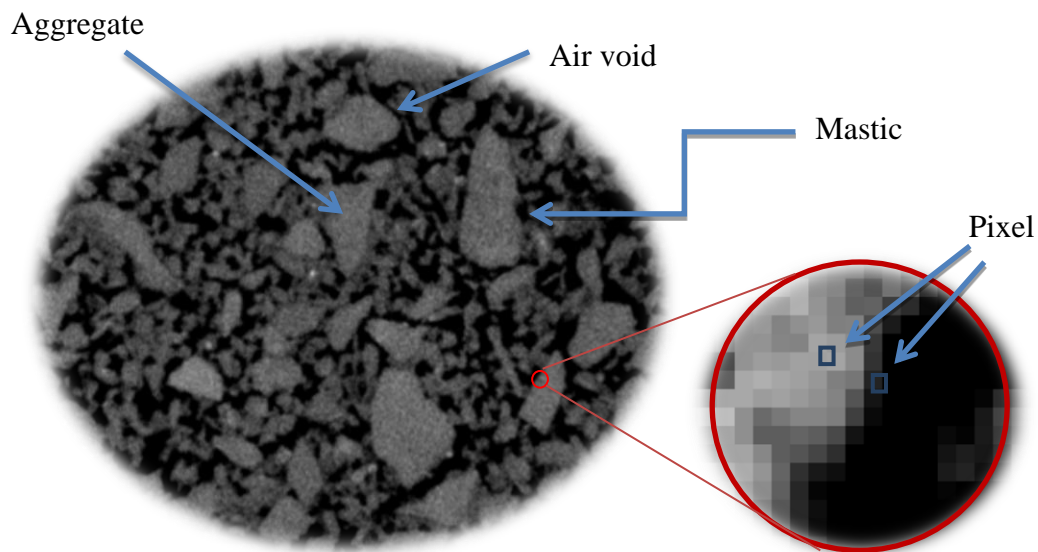
Pixel

Figure 3.3 2D pixel

3.3 Artifacts and Noise

Occasionally, image quality is reduced by noise or artifacts which lead to factual errors in the measurements (Ketcham *et al.*, 2001). Artifacts are generally defined as any feature that appears in the image but is not necessarily part of the scanned object, while noise is part of the scanned information that substantially decreases clarity (RAZAVI, 2006). Remedies of these obstacles range from adjusting the scanning system of the machine to applying image enhancement processes.

Beam hardening and ring artifacts are the most common artifacts. Hardening manifests itself as a non-uniform brightness in the image as shown in Figure 3.4. The reason behind this is the variation in the attenuation between the X-rays that penetrate different distances through the sample cylindrical face.

One way to reduce this is to increase the energy of the X-ray beam or adjusting the back and source filters (Khan, 2009, Onifade *et al.*, 2013).

When the specimen rotates during the scanning operation, particularly with a relatively light weight, specimens can lose their alignment and shift from the centre of the base (Khan, 2009). This will result in rings that appear in the image (Figure 3.4). In addition, scanning conditions such as the temperature, energy level, back and source filters, and data acquisition time can cause the detector to respond differently. Therefore, frequent calibration and control are essential to minimise the defects (Hassan, 2012).
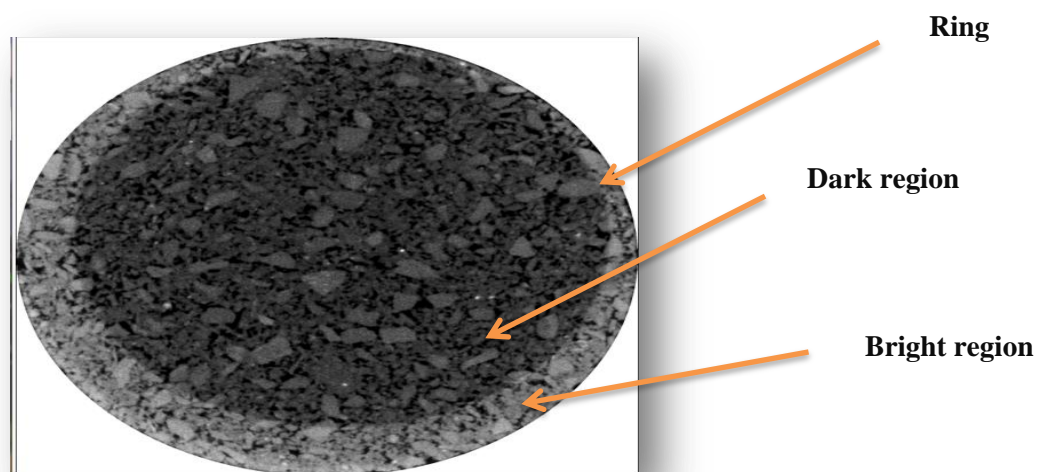
Figure 3.4 Beam hardening and ring artifacts

3.4 Digital Image Processing

3.4.1 Introduction

Digital image processing (DIP) is defined as the process of applying algorithms to enhance the quality and extract reliable information from the image (Masad *et al.*, 1999b). It comprises three main consecutive stages; contrast enhancement and noise removal, thresholding, and post-processing.

Only the utilised filters in this research are addressed here, more details about other filter types can be found elsewhere.

3.4.2 Contrast Enhancement and Noise Removal

Noise adds spurious information and the contrast limits the distinction between different phases. After the removal of the background outside the specimen boundaries in the images, it is vital to enhance the contrast effectively, filter and remove noise to improve the measurements accuracy. A wide range of filtering tools exists to enhance images, however, care should be taken as inappropriate selection may reduce the amount of data rather than rearrange it (Tashman *et al.*, 2007).

Low contrast in an image makes the process of segmentation between different phases extremely difficult. Locally, the different mineral composition of aggregates affects the absorption of X-rays and results in dark and light grey (non-uniform pixel intensity) levels of aggregates (Hassan *et al.*, 2012). Fortunately, the contrast can be improved by performing a contrast enhancement operation. The most common methods include normalisation and linearization, shown in Figure 3.5. The former enhances the contrast through redistributing the grey intensity linearly to the full grey range (0 to 255), while the later increases the contrast in large areas of limited grey variation and reduces the contrast of small areas with high contrast variation (Offrell *et al.*, 2004).
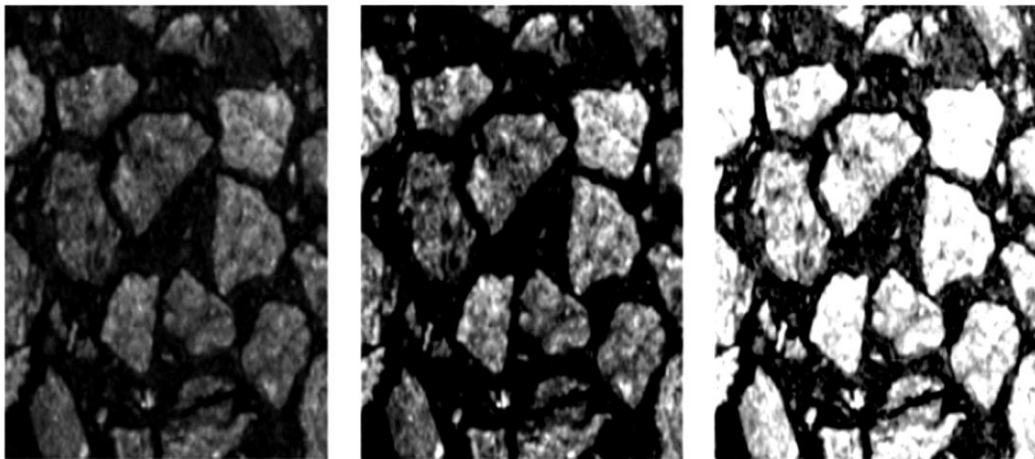
Figure 3.5 Original, normalized and linearized images respectively (Offrell *et al.*, 2004)

For filtering, the most utilised for noise reduction are the neighbourhood category; mean, Gaussian, and median filters. In this group, a neighbourhood window is identified as an N x N pixels matrix in which N can take a value of 3, 5, 7 or 9 (Zelelew *et al.*, 2011). The mean filter replaces the grey level of all pixels in the neighbourhood by the average grey level. While this will decrease the variation of the grey level between neighbourhood pixels and may reduce the threshold accuracy, Gaussian filter weights differently depending on the window position. The median filter works better by replacing the pixels in the neighbourhood by the median grey level with the advantage of edge preservation (Offrell *et al.*, 2004). This is illustrated in Figure 3.6 where the three filters have been applied on the same image.
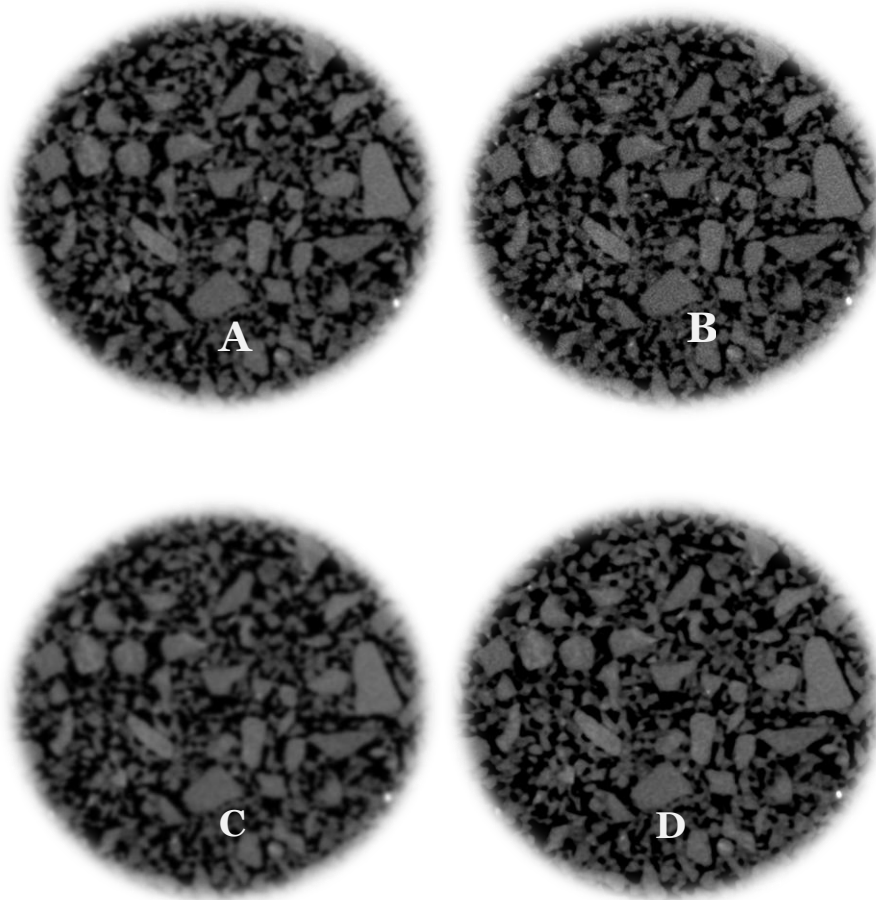
Figure 3.6 Filtering on images: (A) Original, (B) Averaging, (C) Gaussian filter, and (D) Median filter

3.4.3 Thresholding

A key to reliable measurements is a well segmented object through the thresholding technique (Tashman *et al.*, 2007). Thresholding is identified as the process of segmenting a division of interest and removal of the remaining features in the images. In detail; the binary image is converted into a grey scale image, the object of interest is branded through highlighting its corresponding grey range, and then the data of grey levels outside that range are eliminated (Figure 3.7). For 8-bits images there are 256 grey levels by definition and a histogram can be established. A histogram is a graphical representation of the number of pixels at each grey level (Figure 3.8).
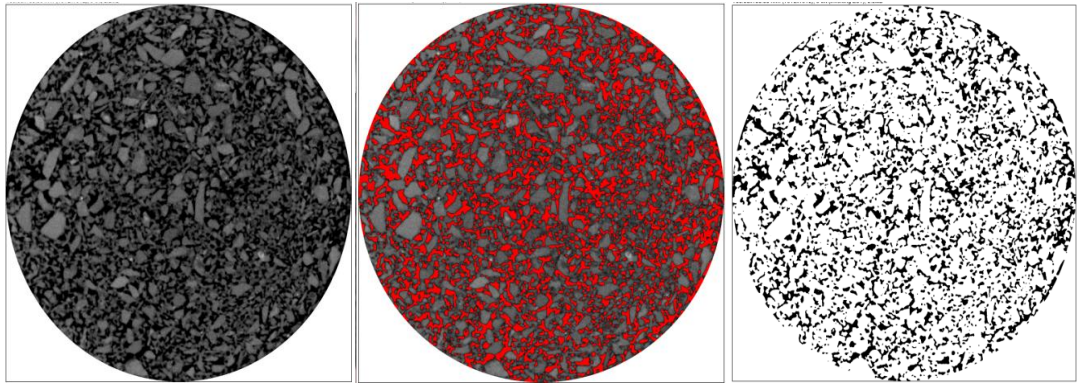
Figure 3.7 Thresholding of air voids in an image
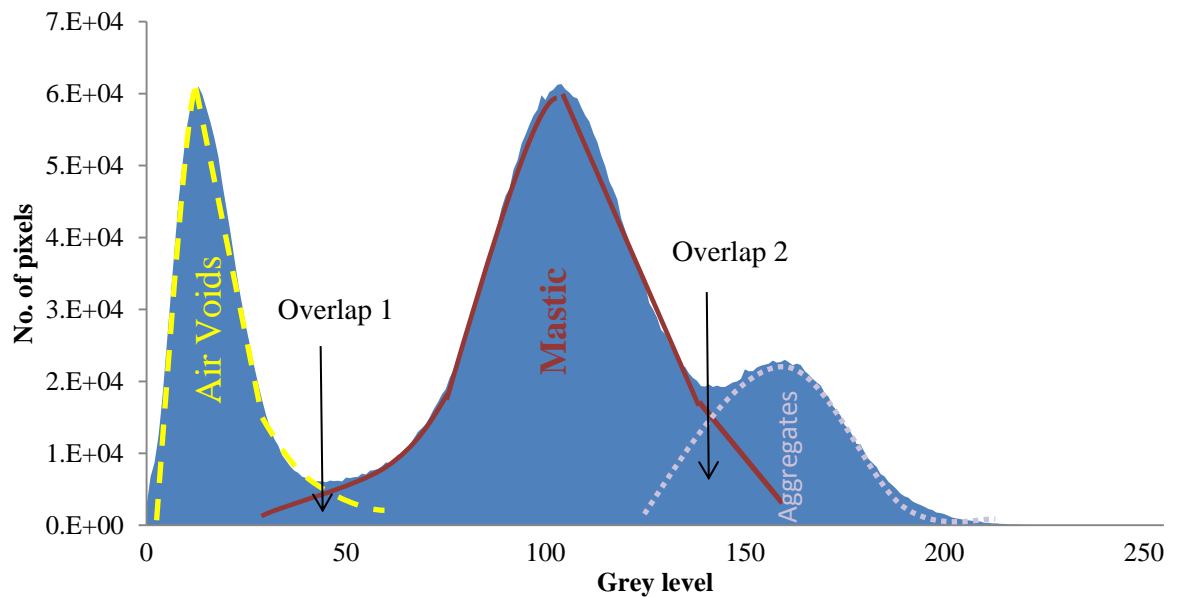
Figure 3.8 A histogram of asphalt mixture

The histogram of a composite, as for asphalt mixture, usually has peaks separated by trenches. This complicates the segmentation process as the trench is an overlap region between different phases and to isolate each phase there is a requirement to identify a specific grey limit within the overlap region. For instance in Figure 3.8, the air voids phase lies between 0 and a grey limit in overlap 1. This obstacle leads to over/under estimation of the components of the mixture and hence incorrect representation of the real quantities. Nevertheless, different techniques were developed to optimise the threshold process.

The 'line-profile' method presents on a graph (Figure 3.9 (A)) the grey value at each distance along the drawn line on the image. This provides estimation to the grey range that each phase occupies. Especially with aggregates of a wide range of mineral compositions, the line criteria may not entirely show the total range of grey level for a phase. In addition, the method is based on visual assessment of the position in which small air voids may not be noticeable. Hassan (2012) applied 'pseudo colour' technique to reveal hidden objects that may not be visible through the grey scale. In this method, each material phase is assigned with a colour spectrum which facilitates the recognition of hidden objects as shown in Figure 3.10.
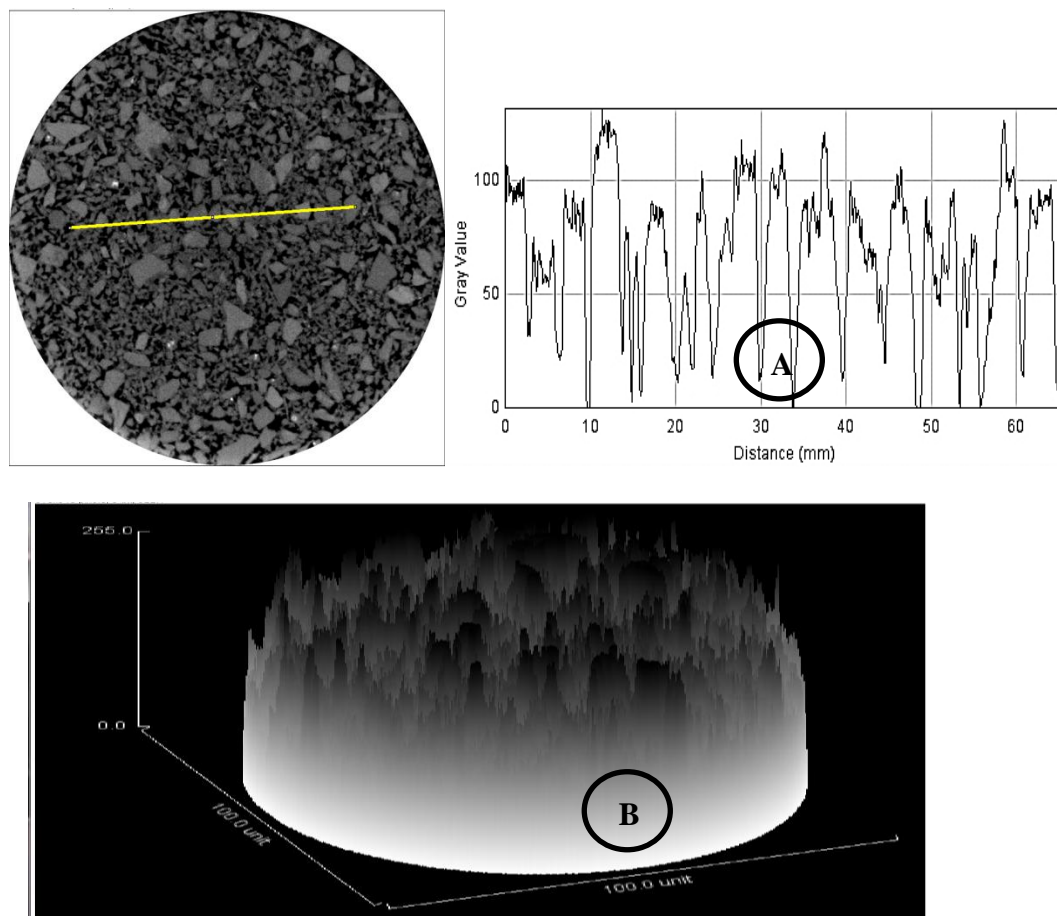
Figure 3.9 (A) Line histogram (B) Surface histogram
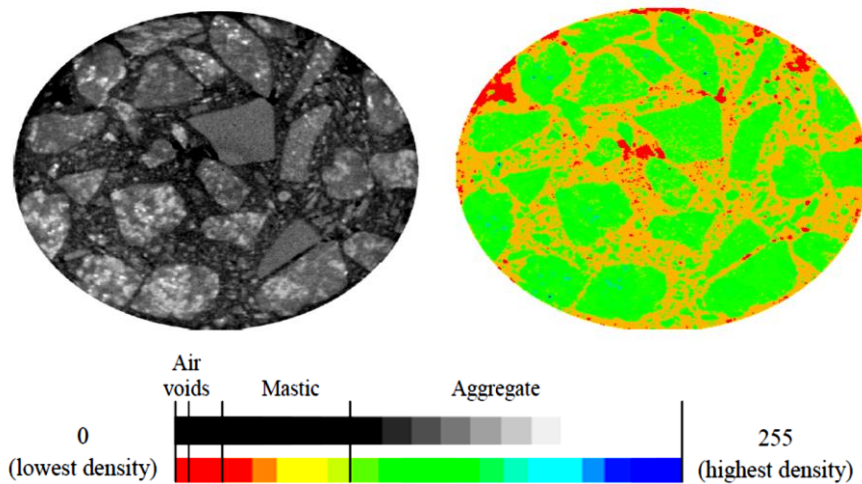
Figure 3.10 Pseudo colour thresholding method (Hassan, 2012)

The volumetric technique based on surface histogram plot has been utilised in this study (Figure 3.9-B). Compared to other methods, it takes into account the complete range of grey level of each object, inspired by (Arambula *et al.*, 2007). Through ImageJ, the histogram is converted to a list of two data columns counting the number of pixels in each grey value. Next, the cumulative number of pixels at each grey value is calculated as a % of the total accumulated number of pixels. The grey level that corresponds to the %accumulated number of pixels conforming the actual volumetric in the specimen is selected as a threshold limit. This method is therefore more representative in terms of volumetrics and is easy and simple to perform. Additionally, the Gaussian smoothing operation can be used before thresholding to help in reducing the overlap regions through redistributing the grey scale to the full range (0 to 255) (Tsai, 1995).

Although a number of studies suggested different techniques to optimise the threshold, the fact remains that establishing a standard method is controversial. The X-ray resolution, different types of scanned objects,

imaging software capability, and human error are influential factors that require applying different types of thresholding for different images.

3.4.4 Post-Processing Enhancement

Once the thresholding is completed, some enhancements are applied for more precise representation. Due to the limitation of X-ray resolution, small size aggregates are displayed as part of the mastic (invisible). Additionally, aggregates may contain holes (missing pixels) due to variation of the mineralogical composition in aggregates as well as touching aggregates have the potential to appear as a single large aggregate or at best; the features between these particles are indistinct (Figure 3.11).
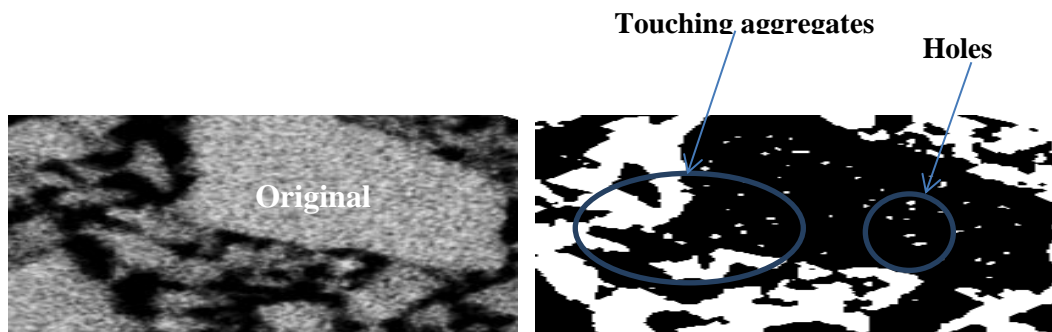
Figure 3.11 Touching aggregates and holes after thresholding

Small size aggregates can be considered as a part of the mastic and not included in the aggregates analysis. Consequently, a clear identification is required to an aggregate size limit that is primarily determined by the X-ray resolution between the division that is to be counted as a part of the mastic and the detectable aggregates division. For missing parts of aggregates 'Fill holes' operation can serve efficiently. Other filters like 'Dilute' can also fill the gaps but will lead to over estimation as boundaries of objects are customarily extended.

Several studies suggested using the Watershed operation to automatically separate touching aggregates (Bruno *et al.*, 2012, Zelelew *et al.*, 2013, Kutay *et al.*, 2010). However, this algorithm over-segments the image and outcomes tiny particles due to irregularity of grey scale aggregates as shown in Figure 3.12 (RAZAVI, 2006). An alternative is through applying the 'Outline' tool to detect edges combined with 'Erode' to separate joined aggregates.

Figure 3.12 Aggregates segmentation processes (A) Original, (B) Watershed, (C) Erode + Outline

Applying the previously mentioned filters and image processing tools, inclusively or partially, and their arrangement varies depending on the image quality as a universal method that can adapt different images is not available (Hassan *et al.*, 2012). Finally, images are rescaled by transforming the pixels numbers into an SI unit before starting measurements on the binary image.

3.5 Measurements from DIP

Identical asphalt mixture samples sharing the same content of total air voids may perform differently under typical loading conditions. This is attributed to the structural arrangements of the components and their characteristics.

Binary images are a rich source of information that can be utilised to describe the structural arrangements and their influence on the performance. The measurements are based on the concept of Stereology where the quantities obtained from a 2D plane represent the 3D features. For instance, the 2D area of an object in the image is calculated through measuring the number of pixels occupied. Then, the area fraction obtained in the 2D images quantifiably corresponds to the 3D volume fraction (Hassan, 2012).

Image processing software, like ImageJ, offer various parameters that describe the distribution and characterise the shape such as: area, Feret's diameter (the longest distance between two points within the boundary), perimeter, centroid, circularity, etc. The following equations define some of the parameters obtained at each slice:

%Area = ($\sum$ area of objects/Area of the slice)x100

Average size = $\sum$ area of object/Number of objects

Circularity = 4πArea/(Perimeter)^2

An air void would have a circularity value close to 1.0 while an elongated crack would have a low circularity value (close to 0.0). This information can be used to distinguish between air voids and cracks developed from deformation (Tashman *et al.*, 2004). Eccentricity (coordinates) describes the distribution of the voids between the centre and the circumference of the circle (i.e. near to the centre or the circumference) (Tashman, 2003).

Since the mixture is heterogeneous, local information can be compared between different parts within the specimen geometry. For instance, the core

and ring method recognizes the difference in the property in the radial direction. The phase within a defined boundary (a ring or circle) can be segmented as shown in Figure 3.13 (Hassan *et al.*, 2012). In addition, shape parameters can be used to characterise aggregates in terms of angularity, form, and texture to study the impact on the asphalt mixture performance (Masad *et al.*, 2003).
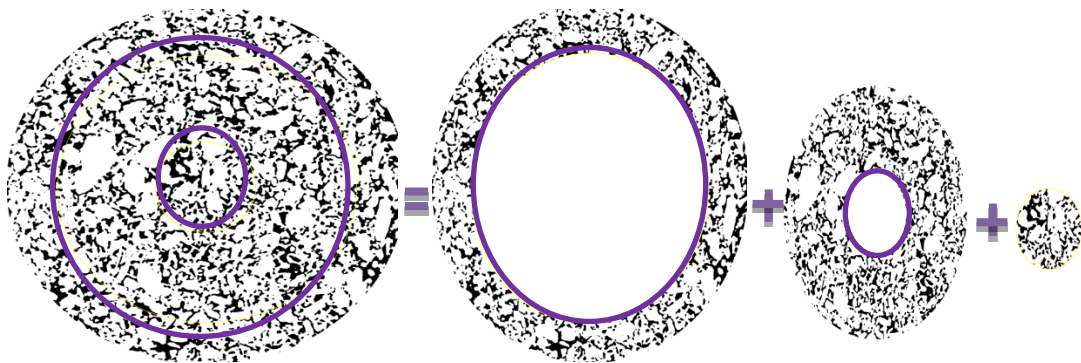
Figure 3.13 Illustration of core and ring virtual cutting technique

3.6 Applications of X-Ray Images on Asphalt Concrete

The applications of X-ray CT in the asphalt mixtures investigated a wide range of interesting aspects. This section seeks to cover related advancement in utilising X-ray CT to determine the microstructure of manufactured specimens and the influence on the mechanical performance.

Masad *et al.* (1999a) investigated the evolution of the internal structure during Superpave Gyratory compaction (SGC) at different levels of compaction (Figure 3.14). It was found that up to a certain limit of compaction, the orientation of aggregates towards the horizontal direction increased after which it started to decrease. With higher number of gyrations

the specimens tended to reduce the air voids content, and led the middle part to become more compacted. On the contrary, Lo Presti *et al.* (2014) found that some SGC specimens had more air voids in the middle than the bottom and top parts. It was concluded that the response to SGC depends significantly on the height and diameter of the specimen that determine the amount of transmitted energy. In general, increasing specimen height results in heterogeneous air voids distribution within the height.
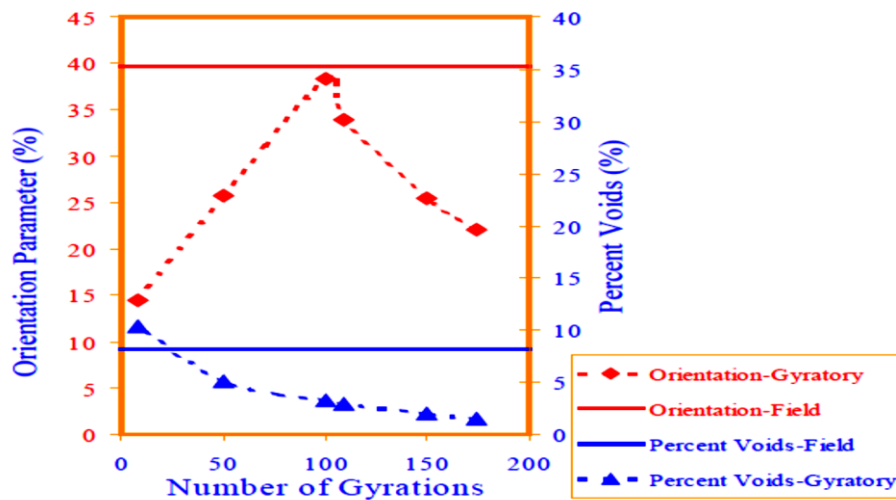
Figure 3.14 Effect of the number of gyration on the void content and aggregate orientation in the SGC (Tashman *et al.*, 2007)

Hassan *et al.* (2012) conducted a comparison between the effect of different compaction methods (gyratory, vibratory and slab rollers) on the aggregate structure. Specimens were sectioned vertically to inner (core) and outer (ring) parts, and horizontally to top and bottom sections through imaging techniques. Coarse aggregates were found to be more concentrated in the bottom part of all specimens due to gravity. For gyratory and vibratory prepared specimens, the inner section showed slightly more content of coarse aggregates than outer section. In the roller compactor, finer aggregates were found to be more concentrated in the outer section of the specimen. This was

attributed to the cutting process in the prepared slab which tended to reduce the size of aggregates in the outer section of the specimen. In terms of orientation, for all types of compaction method, aggregates closer to the centre of the specimen were found randomly distributed while aggregates near the edge preferred to form a circumferential alignment.

Generally, air voids are considered the primary parameter of damage and the main factor to investigate permeability of the material. Tracking the water in the images can be utilised to study the permeability, degree of saturation, and hence moisture damage (Arambula *et al.*, 2007, Khan *et al.*, 2010). Additionally, several studies investigated the air voids characteristics as a parameter to study the deteriorating of the resistance of the pavement. Air voids reduce the effective load transmitting area and hence weaken the material and accelerates the deterioration (Abdul Hassan *et al.*, 2014).

Damage evolution in specimens loaded for mechanical testing can be investigated by comparing the change in the characteristic parameters before and after the test. Khan (2010) found a non-uniform increase in air voids (damage) throughout the specimens in a strain rate test. In addition, specimens tested at high temperature and low strain rate exhibited a greater increase in air voids.

Tashman (2003) investigated damage evolution in specimens loaded in triaxial compression at several pre-identified strains. The study revealed that damage is a localized phenomenon in which a critical section exists within the specimen that leads to failure. The critical section develops larger crack growth higher than the rest of the specimen. Comparing the increase of air

voids between the top, middle, and bottom sections of the tested specimen (Figure 3.15) exhibited significant cracking, dilation, and minor structural change respectively. This emphasises the need for homogenous material manufacturing through laboratory compaction.
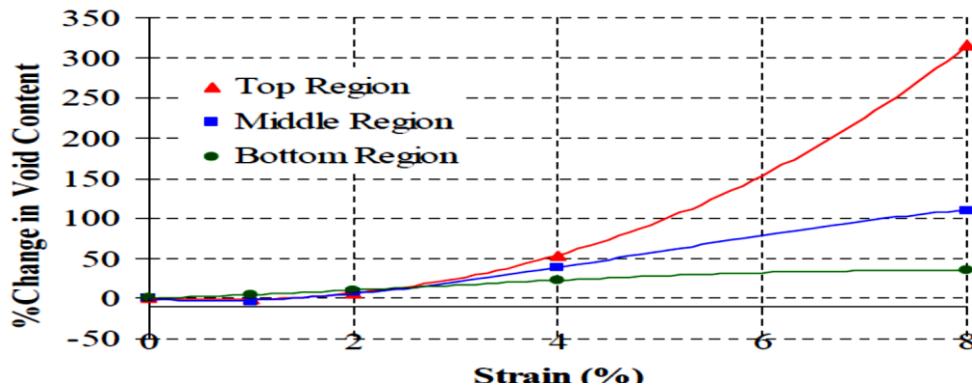
Figure 3.15 Change in the air voids content at different strain levels of the top, middle, and bottom sections of specimens (Tashman, 2003)

The effect of rubber addition on the air voids properties of asphalt mixture was studied by (Hassan, 2012). In comparison to the control mixture (0% rubber), the 2% modified mixture displayed a non-uniform air voids distribution along the height. When the rubber content was increased to 3% in the mixture, the air void distribution displayed less variation between the top, middle, and bottom sections. In addition, increasing the rubber content from 2 to 3% developed 70% increase in the number of air voids, while the control mixture had the highest number as well as the most circular shaped air voids. After applying constant strain rate tests up to approximately the highest stress level at 40°C, the 3% and 0% rubberised mixtures exhibited more damage in the middle than the top sections of the specimen. This highlights the importance of characterising the air voids properties in local sections rather than considering the total air voids content as the middle region had the lowest air voids content before testing.

Monotonic constant strain and triaxial repeated creep and recovery tests were applied on asphalt mixture specimens to an identical final strain level by Saadeh (2005). Comparing the pair of X-ray images before and after testing, it was observed that with the same observed macroscopic strain level, the different loading conditions and stress levels resulted in different microstructural distribution. In addition, specimens in triaxial testing showed less dilation than constant strain tested specimens.

3.7 Summary

X-ray CT is a powerful technique to investigate the internal microstructural of asphalt mixture specimens non-destructively through generated 2D images. This chapter has briefly introduced the fundamental principle of X-ray CT and images generation. Noise and artifacts as part of the system were outlined. As has been presented, effective digital image processing is a key factor to remove noise and enhance image quality to enable the extracting of reliable information. Overall, a standard method to process images and obtain the optimum accuracy is difficult to identify as different generated images and processing environments require irregular processing methods.

The application of X-ray on asphalt mixture has found an extensive interest in different aspects including but not limited to: compaction method characterisation, permeability and water damage, damage evolution, and test conditions. For this study, a key factor to identify the role of air voids and aggregates on the rutting performance is to involve the X-ray CT and image processing techniques.

4. Binder Shear Creep and Recovery Characteristics

4.1 Introduction

The mechanical properties of asphalt mixtures are to a great extend influenced by their binders' viscoelastic properties. In order to improve the understanding of permanent deformation behaviour of asphalt mixtures, a large number of studies investigated the viscoelastic behaviour of bitumen (pure and modified) (Collop *et al.*, 2002, Vlachovicova *et al.*, 2007, Yusoff *et al.*, 2011, Santagata *et al.*, 2013). Bitumen, however, is not alone in an asphalt mixture but with filler constitutes mastic; the cement of the asphalt mixture.

For more accurate representation and stronger correlation with asphalt mixtures, this chapter focuses on mastic rheological properties where bitumen-filler interaction is considered. Two filler types of limestone and granite are mixed with base bitumen in three concentrations to represent the suspension state as well as particle-particle contacts of filler. An intensive experimental program comprising creep and creep-recovery over a wide range of temperatures and loading conditions is detailed. In addition, the viscoelastic behaviour is simulated through a mechanical model and characterised via a molecular model.

4.2 Material Selection

4.2.1 Bitumen

For this study conventional 40/60 penetration grade bitumen was selected as it is widely utilised for asphalt pavement construction in UK. This straight-run bitumen was supplied by Nynas Bitumen Limited. According to BS EN 2000-49:2007 and BS EN 2000-58:2007, the penetration grade and softening point were found to be 40 dmm and 53.8°C respectively.

4.2.2 Mineral filler

In this study filler is identified as particles passing sieve No.230 (63 μm). Two types of mineral filler of limestone and granite were chosen. Limestone was the major selection because of its frequent use in asphalt paving mixtures. It primarily consists of calcium carbonate and is considered chemically stable with little reaction with bitumen (Liao, 2007). The second filler is granite, which is of a type typically used in pavement construction.

Limestone filler was brought from Torr quarry while the granite was supplied by Bardon Hill. The density of limestone and granite fillers based on BS EN 1097-7:2008 was found to be 2.72 and 2.82 Mg/m^3 respectively. According to BS EN 1097-4:2008, the volume of air filled space in the compacted filler (Rigden's voids) was measured to be 26.16% for limestone and 37.62% for granite. The variation in void content in dry compacted filler can be attributed to the geometrical irregularity related to differences in particle shape, texture, and size distribution (Traxler *et al.*, 1933).

4.3 DSR Machine

Dynamic Shear Rheometer (DSR) machines are used to characterise the viscoelastic properties of binders through measuring their rheological parameters over a range of temperatures, load levels and frequencies. The instrument set-up comprises two metal plates sandwiching the sample, a loading unit connected to the upper plate, an environmental chamber for temperature control, and a data acquisition system. The plates are available in 8 mm or 25 mm diameter size, and the upper plate (spindle) can take a smooth flat or a conical geometry. The temperature is controlled by a chamber that continuously supplies circulated water from a separate bath temperature unit. The loading unit is made of a motor shaft connected to the spindle to deliver the required force. The test temperature, strain, angular rotation and other optioned results are continuously recorded and displayed live through the data acquisition system.

Figure 4.1 Gemini DSR type

In this study, a Bohlin Gemini 200 DSR was utilised to perform the required tests, shown in Figure 4.1. The Gemini can apply torque up to 0.2 N.m that

can produce maximum shear stress of 1.99 MPa and 65.18 kPa through the 8 and 25 mm diameter spindles respectively. The sample is always sandwiched between the lower plate and the upper spindle all submerged inside a water chamber to reduce any thermal gradient and thermal equilibrate the sample, as presented in Figure 4.2. During the test, the lower plate remains fixed while the upper spindle rotates to implement one of the following tests: oscillatory, relaxation, viscometry, and creep/creep-recovery test.
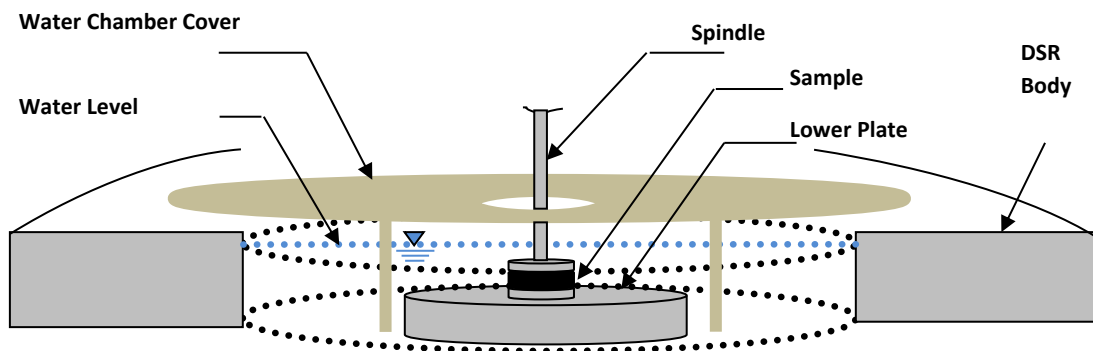
Figure 4.2 Submerged sample in DSR

In the oscillatory test the upper plate rotates in a reversible movement of a sinusoidal fashion within a selected amplitude and frequency. On the other hand, the rotation is kept in one direction when viscometry, relaxation, or creep test type option is selected. Both viscometry and relaxation tests operate under controlled strain mode while creep test is performed in a controlled stress condition.

The creep test in DSR is employed to study the shear deformation behaviour of the bitumen. The spindle moves continuously in one angular direction at a preselected magnitude of constant shear stress for a predetermined time. The automatic machine will quickly apply the required torque to the upper plate to achieve the targeted shear stress. The resulted strain is continuously

calculated at the edge of the upper plate through measuring spindle angular rotation. When the recovery option is selected, after completing the creep loading period, the spindle is freed from any force and the resting sample is continuously monitored (strain at the edge) for a preselected period of time. The controlling parameters are calculated based on the following equations:

$$\gamma = \frac{\theta r}{h} \tag{4.1}$$

$$\tau = \frac{2T}{\pi r^3} \tag{4.2}$$

$$\gamma^* = \frac{\theta^* r}{h} \tag{4.3}$$

Where γ = shear strain, θ = angular rotation, r = radius of the plate, h= gap between the plates=thickness of the bitumen sample, τ= shear stress, T =torque, γ^* = shear strain rate, and θ^* = angular velocity.

The above equations express that the shear stress and shear strain are functions of the radius varying from zero at the centre of the sample to the maximum at the edge. Test results of shear stress and shear strain are calculated at the edge of the spindle (maximum values). Equation (4.2) indicates a linear relationship between shear stress and torque. The instrument can only apply a limiting maximum torque. Consequently, when it is required to apply high stresses, especially with stiff material at low temperature, the 8 mm plate should be utilised (Rahimzadeh, 2002, Airey *et al.*, 2003).

4.4 Sample Preparation

4.4.1 Filler Content

Two mastics of limestone and granite, each at three concentrations (35%, 50%, and 65% filler content by mass of mastic) were used for this study, in addition to the base bitumen. These proportions by mass were selected based on a standard asphalt mixture as will be discussed later. Filler concentration by mass in mastic can be calculated based on the following equations:

$$F_m = \frac{\text{Mass of filler}}{\text{Mass of filler} + \text{Mass of bitumen}} \tag{4.4}$$

The determination of filler content by volume in mastic is given by:

$$F_v = \frac{\dfrac{F_m}{SG_F}}{\dfrac{F_m}{SG_F} + \dfrac{B_m}{SG_B}} \tag{4.5}$$

Where: F_v = Filler concentration by volume, F_m = Filler concentration by mass, B_m = Bitumen concentration by mass, SG_F and SG_B = Specific gravity of filler and bitumen respectively.

According to BS EN 4987-1:2005 and for 10 mm dense bitumen macadam (DBM), asphalt concrete closed graded surface course, the bitumen content in the mixture is 5.2% while the filler content is recommended to range from 3% to 8% of the total aggregate by mass. The equivalent filler content by mass of mixture is between 2.85% and 7.6% which corresponds approximately to 35% and 65% content in the bitumen-filler mastic.

Consequently, mastics were prepared at these limits plus at 50% as a midpoint representing practical mixtures and to investigate the influence of filler content gradual increase. Table 4.1 presents the ID of each binder type and filler contents based on mass and volumes.

Table 4.1 Samples IDs and filler contents

Code	B	M35	M50	M65	M35-2	M50-2	M65-2
Filler type	_	Limestone	Limestone	Limestone	Granite	Granite	Granite
% of total mass	–	35	50	65	35	50	65
% of total volume	–	17	27	41	16	27	40

4.4.2 Material Preparation

Rheological testing of binders requires careful material preparation as the consistency of testing results is determined by the samples uniformity. Additionally, the utilised DSR Gemini 200 is regularly calibrated to maintain repeatable and consistent results. Initially, the bulk quantity of bitumen in the container was heated in an oven to 160°C (approximately the softening point + 100°C). The heating was maintained for a sufficient time until all the bitumen was in a liquid form (especially at the bottom of the container) and continuously stirred gently to achieve homogeneity. For pure bitumen samples (0% filler), the heated bitumen was immediately distributed into 10 ml vials and stored at 5°C for later testing.

For mastic samples, the required mass of heated bitumen was poured into a new heated dry tin. The amount of filler required was heated to 105°C to a

constant mass of moisture-free particles. The accurate mass of bitumen inside the tin was placed on a heating plate at 160ºC. Then carefully and gently, the correct amount of filler was added in small batches with continuous manual stirring to achieve equal distribution and avoid any lump formation possibility. The filler addition was maintained carefully with continuous stirring until the whole mass was mixed properly. Finally, the homogeneous mastic was distributed into several 10 ml vials and stored at 5ºC temperature for later testing.

4.4.3 Test Sample Preparation

Accurate sample preparation is a crucial requirement for true rheological measurements as results are sensitive to the preparation method and sample geometry. Different methods exist to prepare a DSR sample. To achieve repeatability and consistency it is highly recommended to adopt 'hot pour' method (Airey *et al.*, 2003). The list provided below details the followed steps to prepare the sample:

1- Before starting the test, bitumen/mastic inside the vial was heated to 160ºC for 15 minutes.

2- Because of the filler settlement possibility at the bottom of the vial, the heated mastic was stirred continuously for a sufficient time to equally redistribute the filler in the whole binder and remove any air bubbles. Meanwhile, a zero-gap between the upper and lower plate was established.

3- A sufficient amount of heated binder was then poured onto the lower plate centre in order to achieve uniform distribution in later squeezing.

The lower and upper plates' temperature, before pouring the binder, were maintained at 60°C to obtain firm bond with the sample.

4- The upper plate was lowered automatically to the required gap (1 mm in 25 mm parallel plates and 2 mm for 8 mm parallel plates) plus 50 μm.

5- The excess amount of binder that has been squeezed out of the edge is then trimmed carefully with a heated spatula. After careful trimming of the surplus around the sample circumference, the upper plate was again lowered to the target gap.

6- It was found that immediately replacing the chamber cover for temperature control after reaching the required gap results in a lack of adhesion between the upper plate and the sample surface during the test. The improper adhesion manifests itself as a fast upper plate rotation either at the beginning or continuously through the test. The fast rotation provides misleading strain results (error) at the start of the test, while in the other case the sample fails immediately and should be replaced. Therefore, after reaching the required gap and before placing the water chamber cover, the sample was left for 5 minutes to give sufficient time for secure adhesion. This last step was essentially important to insure no water can infiltrate between the upper plate and the sample surface, hence, smooth strain transition results.

7- Finally, the water chamber cover was replaced to submerge the upper and lower plates including the sample in water all under one temperature (circulator water bath). Temperature control is essentially required as any temperature gradient may lead to inaccurate results. After reaching the

desired temperature (with ±0.1°C limit), 15 minutes period was allowed for thermal equilibrium before starting the test.

4.5 Testing Program

The general aim of the testing program is to investigate the filler role by means of bitumen-filler mastic system in permanent deformation behaviour. The steady state deformation behaviour and the recovery property respectively through creep and creep-recovery tests were investigated for pure bitumen and mastics at three different filler contents (35%, 50%, and 65% by mass). A wide range of stress levels and temperatures were employed to comprehensively cover the behaviour under several conditions.

4.5.1 Shear Creep Test

A shear stress was applied to the upper plate and held constant for a time to study the creep deformation of the material. The test was conducted over a range of shear stresses from 1 to 1000 kPa and at three temperatures; 10, 30 and 50°C. The test was stopped when failure occurred in the live data shown on the screen. Failure is identified by the start of the third region as will be illustrated in the results. An 8 mm diameter parallel plate with a 2 mm gap was employed as it was desirable to perform low and high shear stresses.

4.5.2 Single Creep Recovery Test

In the creep recovery test a constant shear load was applied quickly for a specified time after which the loading was released. During the recovery period the strain was continuously monitored until reaching approximately a

zero strain rate. The test was implemented on neat bitumen and mastics at 1 kPa and 10 kPa shear stress at both 30 and 50°C. A 25 mm parallel plate with a 1 mm gap was used in this test as it fitted the test temperature and shear stress range. A series of single creep recovery tests at each testing condition was conducted to characterise the recovery property. The loading time varied in a broad range and reached high strain levels to represent the field condition where the speed is very low (e.g. parking areas, stop signs, etc.).

4.6 Tests Results

4.6.1 Shear Creep Test Results

The shear deformation of the material can be investigated by applying constant shear loading at the outer edge of the disc-shaped sample until it fails. The tests were conducted over a range of stress levels starting from 1 kPa to 1000 kPa at 10°C, 30°C, and 50°C.

Each creep test provides typically the same trend of strain with time as illustrated in Figure 4.3. The curve smoothly changes from primary, to secondary followed by a tertiary region. In the primary region the strain rate $(^{d\gamma}/_{dt})$ decreases with time. The secondary region, which occupies most of the curve, is characterised by approximately a constant shear strain rate. The tertiary region is identified when the strain starts to increase dramatically leading to the failure of the material. Figure 4.4 presents the change of strain rate with time for a typical creep test.
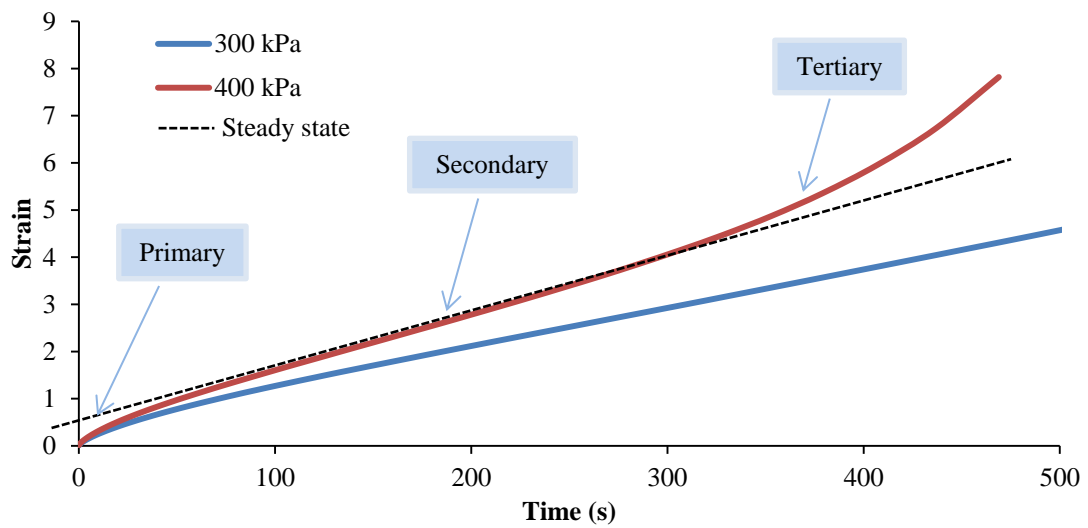
Figure 4.3 Typical creep test result of B @30ºC
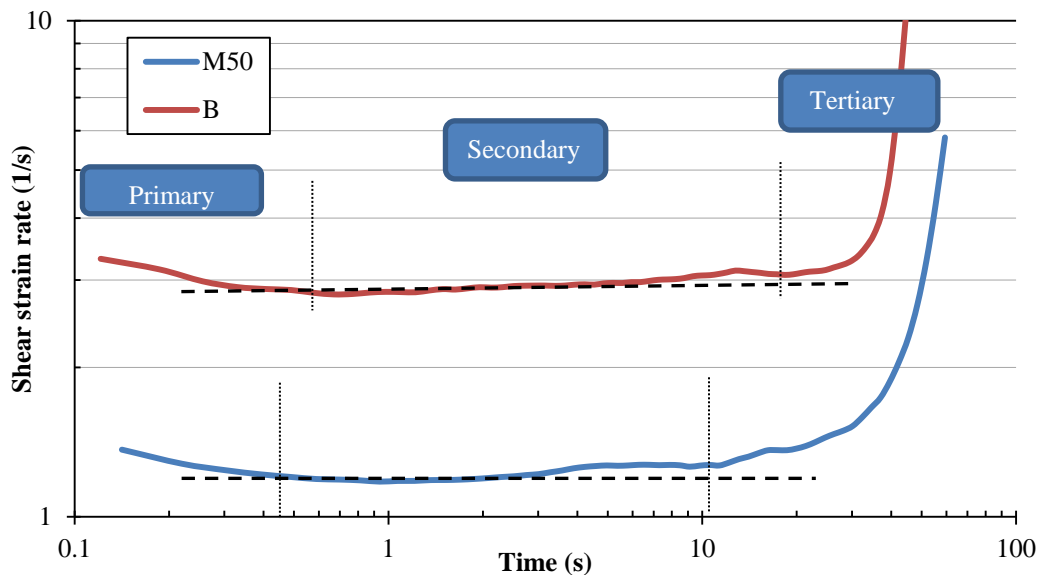
Figure 4.4 Strain rate change with time @10 kPa and 50ºC

The secondary stage where the strain rate is approximately constant is identified as the steady state region. In this region the strain is linearly increasing with time and the slope of the curve is known as the steady-state strain rate 'SSSR' (Taherkhani, 2006, Collop *et al.*, 2002, Cheung *et al.*, 1997a). The value of the SSSR is unique for each binder type at a particular stress level and temperature. Figure 4.5 provides a summary of the B steady state deformation over a range of stress levels at 10, 30, and 50ºC, where the SSSR is plotted against the stress level on logarithmic scales.

As can be seen, for relatively low stresses the strain rate is related to the stress level by a linear relationship with a slope of approximately 1 (see trend line exponent). This indicates that the behaviour is linear viscous within this region (Taherkhani, 2006, Rahimzadeh, 2002). Above 500 kPa the data points lie in a straight line but with a slope of approximately 2 indicating a nonlinear power low creep viscous behaviour. Between these regions the curve is in a transition zone from linear to a non-linear viscous.
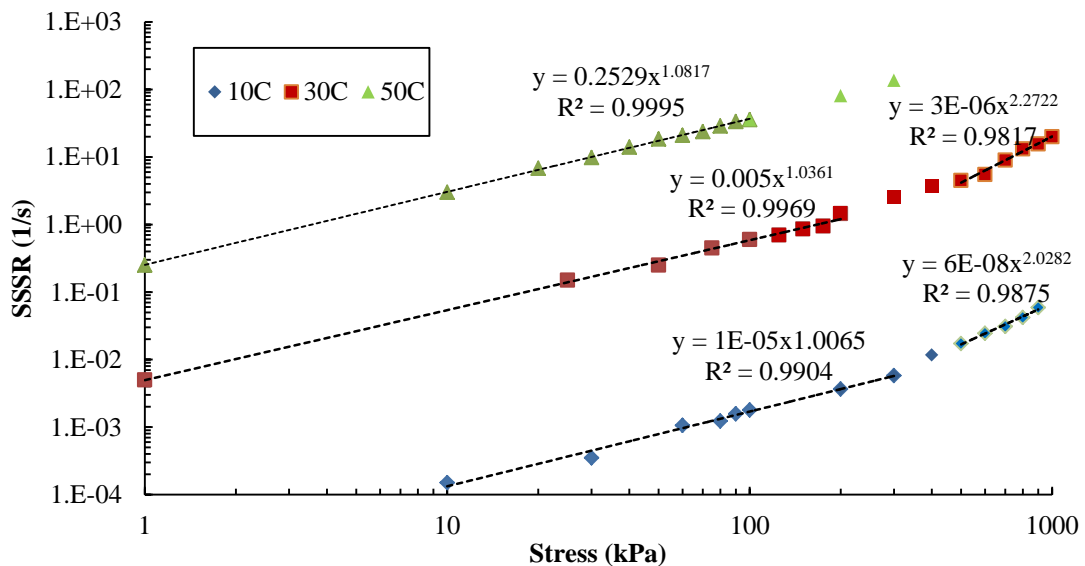
Figure 4.5 Steady state deformation of B

More importantly, the shear stress at which the behaviour shifts from linear to nonlinear (start of the transition zone) is found to be dependent on the temperature. As Figure 4.5 shows, increasing the temperature reduces this shear stress level and accelerates the start of the nonlinear behaviour. The criterion to define the extent of the linear region is determined by the trend-line extension with an exponent approximately 1.0. For B, at 50°C the stress limit was found to be approximately 100 kPa, while for 30°C and 10°C it reached about 200 kPa, and 300 kPa respectively.

It should be noticed that there is a lack of data points for 50oC at high stress levels. This is because at these conditions the bitumen failed quickly and data points were not sufficient to accurately determine the SSSR. These data points can be extrapolated using some models as will be discussed later.

The temperature-dependent of linearity creep behaviour can also be recognized by plotting the steady state viscosity ($\eta^* = \frac{\tau}{\gamma^*}$) against the stress level on double logarithmic scales, as presented in Figure 4.6. Similarly, at low stress levels the behaviour is linear with a constant level of viscosity while at higher stresses the nonlinear behaviour is observed when the viscosity starts to reduce, again depending on the temperature.
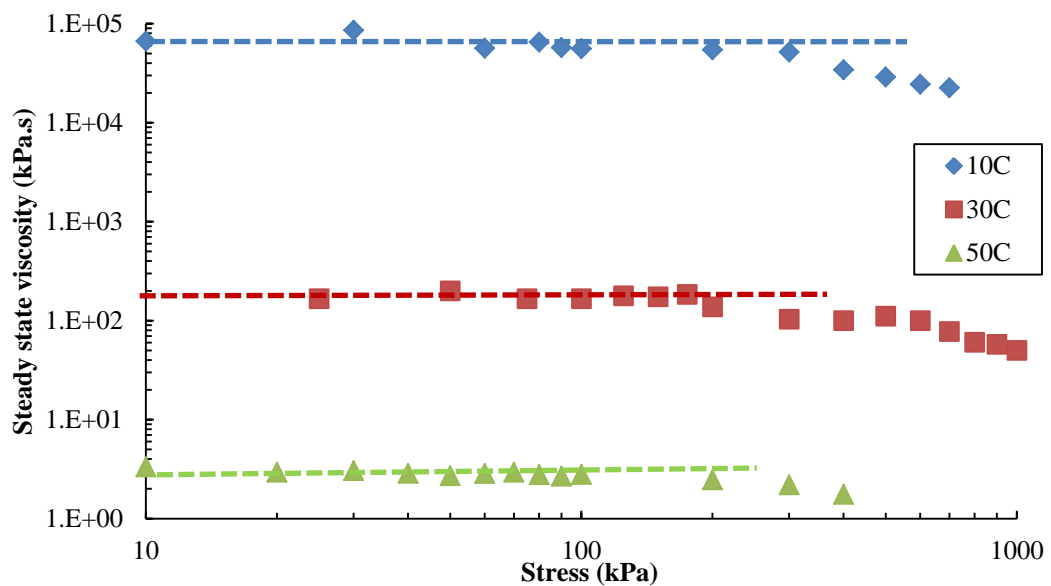
Figure 4.6 Steady state viscosity of B

The test results on M35, M50 and M65 follow the same trend of pure bitumen under shear creep testing. The strain versus time curve in a similar way divides into primary, secondary and tertiary regions as illustrated in Figure 4.7. As can be seen for a typical test condition, the added filler

reduced the strain of the binder and thus the resistance increased with increasing filler content. The next section introduces a new factor to measure the stiffening of the filler.
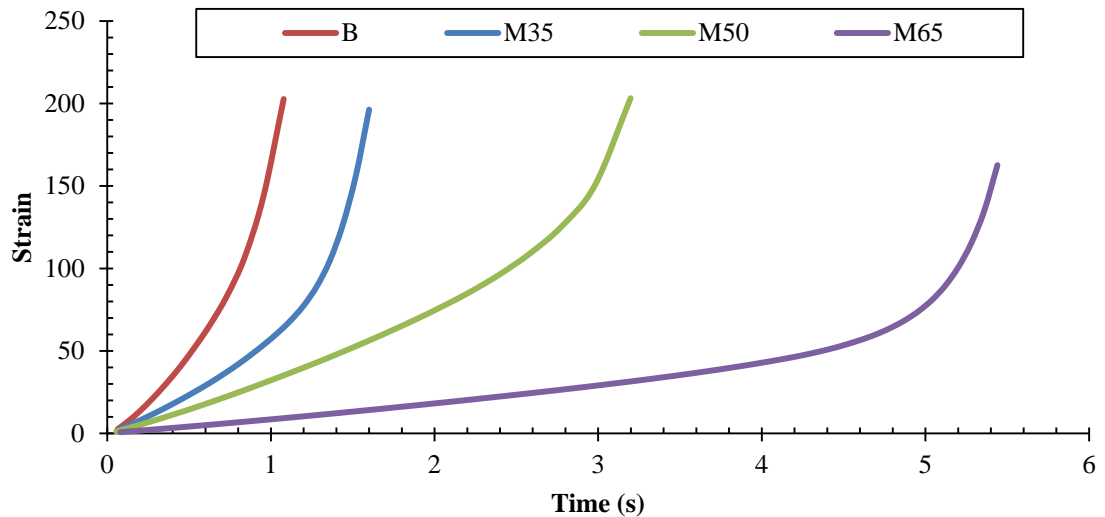
Figure 4.7 Typical result of creep test with 200 kPa @50ºC

4.6.2 Stiffening Effect of Filler

To investigate the stiffening effect of filler on creep behaviour, a new parameter is introduced termed the stiffening factor 'SF'. SF is the strain ratio of the bitumen/mastic and is obtained simply through factoring the 'B' curve by 1/SF until it approximately matches the 'M' curve, as shown in Figure 4.8. The stiffening factor which quantifies the stiffening is a function of stress level, temperature, and filler concentration.
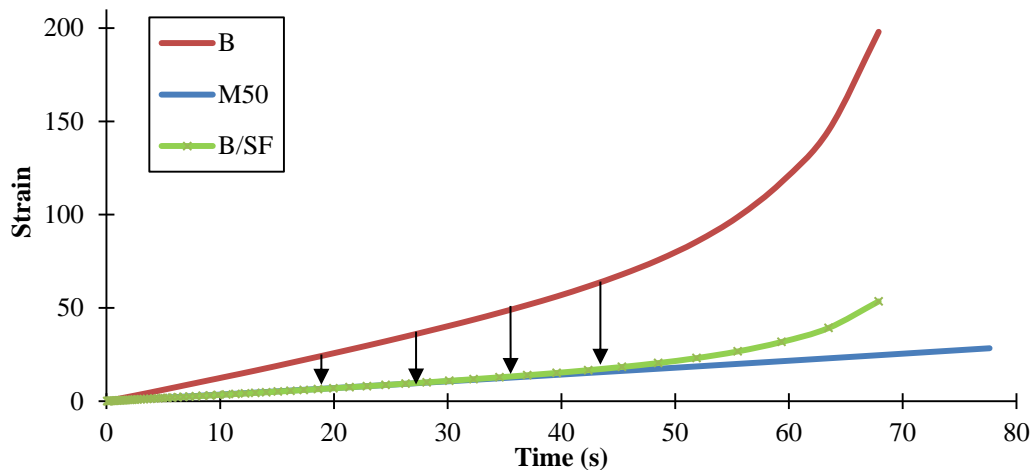
Figure 4.8 Curve fitting @10 kPa and 50ᵒC

Figures 4.9, 4.10 and 4.11 describe the change of stiffening factor with stress
level of M35, M50, and M65 at 50, 30, and 10ᵒC respectively. Figure 4.9
illustrates that, the three mastics SFs exhibit almost a straight line (constant
value) before reaching a stress limit after which SF starts to reduce
nonlinearly. The stress limit at which the nonlinearity starts depends on the
filler concentration in an inverse relationship, approximately 100 kPa for
M65, 200 kPa for M50, and 300 kPa for M35 are the stress limit of linearity
at 50ᵒC. Figure 4.10 shows a similar trend but with a slight extend in the
constant region for the three mastics in a similar order with respect to
linearity limit. Likewise, the increase in stress linearity limit continues to
higher stresses with reducing the temperature to 10ᵒC as shown in Figure
4.11. Consequently, the stress linearity limit is function of both temperature
and filler content. Typical, the same conclusion can be drawn by plotting the
SSSR against stress for mastics and follow the trend line exponent as
presented earlier in Figure 4.5.
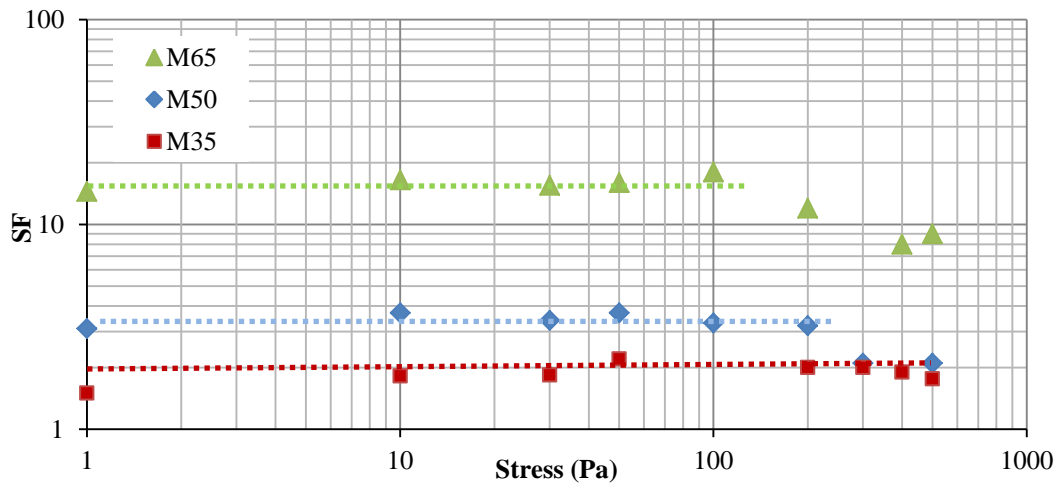
Figure 4.9 SF change with stress @50ºC
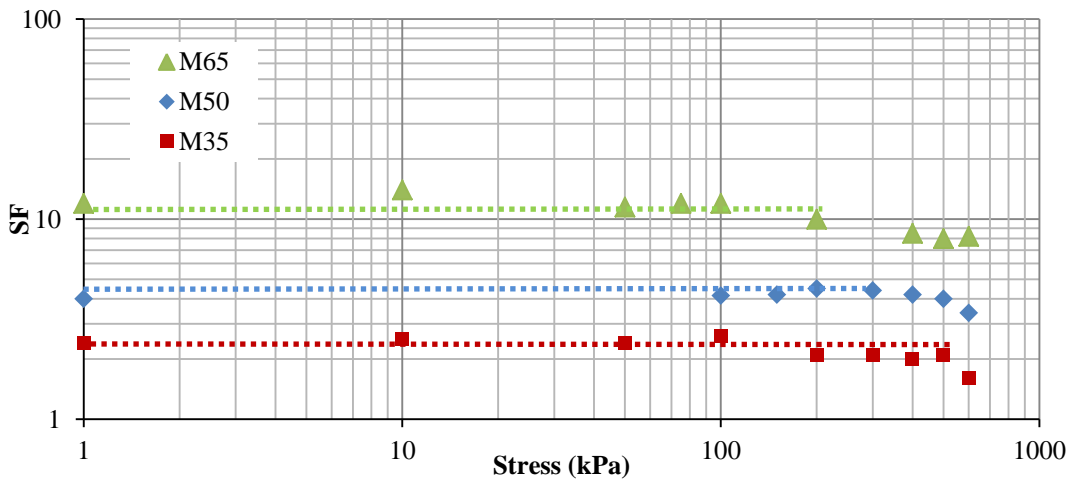
Figure 4.10 SF change with stress @30ºC
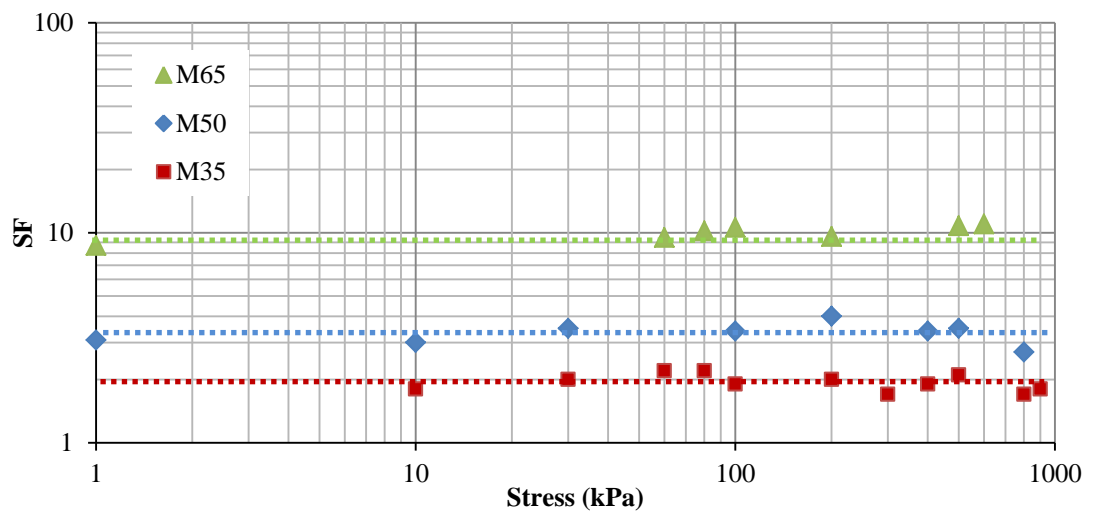
Figure 4.11 SF change with stress @10ºC

The trend with reducing temperature is narrower range between SFs of different mastics. Comparing the SF of the three mastics by taking the average SF in the linear region shows that M65 stiffens the binder by a factor of 10 to 15 depending on the temperature. For M50, SF is typically about 3.5 while it is around 2.5 for M35, all with minor temperature influence. The higher SF of M65 in comparison to M50 and M35 is due to the large volume occupied by filler which becomes the predominant element in the mastic. Thus, as filler volume fraction increases the particle-particle contacts intensifies more. Nevertheless, the response of mastics with different volume fractions of filler concentrations under creep is still governed by bitumen behaviour, following the same typical pattern regardless of temperature.

Theoretically, there is a limit where viscosity reaches an infinite level and flow becomes almost impossible. At this concentration the solid volume fraction is termed the maximum packing fraction ($\emptyset_{max}$) and can be estimated from Rigden Voids standard test. When filler volume fraction in mastic is scaled by this value ($\emptyset/\emptyset_{max}$), an important variable that controls the rheology is introduced and utilised widely in modelling the behaviour of a suspension (Taylor *et al.*, 2010, Faheem *et al.*, 2010). To relate the physical volume concentration to the bitumen-filler interaction the average SF versus ($\emptyset/\emptyset_{max}$) is drawn in Figure 4.12. In line with previous studies (the ratios G* and J* (complex modulus and creep compliance of mastic over bitumen)), an exponential relationship is found to describe the trend. At low concentrations where the slope is relatively low, the stiffening is attributed to

the physical replacement of bitumen by rigid filler particles. When the slope increases significantly, the particle contacts establish and the bitumen-filler interactions becomes higher.

Table 4.2 Average SF and normalised solid fraction

SF	10 °C	30 °C	50 °C	Avg	φ/ φmax
M65	9.5	11.5	15	12	0.555243
M50	3.5	4	3.5	3.67	0.365648
M35	2	2.5	2	2.17	0.230223
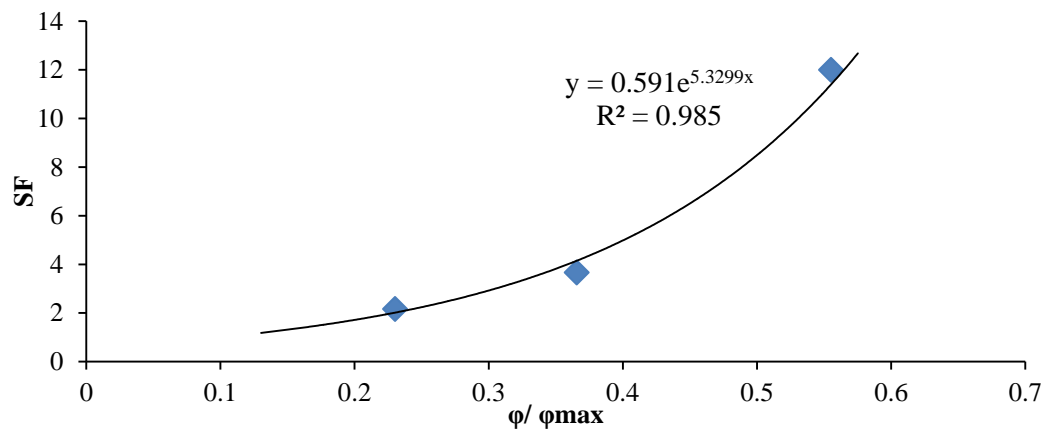
Figure 4.12 SF change with normalised solid fraction

4.6.3 Single Creep Recovery Results

In the single creep recovery test the binder was exposed to a constant shear load for a specific time similar to the creep test but then the loading was removed and the material was allowed to recover. The strain was continuously recorded until the strain rate approximately became zero. A series of this test type was performed at 30 °C and 50 °C at two stress levels; 1 kPa and 10 kPa on B and different mastic types. Figure 4.13 combines a series of typical strain responses for M35 at 1 kPa and 50 °C. To insure compatible results, any plot that had shown deviation from the loading strain line of a typical material was excluded.
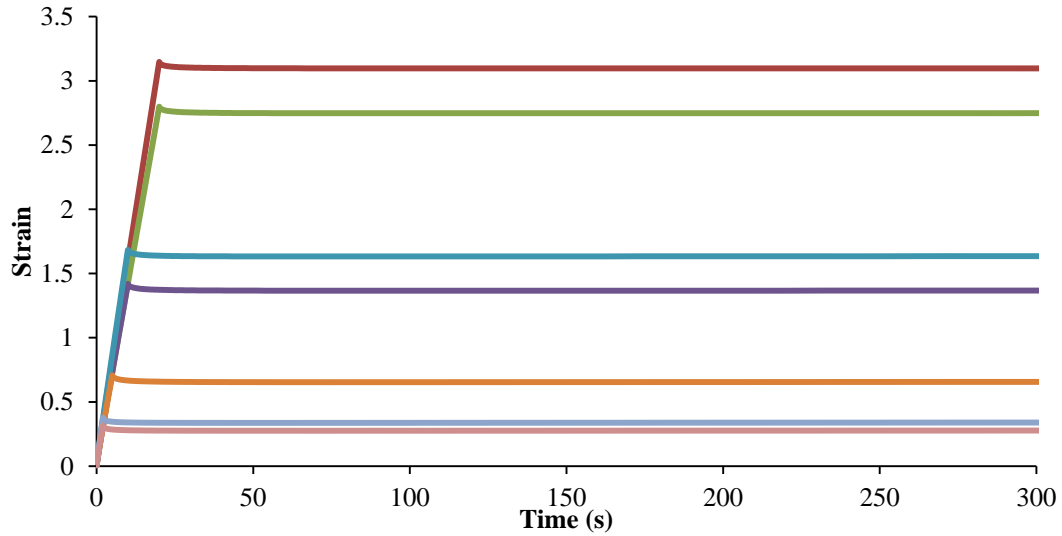
Figure 4.13 Typical result of M35 creep recovery test @1 kPa and 50ºC

To investigate the recovery property under different temperatures and stresses Figures 4.14 and 4.15 summarise the creep-recovery tests at 1 kPa and 10 kPa respectively, where the recovered strain (= total strain – unrecovered strain) is plotted versus the total strain for neat binder and mastics of 35% and 50% filler contents for limestone and granite types.
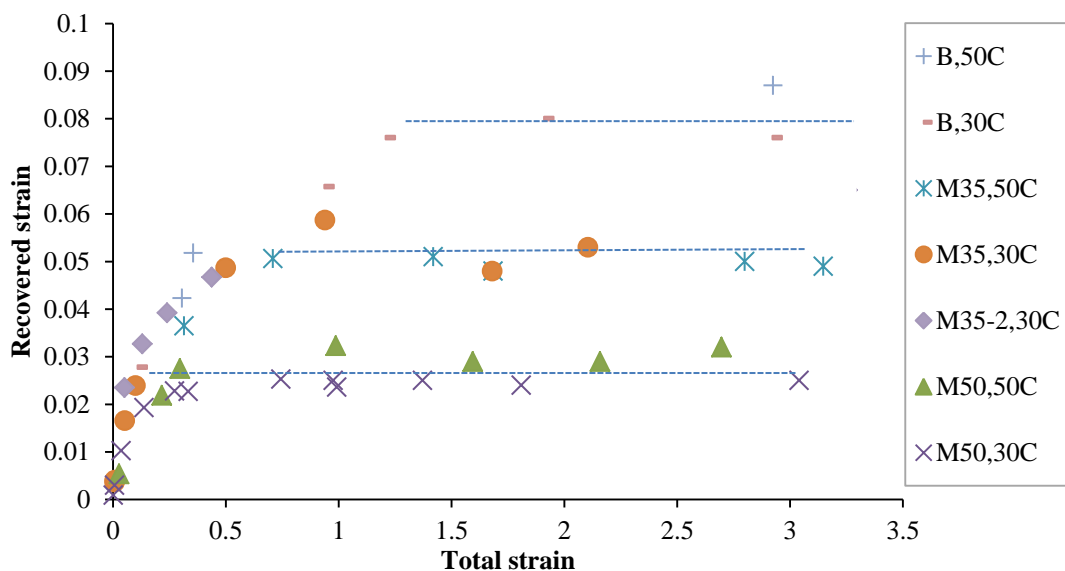
Figure 4.14 Summary of creep recovery test results @1 kPa
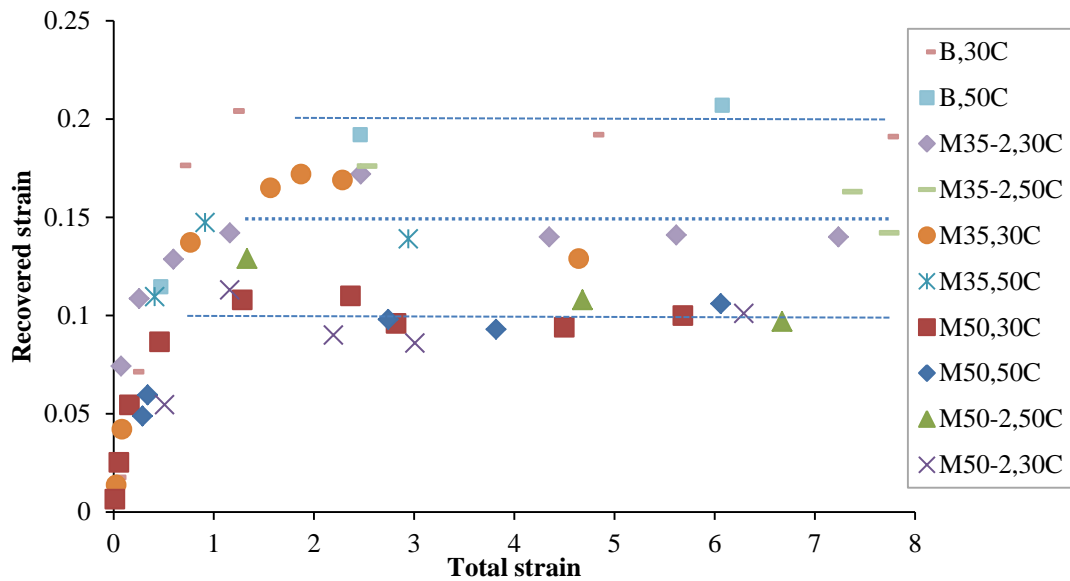
Figure 4.15 Summary of creep recovery test results @10 kPa

Similar to previous findings of (Ossa, 2005, Taherkhani, 2006), the recovered strain , independently, in the beginning is in a linear relationship with the total strain. However, this relationship is limited to very low strain levels. With higher strains the straight line deviates to a constant recovery level according to the stress level and filler content. Thus, for each binder type at one stress level, the recovered strain continuous to increase up to a specific total strain limit after which the recovered strain becomes approximately constant.

This total strain limit rises with increasing stress level without any significance of temperature and filler type. The more filler added to the binder the lower the constant recovery level. Additionally, with reducing the stress level the difference between mastics' constant recoveries become narrower.

4.7 Modelling Creep and Creep Recovery Behaviour

Laboratory testing provides a valuable information tool to investigate the behaviour of materials. Nevertheless, they are inefficient in terms of time and finance in addition to the required operational skills. Using models can provide, on the other hand, a prediction of the behaviour and afford access to information outside the laboratory boundaries.

Recently, a wide range of modelling techniques has been developed to study the mechanical behaviour of bituminous material. An early attempt to model the viscoelastic behaviour of bitumen was by Poel *et al.* (1954). A Nomograph (known as Van der Poel's Nomograph) of correlating between softening point, penetration, temperature, and loading to the stiffness was produced (Read *et al.*, 2003). Although several empirical models were developed to evaluate the linear viscoelastic behaviour (see (Yusoff *et al.*, 2011) for details of these models), their parameters have no physical meaning.

Therefore, more attention is being paid to mechanical models to simulate and understand the viscoelastic behaviour. These models comprise traditionally a spring and a dashpot to simulate the elastic and viscous responses respectively. The two elements can be connected in parallel or in series as in Kelvin and Maxwell models respectively. A combination between the two models generates Burger's model. To perform the simulation, each element has a representing parameter that needs to be estimated. The simulation, after obtaining parameters, when it runs in a numerical form

(finite element package for example), allows an access to localized stresses and strains (Woldekidan, 2011).

4.7.1 Burger's Model

The time dependent behaviour of bituminous material can be simulated simply by using linear viscoelastic mechanical models. The Maxwell element is the simplest expression where a linear dashpot and a spring are connected in series. Connecting them in parallel produces the Kelvin model. A combination of Maxwell and Kelvin models generates the Burger's model. It is used widely due to its ability to describe the elastic, viscoelastic, and viscous response separately (Collop *et al.*, 2006). The response of Burger model under creep loading is given by:

$$\varepsilon(t) = \sigma_0 \left[\frac{1}{E_0} + \frac{t}{\lambda_\infty} + \frac{1}{E_1} \left(1 - e^{-t/\tau} \right) \right] \tag{4.6}$$

Where $\varepsilon(t)$ = the strain as a function of time, σ_0 is the applied stress, E_0 and E_1 = the springs' elastic modulus, λ_∞ and λ_1 = the viscosities of the dashpots, and $\tau = \lambda_1 / E_1$ is the retardation time.

When a constant loading is applied the result will be an instantaneous elastic respond followed by a delayed elastic and then a viscous response (Figure 2.3). Adding more Kelvin elements in series builds a 'generalised Burger's model', illustrated in Figure 4.16, which raises the ability to describe the behaviour over a wide range of loadings. The response is given by:

$$\varepsilon(t) = \sigma_0 \left[\frac{1}{E_0} + \frac{t}{\lambda_\infty} + \sum_{i=1}^{N} \frac{1}{E_1^i} \left(1 - e^{-t/\tau^i} \right) \right] \tag{4.7}$$

 Where N is the number of Kelvin elements.
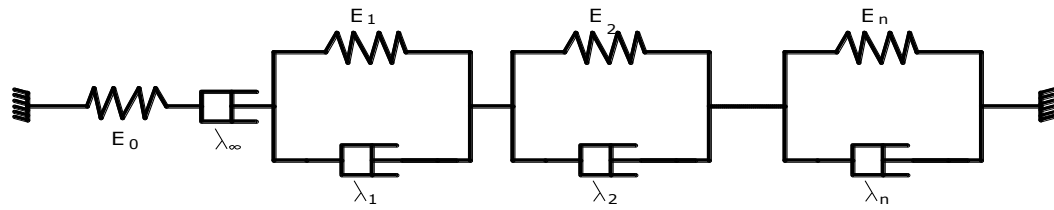
Figure 4.16 Generalized Burger's model

If the loading is removed suddenly at time t_1 the recovery is expressed as follows:

$$\varepsilon\,(t > t_1) = \sigma_0\big[\tfrac{t_1}{\lambda_\infty} + \textstyle\sum_{i=1}^{N} \tfrac{e^{-t/\tau^i}}{E_1^i}(e^{t/\tau^i} - 1)\big] \qquad (4.8)$$

Maxwell spring recovers immediately, Kelvin model due to the parallel configuration recovers over a period of time, while the Maxwell dashpot leaves a permanent strain.

To simulate the viscoelastic behaviour, the model parameters need to be determined. The most common approach is by optimizing the error between the experimental data set and model prediction through regression analysis (Woldekidan, 2011). A Matlab tool that enables different loading configurations in addition to the quick and easy regression process was utilised.

Simulink Design Optimization 'SDO' is a Matlab product that provides models formed by assembling built-in blocks to estimate parameters using numerical optimization. It was employed to simulate both the creep and creep-recovery tests of B, M35, M50, and M65 via building a generalized Burger's model using one set of parameters at each temperature over the linear region of stresses. Although the method was implemented in the time

domain, it can be switched to be applied in frequency domain. Figure 4.17 summarises the followed procedure to obtain parameters. Full details of the procedure are presented in Appendix A.

Build Model
Assemble imported blocks to generate Burger's model

Import Data
Import a set of data experiment (strain and time) to the model

Adjust loading configuration
Adjust the loading block based on the imported data (applied stress and time)

Estimate parameters
Select parameters to estimate and the estimation method

Validate estimation
Import another set of experiment. Adjust the loading configuration accordingly. Run the simulation using the estimated parameters

Simulation fits well
Export estimated parametrs

Simulation doesn't fit well
Repeat parameter estimation

Figure 4.17 Flowchart of parameters determination procedure in Matlab

After the initial estimation is completed successfully the results are compared with another set of data experiments of the same material and temperature for validation purposes. Before starting the validation the input signal (loading-unloading) configuration must be adjusted to the new

validation data set. The validation comparison will be shown in a new graphical presentation combined with the residual graph showing the difference at each point. Table 4.3 presents estimated parameters of B, M35, M50, and M65 at different temperatures. Figure 4.18 illustrates examples of simulated (dots) experiments (lines).

Table 4.3 Burger's model parameters values of creep and creep recovery

ID	Tem °C	E_o	E_1	E_2	E_3	λ_∞	λ_1	λ_2	λ_3
B	10	3.5E+07	9.5 E+04	5E+06	—	8E+07	4E+07	8E+06	—
	30	4.8E+08	22.7E+03	7.2 E+06	—	2.29E+05	5.36E+05	5E+04	—
	50	2.53E+04	11259	_	—	3.2E+03	1.06E+05	-	—
M35	10	3.5E+07	2 E+05	8E+06	—	1E+08	1.5E+08	5E+06	—
	30	1.6E+08	342251	29099	—	445732	55627.6	1195375	—
	50	171692	22397.9	_	—	7301.6	49883.7	-	—
M50	10	1E+08	5.5E+05	_	—	3E+08	1.6E+08		—
	30	6.47E+06	3E+04	7.2E+05	—	1E+06	4E+06	3.5E+04	—
	50	4.44E+06	6.47E+04	_	_	1.67 E+04	3.78E+05	-	—
M65	10	3.5E+07	9.5E+05	5E+07	5E+06	7E+08	7E+08	8E+08	2E+08
	30	1E+06	1E+06	5E+05	5E+03	5E+06	7E+07	1E+07	5E+06
	50	1E+05	2800	_	_	6.3E+04	2E+05	_	_
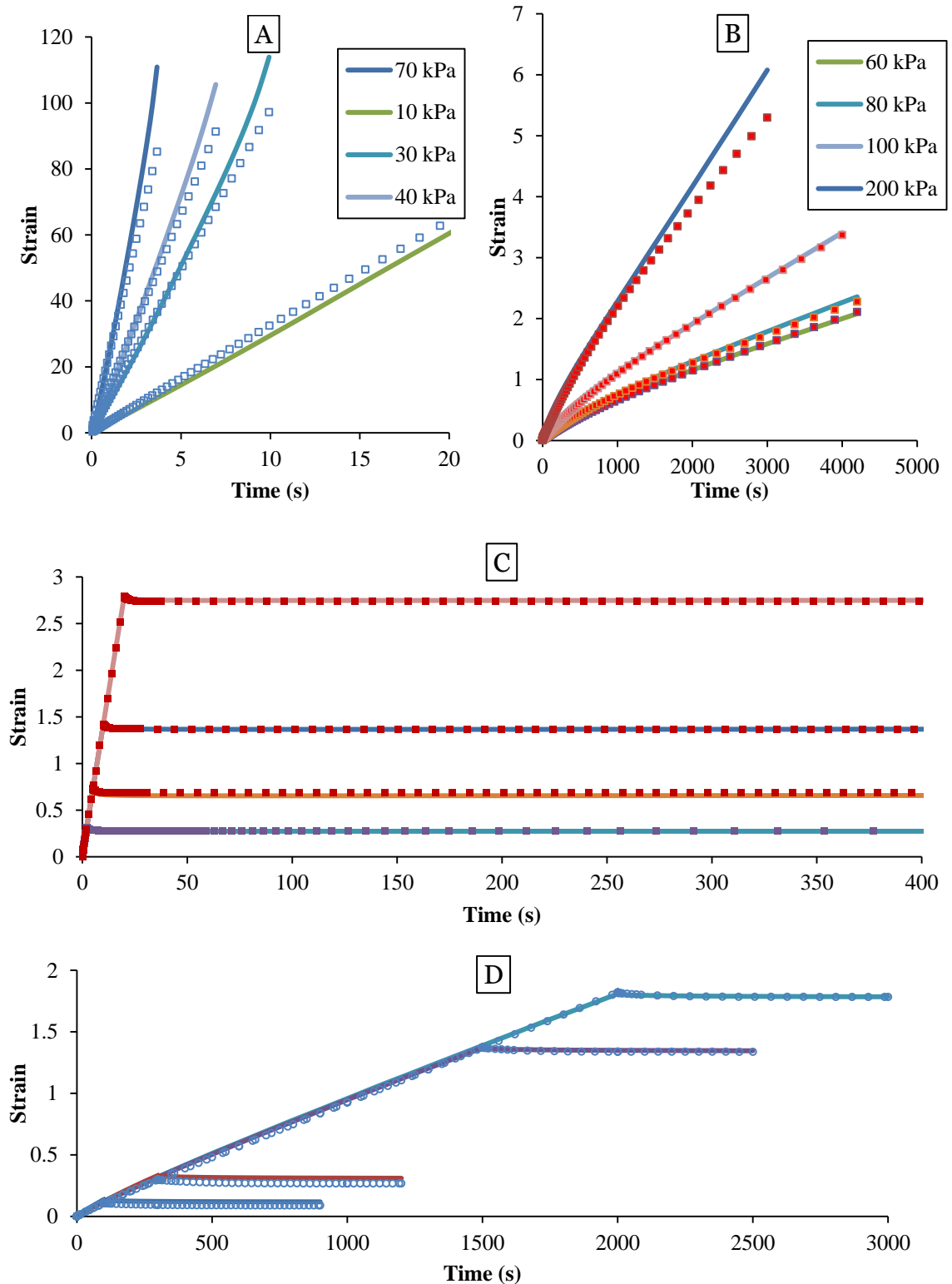
Figure 4.18 Comparison examples of tests results and simulation: (A) Creep, B, 50ºC. (B) Creep, M35, 10ºC. (C) Creep-recovery, M35, 1 kPa, 50ºC. (D) Creep-recovery, M50, 1 kPa, 30ºC

4.7.2 Steady State Constitutive Relationship of Bituminous Materials

To cover entirely the binder behaviour over a wide range of stresses and temperatures, a constitutive model, termed the Modified Cross Model 'MCM' is utilised. The model was originally established by Cross (1965) to describe the pseudo-plastic flow of non-Newtonian fluids with the formation and rupture of structural linkages. Later on, Cheung (1995) extended the work through including the temperature dependency of bitumen. It basically characterises the steady state deformation of bitumen with the stress over a wide range of temperatures. The modified model fits the change from linear to nonlinear behaviour containing the transition deformation under free volume conditions (described by WLF equation) to the diffusional deformation (captured by Arrhenius equation). The model is given by:

$$\eta = \frac{\eta_{oT}}{1+(\frac{\eta_{oT}\dot{\varepsilon}}{\sigma_{oc}})^{nc}} \tag{4.9}$$

Where

$$\eta_{oT} = \eta_{oc}\exp\left(\frac{Q_c}{RT}\right), \text{for } T > T_g \tag{4.10}$$

$$\eta_{oT} = \eta_s \exp(-\frac{2.303C1(T-T_s)}{C2+(T-T_s)}), \text{for } T \gg T_g \tag{4.11}$$

η = Viscosity, η_{oT} = pre-exponential for viscosity (i.e. the viscosity before the exponential relation starts), σ_{oc} = failure strength of structural linkage, nc =material constant, η_{oc} and η_s= material constants, Q_c = thermal

activation energy, T_g = glass transition temperature, C1 and C2 = thermal universal constants.

The model was applied on the SSSR results of shear creep tests. The transition temperature from equation (4.10) to (4.11) was found to satisfactory fit the B data at 31°C. This temperature is different from Cheung's (35.2°C) due to the difference in molecular structural between bitumen types. Equation (4.10) was fitted to data results at 10 and 30°C temperatures, while equation (4.11) was applied at 30 and 50°C.

Figure 4.19 illustrates the fitted MCM-Arrhenius and MCM-WLF equations to the B experimental data (dots) in double log scales. As it can be seen, there is a satisfactory agreement with all temperatures and stress ranges. At 50°C the data points at high stresses (above 300 kPa) are not included. This was due to the bitumen being very liquid in such a way that failure occurred very quickly. Data points were limited and it was difficult to determine the SSSR. Therefore, missing data points were extrapolated from the model as shown in the figure. The corresponding material parameters for B are presented in Table 4.4.
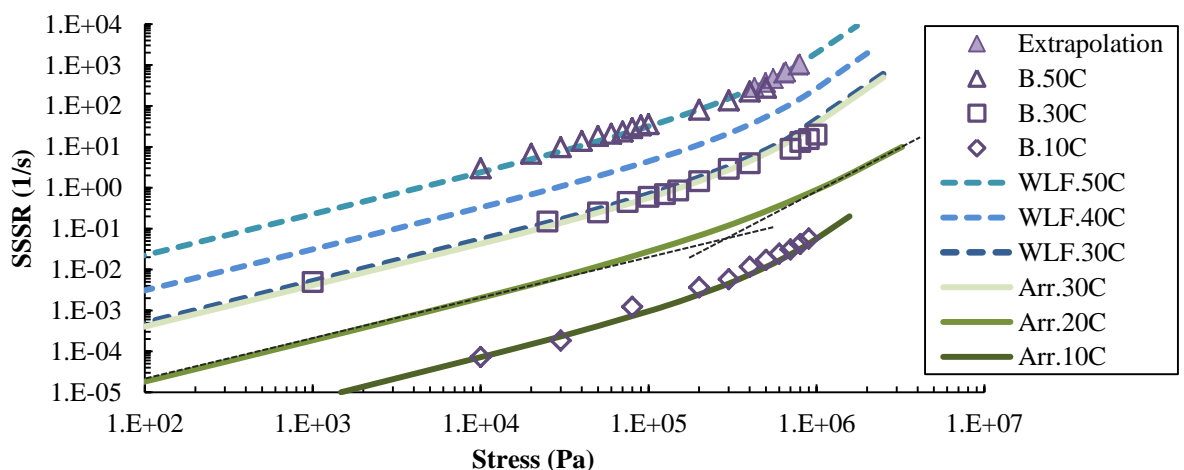
Figure 4.19 Steady state deformations of B and MCM

Table 4.4 Summary of MCM parameters of binders

Parameter	B	M35	M50	M65
	Arrhenius			
σ_{oc} (Pa)	4.80 E+05	4.00E+05	2.85E+05	2.05E+05
nc	0.70	0.60	0.55	0.57
η_{oc} (Pa. s)	1.30E-34	2.65E-34	5.85E-34	2.21E-33
Q_c (J/mol)	228E+03	228E+3	228E+3	228E+3
R	8.314	8.314	8.314	8.314
	WLF			
η_s (Pa.s)	1.7E+05	3.9E+05	7.5E+05	5.0E+06
$C1$	8.86	8.86	8.86	8.86
$C2$	101.6	101.6	101.6	101.6
T_s (°C)	31	31	32	31

Similarly, Figures 4.20, 4.21, and 4.22 respectively for M35, M50, and M65 data points combined with MCM fitted model were produced. Table 4.4 shows the material parameters for each type. The coefficient of determination (R^2) was calculated to be greater than 0.985.
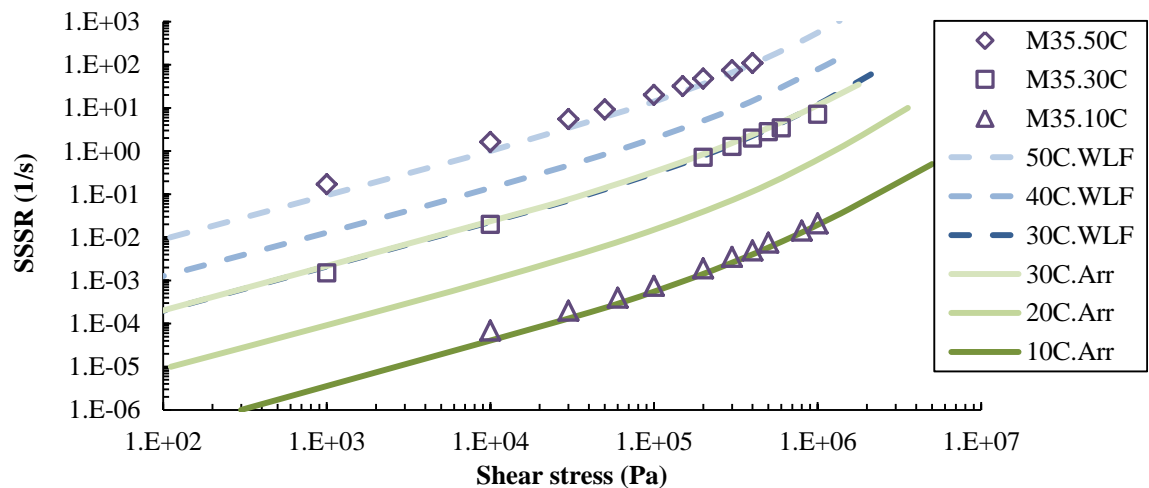
Figure 4.20 Steady state deformations of M35 and MCM
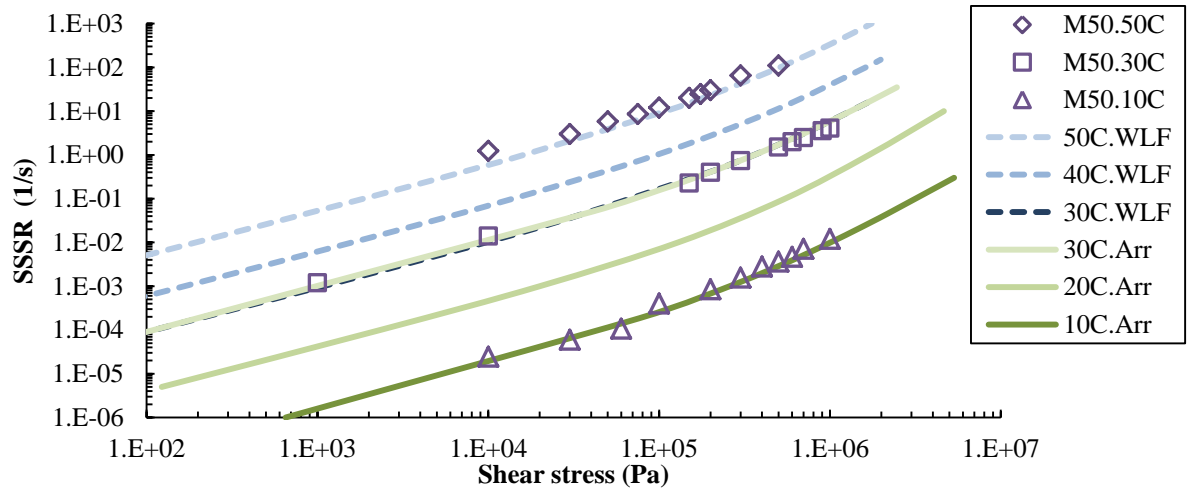
Figure 4.21 Steady state deformations of M50 and MCM
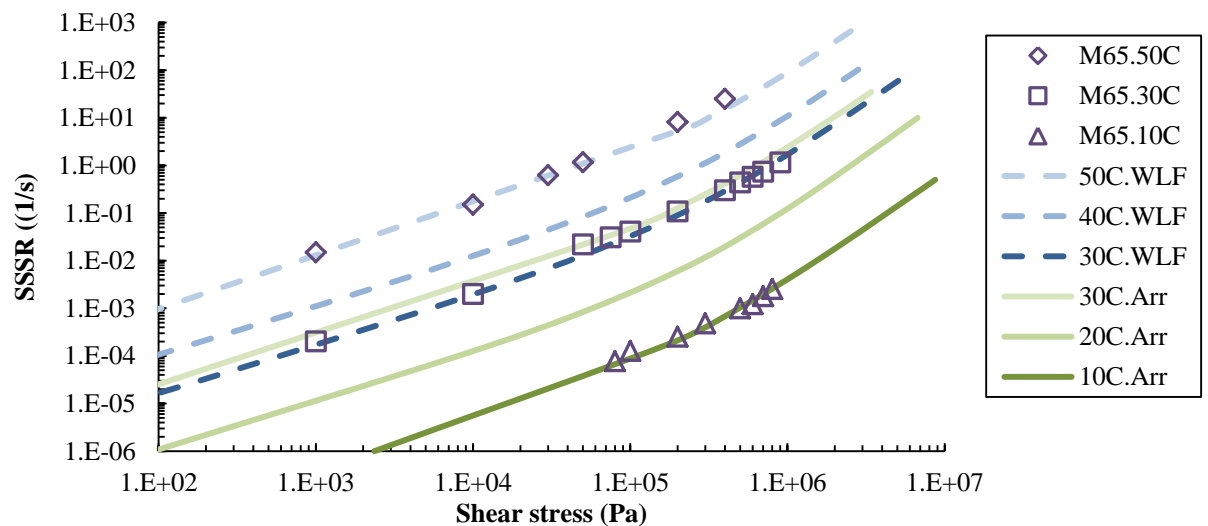
Figure 4.22 Steady state deformations of M65 and MCM

The figures show that MCM provides an excellent fit with the pure binder as well as mastics with filler inclusion. However, adding the filler to the bitumen had many effects. The mastic is a more nonlinear material in comparison to the pure bitumen. The nonlinearity range extends towards lower stresses with increasing filler content as revealed previously. This can also be observed through MCM determined parameters where the mastic has a smaller value of σ_{oc}, as well as, the stiffening of filler is reflected by increased η_{oc} values in line with increasing the filler content.

Cheung (1995) proposed that the change from linear to nonlinear deformation at high stress levels is due to the rupture of structural linkage in the molecular network and is related to a single stress level for a specific binder. It is suggested from previous results that the filler inclusion accelerates the rupture of structural linkage of bitumen as does the temperature.

Bitumen structure is regarded as a colloidal system consisting of high molecular weight of asphaltenes. The rheology of bitumen is highly influenced by asphaltene particles content, size and shape. The degree at which linear behaviour of bitumen extends is influenced by the interaction of asphaltene molecules and other entities. Asphaltene molecules themselves, at high temperatures lose their bond combined with a change in their size and shape (Read *et al.*, 2003). Therefore, the extension of the Newtonian behaviour, in terms of temperature dependence, can be partially explained by the molecular structure of the bitumen. However, Newtonian concept is still not well understood under shear in terms of bitumen structure and constitutional relationships.

4.8 Conclusions

Although bitumen rheological properties were investigated extensively, the fact remains that binder acts as mastic in asphalt mixtures with the inclusion of filler. Testing mastic rather than pure bitumen represents and relates more to the actual asphalt mixture performance. The results presented in this chapter highlight several aspects of permanent deformation in terms of filler inclusion, temperature and stress level.

The shear creep behaviour of bitumen and mastics of limestone filler with different filler contents have been measured in the DSR over a range of stress levels and temperatures. At low stress level the SSSR was found to be linear with the stress level, characterised by a power law model with a creep exponent of approximately 1. At high stresses the behaviour deviates to a nonlinear viscoelastic with a creep exponent around 2. Between these two regions there is a transition zone from linear to nonlinear viscoelastic behaviour. The stress linearity limit is a function of temperature in an inverse relationship.

A new stiffening factor (SF) was introduced which represents a simple method to express the degree of stiffness which bitumen gains due to filler inclusion. At low stresses, SF was found to be constant and then reduces nonlinearly at high stresses. The extension of SF linearity is dependent on both temperature and filler content. At high temperature and/or high filler content the linearity reduces and vice versa. While M35 stiffened the bitumen by approximately 2 times, M50 and M65 showed greater stiffening by 3-4 and 10-15 times respectively. In line with (Liao, 2007, Taylor *et al.*, 2010); at low (35%) and intermediate (50%) filler contents the filler is considered as a suspension of solid particles in bitumen while filler skeleton builds up and significantly influences the behaviour at higher concentration (65%). Nevertheless, bitumen is still the element that controls the behaviour, being stiffened by filler.

Results from single creep recovery test on bitumen and mastics reveal that the recovered strain is at the beginning directly proportional to the total strain independent of stress, filler content and temperature, prior to a total

strain limit after which the recovered strains become constant. This total strain limit increases with increasing stress level and/or reducing filler content. Thus, the recovery property of bitumen is reduced by increasing filler content. The recovered strain when it becomes constant is insignificantly influenced by temperature or filler type.

The experimental results of creep and creep-recovery tests were successfully simulated through the generalized Burger's model via a Matlab tool. The Modified Cross Model (MCM) was fitted to the steady state strain rate versus stress and found to be in excellent agreement.

5. Developing Multiple Stress-Strain Creep Recovery Test

5.1 Introduction

Rutting has the potential to lead to hazardous driving conditions and is a concern for the asphalt community. The performance of asphalt mixture is primarily governed by the properties of the used bitumen. The failure of 'G*/sin δ' to effectively represent a binder rutting evaluation parameter, PMBs in particular, raised the demand for developing a new satisfactory test. While most published work from Europe has been concerned with evaluating binders to rutting based on their stiffness (Giuliani F., 2006, Morea *et al.*, 2010, Vlachovicova *et al.*, 2007), work originated in the US has mainly been concerned with ranking binders based on their recoveries in a multiple stress form (D'Angelo *et al.*, 2007a, Zoorob *et al.*, 2012, D'Angelo, 2010, Wasage *et al.*, 2011).

This section details the development of a new multiple stress-strain creep recovery 'MS-SCR' test, as well as contributes to the understanding of thermo-rheological behaviour of bitumen-filler interactions. The test is innovated to evaluate different binders based on two rutting resistance mechanisms; recovery and deformation resistance. The same 40/60 pen base bitumen and the two mastic types that were prepared at three

concentrations (35%, 50%, and 65% filler content by mass of mastic) were utilised. In addition, two PMBs using the same base bitumen type were prepared and examined to validate the effectiveness of the test.

5.2 MS-SCR Test, the Design

Literature review revealed the MSCR (D'Angelo *et al.*, 2007a) as the most recent advancement in favour of binders rutting evaluation tests. Of the previous tests, it represents more the field condition, is easy and quick to perform, and with the 10 stress levels applied the binder stress sensitivity can be assessed. At each stress level 10 cycles of 1 s loading and 9 s unloading are implemented. The average unrecovered strain divided by the associated shear stress yields the J_{nr}; the non-recoverable creep compliance, the evaluation parameter in MSCR. However, based on the following observed remarks, modifications to the test are applied as detailed in follow.

<u>Observations</u>:
- The strain reached at each cycle in MSCR test varies depending on the material's stiffness. This can be observed through creep loading test results in the previous chapter (Figure 4.7). Additionally, results of single creep-recovery tests revealed that recovered strain is dependent on the total applied strain at each stress level.
- The strain response varies in repeated cycles within one stress level. Although 10 cycles are performed, it requires around 50 cycles before reaching a stable strain value (Bahia *et al.*, 2001, Golalipour, 2011).

- The 9 second recovery period is not satisfactory to fully release the stored delayed elastic strain, potentially affecting the subsequent loadings and recoveries accumulatively.

- The MSCR classifies binders based on their recoveries. However, there is an inevitable requirement to recognize the stiffening effect (deformation resistance) especially when the recovery is reduced with stiffened materials as in mastics.

Modifications:

- Each stress is accompanied with a targeted strain limit to be reached repeatedly at each cycle. Consequently, different binders will deform equally but will vary their loading times depending on their stiffness. Different timings reflect a wide range of traffic conditions.

- Additionally, the reached (targeted) strain at each stress level that is repeated at each cycle will remove any requirement of higher number of cycle repetitions.

- 5 minutes recovery time is allowed at the 10th cycle of each stress level which removes any delayed elastic effect between stresses and offers a comparison between short and long recovery behaviours.

- Two factors are introduced to distinguish between the two rutting resistance mechanisms: stiffening and recoverability.

The idea of targeting a specific strain at each stress level is to establish a unified condition of testing. The applied stresses and their corresponding strains in MS-SCR, presented in Table 5.1, are derived based on an approximated linear relationship. More specifically, a ratio of 1.896 has been

selected based on the machine capability assessment as well as the limiting

strains reached by the pure bitumen (pure bitumen has the lowest stiffness).

Typically for this 40/60 pen bitumen examined at low (25 Pa) and high (25.6

kPa) stresses produced strains of 0.58% and 350% respectively within 1 s

loading at 50°C. The linear relationship of applied stress-strain will examine

any deviation from linearity experienced by the tested binders. A schematic

diagram presenting the MS-SCR test is shown in Figure 5.1.

Table 5.1 Applied stresses and their associated strains

Stress (Pa)	25	50	100	200	400	800	1600	3200	6400	12800	25600
Strain (%)	0.6	1.13	2.2	4.09	7.75	14.69	27.86	52.83	100.15	189.88	350
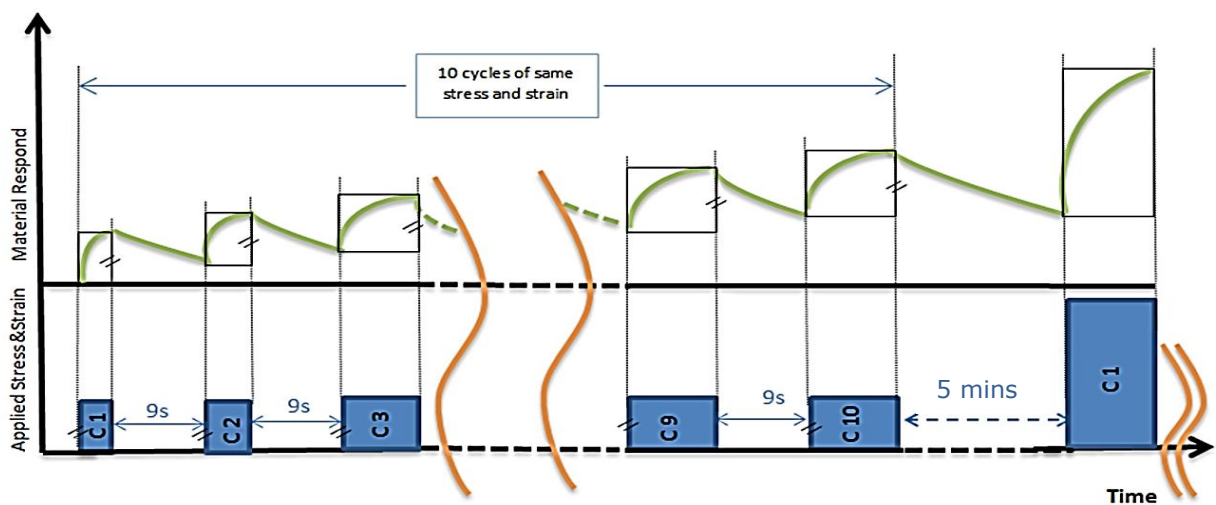
Figure 5.1 Schematic diagram of MS-SCR test with illustration of material response (without a scale)

5.3 Testing Equipment and Materials

A Kinexus DSR type from Malvern with a torque limit up to 0.2 N.m and

fitted with a rapid environmental controller (-40 to 200°C) was employed,

shown in Figure 5.2. In comparison to the old DSR generation, the machine

software offers high flexibility to customise a required test with precise

resolution (0.1 nNm torque resolution and 0.001°C temperature accuracy). In addition, temperature is controlled by air pressure to avoid any possible de-bonding between sample and plates as liquid may interfere in routine temperature control systems. 25 mm diameter parallel plates with 1 mm gap were used for all samples utilising the 'hot pour' sample preparation method.

Figure 5.2 Kinexus DSR type

MS-SCR test was performed at 30, 40 and 50°C on neat bitumen and two mastics with limestone and granite at three filler contents (35%, 50%, and 65%). In addition, two PMBs, elastomer SBS and plastomer EVA, were mixed with the 40/60 pen bitumen at 5% content of the total mass. Preparation of PMBs was by adding polymers in small amounts to the heated bitumen with continuous blending through a mechanical shear mixer, shown in Figure 5.3. The hot PMBs were then distributed into 10 mm vials, left to cool and then stored at 5°C for further testing. From visible inspection, incompatibility was observed with SBS polymer. Nevertheless, preparation was resumed to examine the MS-SCR ability to recognise how well the blending with polymer has taken place in a PMB. Tested materials are presented in Table 2 with

their codes. The reason behind testing polymer is to examine the validity of the new test to efficiently characterise PMBs.
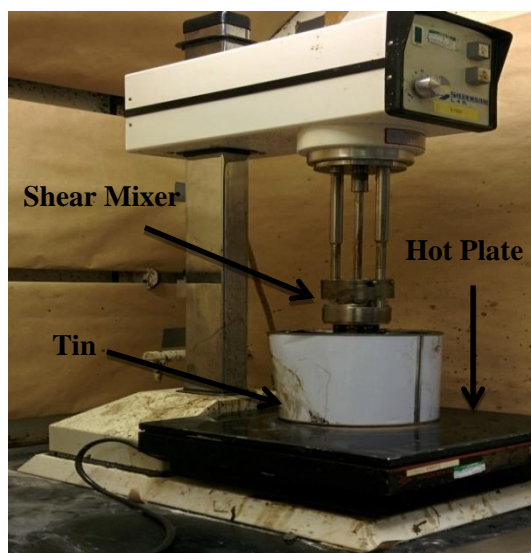
Figure 5.3 Mechanical mixer

Table 5.2 Binder types and codes

Code	B	M35	M50	M65	M35-2	M50-2	M65-2	P1	P2
Modifier type	–	Limestone	Limestone	Limestone	Granite	Granite	Granite	SBS	EVA
% of modifier of total	–	35	50	65	35	50	65	5	5

5.4 MS-SCR Test Results

Representative results for MS-SCR test at 40ºC are shown in Figure 5.4 describing accumulated %strain with time. Results clearly display a variation between accumulated strains based on their recoveries as well as discrepancy in loading times depending on the material stiffness. Similarly, the variation and discrepancy applies within repeated cycles at each stress level. A closer view of cycle 1 (C1) and cycle 9 (C9) comparison of %strain with time at 40ºC is illustrated in Figure 5.5. Dotted lines at 25 Pa are plotted against the left Y-

axis while full lines of 1600 Pa follow the secondary Y-axis. As can be seen, each material reaches the target strain at each cycle but varies its loading time at each cycle and stress level, as well as their recoveries within the allowable recovery time (9 s). The MS-SCR pays attention to both the unloading and the loading phases. Further investigations of creep loading and recovery of different binders' behaviours with MS-SCR test are discussed in the next sections.
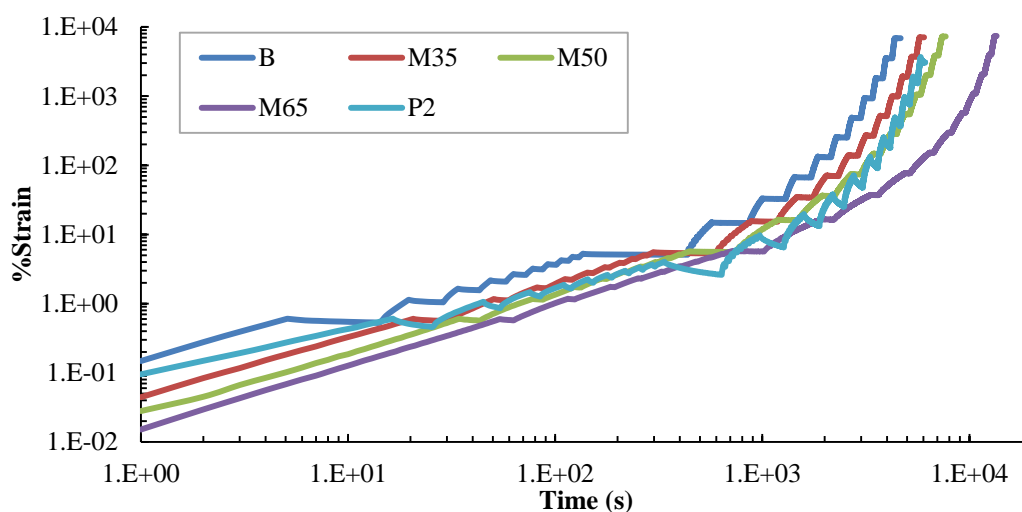
Figure 5.4 Typical results of MS-SCR @40ºC
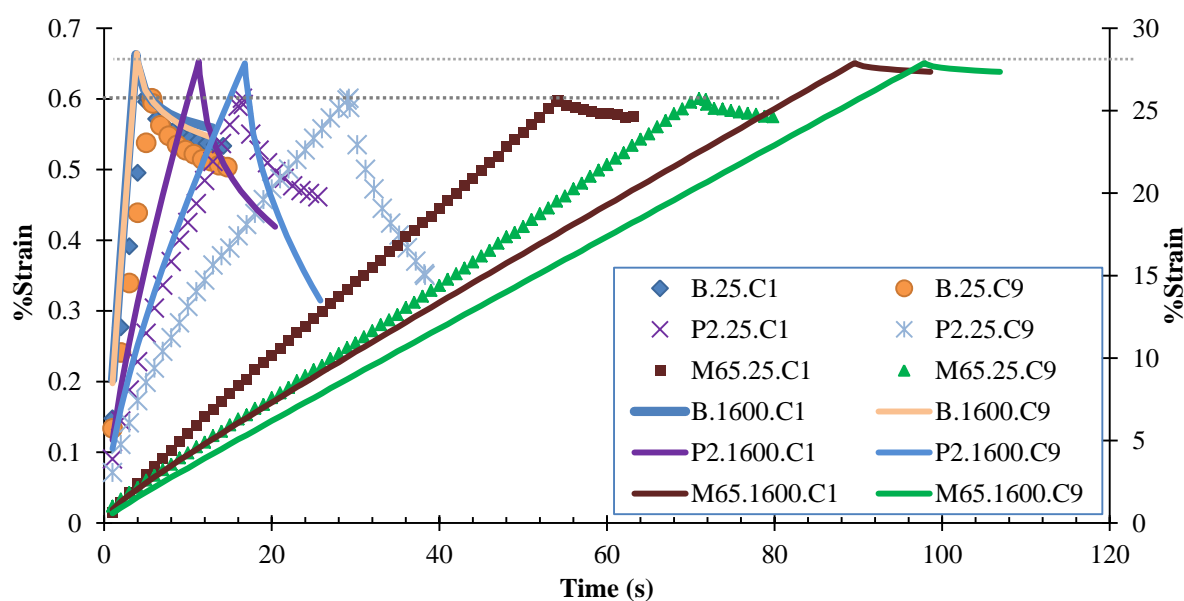
Figure 5.5 Loading and recovery of different cycles @40ºC

5.4.1 Normalized Recoveries

Single creep recovery testing in the previous chapter revealed that the recovered strain preserves a constant level after reaching a strain limit. It is interesting to re-observe the recovery in the MS-SCR test in Figure 5.6. As can be observed, different binders present different recoveries and increasing the stress-strain raises the recovered strain. Except for P2, at each stress-strain level the short recovered strain achieves approximately a constant value for each cycle repetition. While the incompatibility modification, P1, does not show significant improvement, P2 containing connected molecular structure extensively raised the recovery in comparison to the other binders. Moreover, the short recovered strain of P2 at each stress level continues to increase with each repeated cycle before reaching a constant value. Finally, the long recovery at the last cycle of each stress level is as expected greater than the short recovery.
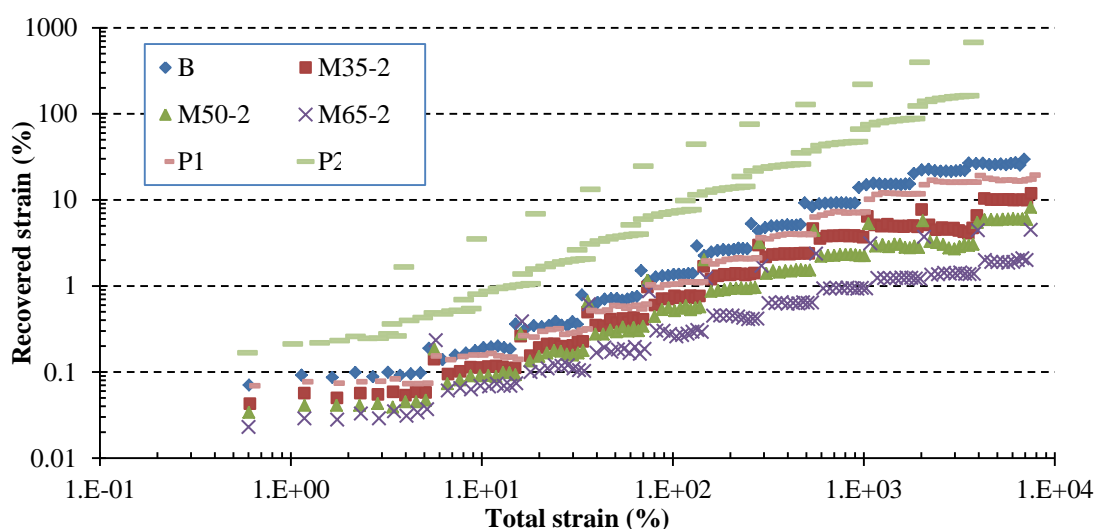
Figure 5.6 Recovered strain and total strain @40ºC

Similar to J_{nr} in MSCR, two parameters are introduced to characterise the recovery in MS-SCR; the normalised short and long recovery. They are

defined respectively as the average recovered strain of the first 9 cycles and the long recovered strain of last cycle (cycle 10) both normalised by the corresponding stress. Mathematically expressed by:

$$R_{ns} = \frac{\sum_{i=1}^{9} R_i}{9 \, \tau_m} \tag{5.1}$$

$$R_{nl} = \frac{R_{10}}{\tau_m} \tag{5.2}$$

Where R_{ns} is the average normalized short recovered strain for stress level τ_m, R_i is the recovered strain at cycle i, R_{nl} is the long normalised recovered strain at stress level τ_m, R_{10} is the recovered strain at cycle 10, and τ_m is the shear stress that ranges from 25 Pa to 25.6 kPa.

A summary of the two parameters at 30, 40 and 50ºC is plotted in Figures 5.7, 5.8, and 5.9 respectively. Several observations are highlighted. Results demonstrate that both recovered strains follow a constant level before they start to reduce at high stress levels. This is in line with the trend observed from the single creep recovery test (Figure 4.14 and 4.15) where the linear relationship there corresponds to the constant level here, and afterwards the drop here simulates the constant recovery stage of the single creep recovery test. Nevertheless, in the MS-SCR the reduction in recovery from the constant stage occurs at a lower stress level for the long recovery compared to the short recovery. Also, the higher the temperature, the shorter is the constant recovery stage.

In terms of filler content, the more filler that is added to the binder, the shorter is the constant stage. This points that the limiting strain level after which the recovery becomes constant (back in Figures 4.14 and 4.15) reduces when the filler content is increased. In terms of filler type, in short recovery the mastic with the better performance varied between the two types depending on the stress and temperature (for illustration clarity the comparison is not shown at 50°C), nevertheless, long recovery exhibits stabilisation to practically similar values.
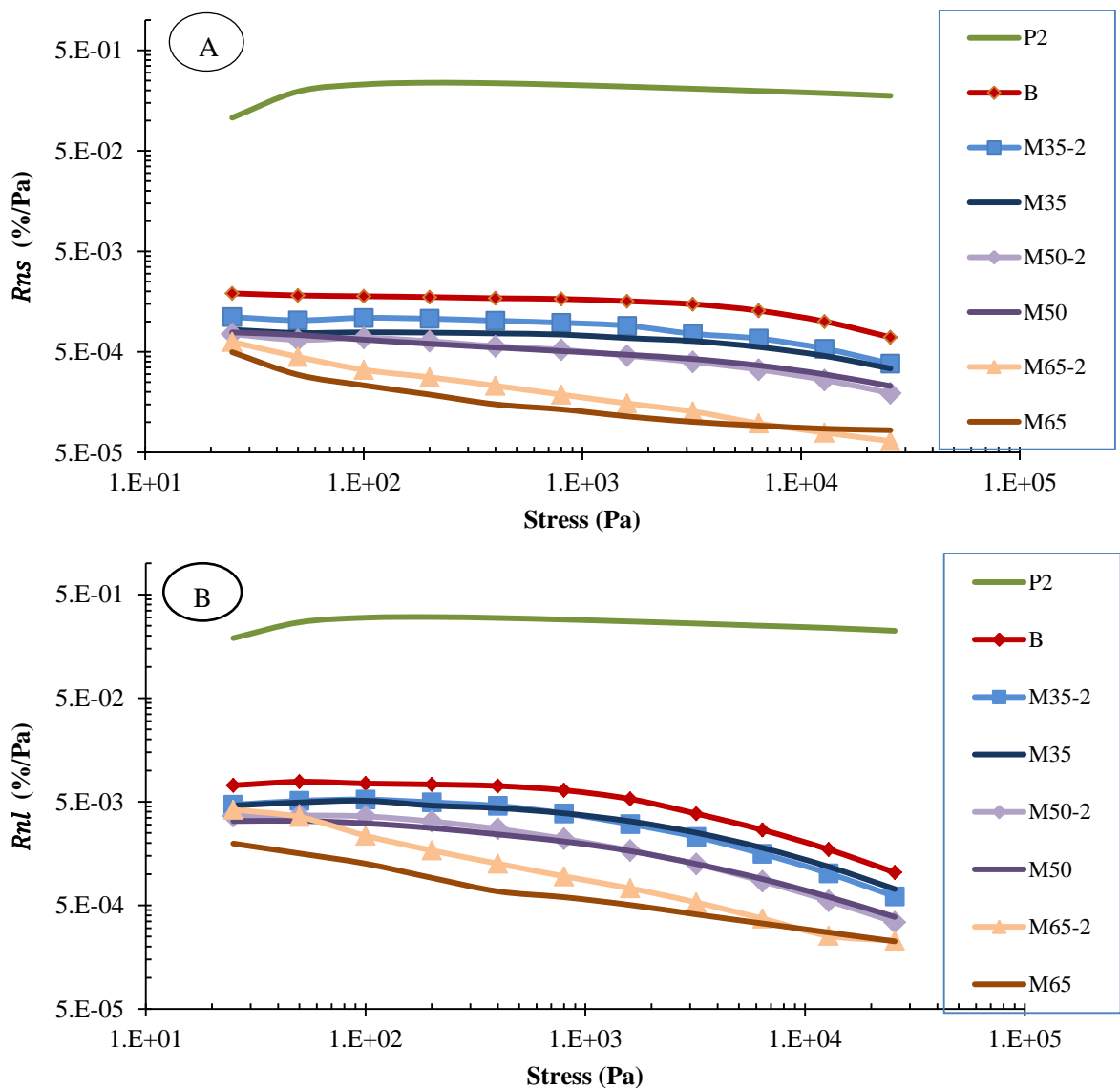
Figure 5.7 Normalized recoveries @30°C (A: Short, B: Long)
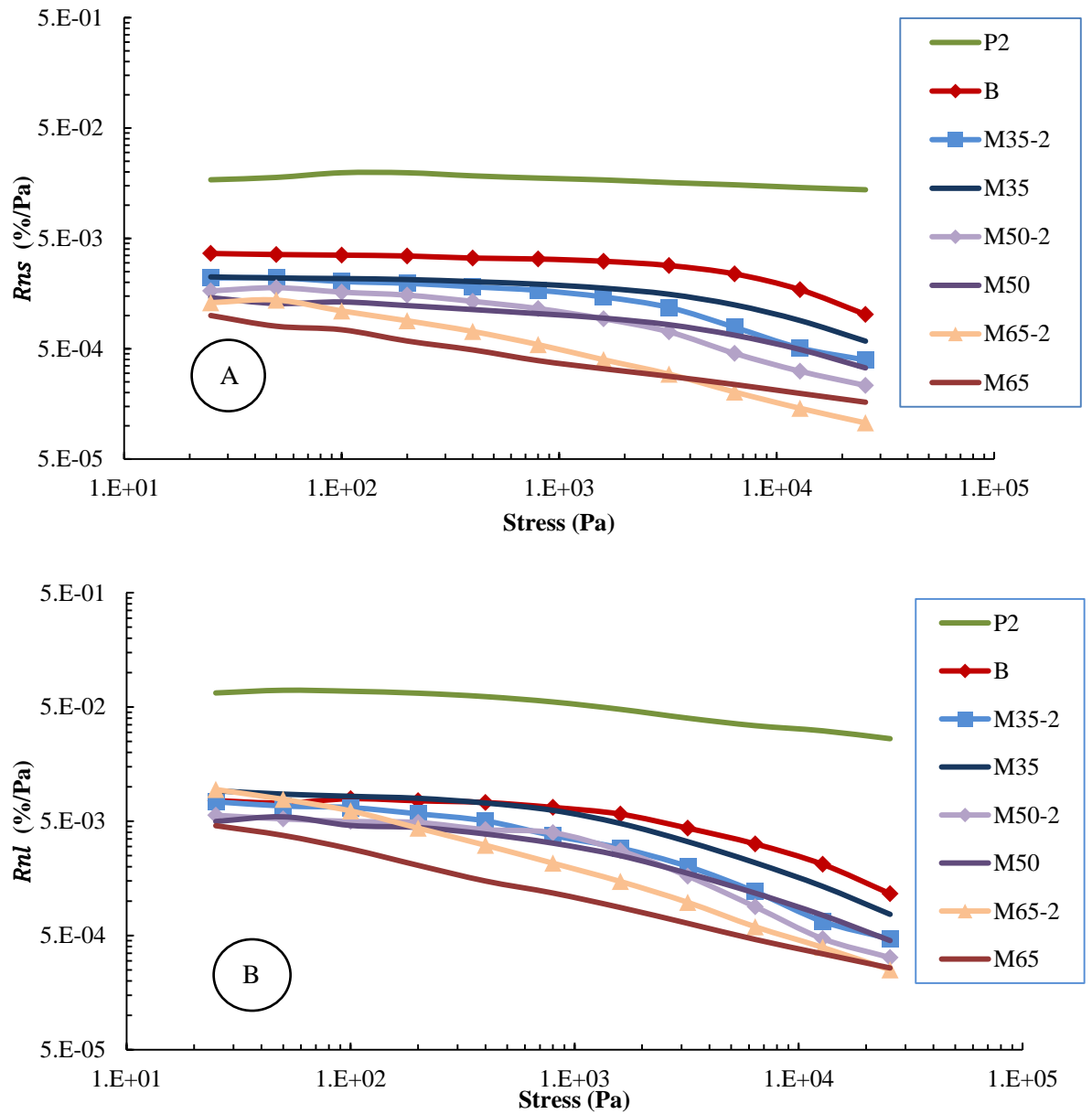
Figure 5.8 Normalized recoveries @40ºC (A: Short, B: Long)
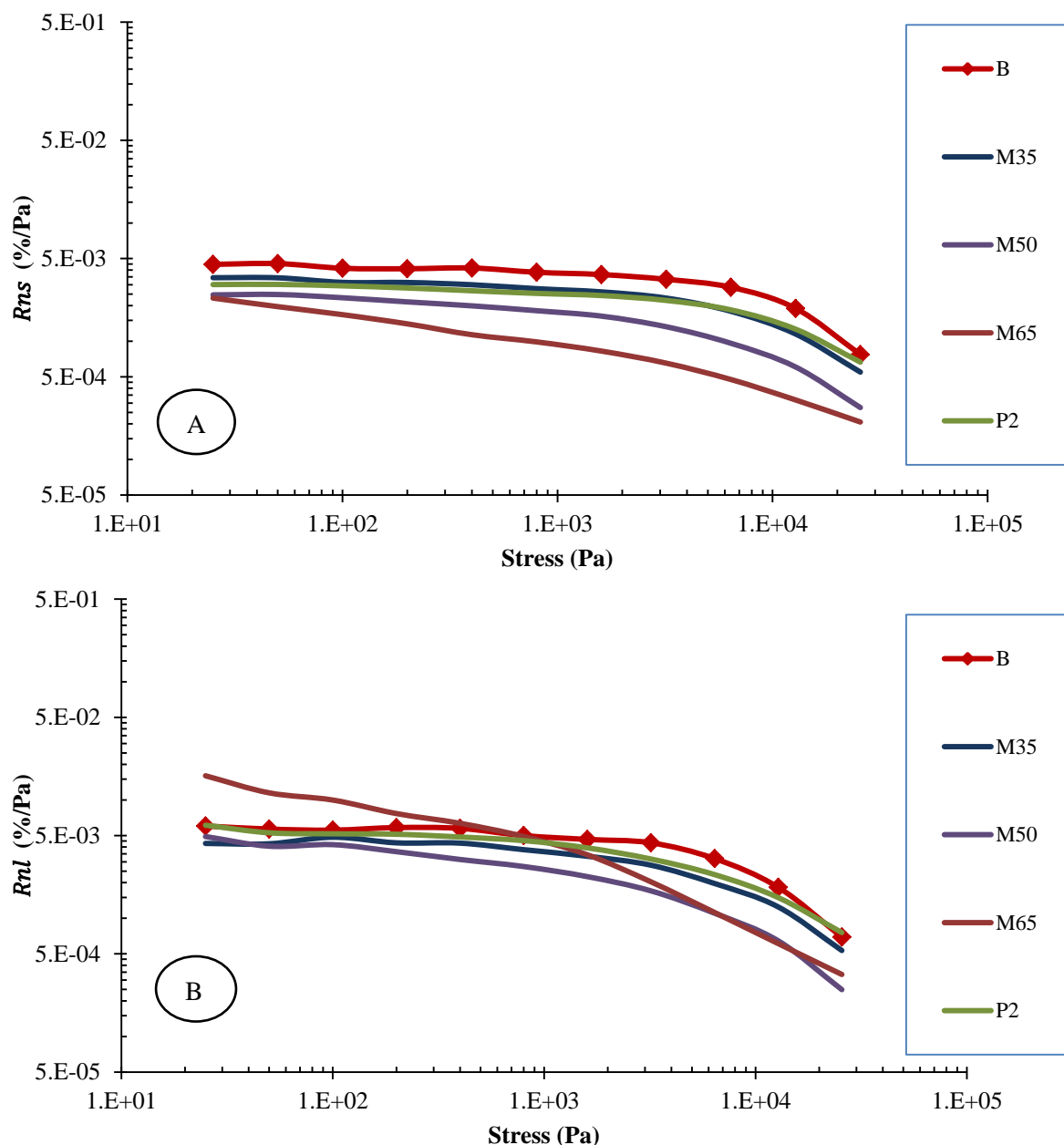
Figure 5.9 Normalized recoveries @50ºC (A: Short, B: Long)

Two distinctive observations can be seen for P2 and M65. P2 recoverability dramatically dropped at 50ºC, likely due to the destruction of molecules networks at high temperature. Thus, polymer recovery sensitivity to temperature appears to be higher than pure and filler modified binders. With high filler content (65%) at low stresses, there is a pre-stabilization period where particles re-orientate themselves to reach the packing state of high

friction. Consequently, the recoveries of M65 at low stress levels are greater than expected at long periods.

5.4.2 Cycle and Stress Loading Behaviour

Both filler and polymer stiffened the bitumen by reducing the deformation under creep loading. On the other hand, mastic recovery property is reduced by filler inclusion. Therefore, a second factor is required to distinguish between the two mechanisms of rutting resistance; recovery and stiffening. The notion of stiffening factor was derived through the concept of mechanical modelling.

For viscoelastic materials those models comprise physical elements such as springs and dashpots combined to properly simulate the behaviour (Woldekidan, 2011). In the time-domain of bituminous material testing, creep that represents increased deformation with time under constant loading is extensively simulated via the Burger's model. Apart from its experimental data simulation, it involves retardation time which describes the rate of strain growth over a certain time period. A lower rate of strain growth is an indication of higher resistance. After the instantaneous elastic deformation upon load application, the loading time to reach a specific strain value can represent a comparison factor of a material stiffness.

In the MS-SCR test the strain and stress levels are constants at each cycle but 'loading time' varies depending on the material stiffness and can be employed to measure the deformation resistance.

For instance, Figure 5.10 illustrates an example of how a material (M65) changes the time required to reach the required strain in cycle 1 and cycle 10 at 800 Pa stress at 30, 40 and 50°C. Similarly, between different stress levels the material also varies the loading time as shown in Figure 5.11. The cycle loading time can therefore vary depending on the temperature, cycle number, and stress level. Two features associated with creep loading time are identified; the change of cycle creep time at one stress level that recognizes loading history (cycle loading time), and creep time change with stress increase (normalised creep time).
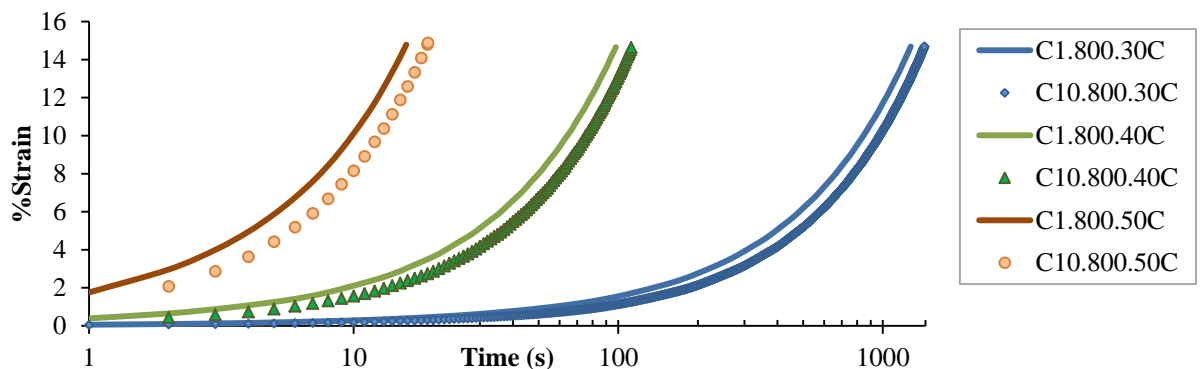
Figure 5.10 Comparison between cycle 1 and 10 loading time of M65 @30, 40, and 50°C
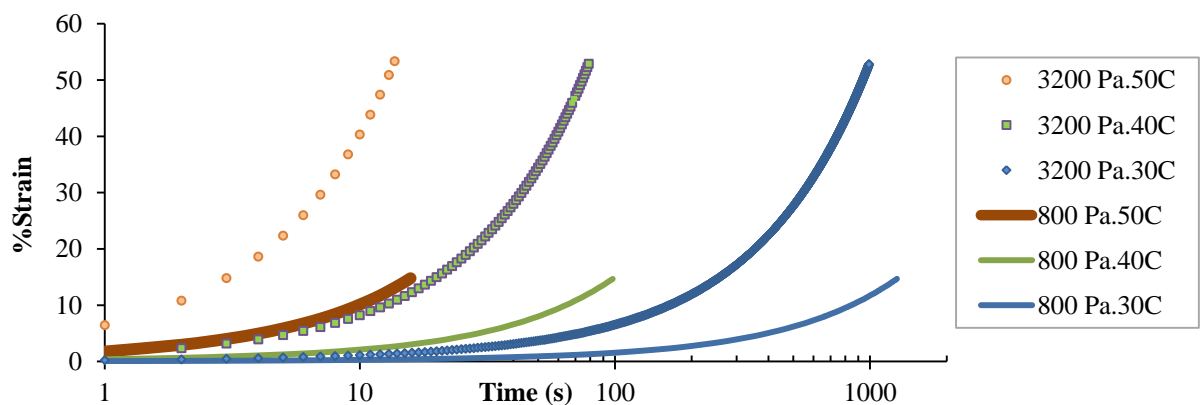
Figure 5.11 Comparison between 800 and 3200 Pa shear stresses loading time of M65 cycle 1 @30, 40, and 50°C

5.4.2.1 Cycle Loading Behaviour

The cycle creep time is defined as the loading time required to reach the target strain at each cycle. Figure 5.12 compares the cycle creep time between the first cycle and the last (10th) cycle at 30, 40 and 50°C for B and P2 at each stress level. It can be seen for pure bitumen that, although loading time is not changing with repeating the cycles, it decreases slightly with increasing stress level. Similarly, P2 exhibits shorter loading time to reach target strain level at high stresses in both cycles. However, there is a gap that appears at 30°C between the two cycles loading times that reduces with increasing the temperature.
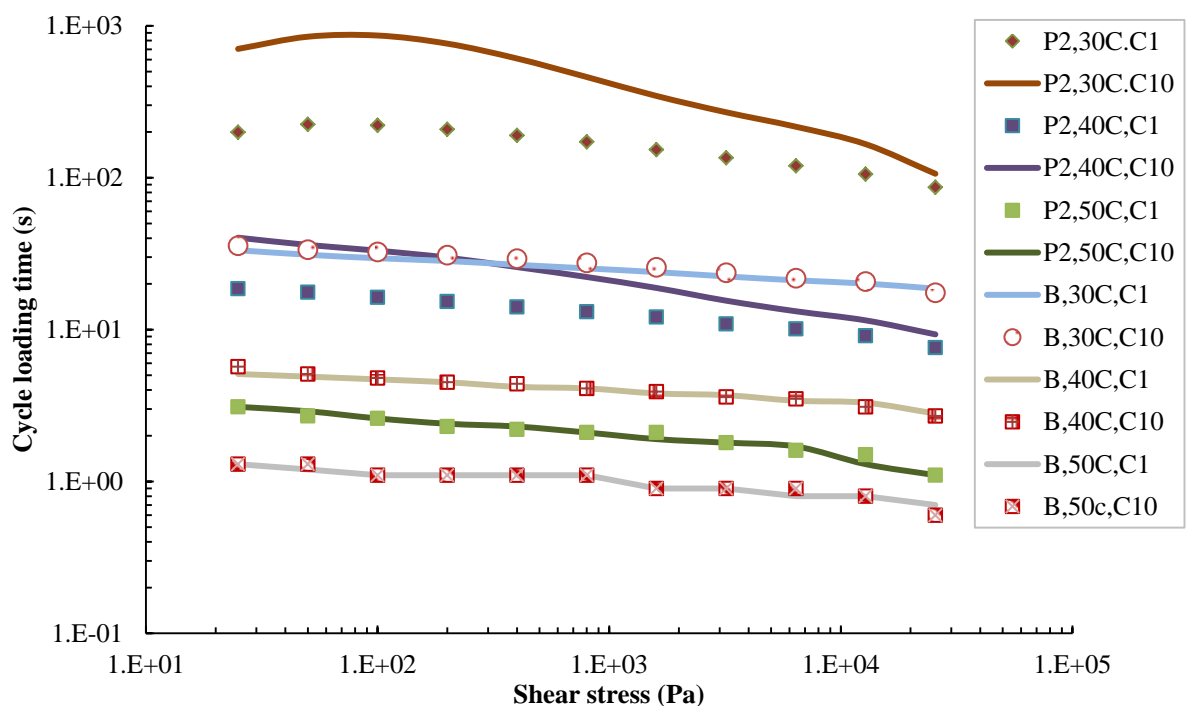
Figure 5.12 Loading time behaviour of cycle 1 and 10 of P2 and B

The reason behind the gap is the delayed elastic effect gained by insufficient 9 s recovery time (Zelelew, 2008, Masad *et al.*, 2009) which generates unrecovered strain energy. The stored energy resists deformation at the following loading period. The delayed elastic effect between cycles can be

seen to reduce at high stresses and vanishes at high temperature, as illustrated in Figure 5.13 (25 Pa follows the left Y-axis, 6400 Pa follows the right Y-axis). Consequently, the delayed elastic effect is more influential at low temperatures for PMBs.
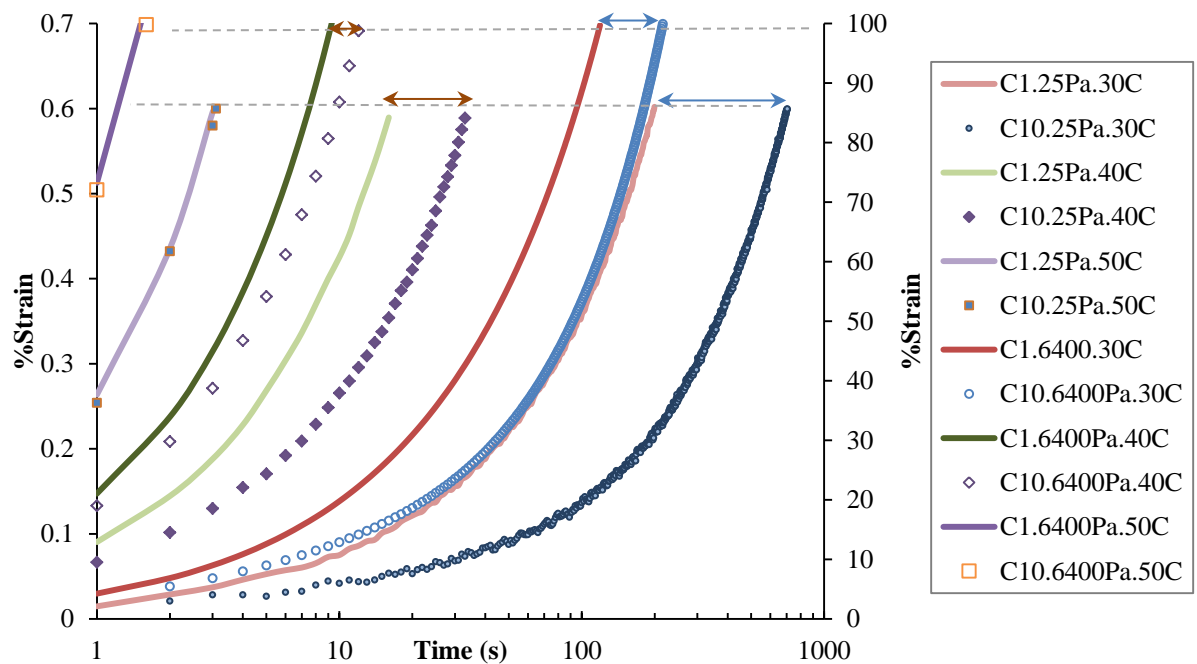
Figure 5.13 Example of variation in P2 cycle loading time with stress and temperature

Again, mastic with high filler content in Figure 5.14 exhibits longer loading time with increasing number of cycles at low stress levels similar to P2 (for brevity only one mastic type is shown as typical trend was observed with the other mastic). Mastic, on the other hand, has the lowest recovery, and B recovery lies between mastic and P2 (Figure 5.6). There is no change in loading time between cycles with B as Figure 5.12 illustrates (i.e., not much delayed elastic effect). This suggests that mastic with filler inclusion has a different mechanism that causes longer loading times with cycle repetition at low stresses.
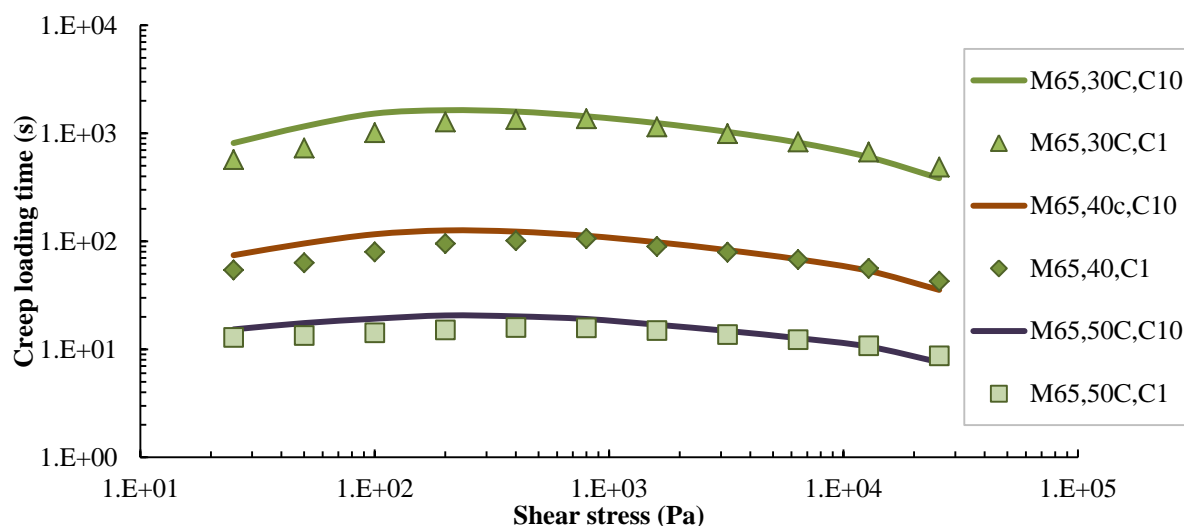
Figure 5.14 Loading time behaviour of cycle 1 and 10 of M65

A support of this can also be recognised by earlier matching trend between cycles with M65 in comparison to P2, as well as independent on the temperature the matching pattern is followed. A logical explanation at this case can be; filler particles structural orientation reorganizes itself through increasing their frictional resistance before reaching a 'stabilised condition'. Following the stability state is the particle-particle full contact resistance being established. Finally, both M65 and P2 trend exhibits a plateau stage followed by a decrease with increasing the stress level. This observation will be explained later.

5.4.2.2 Stress Loading Behaviour

To measure the stiffening effect of modifier (either polymer or filler) in respect to stress increase, the max normalised creep timing 'NCT' is introduced. The ratio of modified bitumen maximum creep time within the 10 cycles over the pure bitumen maximum creep time at the same stress level and temperature produces the NCT (pseudo stiffening effect parameter). The normalization measures the stiffening introduced by modification where the

thermo-rheological interaction is taken into consideration. Mathematically given by:

$$NCT = \frac{\max(T_m^{\tau_i})}{\max(T_B^{\tau_i})} \tag{5.3}$$

Where: $T_m^{\tau_i}$ and $T_B^{\tau_i}$ are the creep times of the 10 cycles at stress level τ_i of the modified and pure bitumen respectively.

Figure 5.15 plots the comparison between binders NCT versus stress level. As can be seen, the stiffening increases with increasing filler content and/or reducing the temperature. The reduction in stiffening due to temperature increase indicates that the rate of strain accumulation is higher in the pure binder than modified one. Therefore, the change in the strain rate of stiffened binders is less sensitive to temperature change than pure binder.
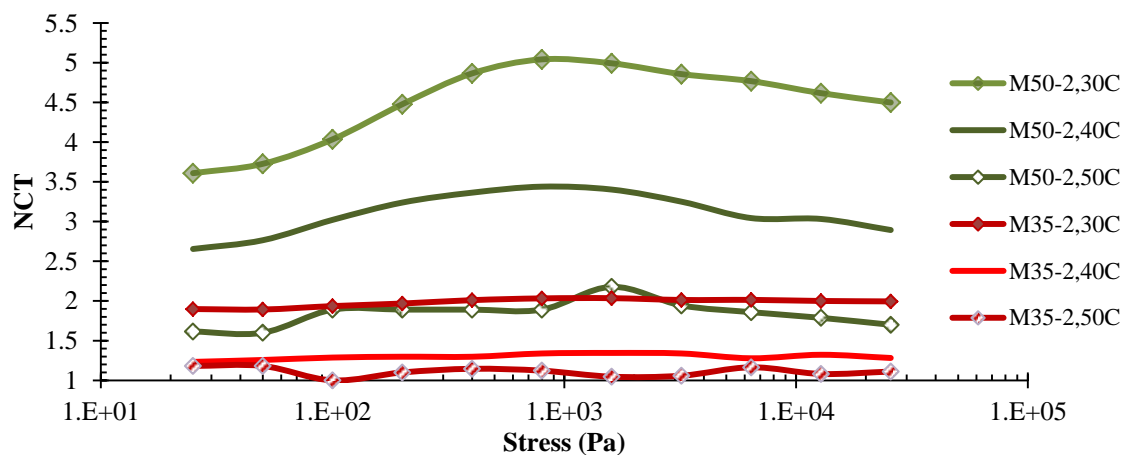
Figure 5.15 NCT versus stress of mastics with 35% and 50% filler contents

While low and intermediate filler contents demonstrate almost constant values across the stress levels at one temperature, mastic with high filler (65%) content displays a trend of initial increase to reach a plateau region followed by a continuous decline (Figure 5.16). The trend is distinct at low

temperature and the curve tends to straighten by increasing the temperature. Perhaps, the increase and decrease of the curve are intrinsic signs of nonlinearity.
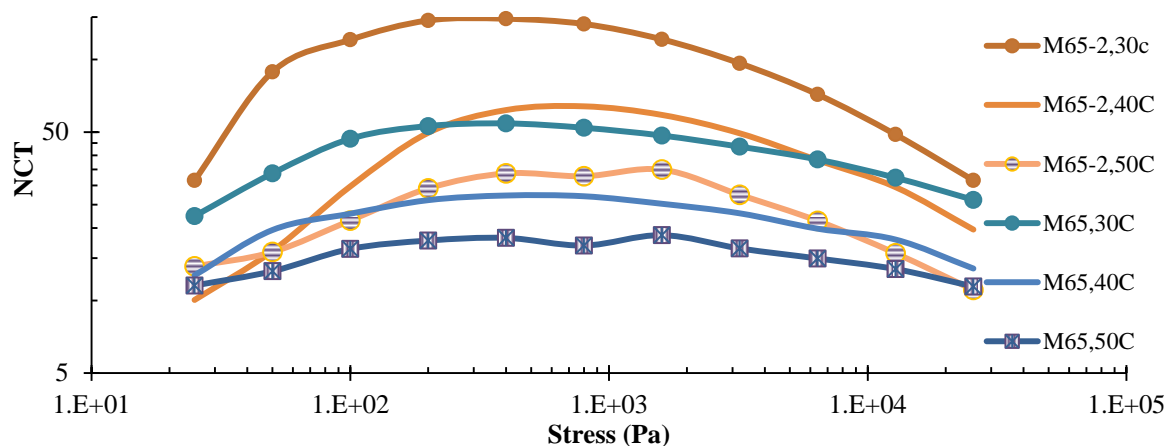
Figure 5.16 NCT versus stress of mastics 65% filler content

To check the hypothesis the creep compliance $J_{(t)}$ = strain/stress of the first cycle at each stress level is examined. The first cycle is chosen to remove any possible history influence on loading. Figure 5.17 compares between the neat bitumen (B) and highly filler modified mastic (M65) at 40°C. There is no observable change in the $J_{(t)}$ versus time slope for B as a function of the different stresses. On the other hand, M65 presents three stages related to the slope of $J_{(t)}$ versus time; a reduction of the slope between 25 to 400 Pa, a constant slope (400 to 1600 Pa), and finally an increase in slope (above 1600 Pa). These three stages as a function of stress level are typical of the relationship observed with the NCT trend. The stage at which the slope remains constant is by definition an indication of linear behaviour (i.e., stress independency). The early nonlinearity can be postulated as particle-particle contact interlocking establishment stage. The source of the second

nonlinearity stage at which NCT starts to decrease, or increase of $J_{(t)}$ slope, will be discussed in section 5.4.3.
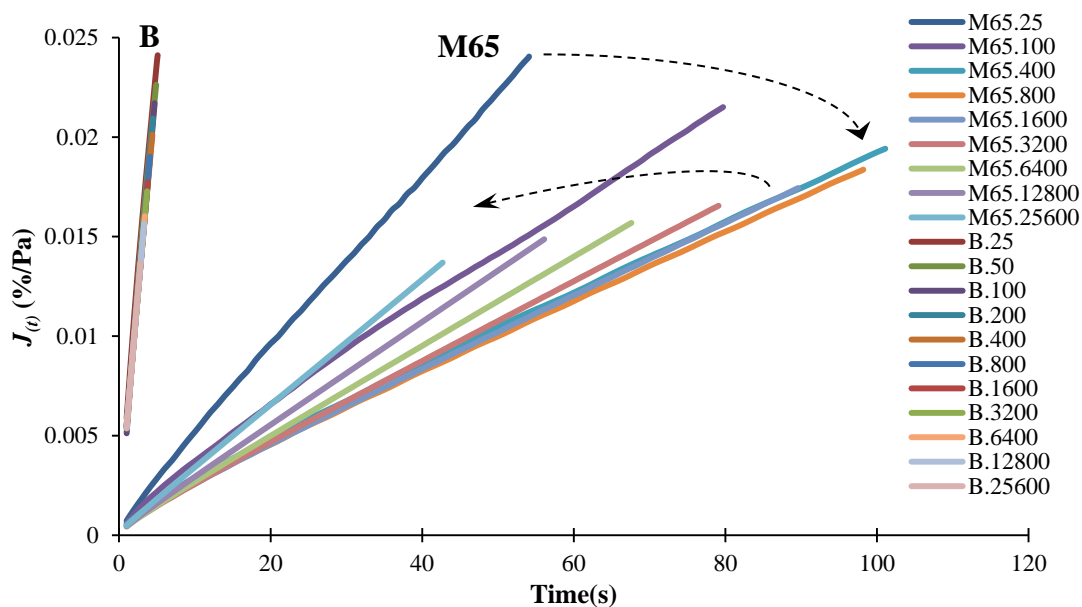
Figure 5.17 Creep compliance of first cycle change with time @40°C

Again, P2 in Figure 15.18 exhibits at 30°C an initial increase at low stresses before it starts to decline as in 40 and 50°C. As expected, P1 with polymer inconsistency shows no sign of stiffening with a constant value along the stress levels. Similar to the fillers which spend some time to establish particles interlocking, P2 forms its molecular network in the first nonlinearity stage. An illustration of $J_{(t)}$ changing its slope with stress increase of P2 at 30°C is presented in Figure 5.19. Parallel to M65, the slope follows three stages of slope change. The decrease of NCT at high stress levels at low temperature testing as pointed earlier is a second nonlinearity stage and the following section provides more investigation about the source of this nonlinearity.
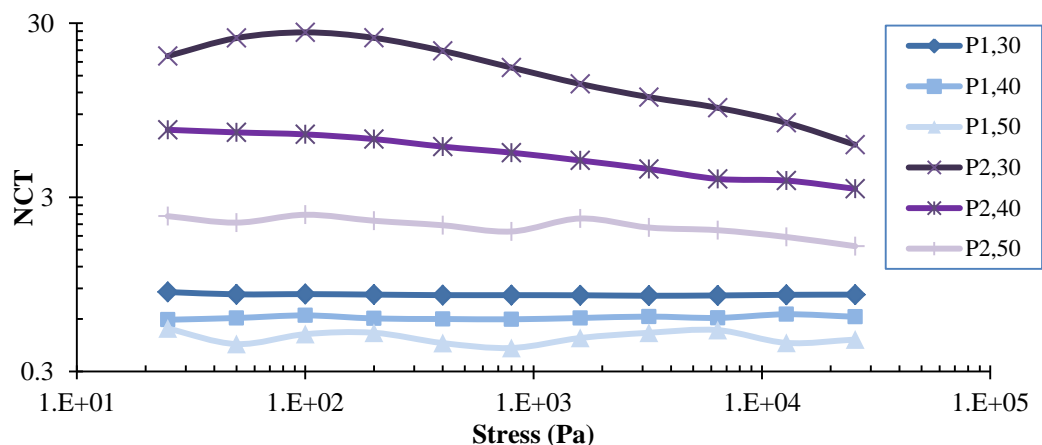
Figure 5.18 NCT of PMBs change with shear stress
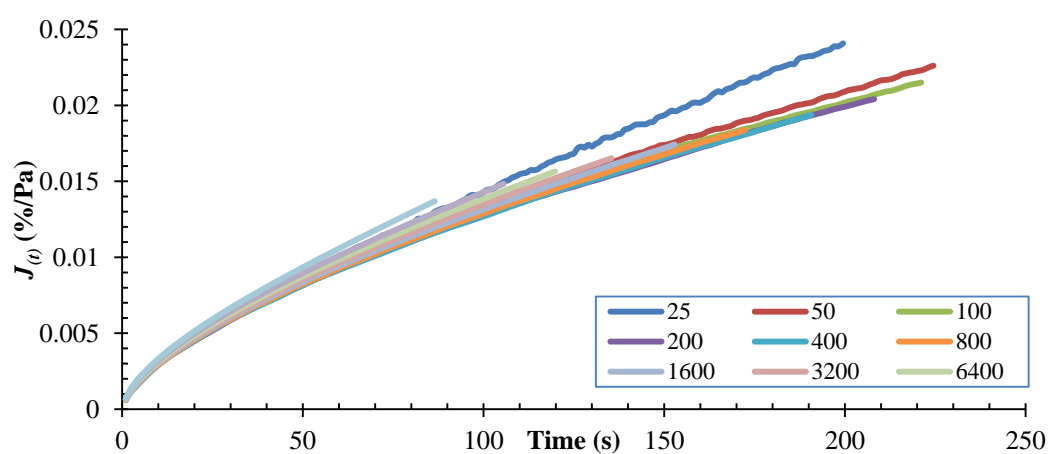
Figure 5.19 Creep compliance of first cycle against time of P2 @30ºC

5.4.3 Normal Force Effect in the DSR

Although a wide range of studies has intensively used DSR machines to characterise the binder linear and nonlinear viscoelastic properties, there is poor attention paid to the actual source or cause of nonlinearity (Motamed *et al.*, 2012).

DSR machines control the gap and maintain the thickness of the sample constant during the test via an automated normal force. Normal force is directly acting on top of the torqued sample face and can potentially affect the material response creating two forms of applied stress. Measurements on

the deformed sample are usually taken at the top edge (Figure 5.20) where the normal force directly acts on. The change in the normal force will be observed to study any correlation with the previously obtained parameters trends.
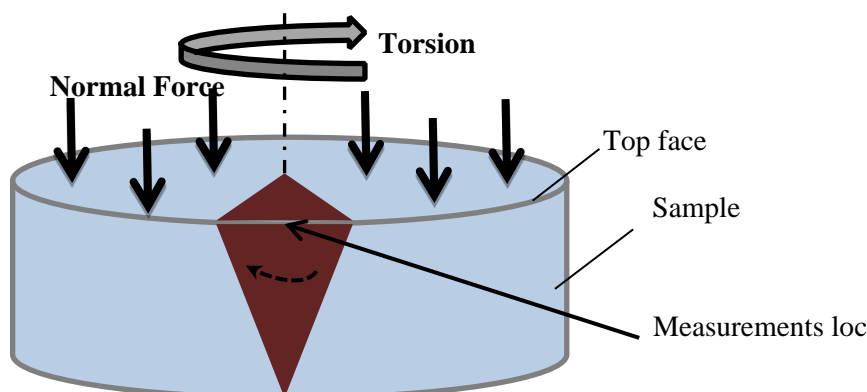
Figure 5.20 Schematic diagram of DSR sample acting forces

A full recording of the normal force during the MS-SCR test is presented in Figure 5.21. As can be seen, the compression normal force varies between stresses and cycles. It relaxes when the recovery is undergoing. Therefore, only creep loading part is affected by the normal force. Mastics with low (35%) and intermediate (50%) filler contents relatively to B have marginal effect on the normal force value. To study the effect with temperature change, Figure 5.22 compares the maximum normal stress at each shear stress level at 30 and 50°C of M65, M65-2, P2, and B.
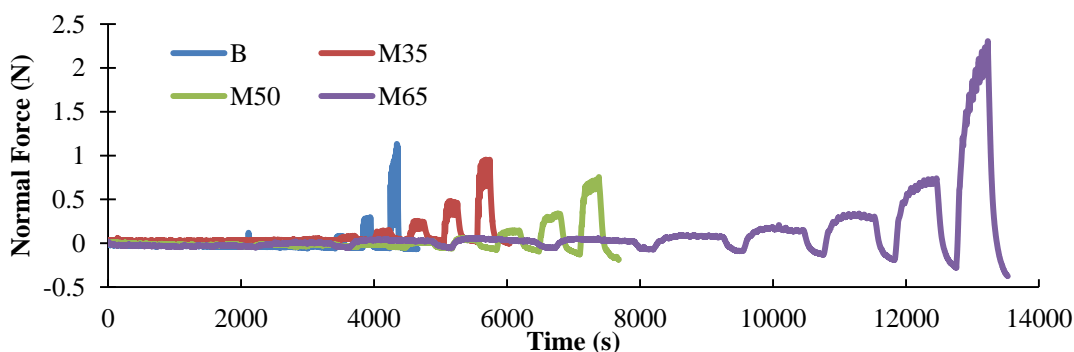
Figure 5.21 Normal force versus time in MS-SCR @40°C
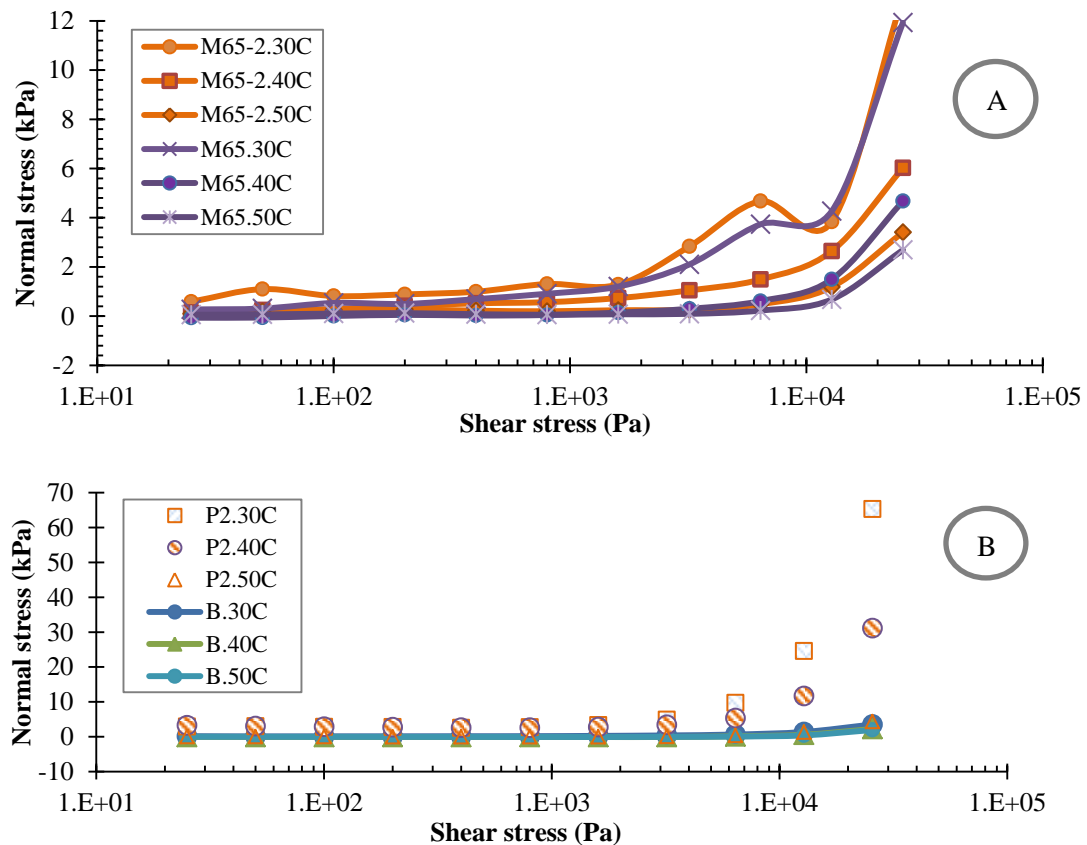
Figure 5.22 Normal stress versus shear stress in MS-SCR test

As can be noticed, there is a constant level of marginal normal stress after which it rises considerably. The development of normal stress is an indication to dilation of the sample. Deshpande *et al.* (1999), introduced the shear box analogy to explain the dilation or increase in the free volume of bituminous samples. It states that as the shear creep loading increases, particles establish their packing by riding each other. This leads the DSR to apply normal force due to the increased thickness at the vertical direction. In addition, the normal stress is increasing more with reducing the temperature by means of more dilation rate. Mastic with concentrated filler content is producing greater normal stresses at all temperature levels than pure bitumen.

In terms of filler type, the variation in normal stress between different mastic types is negligible. The dilation is an indication of particle interlocking. For M65 at 40°C, the normal stress starts to increase at stress level 3.2 kPa which is identical to the stress level at which the $J_{(t)}$ slope starts to increase after the secondary constant slope stage in Figure 5.17. The same remark is obtained at 30 and 50°C for M65, as well as P2 and M65-2.

This is a clear evidence of normal force shifting the mastic behaviour with high filler content to a nonlinearity phase. This type of nonlinearity is referred to an 'interaction nonlinearity' type. It states that due to the presence of other load component, normal force for instance, the material shear strain response changes (Motamed *et al.*, 2012). P2 is producing considerably higher normal stresses in comparison to the rest, its nonlinearity with NCT trend had been checked to be in line with normal force increase. However, no indication was found to cause the P2 high normal force value of up to approximately six times of mastic with high filler content.

5.4.4 Conclusions and Discussion

The literature reviewed the process of developing binder rutting evaluation parameters including the most recent MSCR test. On the other hand, although filler inclusion stiffened the bitumen it reduced the recovery property of the binder (Chapter 4). Therefore, a new multiple stress-strain creep recovery test was designed and proved to efficiently distinguish between the two rutting mechanisms; recovery and stiffening. Important observations have been concluded from the results:

1- The recovery property that relies on networking between molecular structures in consistent PMB is highly sensitive to temperature.

2- The short and long normalised recoveries maintained a constant level before starting to reduce at high stresses, and reduced earlier for the long recovery. In terms of filler content, the more filler that is added to the binder, the shorter is the constant stage. While filler type does not appear to influence the long recovery, the short recovery exhibited variable recovery rates depending on the temperature and stress level.

3- The 'delayed elastic' effect significantly influences the cyclic behaviour (both loading and unloading stages) of PMBs at low temperature. Mastics of high filler concentrations, demonstrate a different mechanism of pre-interlocking stage that affects cyclic behaviour and is temperature independent. However, the deformation rate in both modified binders (mastics and PMBs) was found less sensitive to temperature change than pure bitumen.

4- Examining the linearity in MS-SCR test, results revealed two nonlinearity phases that are experienced by the modified binders. At the early stages of MS-SCR within low stress levels the nonlinearity is possibly triggered by the ongoing process of particles full contact establishment and networks formation in highly concentrated filler mastics and PMBs respectively. The high normal force acting beside the high shear stress transferred the material to a second nonlinearity; classified as 'interaction nonlinearity' type. Between the two nonlinear phases the range of stresses that linear viscoelastic stage occupied was relatively short.

6. Mortar Shear, Uniaxial and Triaxial Deformation Behaviour

6.1 Introduction

Uniaxial and triaxial testing on idealised mixtures of single sized aggregate, as detailed in Chapter 2, revealed that their steady state deformation behaviour follows the bitumen trend of being linear viscous at low stress levels and nonlinear at high stress levels (Deshpande *et al.*, 1999, Deshpande *et al.*, 2000, Khanzada, 2000). The stiffening effect of single aggregates was found to be only dependent on their volume fraction.

The focus on this chapter is to understand the influence of fine aggregates with different gradations on the deformation behaviour with the aim of (1) producing a mortar type that most resembles the fine part of an asphalt mixture (Izadi *et al.*, 2011) (2) studying the characteristics of the steady state deformation behaviour of mortars with different mixture proportions (3) measuring the stiffening effect of fine aggregates under shear, uniaxial compression, and triaxial testing based on the response of the mortars to their corresponding mastics.

In this chapter an extensive experimental programme on mortars is presented. Manufacturing process and the testing procedure are detailed in

the first and second sections respectively. The following section presents and analyses the results. Finally, the stiffening effect of fine aggregate is evaluated utilising the extended MCM.

6.2 Experimental Programme

6.2.1 Material Selection

This chapter deals with mortar mixtures that contain bitumen, filler (less than 63 μm), and fine aggregates (sizes between 2 and 0.125 mm). For compatibility, the same 40/60 pen base bitumen and limestone filler utilised previously were used in the mortars. The granite fine aggregate was supplied from Bardon Hill quarry. Previously prepared mastics with 35%, 50%, and 65% filler contents by mass were used in the mortars.

6.2.2 Mix Design

The mortars were prepared with the same mastics (M35, M50 and M65) tested in Chapter 4, mixed with three fine aggregate gradations. The aim of this scaling up was to produce demonstrative mortars able to reflect the influence of fine aggregates and their interactions with mastics over different testing conditions.

The fine aggregate gradations of mortars are derivatives of the original 10 mm DBM asphalt mixture type (BS 4987-1:2005) upper, lower and mid-range aggregate gradations. The fine aggregate proportions remain the same but were normalised by the maximum aggregate size of 2 mm. The method of designing the mortar mixture is based on fixing the binder content and their

filler proportion that are available in the asphalt mixture, and then adjusting the fine aggregate gradation accordingly.

Three particle size distributions are shown in Figure 6.1 that have been obtained by scaling up the upper and lower limits as well as the mid-range of the 10 mm DBM aggregate gradations to a maximum size of 2 mm. This was followed by redistributing the fine aggregates proportionally based on the bitumen and filler contents. For instance, fine aggregates content between 2 mm and 1 mm by mass is 24% of the total aggregate for the upper limit after scaling up. With 5% bitumen content and 9.3% filler content to produce 'M65' mortar type; this becomes 26.24% of the total mortar mix (or 27.7% of the total aggregate mass excluding bitumen). This mortar composition contains the actual filler/bitumen contents in the standard asphalt mixture as well as the previously utilised mastics.

The maximum size 2 mm aggregate was selected as investigation of the full asphalt mixture in Chapter 7 includes X-ray scanning which only allows the detection of aggregates above 2 mm. The minimum size of 0.125 mm will prevent any possible increase in the quantity of filler.
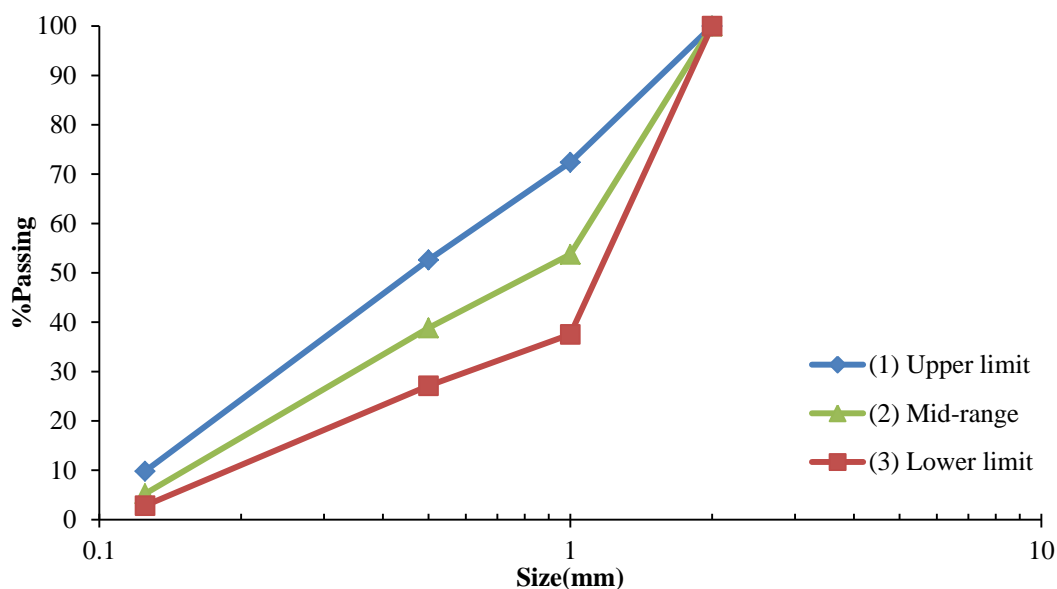
Figure 6.1 Mortar mixtures: fine aggregate gradations

Practical consideration should be given to the bitumen content in mortars as too much bitumen produces samples that creep under self-weight, or too low content results in high air voids and therefore fragile specimens (Zelelew, 2008). In this study three bitumen contents 5, 7, and 8% by mass of total mortar were used. The filler content varied based on the bitumen content but matched the actual filler/bitumen proportions (35%, 50%, and 65%).

Table 6.1 details the composition of the manufactured mortar mixtures. The first code in the sample ID refers to the mastic type followed by the bitumen content in the mortar. Average air voids for each mortar were measured on 5 samples cored from different positions based on densities according to BS EN 12697-8:2003. The actual full mixture bitumen content is 5.2% and thus, mortars with 5% bitumen content were considered the reference mortar type.

Table 6.1 Mortar mixtures compositions

Mixture ID	Mastic type	%Bitumen by mass of mortar	Aggregate gradation No	%Filler by mass	%Fine aggregate by mass	Average Air voids
M65-5%	M65	5	1	9.3	85.7	8.6
M65-7%	M65	7	1	13	80	7.4
M65-8%	M65	8	1	14.8	77.2	7.5
M65X-5%	M65	5	3	9.3	85.7	10.5
M50-5%	M50	5	2	5	90	13.5
M35-5%	M35	5	3	2.7	92.3	16.5
M35-8%	M35	8	3	4.3	87.7	14.6

6.2.3 Specimen Manufacture and Sample Development

Available laboratory compaction methods can produce similar specimens but of different mechanical properties. It is required in this study to produce specimens with uniform air voids along the height. The Superpave gyratory compactor (SGC) combines a rotary shearing and a vertical force to compact a specimen to a target density. Izadi et al. (2011) revealed that mortar samples produced by SGC provided the greatest resemblance in terms of microstructure to a full scale asphalt mixture from X-ray evidence.

Initially the mastics were prepared as detailed in Chapter 4. The required amount of mastic and the batch of fine aggregates were then heated at 220°C and mixed manually for about 3 minutes (according to BS 12697-35:2004). The correct quantity of mortar mixture was placed in a 150 mm diameter gyratory mould. The mould was heated and lubricated with silicone grease on the internal surfaces before the mixture was poured. Then, each specimen was compacted in the SGC to a 250 target number of gyrations which was

approximately the limit of achievable maximum density (Figure 6.2). Compaction was conducted at 600 kPa vertical pressure and 1.25° internal angle.
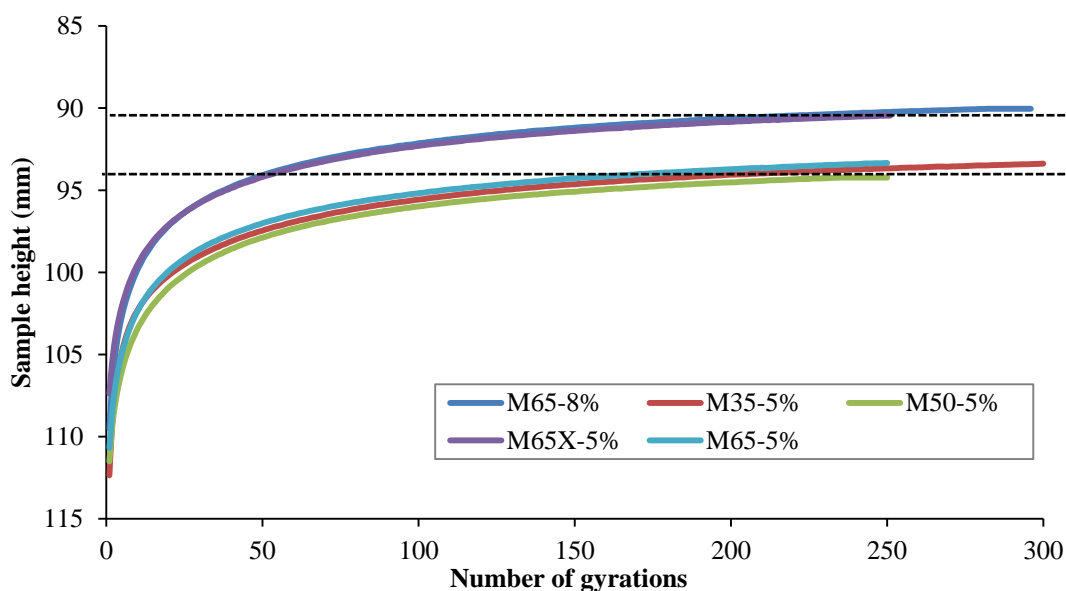
Figure 6.2 Mortar samples densities during gyratory compaction

After cooling, each specimen was carefully extracted from the mould and stored at 5°C. For shear and uniaxial compression tests, each specimen was trimmed equally from both sides with a saw cutter to a final 50 mm height and then samples were cored by a 20 mm internal diameter mechanical barrel, Figure 6.3 (A). The 20 mm diameter is acceptable in respect of being at least 10 times the maximum aggregate size (Deshpande *et al.*, 2000) and for coring practicality, while the 50 mm height was tall enough to provide shearing response from torsion. The relatively high filler content made it impossible to core samples less than 20 mm diameter without damaging the coring barrel.
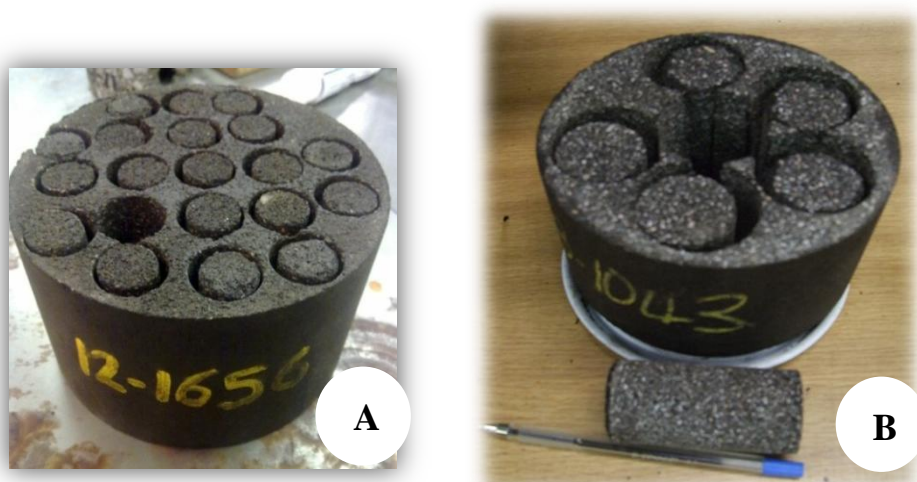
Figure 6.3 (A) Shear and uniaxial compression cored samples (B) Triaxial cored samples

For triaxial testing, specimens were cut equally from both sides to reach 76 mm final height. Then samples of 38 mm diameter were cored carefully by a mechanical barrel and checked for a uniform height, Figure 6.3 (B). The 38 mm diameter was chosen to fit the available standard triaxial cell, while the height was selected to fulfil a ratio of 2 between height to diameter as identified in (Deshpande *et al.*, 2000, Taherkhani, 2006). Any sample of either geometry that presented a non-vertical alignment was excluded.

6.2.4 Test Equipment and Sample Set-up

For shear creep testing, the Gemini DSR machine was modified by fitting an extended temperature cell (ETC) for temperature control, as shown in Figure 6.4. For sample testing preparation, a sufficient amount of instant adhesive glue was placed between disposable plates and the two surfaces (top and bottom) of the sample. The sample was clamped to solid fixtures by two bolts through the disposable plates on both sides (Figure 6.5) and then connected to the Gemini shaft. Full details of the process are presented in Appendix B.
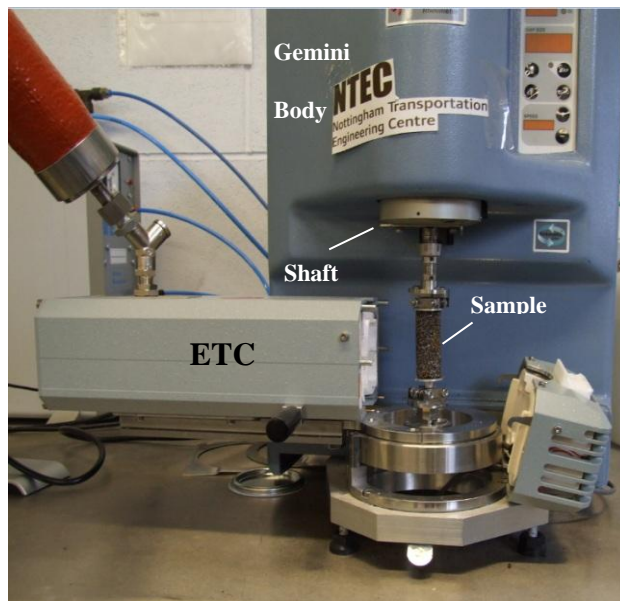
Figure 6.4 Sample installation in Gemini
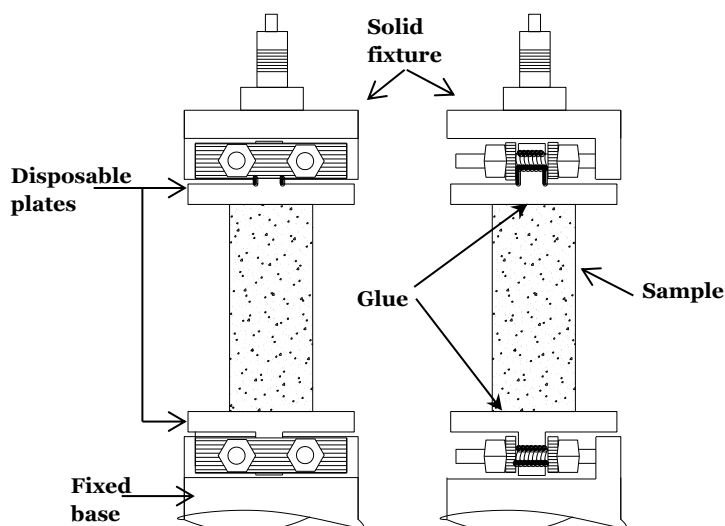
Figure 6.5 Schematic illustration of solid fixture and glued sample (without scale)

A DSR 'machine compliance' phenomenon occurs when high torque is applied on a relatively stiff material. At this condition the sample will twist but so will the sample installation system (glue + solid fixtures). Consequently, the final displacement result will include both the sample and the instrument displacements.

A series of creep-recovery tests on a stiff aluminium dummy specimen (18 mm diameter and 50 mm height) was conducted to measure the compliance at 30°C and 50°C. The shear loading ranged from 10 to 110 kPa for 10 minutes and the recovery was allowed for 30 minutes between each stress level. The test results at 50°C are shown in Figure 6.6 where the normalised compliance by shear stress shows approximately a constant level within the loading time.
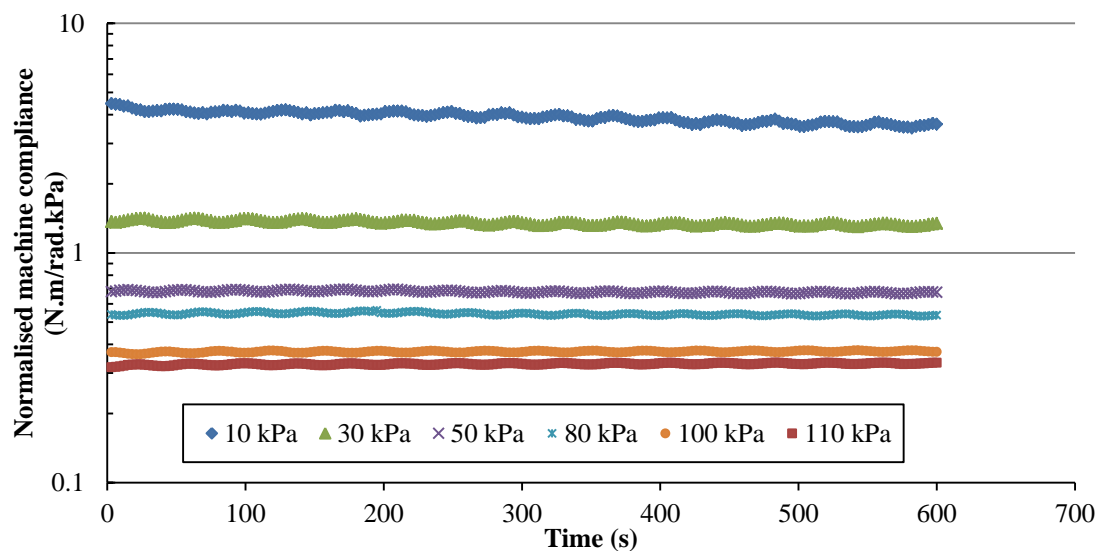
Figure 6.6 Normalized creep machine compliance change with time @50ºC

Creep compliance was measured and found constant at about 22.2 mrad/N.m in the loading part (both temperatures) while full recovery was obtained during the unloading phase. The correction on any mortar test can be applied by first, multiplying the applied torque by the compliance to get the instrument angular displacement, and then subtracting this value from the measured angular displacement. Aluminium shear modulus is approximately 2.6E+10 Pa and with maximum torque of 0.2 N.m of the machine, the aluminium compliance can be calculated to be 1.87E-04

rad/N.m. This low value can be neglected as it contributes only about 1% of the total compliance.

To assess the thermal equilibrium time for mortar samples, amplitude sweep tests with 1 Hz single frequency at 1 kPa and 10 kPa shear loading were applied at 30, 40 and 50°C. Figure 6.7 plots the complex modulus/sin(phase angle) (G*/sin (δ)) against time. Testing at 30°C required around 3500 s to achieve a stable value while higher temperatures required less time. However, taking into consideration the different compositions of the mortars, the thermal equilibrium time was set to 1 hour for shear creep before commencing the test.
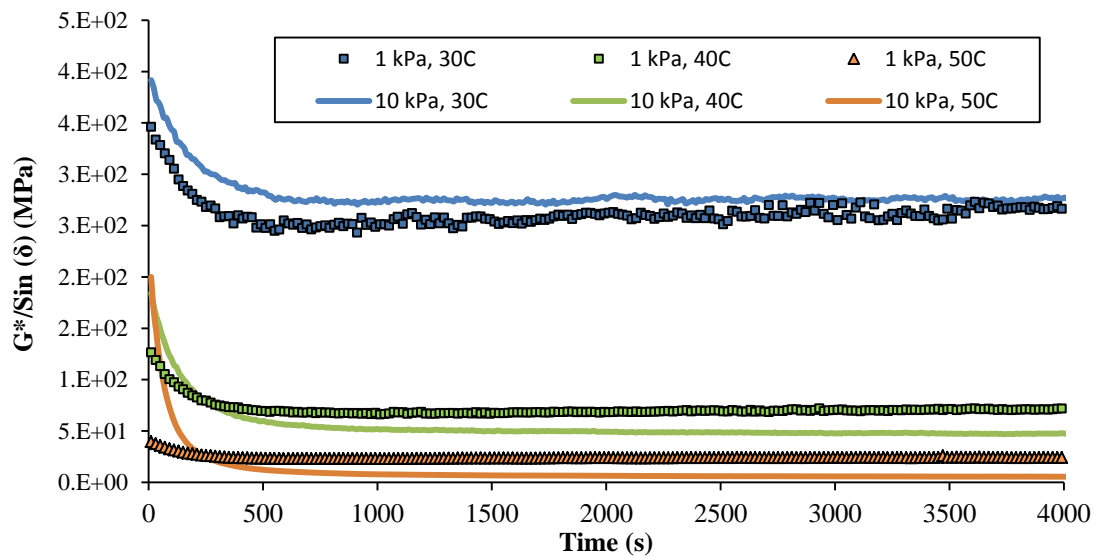
Figure 6.7 Thermal equilibrium time for mortar samples in the DSR

For uniaxial compression tests, an Instron machine was employed. The major components of the electromechanical system as shown in Figure 6.8 include: loading frame with integral controller, loading cell mounted on a moving crosshead, frame base, control panel and computer system with

Bluehill® software, and an environmental chamber to control the temperature. The chamber has a -150 to 600°C operational range with ±0.5% accuracy and ±2°C temperature stability. The loading cell of ±0.025 N accuracy was connected to the specimen by a ram passing through the chamber roof and continuously monitored the applied loading with feedback from the control system. A lubrication system of silicon graphite powder and silicon grease was used to reduce friction between the sample surfaces and plates (Dunhill *et al.*, 2002, Deshpande *et al.*, 1999). Prior to testing, each sample was kept for 1 hour inside the environmental chamber in the target temperature to achieve thermal equilibrium.
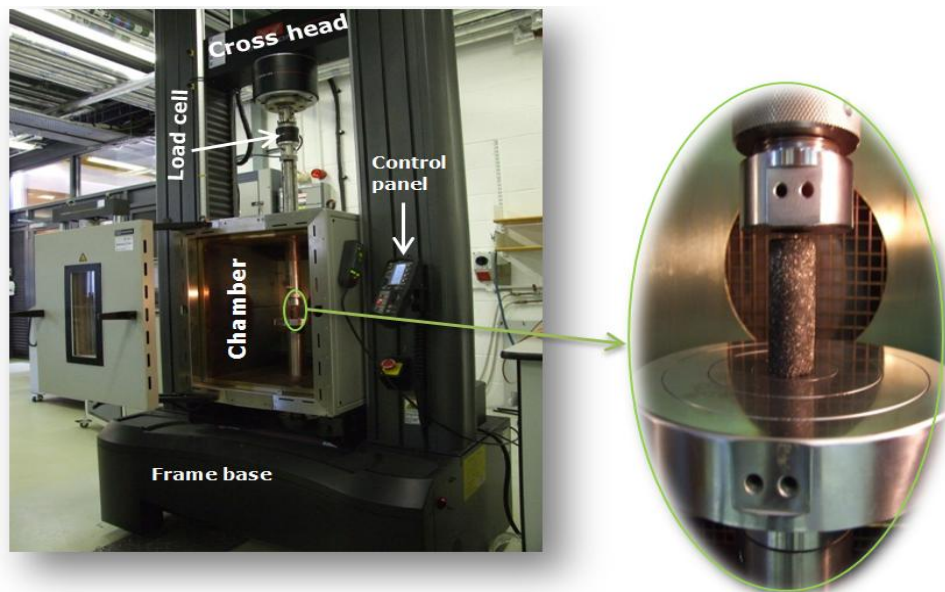
Figure 6.8 Sample inside Instron conditioning cabinet

The triaxial testing was performed in the same Instron machine that was utilised in uniaxial testing, fitted with a triaxial cell. The triaxial cell was designed for a standard soil 38 mm diameter sample size and was located inside the environmental chamber room as photographed in Figure 6.9. The

cell consists of a submersible piston, cell chamber, an aluminium base, valves and a pressure gauge.

Figure 6.9 Sample in the triaxial cell inside the Instron machine

As used in uniaxial testing, a friction reduction system was placed at both end surfaces of the sample. Samples were sealed from the air pressure by an impervious latex membrane inside the cell. Two platens were connected to the sample upper and lower surfaces inside the membrane. The membrane was fastened by two rubber O-rings on the platens at the ends of the samples. After checking the plates' alignment to prevent any loading eccentricity, the cell chamber was fastened tightly to the base and checked for any air leaks. The cell was left inside the environmental chamber overnight (or for a minimum of 6 hours) to ensure a uniform temperature of the test set-up. A schematic diagram of the triaxial set-up is shown in Figure 6.10.
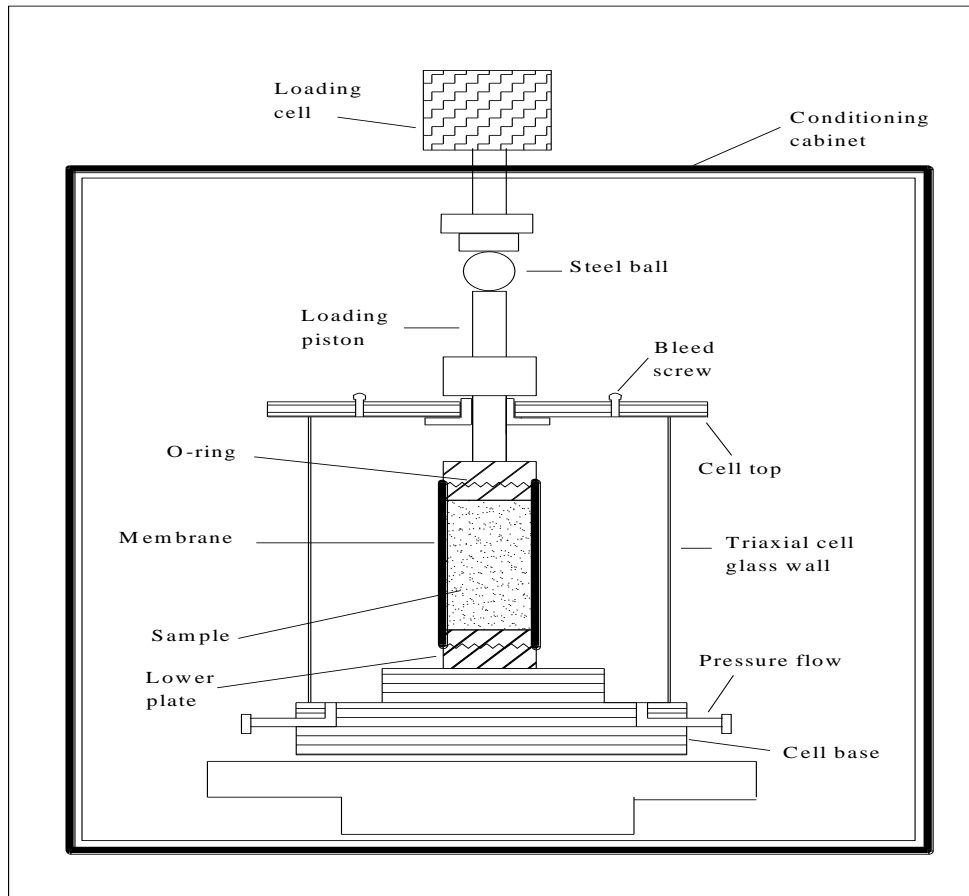
Figure 6.10 Schematic diagram of the triaxial cell (without scale)

The axial loading was applied to the specimen from the loading frame through the submersible piston via a steel ball. The loading cell on the frame applied the required force, monitored the axial deformation and provided the feedback signal to the acquisition system. The required confining cell pressure was achieved through an air pressure pipe connected to the cell through a pipe and measured by a connected gauge.

6.2.5 Testing Protocol

Shear creep test

In the shear creep test, a stress was applied and held constant until the material failed and the resulting strain was recorded as a function of time.

The test was performed at 30°C and 50°C with shear stresses ranging from 10 kPa to 110 kPa.

Single shear creep recovery test

The shear recovery property of the mortar was investigated by performing a series of single shear creep recovery tests. A constant shear stress was applied for a predetermined time and then released during the recovery period. The strain was continuously recorded during the loading and unloading phases until it reached approximately a constant level. The test was implemented at 30°C and 50°C with 10 kPa and 50 kPa shear stress.

Uniaxial compression test

In the uniaxial compression test, the loading frame was lowered until it touched the sample upper surface with a small load. The target stress was then applied quickly within 30 to 50 milliseconds and held constant until failure was observed. The strain was recorded as a function of time and then data were taken from the acquisition system. The test was performed at 30°C and 50°C with a range of 10 to 110 kPa axial stress.

Triaxial test

A similar loading procedure to the uniaxial compression was followed but before starting the loading the target air pressure was slowly supplied through a regulator and monitored by a pressure gauge. The axial loading and deformation were continuously recorded and displayed on a connected computer screen during the test. The test was implemented at 30°C and 50°C with an axial stress ranging from 30 kPa to 300 kPa.

In the triaxial test two of the three principal stresses are identical due to the symmetry arrangement and equal to the confining stress. The sum of the confining stress and axial (deviator) stress gives the third principal stress (Figure 6.11). The mathematical representations of the principle stresses are given by:
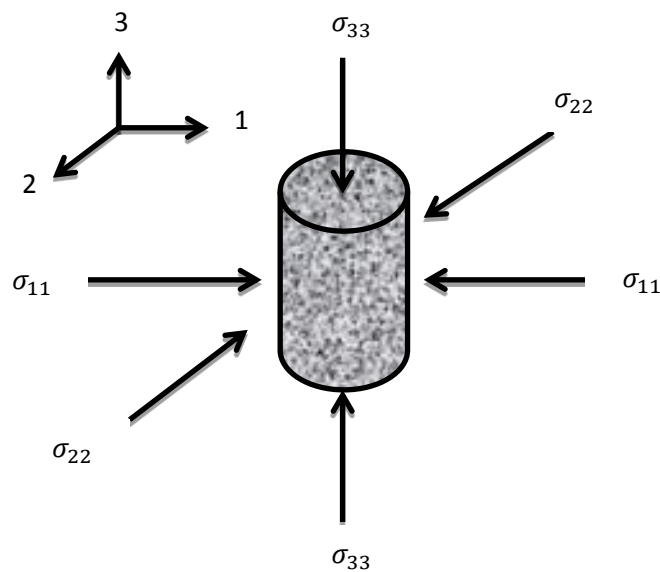
Figure 6.11 Schematic diagram of principal stresses in triaxial test

$$\sigma_{11} = \sigma_{22} = P \tag{6.1}$$

$$\sigma_{33} = \frac{Q}{A} + P \tag{6.2}$$

Where P = confining stress, Q = axial load, A = cross sectional area of the sample.

The mean (σ_m) stress and deviatoric stress (σ) are given by:

$$\sigma_m = \frac{\sigma_{11} + \sigma_{22} + \sigma_{33}}{3} = \frac{Q}{3A} + P \tag{6.3}$$

$$\sigma = \sigma_{33} - \sigma_{11} = \frac{Q}{A} \qquad (6.4)$$

The triaxal test was performed at a single stress ratio of 0.5. The stress ratio was identified by Deshpande *et al.* (1999) as $\alpha = \frac{\sigma_m}{\sigma}$. The reason for selecting 0.5 is based on the equipment capacity as well as no sign of creep deformation being obtained with a further increase in the stress ratio. With a higher stress ratio the stiffening was significantly higher and the resulting deformation was very low even at 50°C.

6.3 Testing Results

6.3.1 Mortar Shear Creep

Constant shear stress tests were conducted on mortars at 30°C and 50°C with stresses ranging from 10 kPa to 110 kPa. Typical results are shown in Figure 6.12(A) where shear strain is plotted as a function of time, and Figure 6.12(B) shows a shear cracked sample. Similar to the binder, the strain passes three stages; starting with a region where strain rate decreases with time, followed by a constant steady state strain rate (SSSR) region, and eventually a dramatically increasing strain rate that indicates failure of the material. As can be noticed, the SSSR increases with increasing stress level at a given temperature. A summary of SSSRs against stress levels at 30°C and 50°C is presented in Figures 6.13 and 6.14 respectively.
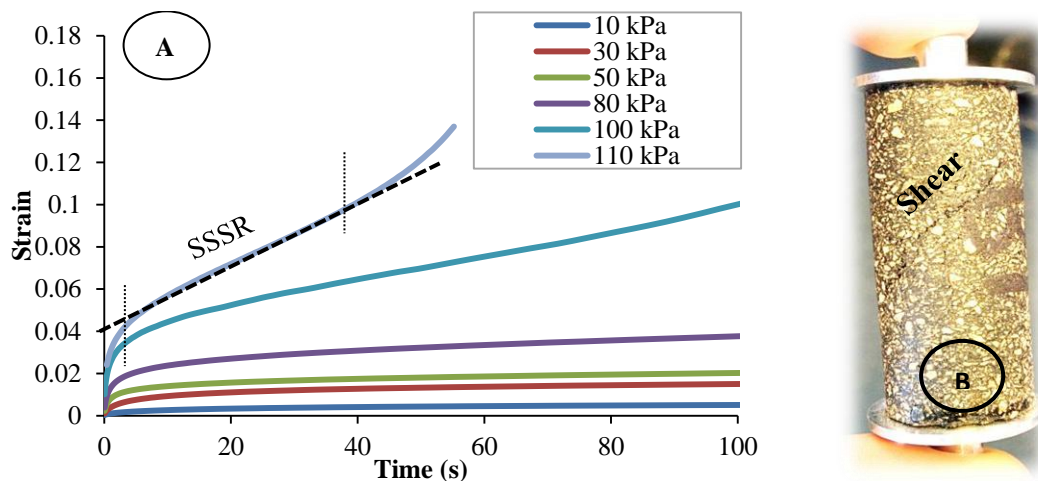
Figure 6.12(A) Combined results of M65-8% shear creep test at 50ºC, (B) Shear cracked sample
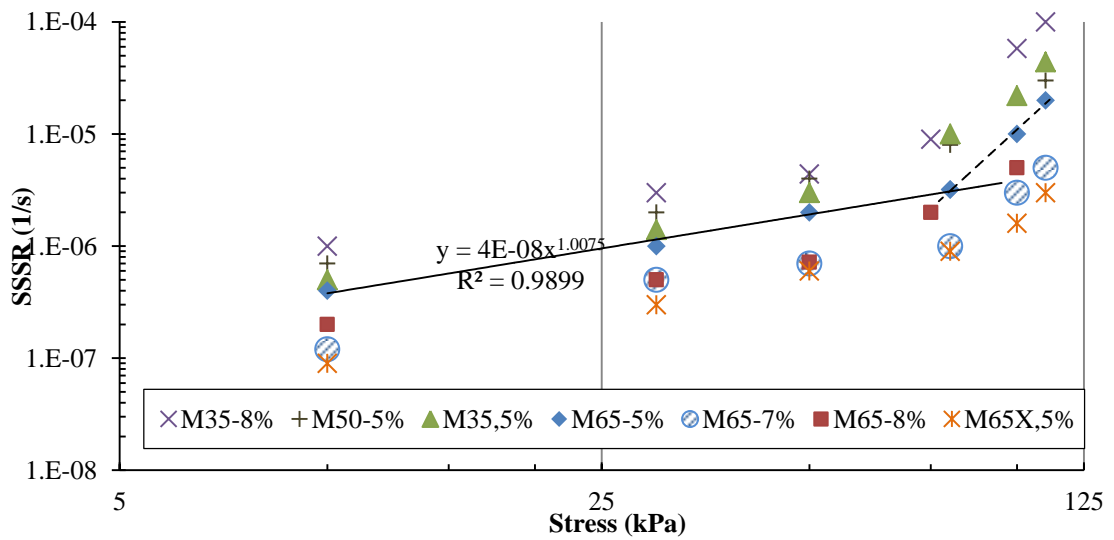
Figure 6.13 Summary of mortars steady state deformation behaviour @30ºC, shear creep test
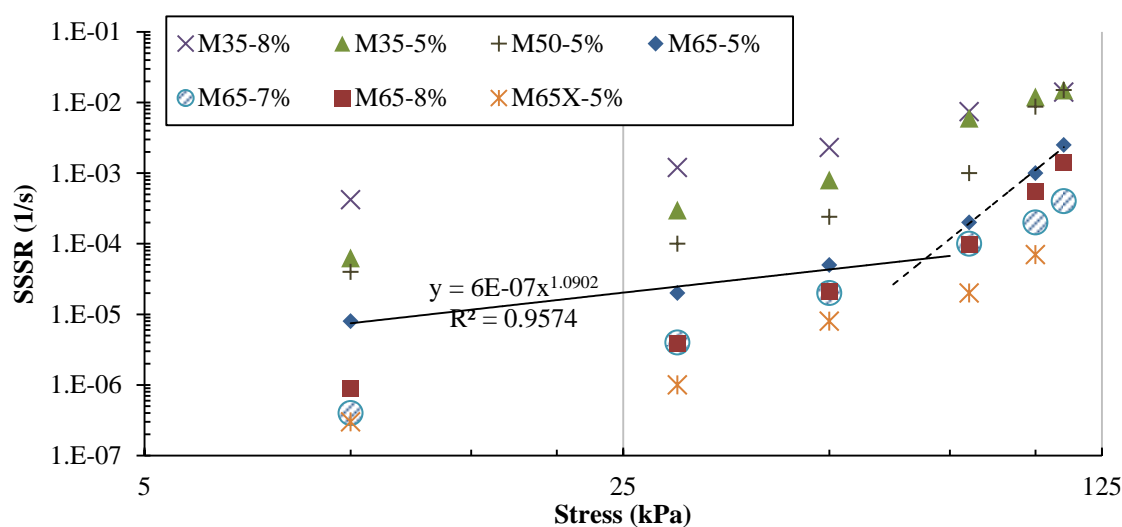
Figure 6.14 Summary of mortars steady state deformation behaviour @50⁰C, shear creep test

The observed steady state deformation behaviour of mortar mixtures is in the same form as that of the pure bitumen and mastics. Due to the fine aggregate inclusion the material is stiffened and its stress linearity limit changed. Again the stress limit at which linearity ends was determined using the trend line extension criterion in the SSSR against stress plot. At low stress levels, the SSSR values tend to lie on a straight line with a slope of approximately 1 representing a linear behaviour. Above that stress level the straight line gradient increases indicating a non-linear or a transition to non-linear performance (for brevity only M65-5% trend lines are shown). The stress level associated with the linearity limit varies between the different mortar mixtures.

At 30°C all the M65 mortars with 5%, 7%, and 8% bitumen contents reached a stress linearity limit of approximately 80 kPa. Similar observations were obtained for M35 with 5% and 8% bitumen content but at a stress limit less than 80 kPa. Thus, bitumen content, at least at these contents, has an

insignificant effect on the linearity limit for the same mortar type. Although M35-mortars had less filler in comparison to M65-mortar, the higher content of fine aggregates induced more non-linearity observed by the reduced stress linearity limit.

In contrast to the findings at 30°C, testing at the higher temperature of 50°C reduced the linearity limit of all the mortar mixtures to less than 80 kPa, and a lower linear stress limit is attained by increasing bitumen content for both mortars (M35 and M65). It would therefore appear that the mortar linearity limit under shear is only sensitive to bitumen content at higher temperatures.

A different scenario was found with the combination of M65 mastic and the finest aggregate gradation number (3), i.e., M65X-5%. This mortar with 5% binder content exhibited a superior performance to the other mortars. The filler interlocking in M65 established a dense structural network with large amount of fine aggregate content in the mixture. However, the linearity limit is reduced to less than that seen for the normal M65-mortar (5% to 8% bitumen content) at 30°C and similar to the M35-mortar obtained with the large fine aggregate content. Therefore, fine aggregate gradation is more influential than filler and binder content on shear creep linearity determination.

On the other hand, M65-Mortars with the highest filler content exhibited higher resistance more than M35 and M50 mortars at both 30 and 50°C.

This reveals that mortar shear deformation resistance is a filler content dependent mechanism more than fine aggregate.

6.3.2 Single Shear Creep Recovery Results

The recovery property of mortar mixtures is characterised by performing single shear creep-recovery tests in the Gemini-ETC DSR machine. A constant shear load was applied for a predetermined strain followed by load removal with continuous data recording until strain reached approximately a constant level. The recovered strain is again monitored with applied stress levels of 10 kPa and 50 kPa at 30°C and 50°C for mortars M35-5%, M50-5%, and M65-5%. Figure 6.15 combines typical results of a series of single shear creep recovery tests which illustrates the strain change with time at different loading periods. Upon the load removal, there is an instantaneous recovery (elastic) followed by a time dependent recovered strain then a permanent irrecoverable strain.
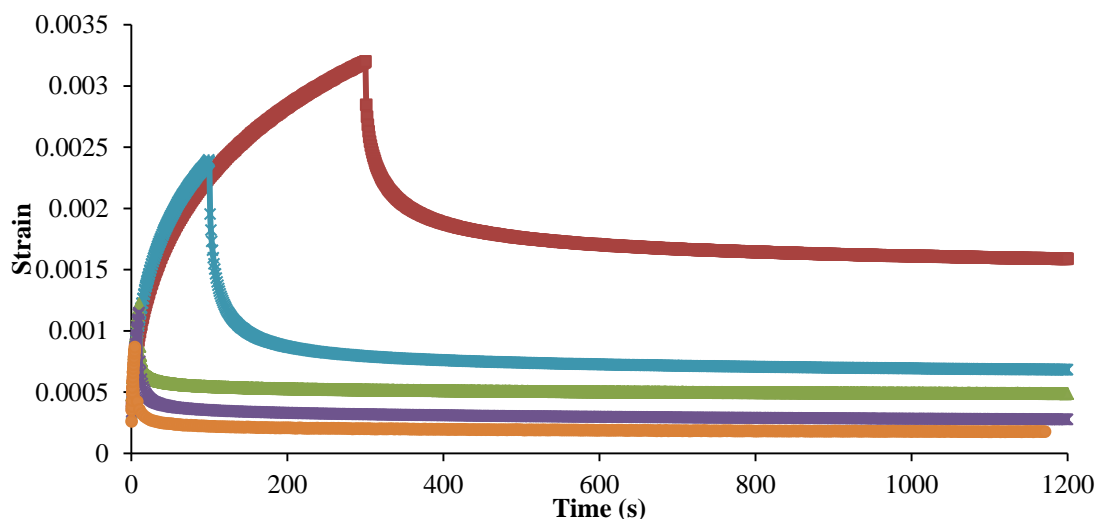
Figure 6.15 Combined results of M65-5% single creep recovery at 10 kPa and 50°C

Figures 6.16 and 6.17 summarise results of mortar mixtures at 10 kPa and 50 kPa respectively where the recovered strain is plotted against the total strain for each test. Similar to the previously obtained trend for mastics and bitumen, the recovered strain at low total strain values independently increased linearly, followed by a constant recovered strain after reaching a total strain limit. This total strain limit is dependent on the stress level and fine aggregate content with insignificant influence from temperature. Because of the machine torque constraint, constant recovered strain stage was only reached with 10 kPa applied stress while the 50 kPa stress results were limited to the first linear part. In Figure 6.16, although filler content is great with M65-5%, it has reached a constant recovered strain level higher than the other mortars. The greater fine aggregate content in M35-5% and M50-5% noticeably reduced the effect of filler and consequently obtained lowered constant recovered strain level in comparison to M65-5% with high filler content.
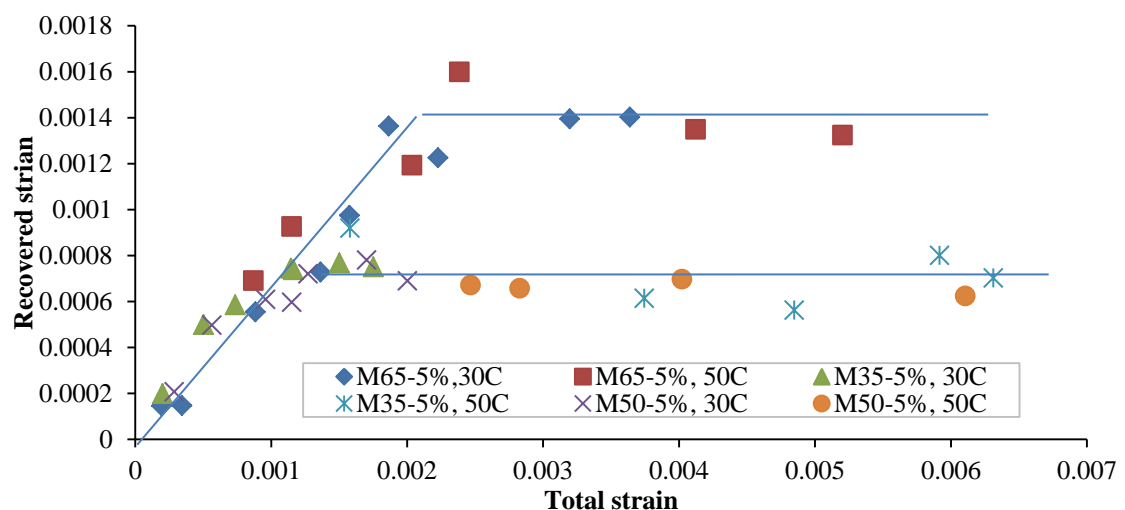
Figure 6.16 Summary of creep recovery test results of mortars at 10 kPa shear loading
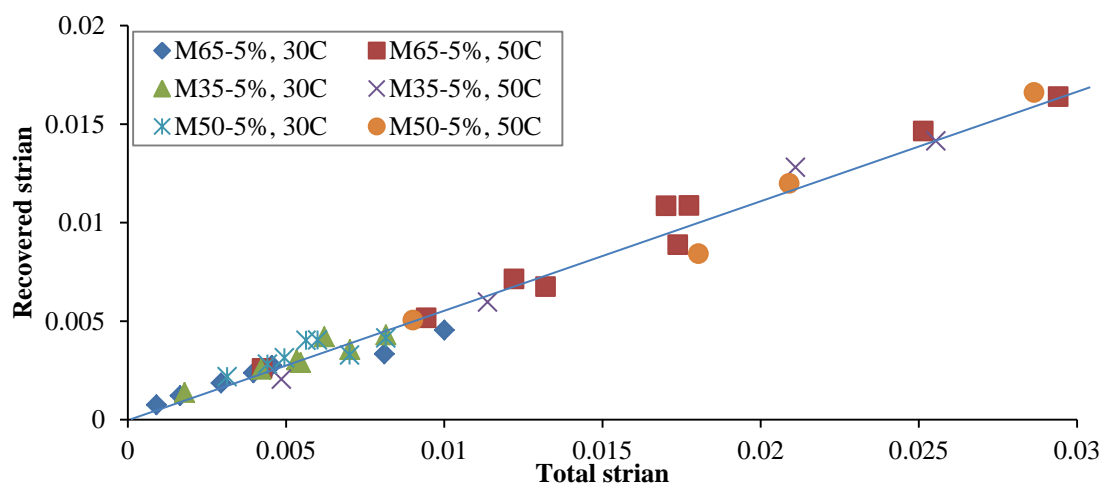
Figure 6.17 Summary of creep recovery test results of mortars at 50 kPa shear loading

Comparing the 10 kPa stress-recovery tests results on mastics (Chapter 4, Figure 4.15) and mortars, the inclusion of the fine aggregates increased the slope of the linear part, representing more recovery. However, the total strain after which the recovery becomes constant significantly decreased in the mortar. Thus, although fine aggregates raised the recovery line in the linear relationship part irrespective of gradation type and temperature, they lowered the constant recovered strain level. Additionally, the constant recovered strain of the bituminous materials is influenced more by fine aggregate than filler.

It is worth mentioning that comparison between the uniaxial compression and shear recoveries was planned in the research programme. However, the uniaxial compression required a pre-loading phase before reaching the target stress. The initial response in the compression tests was therefore not a true measurement of the exact strain mainly due to the lubrication system on the sample surfaces and the lack of an accurate system to zero the gap between the loading frame and sample as obtained in the DSR machine.

6.3.3 Uniaxial Compression Results

The same trend of strain change with time is observed at both testing temperatures (30°C and 50°C) in terms of primary, secondary and tertiary regions. The SSSR occurs within the secondary region followed by a dramatic increase to failure. Compression resistance of all mortars was higher than shear resistance at both 30°C and 50°C.

Again, the trend line criterion was utilised to determine the linearity limit. At 30°C, all the mortars preserved linearity up to the maximum applied stress of 110 kPa. At 50°C, neither M65-5% nor M65X-5% reached non linearity as shown in Figure 6.18. Nevertheless, the linearity limit reduced to between 80 and 100 kPa and to less than 80 kPa when the bitumen content was increased to 7% and 8% respectively. M50-5%, M35 with 5 and 8% bitumen content had a linearity limit less than 80 kPa. Once again increasing bitumen content reduced the linearity limit, with the linearity limit being governed by bitumen content, fine aggregate gradation and content at high temperature.
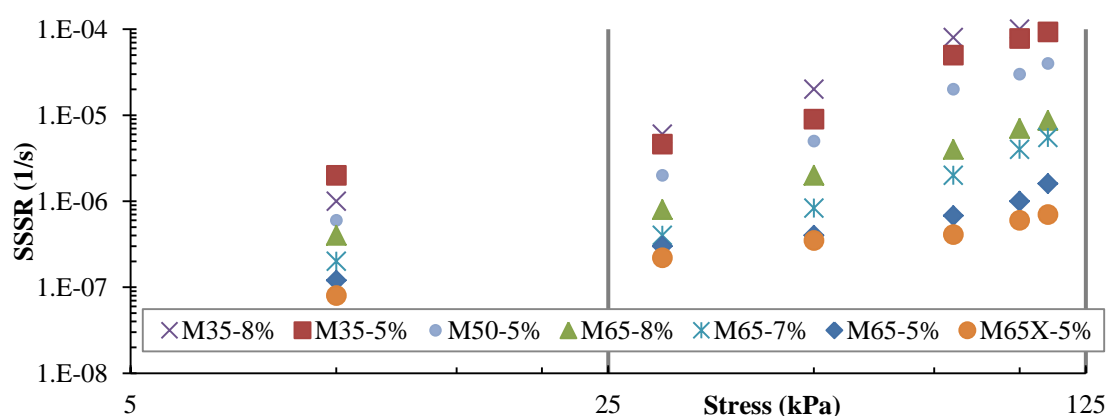
Figure 6.18 Summary of mortar steady state deformation @50°C, uniaxial compression test

Similar to shear deformation, almost all the mortars corresponding to M35, M50 and M65 at 5% binder content achieved a similar level of deformation at 30°C. However, the difference is noticeable at 50°C with less deformation occurring for mortars of higher filler contents. Therefore, although the M35-mortars had higher fine aggregate content, the performance of M65-mortar is much better. The filler content is more dominant in terms of uniaxial compression resistance than the fine aggregate content. Additionally, an improved resistance is gained when mastic M65 is matched with M3-mortar's aggregate gradation (M65X-5%) where more fine aggregate content is available.

6.3.4 Triaxial Results

The creep behaviour can be observed in Figure 6.19 where the strain (blue line with the secondary Y-axis) follows the same pattern of primary, secondary and then a tertiary region (the green line of strain rate follows the primary Y-axis). Due to the confinement boosting the stiffness of the mortars, most of the tested samples merely attained the steady state and didn't reach the failure region even with long loading periods at relatively high stresses (300 kPa) at 30°C.
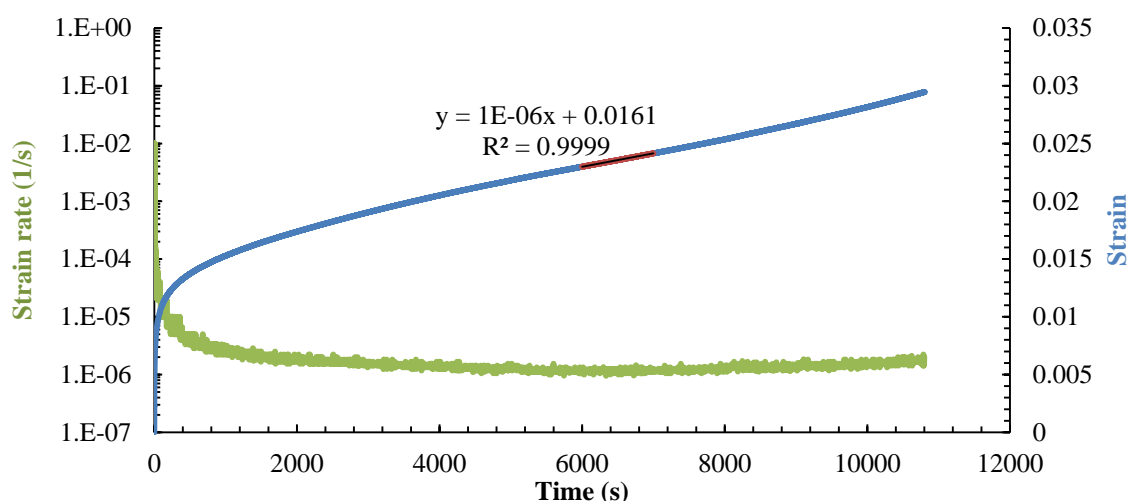
Figure 6.19 Strain and strain rate change with time of M50-5% @30ºC and 300 kPa axial stress

Figure 6.20 summarises the linear part of SSSR against stress level on double logarithmic scales. As can be read from the power law trend line at 50ºC, the M50-5% and M65-5% linearity limit was not exceeded up to 110 kPa applied deviatoric stress. At 30ºC, up to 200 kPa and 300 kPa, M50-5% and M65-5% respectively preserved their linear viscous behaviour. Additionally, M35-5% never attained steady state even with 300 kPa applied stress. Increasing the applied axial stress, with a 0.5 constant stress ratio identified earlier, the confining stress also increased and the material presented more resistance. This is due the confining stress influence on aggregate particle movement and causing the material to interlock more. This phenomenon was noticed by Deshpande *et al.* (1999) and referred to as 'lock-up'.
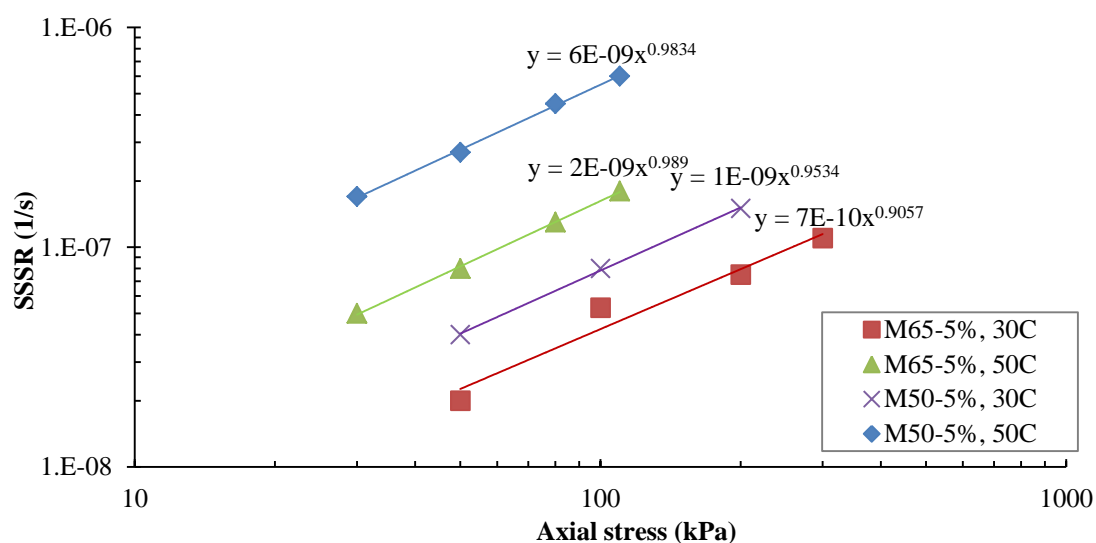
Figure 6.20 Summary of linear steady state strain rate deformation of mortar triaxial test results

6.3.5 Stiffening Effect of Fine Aggregates on Mastics

Adding fine aggregate stiffened the mastics to different levels depending on the fine aggregate gradation, testing temperature and stress state. To measure the stiffening effect of fine aggregate, Deshpande et al. (1999, 2000) extended the Modified Cross Model (MCM) by adding a stiffening factor to the equation. The modified MCM equation is given by:

$$\frac{\sigma}{\sigma_0} = \frac{S\dot{\varepsilon}}{\dot{\varepsilon}_0}\left(\frac{1}{1+\left(\frac{S\dot{\varepsilon}}{\dot{\varepsilon}_0}\right)^{nc}}\right) \tag{6.5}$$

Where S is the stiffening factor; the ratio of the SSSR of mastic to the corresponding mortar.

The stiffening effects obtained by different fine aggregate inclusions with shear, uniaxial compression, and triaxial tests in relation to M35, M50, and

M65 mastic are presented in Figures 6.21, 6.22, and 6.23 respectively. 'C', 'S', and 'T' in the legends refer to uniaxial compression, shear, and triaxial testing respectively.
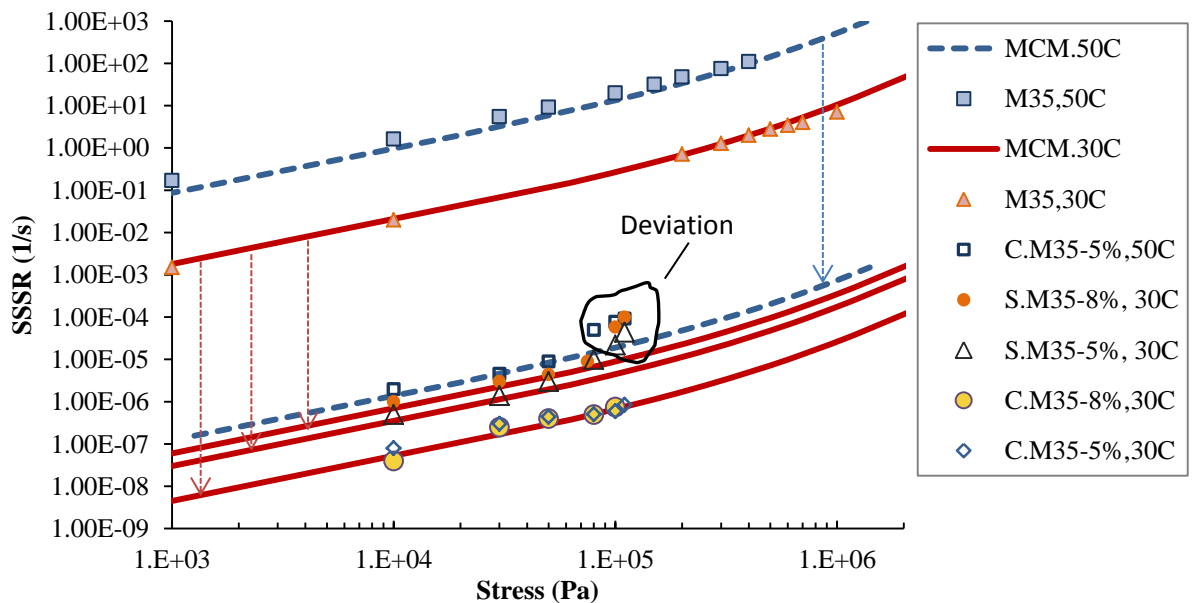
Figure 6.21 Steady state deformation of M35 and the corresponding M35-8% and M35-5% mortars with MCM
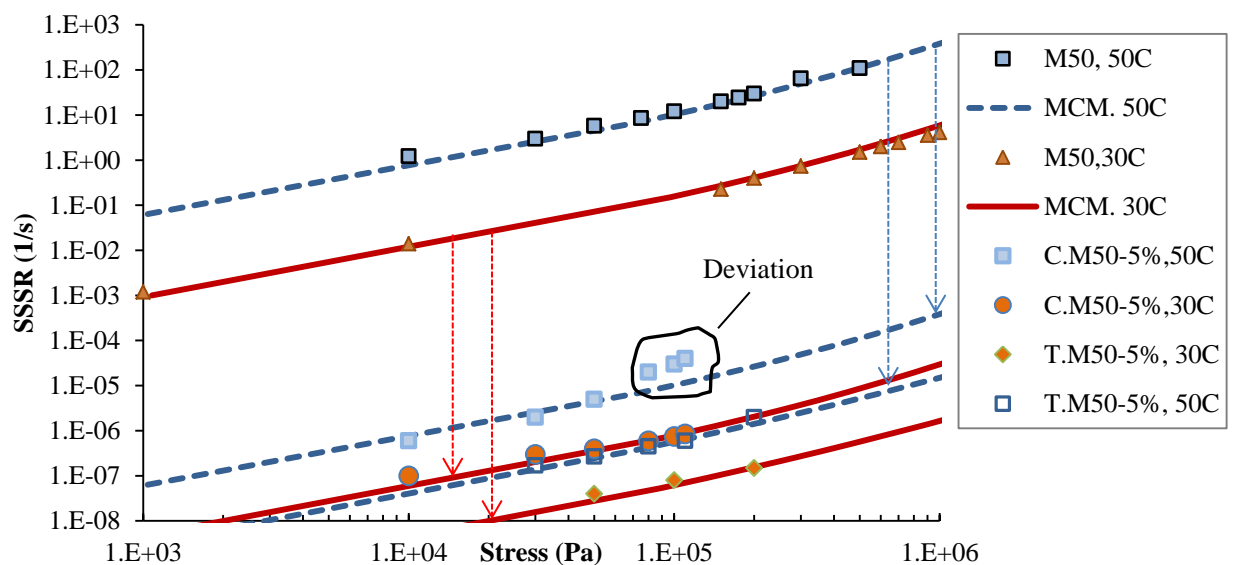
Figure 6.22 Steady state deformation of M50 and the corresponding M50-5% mortar with MCM
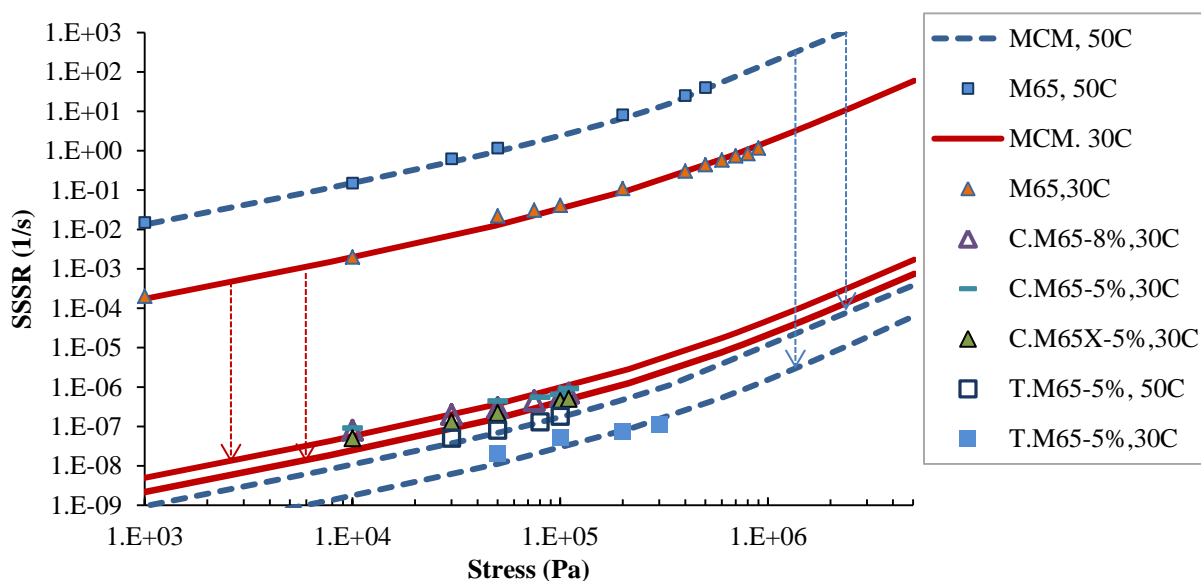
Figure 6.23 Steady state deformation of M65 and the corresponding M65-8%, M65-5%, and M65X-5% mortars with MCM

The figures show that the shape of the mortars' steady state deformation curves is in a good agreement with the equivalent mastics as described by the modified MCM. The agreement suggests that the stress dependence of the deformation is governed by the mastic binder (Deshpande *et al.*, 1999). However, high applied shear stresses at 30°C and 50°C, as well as uniaxial compression at 50°C, results in data that deviates from the MCM curve prediction of the non-linear phase. Therefore, this deviation suggests that the dependence of the deformation is significantly impacted by fine aggregate gradation at high stresses.

The temperature dependence of the mix is governed by the bitumen as proposed by (Deshpande *et al.*, 2000) is due to the free volume of the bitumen microstructure that does not interact with the large aggregates. This may apply when the bitumen content is high and filler with small particles is not included. In fact, mastic alone with different filler contents had shown a

deviation from the pure bitumen response as discussed previously in Chapter 4 and reflected by changes in parameter values in MCM. However, the filler and fine aggregate interaction under different conditions is complex and requires more investigation.

Table 6.2 compares the stiffening value of each mortar type at 30°C and 50°C under uniaxial compression, shear and triaxial tests. The stiffening factors measure how much the fine aggregates add to the overall resistance of the equivalent mastics. When a deviation from the MCM curve is present, only the linear region of each mortar mixture is considered.

Table 6.2 Fine aggregates stiffening factors

Mortar ID	Uniaxial compression		Shear		Triaxial	
	30ºC	**50ºC**	**30ºC**	**50ºC**	**30ºC**	**50ºC**
M35-5%	4E+05	8E+05	6E+04	1.1E+04	_	_
M35-8%	4E+05	8E+05	3E+04	3E+03	_	_
M50-5%	2E+05	1E+06	2E+04	2.3E+04	2.8E+06	2E+07
M65-5%	4.5E+04	1.9E+06	7E+03	2E+04	1.1E+06	1.4+E07
M65-8%	4.5E+04	4E+05	1.1E+04	1.5E+05	_	_
M65X-5%	8E+04	3.2E+06	2.3E+04	6E+05	_	_

From Table 6.2, for uniaxial compression with high fine aggregate content or low filler content, increasing bitumen content is insignificant in terms of fine aggregate stiffening within the testing temperature range. Both M35 mortars with 5% and 8% bitumen content achieved the same stiffening factors at 30°C and 50°C (4.0E+05 and 8.0E+05 respectively). In addition, the stiffening at 50°C is double that at 30°C within the linear region. Mortar

M50-5% also increased the stiffening by 5 times by increasing the temperature in the uniaxial test.

Bitumen content variation didn't influence the stiffening effect of fine aggregate under uniaxial compression, except when the filler content is relatively high (M65) at high temperature. Thus, fine aggregate stiffening at high temperature is only sensitive to bitumen content at relatively high filler content. In addition, at both 30°C and 50°C the stiffening due to the large amount of fine aggregate in M65X-5% increased by an average of 1.7 times over the stiffening in M65-5%. In terms of triaxial resistance, comparing the stiffness between M50-5% and M65-5%, there is clearly more resistance to deformation through the inclusion of coarse gradation of aggregate rather than filler content. This point can also be drawn through the high resistance in M35-5% of the coarsest gradation that prevented the steady state condition being reached at high triaxial stresses.

On the other hand, shear stiffness of fine aggregate mortar exhibits a considerable influence of bitumen content and varies depending on the filler content. The larger amount of fine aggregate in M65X-5% in comparison to M65-5% increased the stiffening by 3.2 to 30 times with shear deformation at 30 and 50°C respectively.

Compression and triaxial resistance improved as evidenced by an increase in the stiffening factor from 30°C to 50°C for all mortar types. However in shear, with temperature increase, M35 mortars showed a reduction in the stiffening, M50 almost stayed constant, and the stiffening increased

considerably with M65 mortars. Thus, when the temperature increases, the shear resistance gained by fine aggregate inclusion is increased only when the filler content is relatively high.

6.4 Discussion

The extended MCM developed by Deshpande *et al.* (2000) was utilised to compare the stiffening effect of fine aggregates in shear, uniaxial compression and triaxial. It was suggested that the temperature dependency of the steady state deformation behaviour is governed by the binder. The stiffening was measured for each mortar type with each stress form from the corresponding mastic shear deformation discussed in Chapter 4. The experimental results suggest that the nonlinearity dependency of the deformation can take a different inclination from the original mastic. It does not depend on the mortar composition alone but also on the type of stress application.

The shear deformation in the DSR machine is accompanied by a normal stress that can transform the deformation quickly to give a nonlinear performance as discussed in Chapter 5. There was no access to the normal force measurements in the Gemini-ETC with mortar testing. However, as illustrated in Chapter 5, with high filler content in mastics the deviation to nonlinearity due to the axial stress (normal force) was recognized. In fact, the dilation rate is higher with mortars including fine aggregate which will generate greater normal stresses than in mastics. In the case of high

temperature (50°C) for the uniaxial compression test the bitumen is very soft and the fine aggregates' rigidity can be lost.

On the other hand with the triaxial test, it is believed that fine aggregate can significantly influence the dependency of the steady state deformation on the binder. The interlocking of aggregate contacts, solidified by confinement, can limit the binder governance at high stresses or temperatures. Therefore, without confinement at high temperature in uniaxial compression the solidity of the fine aggregate structure is reduced with the binder being very soft. When increasing the stress ratio and therefore the confining stress beyond a certain limit, 'lock-up' of the fine aggregate structure occurs and no deformation can be obtained (Deshpande *et al.*, 1999).

6.5 Conclusions

A new type of mortar mixture, whose mastic 'filler-bitumen' content corresponds adequately to the actual content in a 10 mm DBM standard asphalt mixture, has been introduced. The deformation behaviour of shear, uniaxial compression, and triaxial has been characterised by the steady state strain rate over a wide range of applied stresses at 30 and 50°C. Preliminary conclusions of the deformation behaviour can be drawn:

1- It was found that the behaviour is always linear at low stresses and non-linear viscous at high stresses in the same form as for pure bitumen and mastics. The linearity extension varied between mortar mixtures and stress type.

2- The shear deformation was always greater than uniaxial and triaxial compression. The shear stress linearity limit was found to be sensitive to bitumen content only at high temperature. The fine aggregate was observed to play a more dominant role than bitumen and filler contents in determining the linearity, and the linearity limit reduced with increasing the content of fine aggregates. The shear deformation resistance was experimentally perceived to be a filler content dependent mechanism rather than fine aggregate.

3- The results from single shear creep recovery showed a bitumen trend of linear and independent relationship between the total strain and the recovered strain before reaching a total strain limit after which the recovered strain remained constant. In the linear relationship phase, fine aggregate in mortars achieved a higher recovery slope than mastic. The total strain limit after which the recovered strain reached a constant value was found to rely on the stress limit in a proportional relationship and was insignificantly affected by temperature. Additionally, reducing fine aggregate fraction raised this total strain limit to a higher value.

4- Mortars increased their deformation resistance and increased their stress linearity limit in uniaxial compression in comparison to shear. The deformation resistance is perceived to be governed by filler content more than fine aggregates content.

5- Triaxial test results of mortars showed the high stiffening effect of confining pressure on the behaviour. Both the stiffness and stress linearity limit were increased significantly by the confinement condition.

6- Mortar steady state deformation was adequately captured by the extended MCM which measured the fine aggregate stiffening in relation to the corresponding mastics. The stiffening factor is a function of temperature, volume fraction of fine aggregate and gradation. The deviation of results from the related mastic MCM expectation suggests that the nonlinearity dependency of mortar shear deformation is influenced by the fine aggregates.

7- The determined stiffening factor values demonstrate that bitumen content is insignificant in terms of mortar uniaxial compression resistance with different filler contents except at large filler content and high temperature. On the other hand, the shear resistance of mortars is dependent on the bitumen content and the dependency varies based on the filler content. Triaxial deformation resistance is perceived to be governed by fine aggregates and insignificantly affected by filler content. In general, an increase in temperature increases the fine aggregate stiffening of uniaxial compression and triaxial, while mortar shear deformation resistance was noticed to increase only when filler content is relatively high.

7. Uniaxial Deformation Behaviour of Asphalt Mixtures

7.1 Introduction

Following previous chapters, the main focus in this chapter is on characterising coarse aggregates and air voids in the full scale asphalt mixture. The experimental design and procedure of specimen manufacturing, testing, and X-ray CT with image analysis are detailed.

A preliminary assessment of the available X-ray CT facility and imaging software on characterising asphalt mixtures is briefly discussed. Uniaxial compression constant stress and constant strain rate tests on a 10 mm DBM asphalt mixture with different aggregates gradations are described to study the steady state condition. The results were used to determine the stiffening effects of coarse aggregates (above 2 mm) that are contained in asphalt mixtures based on their corresponding mastic as measured through the MCM. In addition, before and after testing, characterisation of the air voids and aggregates via image analysis is detailed as a link between the microstructure and the mechanical performance.

7.2 Preliminary Investigation

It was necessary before embarking on any interpretation of the

measurements to evaluate the images produced from the X-ray CT through the available software. Four samples of 100 mm diameter were manufactured (Figure 7.1). The first sample was manufactured with aggregates ranging from 4 to 0.5 mm and X-rayed at different intervals, while the rest were prepared with single-sized aggregates and scanned at 0.5 mm intervals. Table 4.1 details the geometry and specifications of each sample. The laboratory air void content for each sample was measured based on BS EN 12697-8:2003.

Figure 7.1 Prepared samples for X-ray

Table 7.1 Sample properties

Sample ID	Aggregate size	Bitumen mass %	Aggregate mass %	Air voids (%)
1	4>size >0.5	6.5	93.5	21.1
2	4> size >2.8	3	97	29.0
3	2> size >1	3	97	32.7
4	0.5>size >0.25	6.05	93.95	30.1

For thresholding, a histogram-based method is used and images were processed through ImageJ software (detailed steps are in Chapter 3). Two important aspects are addressed; selecting scanning interval in the X-ray machine and determining the detectable aggregate size.

7.2.1 Scanning interval

Narrower slice scanning intervals produce more precise measurements as less information is skipped. On the other hand, X-ray scanning is time consuming (8 minutes is approximately the acquisition time to generate a slice). Therefore, an optimum slice interval is required considering the time consumption and the demand on the available X-ray CT facility. Figure 7.2 compares the air voids distributions of sample 1 scanned at different intervals starting from the ultimate 0.083 mm up to 2 mm. As can be observed, the best option that convoyed satisfactory details of air voids distribution with practical scanning time consideration is 0.5 mm. The 0.5 mm trend follows the detailed 0.083 mm scanning and demands less time to scan the entire specimen.
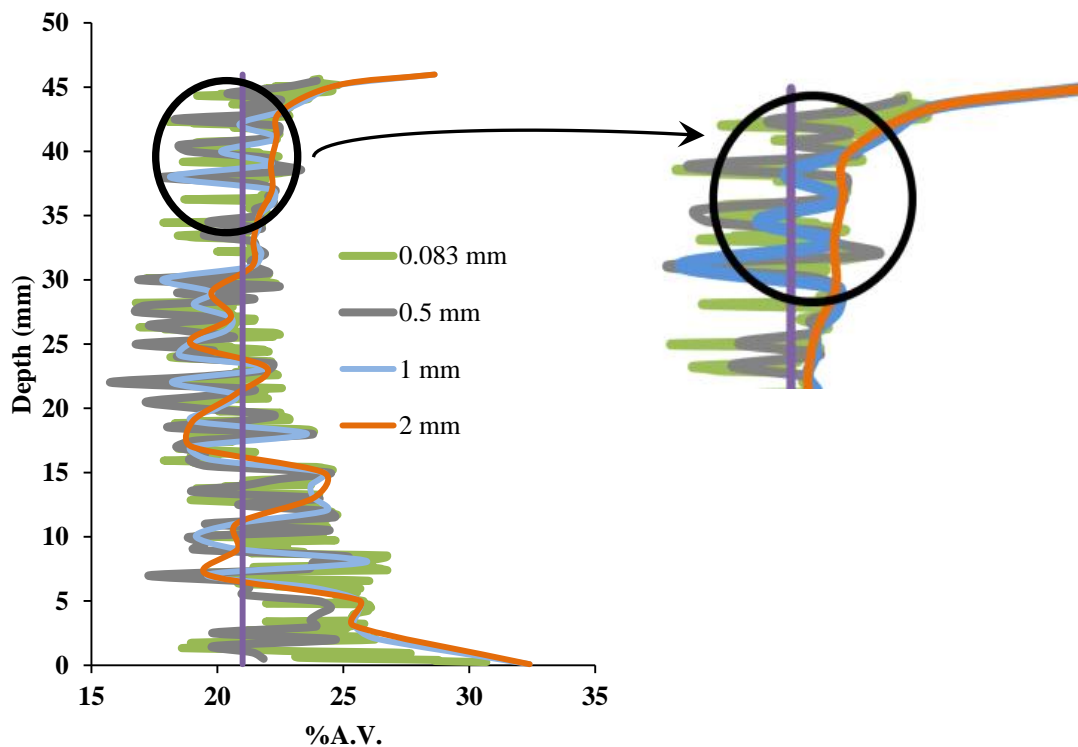
Figure 7.2 %A.V. distribution with different scanning intervals

7.2.2 Aggregate Size Visibility in the Specimens

To determine the minimum size of aggregate that is practically visible and measurable, specimens with different sizes were scanned as displayed in Figure 7.3. Thresholded aggregates are in red after suitable filtering processes. Clearly samples 4 and 3 exhibit overlapping of small neighbourhood aggregates as well as display a joined phase with the binder. While sample 1 shows relatively lower overlapping of aggregates, sample 2 presents more clarity in terms of segmented aggregates. The average sizes of aggregates for the four specimens along the height are shown in Figure 7.4. The dotted lines of the aggregates size limits in the mixtures that are drawn in the plots help to assess the amount of variation from the actual limit.
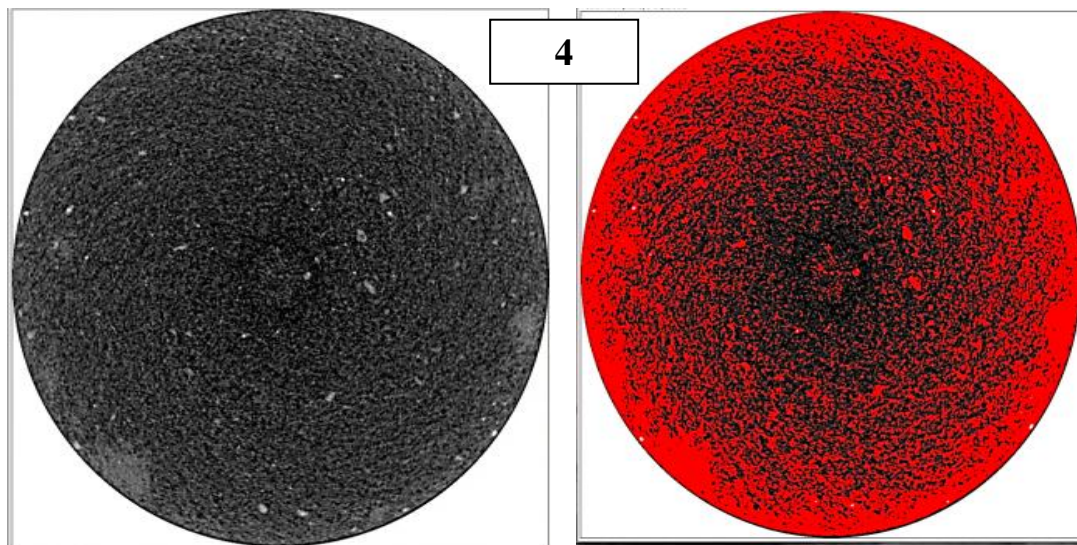
Figure 7.3 continues below
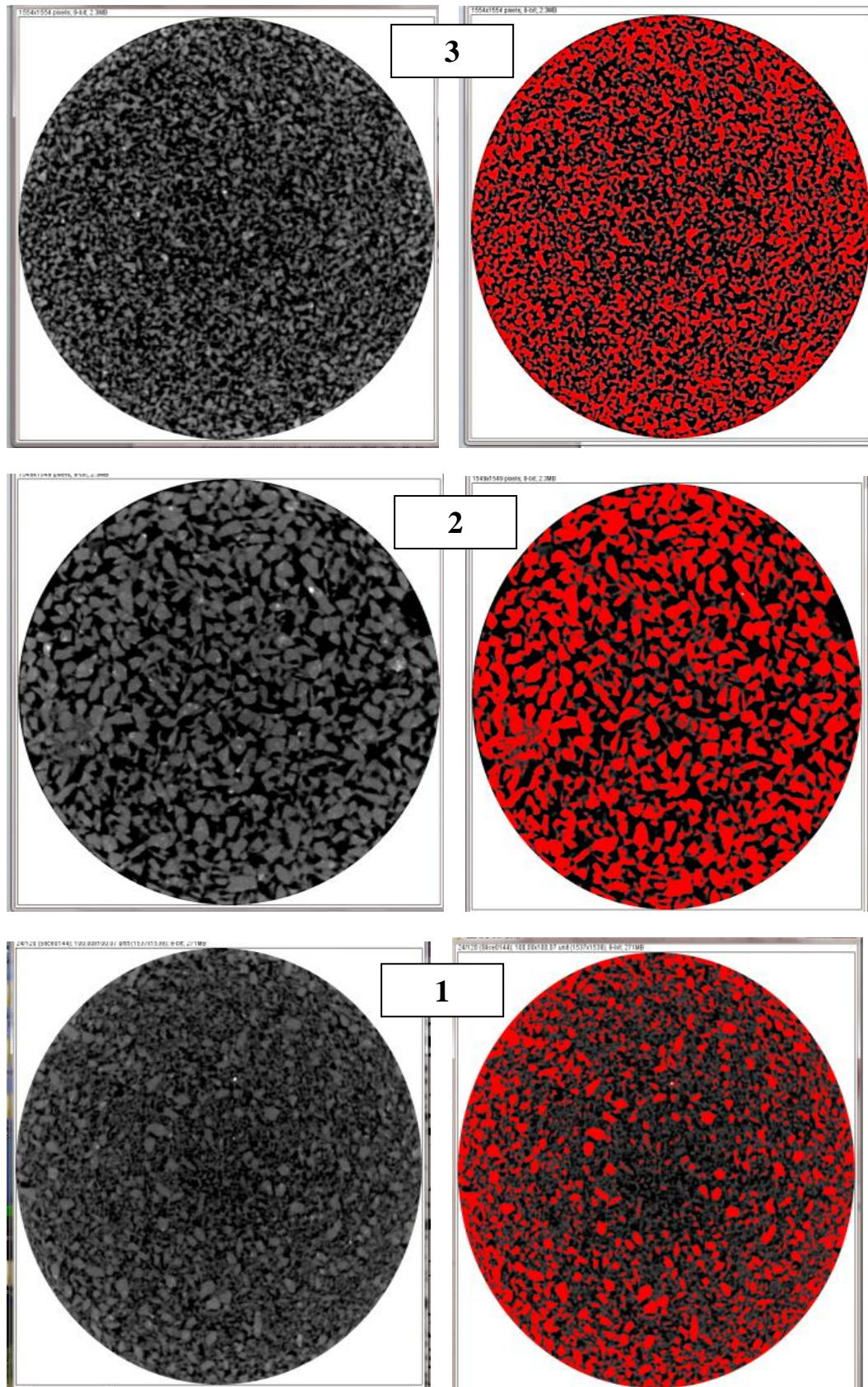
Figure 7.3 Scanned samples and thresholded aggregates
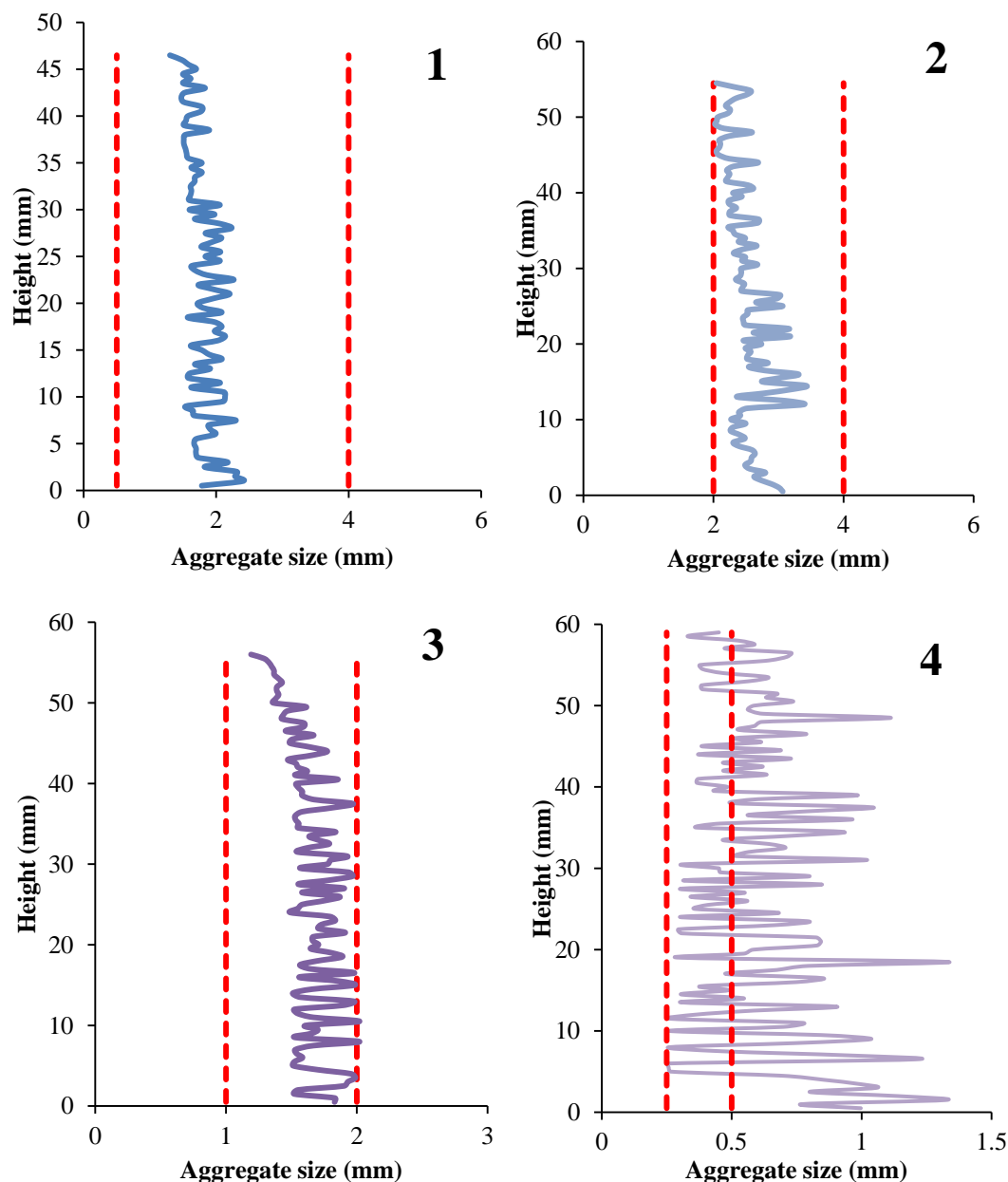
Figure 7.4 Aggregates size distribution in the four samples

As can be seen, there is an overestimation of aggregate size in samples 3 and 4 because of the joined small aggregates that are displayed as a single aggregate due to the resolution limit. Sample 2 shows a reasonable estimation of average 2 mm aggregate size. Similarly, sample 1 with different aggregate sizes estimates 2 mm as an average size with different sizes in the mixture. Therefore, it was decided not to include any aggregate that is less than 2 mm size in the analysis stage. The elimination of aggregates of less

than 2 mm from each image can be processed through ImageJ software.

7.3 Specimen Preparation and Test Equipment

7.3.1 Specimen Preparation

10 mm Dense Bitumen Macadam (DBM) mixture (BS EN 4987-1:2005) was selected to complete the chain of compatible material testing following the previous chapters. 40/60 penetration grade bitumen, limestone filler and fine granite aggregates utilised previously, and coarse granite aggregates (above 2 mm) from Bardon Hill were used in the asphalt mixture. Granite aggregate of relatively high density was specifically selected to improve image quality by the increase in the contrast from the other components. Three aggregate gradations of upper limit, middle, and lower limits of the 10 DBM (Figure 7.5 and Table 7.2) asphalt mixture were arranged by individual grading (sieving). The bitumen content for the DBM was 5.2% by mass of the total mixture as recommended in the standard.
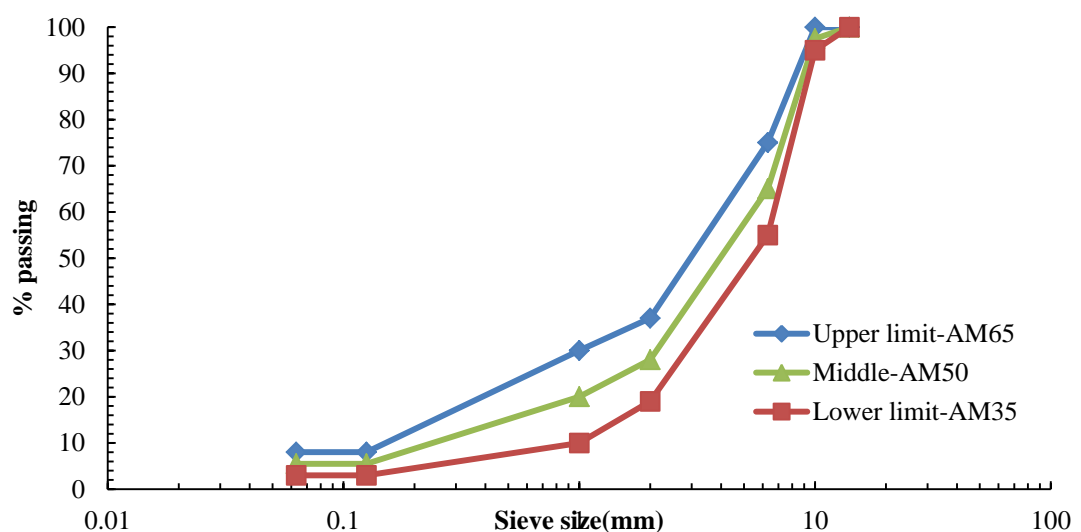
Figure 7.5 Aggregate gradation curves for 10 DBM mixtures

Table 7.2 Recommended aggregate grading for 10 DBM mixture

| Sieve size (mm) | % Passing by mass | | |
| | AM65 | AM50 | AM35 |
	Upper limit	Middle	Lower limit
14	100	100	100
10	100	97.5	95
6.3	75	65	55
2	37	28	19
1	30	20	10
0.063	8	5.5	3

Gyratory compacted specimens were prepared in accordance to BS EN12697-31: 2007. Initially, the correct proportions of limestone filler (less than 63 micron), fine granite aggregate (between 2 and 0.125 mm), and coarse aggregate (between 14 and 2 mm) were heated to 160°C in an oven. The hot bitumen (160°C) was removed from the oven and stirred gently. The heated bitumen and aggregates batches were then mixed for 3 minutes in a mechanical mixer and the required amount was poured into a preheated gyratory mould. Cylindrical specimens were manufactured to provide uniform stress distribution within the sample at a 100 mm diameter to satisfy a dimensional requirement of minimum 10 times the largest aggregate size (Deshpande *et al.*, 2000). The height 100 mm was also chosen to give an acceptable aspect ratio of 1 with the diameter for creep test specimen (Erkens, 2002). Ideally, an aspect ratio of 2 is required to assume that no confinement in the middle third of the specimen will be present and only pure uniaxial compression will take place. Due to the limitation of the available gyratory, a 100 mm height was used with friction reduction system which provides a response close to aspect ratio of 2 (Taherkhani, 2006).

The gyratory compaction applied 0.6 MPa vertical pressure at 1.25° angle of gyration and 30 rpm speed (Figure 7.6). To achieve compatibility with the previous chapter (mortar), each asphalt mixture specimen was exposed to 250 gyrations. Specimens were then trimmed equally on both sides through sawing and the air voids content was measured according to BS EN 12697-8:2003 via the sealed specimen method. Mixtures' IDs, their mean air void contents including the maximum, minimum and standard deviation are presented in Table 7.3. It can be observed that the air void (AV) content of AM35 is high. This is attributed to the relatively low content of filler and fine aggregates that fill the AVs.

Table 7.3 Specimen ID and air void content analysis

Mixture ID	Minimum AV	Maximum AV	Mean AV	Standard Deviation
AM65	3.6	5.7	4.56	0.92
AM50	8.5	12.4	9.5	1.125
AM35	9	17.1	14.9	2.0

Figure 7.6 Gyratory compactor

7.3.2 Testing and Scanning

Specimens were tested in constant strain rate and constant stress tests at 30 and 50ºC. The two test types are used widely as simple methods to determine the compressive strength of the asphalt mixture (Hassan *et al.*, 2012, Taherkhani, 2006, Khanzada, 2000, Cai, 2013, Gu *et al.*, 2014). The essential details of the testing apparatus are shown in Figure 7.7.
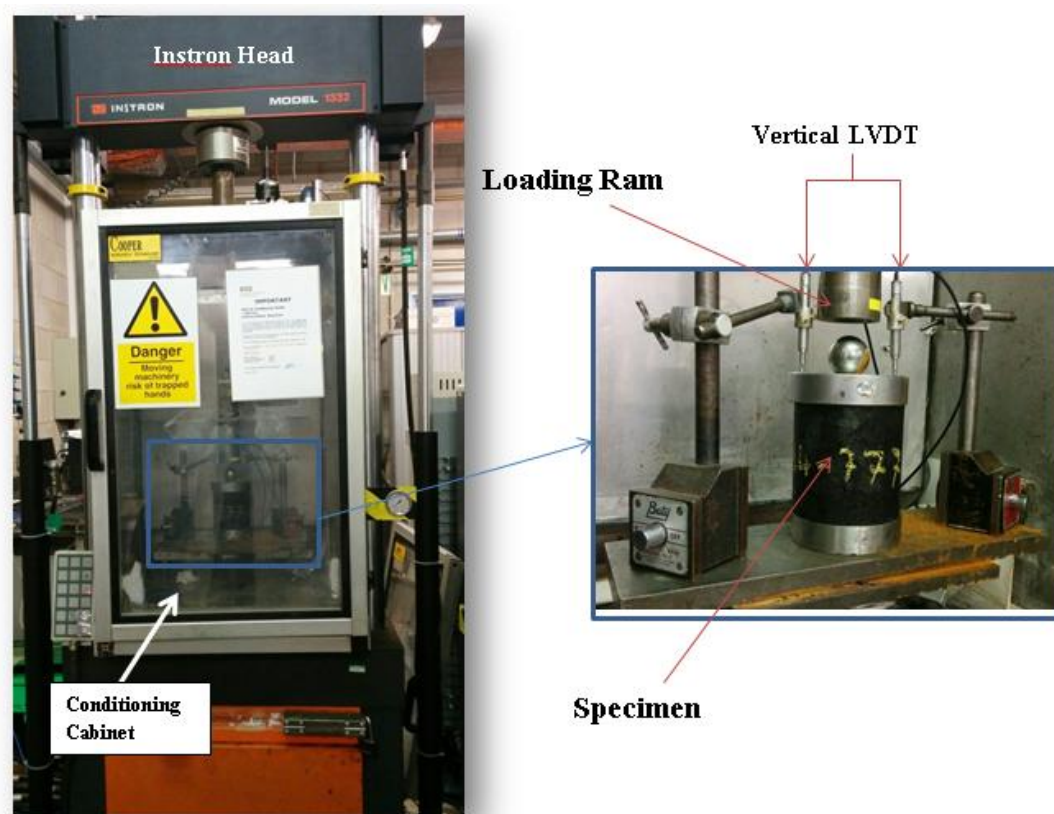
Figure 7.7 Uniaxial test equipment

A hydro-mechanical Instron machine was utilised with a conditioning cabinet to conduct the test. The machine consists of a loading frame of maximum 100 kN servo-hydraulic actuator. A loading cell mounted on the frame controls the system by adjusting the oil flow to the actuator to target and maintain the loading rate. An arrangement of Linear Variable Differential Transformers (LVDTs) to monitor the movement of the

crosshead stroke and continuously feedback signals to the control system was set up. Two LVDTs were aligned vertically at 180° apart and mounted on arms that are firmly fixed on the base. The axial deformation was simultaneously recorded via the calibrated LVDTs which have high resolution and can detect to 1×10^{-6} mm of displacement.

Top and bottom surfaces of specimens were lubricated by silicon grease and graphite powder to reduce the friction with the platen. The specimen and equipment were conditioned at the target testing temperature for 12 hours. Before commencing the test, the specimen was exposed to a pre-loading phase of 0.05 kN to allow the friction system to deform and minimize measurement errors (Taherkhani, 2006). Part of tested specimens was scanned before and after the test in the X-ray machine. Immediately after finishing the test the specimen was stored at 5°C to minimise geometrical changes before starting the second X-ray scanning.

7.4 X-ray CT of Manufactured Specimens

The X-ray facility was operated to produce 2D images at 0.5 mm interval. For each mixture type two specimens were X-rayed. The obtained set of images is saved in a TIFF format of 8 bits type (0 to 255 grey levels). After completing the image processing (filters) and thresholding as described in Chapter 3, objects of interest (air voids and aggregates) were extracted from images and parameters were measured. The following section details the characteristics of each asphalt mixture type in terms of air voids and aggregates after compaction and before testing.

7.4.1 Air Voids Vertical Distribution

Air voids (AVs) characteristics influence the mechanical performance of the asphalt mixture (Masad *et al.*, 2002a, Tashman *et al.*, 2002, Thyagarajan *et al.*, 2010, Kassem *et al.*, 2011). Thus, this part of the research assesses the vertical heterogeneity of AVs in the specimens as shown in Figure 7.8. It can be clearly observed that the distribution in the vertical direction is non-uniform and regardless of the mixture type the concentration in the middle is more than the top and bottom parts by up to approximately 35%. This pattern follows the same air voids distribution in (Tashman, 2003) where the middle part of the specimen is of a lower compaction.
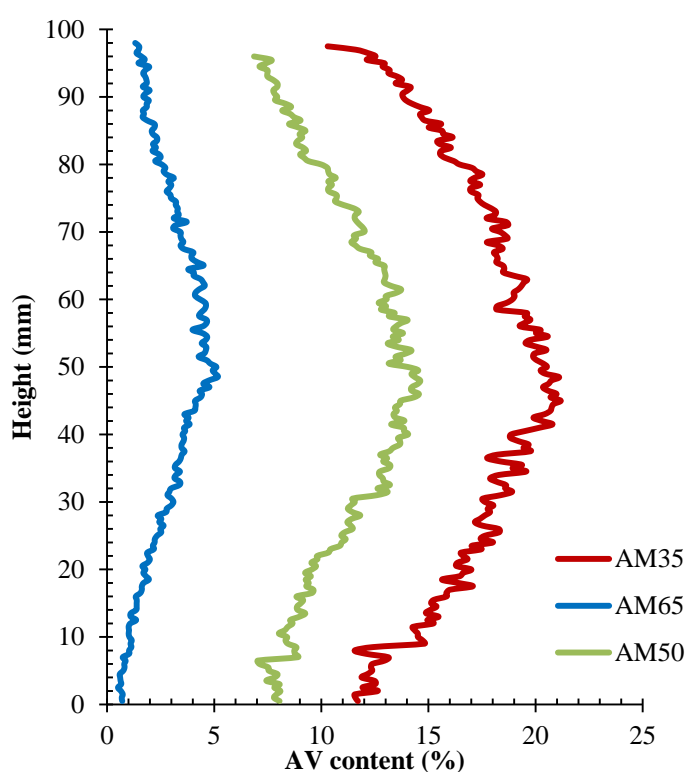
Figure 7.8 AV distribution in the vertical direction of the three mixture types

This phenomenon appears in relatively tall specimens when little compaction energy is transmitted to the middle region. The transmitted compaction

energy follows a cone shape that has maximum level at the gyratory mould edges as shown in Figure 7.9. Several studies concluded that specimen dimensions significantly influence the amount of transmitted compaction energy (Lo Presti *et al.*, 2014, Thyagarajan *et al.*, 2010, Dubois *et al.*, 2010). It was also found that gyratory specimens produced at height/diameter ratio of more than 1 exhibited higher AVs in the middle. In other words, the compaction energy is not well transmitted to the middle part.
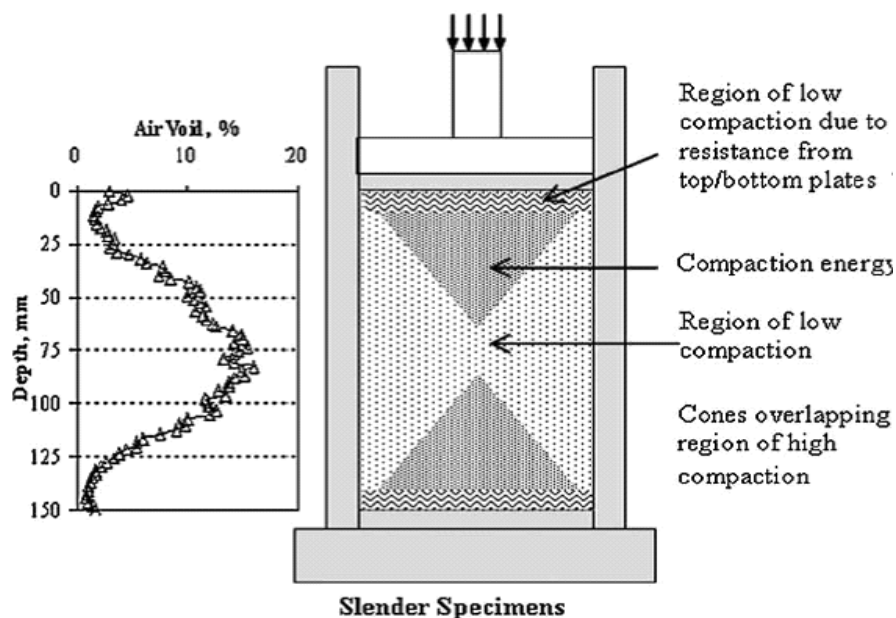
Figure 7.9 Compaction energy in gyratory compaction (Thyagarajan *et al.*, 2010)

The AVs properties are presented in Figure 7.10 where the count, average size, and circularity along the height are shown. As can be seen, the mixture with coarse aggregate gradation (AM35) exhibits larger size and lower number of AVs in comparison to the fine aggregate gradation (AM65) of smaller size and larger in number.

Thus, although both AM65 and AM35 have greater AV content in the middle (Figure 7.8) more than the top and bottom sections, the former is caused by

the large number of voids while the latter is formed by the greater size of AV. Average size and numbers of AV have an important effect on the damage mechanism of specimens under loading. Separated small size AVs are speculated to induce relatively lower strains while large ones are likely to form high stress concentration zones and potentially propagate to form cracks (Hassan, 2012). In addition, the shape of air voids is affected by the size. Small AVs (AM65) tend to follow a circular shape more than elongated voids (AM35) as illustrated in Figure 7.10- C. However, both types share more circularity in the top and bottom parts indicative of higher compaction (Hassan, 2012).
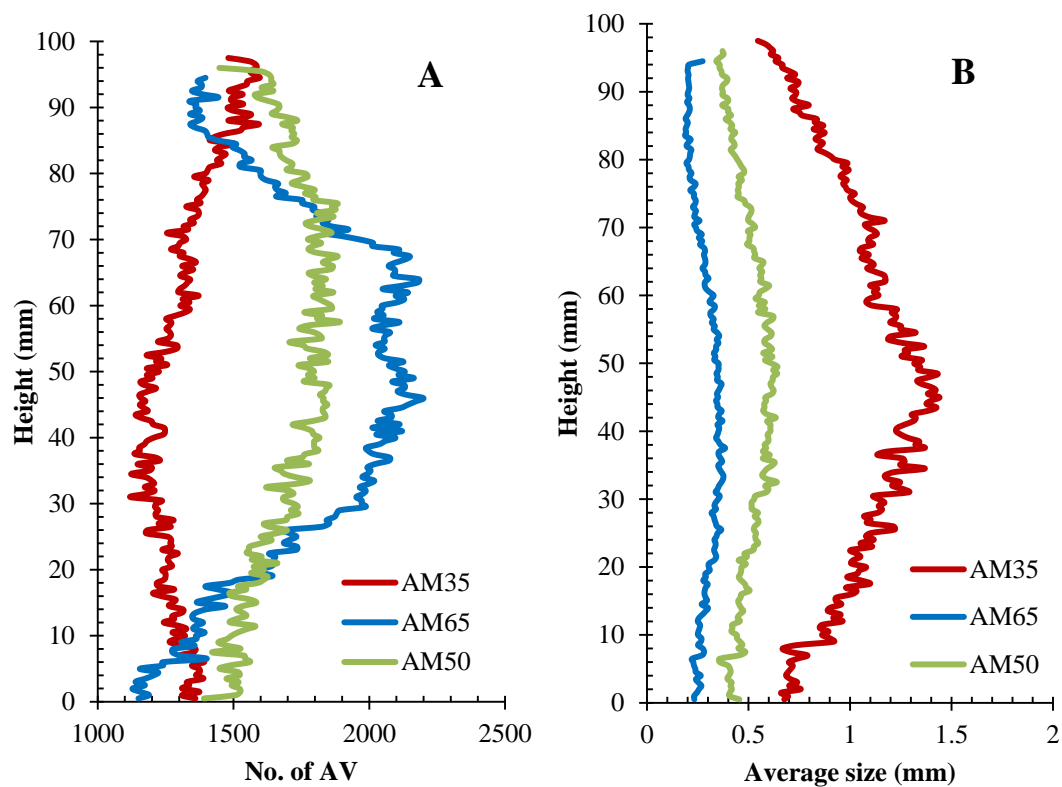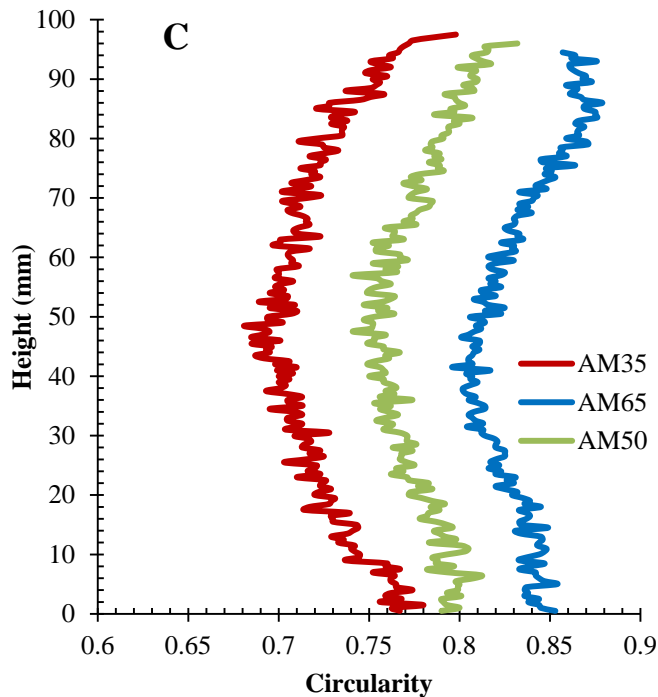
Figure 7.10 Distribution of air voids (A) number (B) average size (C) circularity

7.4.2 Air Voids Radial Distribution

The ring and core process (Section 3.5) is applied to reveal the AV distribution in the radial direction. The specimen is virtually divided into a central core (from centre to 25 mm radii) and rings (25 to 50, 50 to 75, and 75 to 100 mm). All different gradation types showed similar trend of radial AV distribution, presented in Figure 7.11 (for brevity only one type is shown). As can be seen, the trend of higher AV concentration in the middle part can be observed in the core and ring sections. However, in the middle part of the specimen, moving from the centre towards the circumference of the specimen, the AV content reduces slightly. This suggests that the gyratory compaction energy reduces in the radial direction towards the centre.

The motion of the axis of the gyratory mould which creates a conical surface of revolution under the action of vertical loading during compaction (Figure

7.12) results in the generation of horizontal shear loading. The high AV concentration in the centre suggests that the effect of the horizontal shear force is decreasing towards the centre.
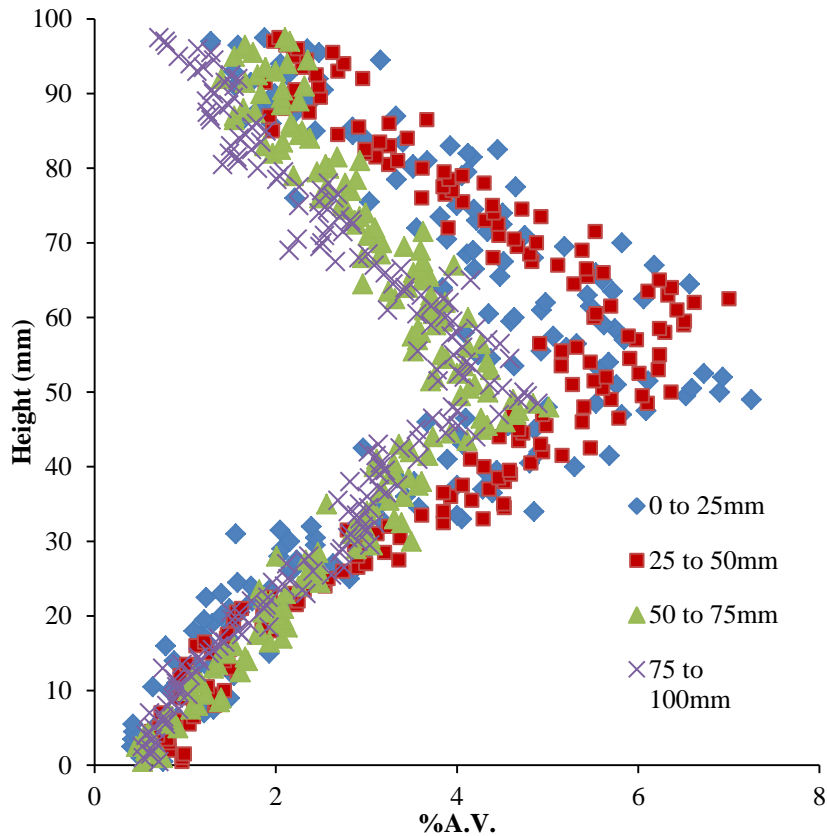
Figure 7.11 Distribution of AV in the radial direction
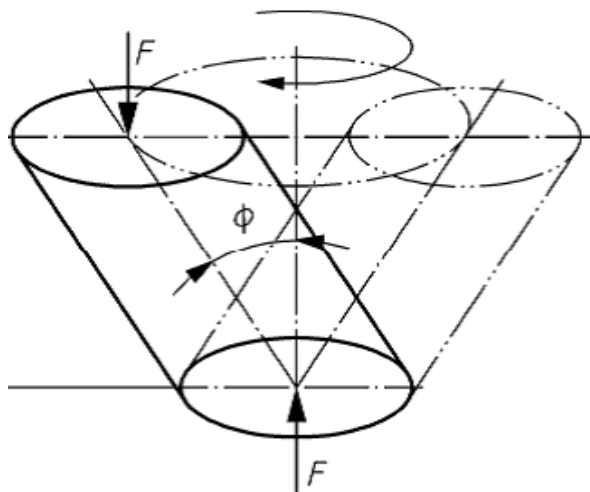
Figure 7.12 Motion diagram of mould and axial force in gyratory compactor (BS EN 1697)

7.4.3 Aggregates Characterisation

Aggregates distribution and segregation are presented in this section. Only coarse aggregates (above 2 mm) are involved in the analysis as fine aggregates (less than 2 mm) are considered part of the mastic due to the resolution limit of the X-ray scanner. The threshold value of the coarse aggregate was determined based on the volumetric amount in the real mixture (Figure 7.13). In comparison to air voids, aggregate characterisation through X-ray is limited because of the difficulties in segmentation. Due to different mineral aggregate compositions, a wide range of grey levels develop which overlap the other components (Hassan, 2012).
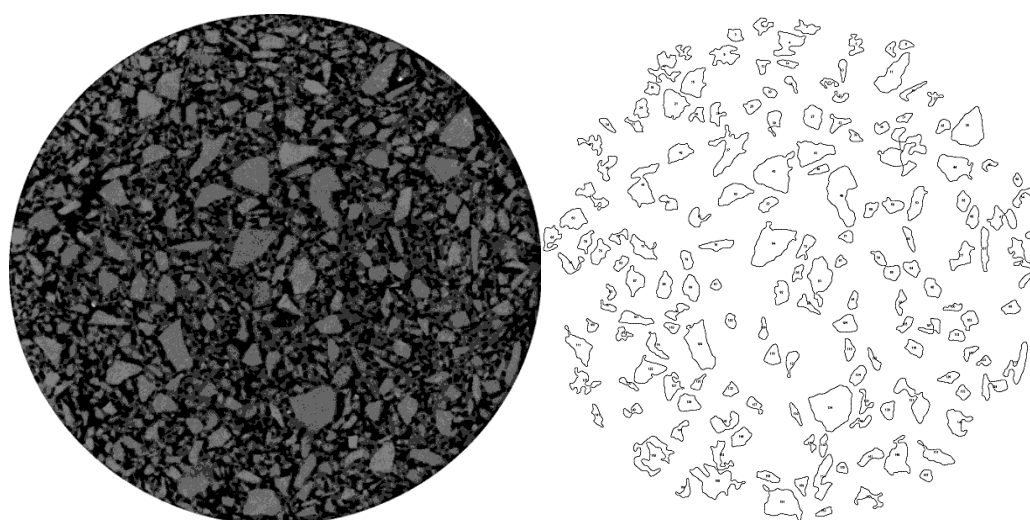
Figure 7.13 X-ray CT image and thresholded aggregates (above 2 mm)

Aggregates Positioning

Aggregate structure in the specimen has a great effect on permanent deformation resistance (Gibb, 1996). The distribution of aggregates of the three mixture types and the mortar of one type (bitumen and aggregates less than 2 mm) along the height are presented in Figure 7.14(A). As can be seen, the mortar is fairly evenly distributed along the height (for brevity only one

mortar type is presented). On the other hand, aggregate distribution follows the opposite trend of the AV for the three mixtures. The top and bottom parts are packed of aggregates about 40% more than the middle.

For the radial distribution of aggregates, the centre of aggregates at each 10 mm height of the sample centre (R) is presented in Figure 7.14 (B). The aggregates radial distribution along the height is structured in a barrel shape that has aggregate concentration in the middle section closer to the circumference. Additionally, the finer the aggregate gradation, the more distant the aggregates centres are from the specimen centre. The centre of the middle section of the specimen is more concentrated with AVs as presented earlier.
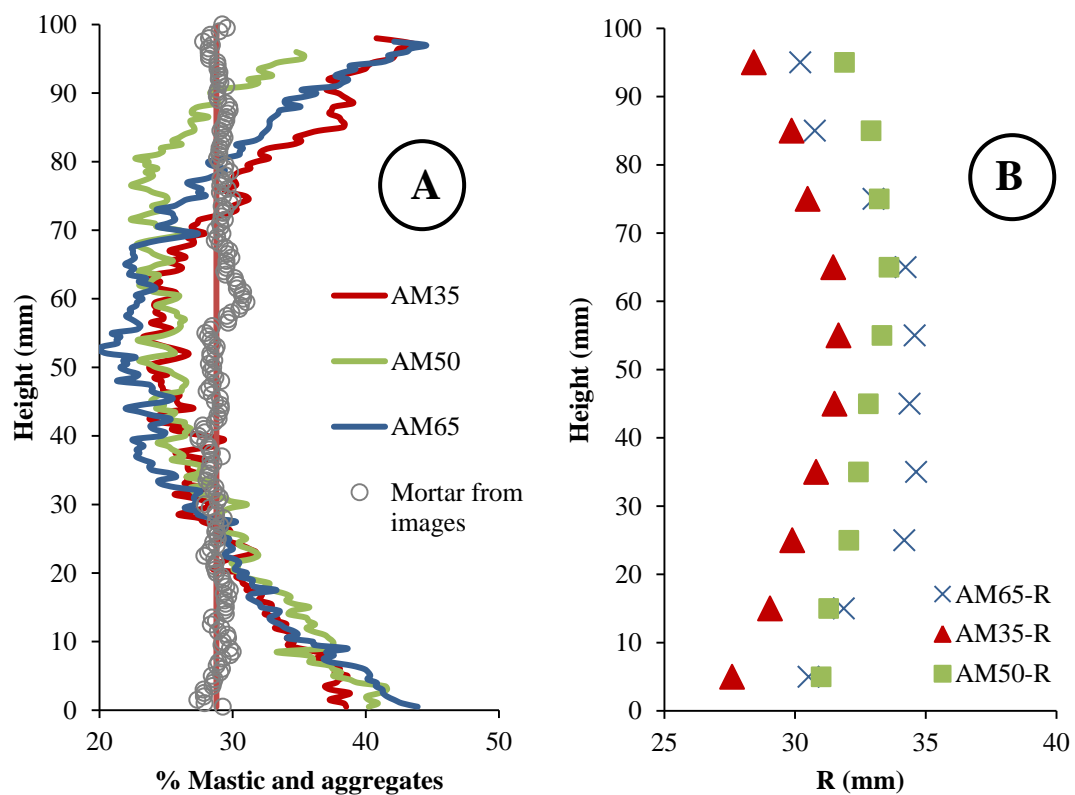
Figure 7.14 (A) Aggregate content and (B) Aggregates centre in the vertical direction

Segregation of Aggregates

An asphalt mixture specimen, ideally, should have a uniform distribution of aggregates across its volume. Nevertheless, due to the compaction process, segregation occurs and leads to poor performance (Hunter *et al.*, 2004, Tashman *et al.*, 2001). In this study, segregation was measured as a representation to size distribution. Specimens were virtually sectioned into top, middle, and bottom equal parts in the vertical direction, and outer and inner parts in the radial direction (Figure 7.15). In each section, the average area of aggregates in each slice was calculated, followed by the segregation calculation based on the following equations (Hassan *et al.*, 2012):

S_V = (Average of aggregate area in the top or bottom part - Average of aggregate area in the middle part) / (Average of aggregate area in the middle part)*100

S_H = (Average of aggregate area in the outer part - Average of aggregate area in the inner part) / (Average of total aggregates area in the inner)*100

Segregation in aggregates is quantified here as the percentage increase or decrease in the top-bottom and outer part of the specimen in relation to the middle and inner part respectively. The segregation was calculated as presented in Table 7.4.
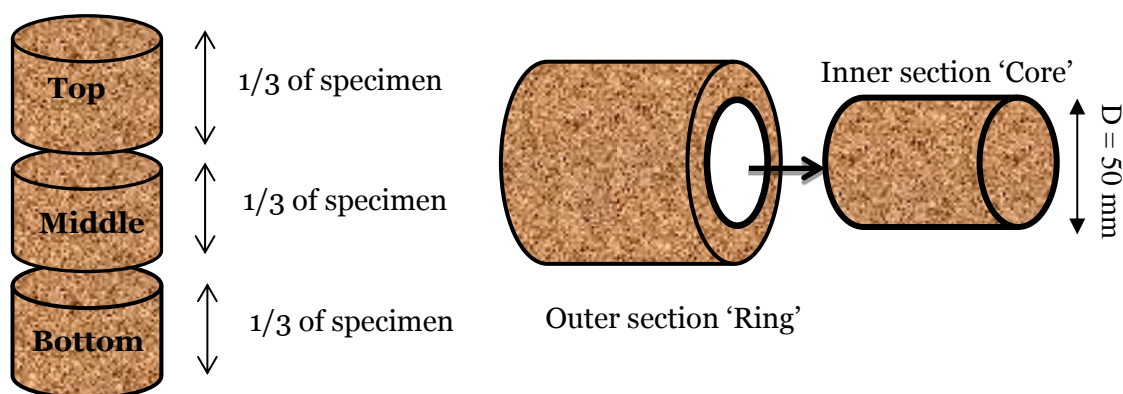
Figure 7.15 Illustration of radial and vertical sections of specimen for segregation analysis

Table 7.4 Vertical and horizontal segregations

Sample Type	Vertical segregation					Horizontal segregation		
	Average area-Top (mm²)	Average area-Middle (mm²)	Average area-Bottom (mm²)	$S_V(\%)$ Top	$S_V(\%)$ Bottom	Average area - Outer (mm²)	Average area - Inner (mm²)	$S_H(\%)$
AM65	13.51	12.01	33.8	12.47	181.3	28.3	9.5	197
AM50	14.8	13.08	31.6	13.15	141.2	23.3	10.3	126.2
AM35	18.54	16.1	23.14	14.8	43.3	22.7	10.3	120.5

Both vertical and radial segregations exhibit non-uniform distribution of aggregates sizes in the specimens. For all mixture types; coarse aggregates are more concentrated on the top and bottom parts of the specimen more than the middle, and closer to the circumference than to the centre. The vertical bottom segregation is greater than the vertical top segregation possibly due to the settlement of coarse aggregate on the bottom of the gyratory mould because of gravity upon pouring the hot mix into the mould. While the vertical top segregation is approximately equal in the three mixes,

the bottom vertical segregation is showing a trend of significant increase with increasing filler and fine aggregates in the mixture. In the radial direction, a major segregation is presented where the aggregate size in the outer part reached up to approximately 2 times that in the inner part. Again, this is as pointed out earlier because of the reduced horizontal compaction energy towards the centre from the circumference.

To detail the distribution of aggregates sizes in the inner and outer sections, the average feret diameter every 10 mm depth is presented in Figure 7.16. While the core section exhibits approximately regular size distribution within the height, the ring section shows larger sizes in general and more concentration of larger sizes at the top and bottom. Relatively smaller size coarse aggregates tend to accumulate in the core section of the sample and in the middle of the ring section. The reason behind this is thought to be because of the accommodation of coarse aggregates close to the circumference and their interlocking which transmits the compaction energy within certain areas (Hassan *et al.*, 2012).
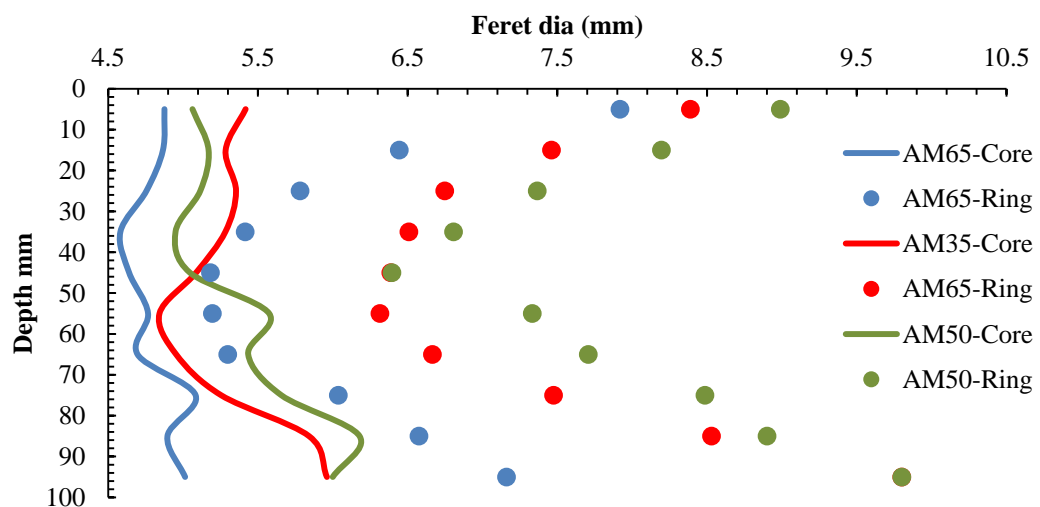
Figure 7.16 Distribution of aggregate size in the core and ring sections

From the above study of AV and aggregate distributions in the vertical and radial directions, a conclusion is drawn. The compaction energy in the vertical direction takes a cone shape which is a minimum in the centre part of the specimen (Thyagarajan *et al.*, 2010). Similarly, for the horizontal direction, since the AV tends to increase towards the centre and aggregates decrease, the horizontal compaction effort may produce a double cone shape at each side as illustrated in Figure 7.17. The overlapping between the two cones where the energy is minimum is perceived to be determined by the specimen height. However, further investigation is required to study the combined effect of horizontal and vertical compaction efforts in relation to the height and diameter of the specimen.
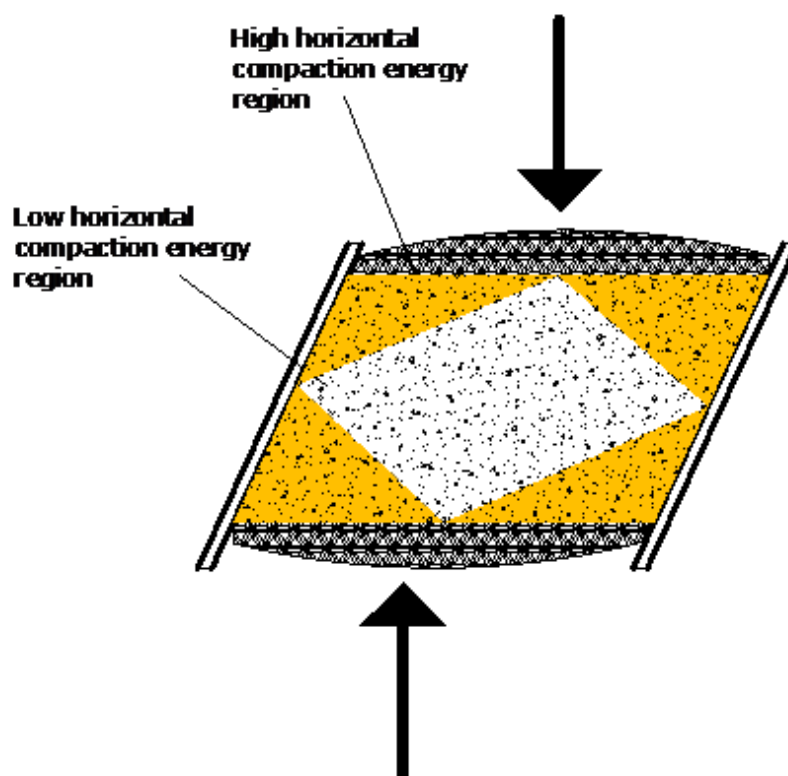
Figure 7.17 Horizontal compaction energy distribution in gyratory mould

7.5 Testing Results

7.5.1 Observations

Constant strain rate and constant stress creep test were carried out on the three types of mixtures at 30 and 50ºC. During the test the axial load and the axial deformation were recorded continuously as functions of time.

As presented in Figure 7.18, for constant strain rate test results the stress exhibits three distinct regions. In the first region where the stress is increasing the material is hardening, then the stress reaches its peak level in the secondary region followed by a decrease in the stress in the final region (softening). The test was stopped when the peak stress dropped by approximately 10%. The maximum reached stress is defined as the steady state creep stress beyond which the material starts to soften (Deshpande *et al.*, 1999). For a material, the peak stress increases with increasing applied strain rate. At one temperature, before starting the softening of the material, the region of the peak stress stretches more with reducing strain rate.
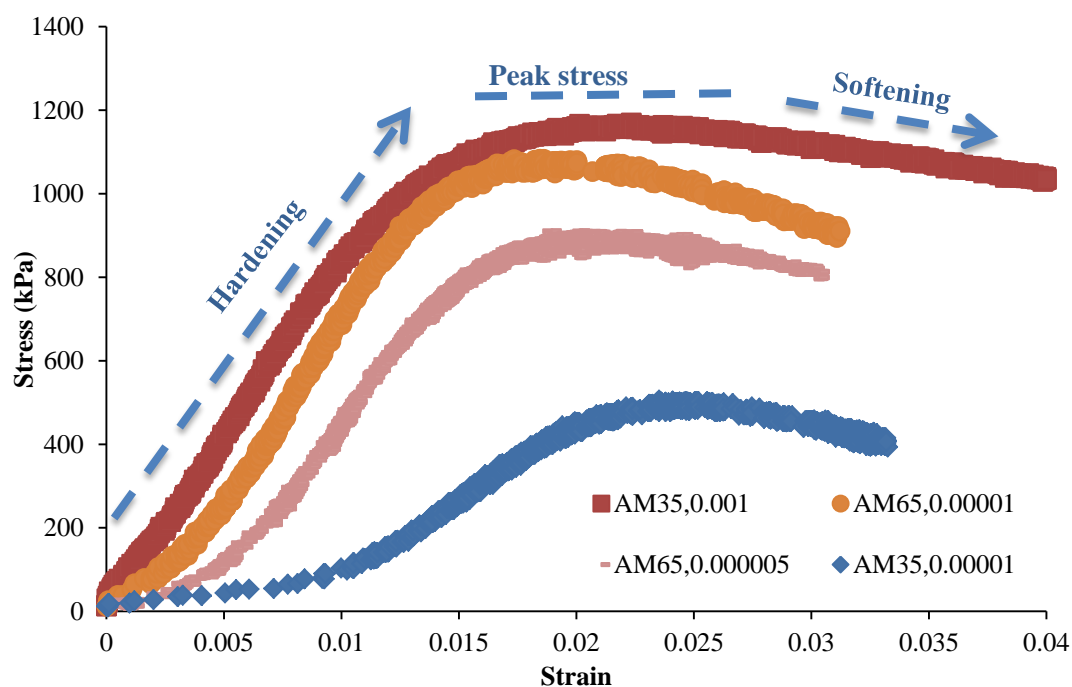
Figure 7.18 Constant strain rate test results at 30°C

As can be seen, AM35 exhibits more ductile behaviour (flatter curve) as compared to the sharp peak stress region in AM65 indicative of a more brittle behaviour in AM65 than AM35 (Taherkhani, 2006). In addition, as a sign of damage acceleration, the rate of stress decrease in the softening region in ascending order is AM35, AM50 and AM65. The average axial strain corresponding to the peak stress was found to be approximately 0.0213, 0.020, and 0.017 for mixtures AM35, AM50, and AM65 respectively independent of the strain rate at 30°C.

For the constant creep stress (Figure 7.19), the strain trend follows the same pattern of pure bitumen comprising three regions as identified in Chapter 3. The strain rate in the secondary region is identified as the steady state strain rate (SSSR). The test was stopped when the strain started to increase dramatically in the beginning of the third region. Some observation remarks are highlighted. At a particular shear stress and temperature, the strain in

mixture AM65 exhibits a larger level (more extension) at each region followed by AM50 and then AM35 (i.e. mixture AM65 requires more time to failure). This indicates longer times to reach the steady state condition, and thus mixture AM65 is stiffer (less deformation) than AM50, and AM50 is stiffer than AM35. AM65 has the lowest volume of coarse aggregates but considerably higher filler content.
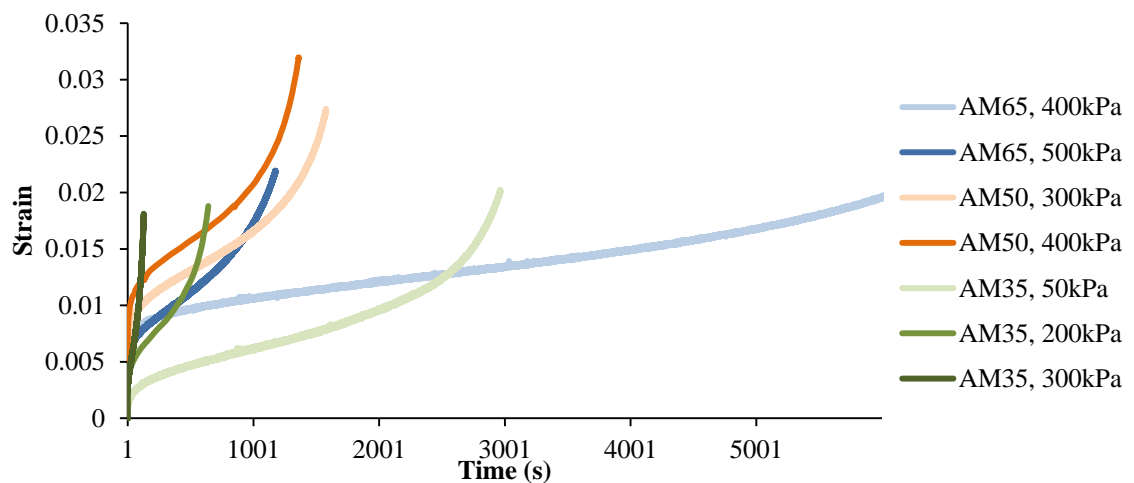
Figure 7.19 Uniaxial constant stress test results at 50°C

Figure 7.20 compares the axial strain value at which approximately the steady state condition is reached at 50°C combined with lines of average values for the three mixtures. Within the experimental error and consistent with Taherkhani (2006), the data points indicate stress independency pattern. The average strain value of AM35 is considerably lower than the other two mixtures. Reaching the 'full interlock' (steady state) condition requires more effort for aggregates to re-orientate themselves when the binder's viscosity is relatively high due to the large filler inclusion.
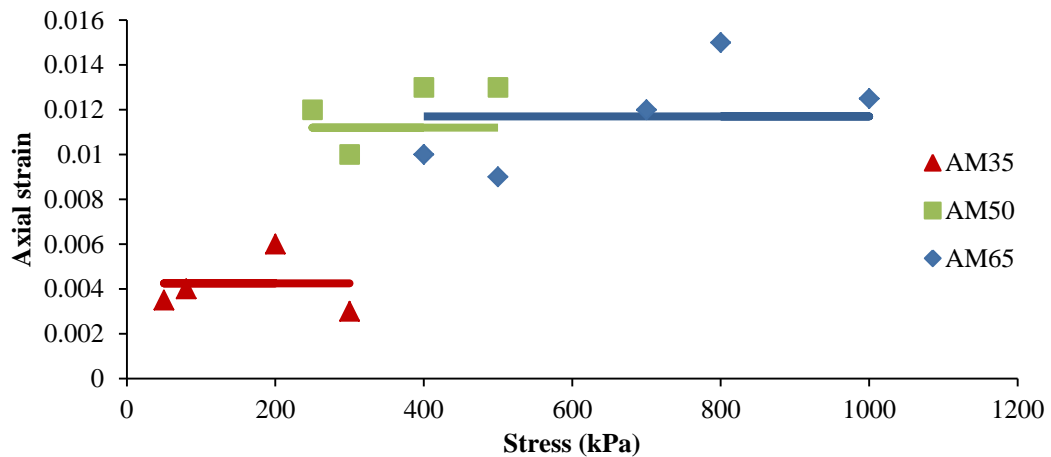
Figure 7.20 Strain level at the beginning of steady state region at 50°C

In addition, the high air void content in AM35 enables more room for the aggregates to move or rotate freely. The effective area that resists axial deformation is identified as the total cross section area minus the area fraction of air voids (Wang *et al.*, 2004, Elseifi *et al.*, 2011). Therefore, the developed strain in the AM35 mixture which contains high air voids content is significantly large and accelerates towards failure.

7.5.2 Steady State Behaviour

As presented in the previous chapters, the SSSR was found to have a linear relationship with the steady state stress at low stress levels. At higher stress levels the relationship transformed to nonlinearity. At the asphalt mixture scale, the determination of the linearity stress limit using the adopted trend line criterion was not always accessible. At low compression stresses (less than about 100 kPa) the steady state condition of the asphalt mixture was not reachable at 30°C even with long loading times (more than 8 hours). However, speaking generally, at 50°C with stress less than 250 and 400 kPa the trend line pointed to a linear relationship for mixture AM35 and AM50

respectively (Figure 7.21). Thus, it can be perceived that the coarse aggregate gradation has a lower stress linearity limit compared to the fine aggregate gradation.
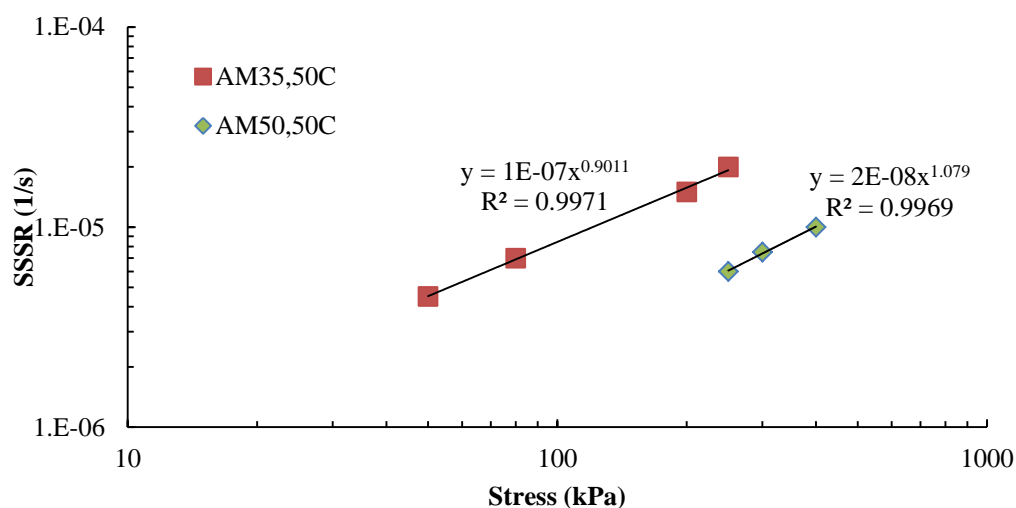
Figure 7.21 Linear part of steady state deformation of AM35 and AM50 at 50ºC

The steady state strain rate and stress of all tests (constant stress and strain rate) at 30 and 50ºC are summarised in a double logarithmic scale in Figures 7.22 for M35 and AM35 (A), M50 and AM50 (B), and M65 and AM65 (C) respectively. Also, combined in the plots are the experimental results of the corresponding mastic at each mixture and the MCM developed by Cheung (1995). The MCM at the mortar scale are the same as for the corresponding mastic but shifted by the inclusion of the stiffening factor (see Section 6.3.5 for details).
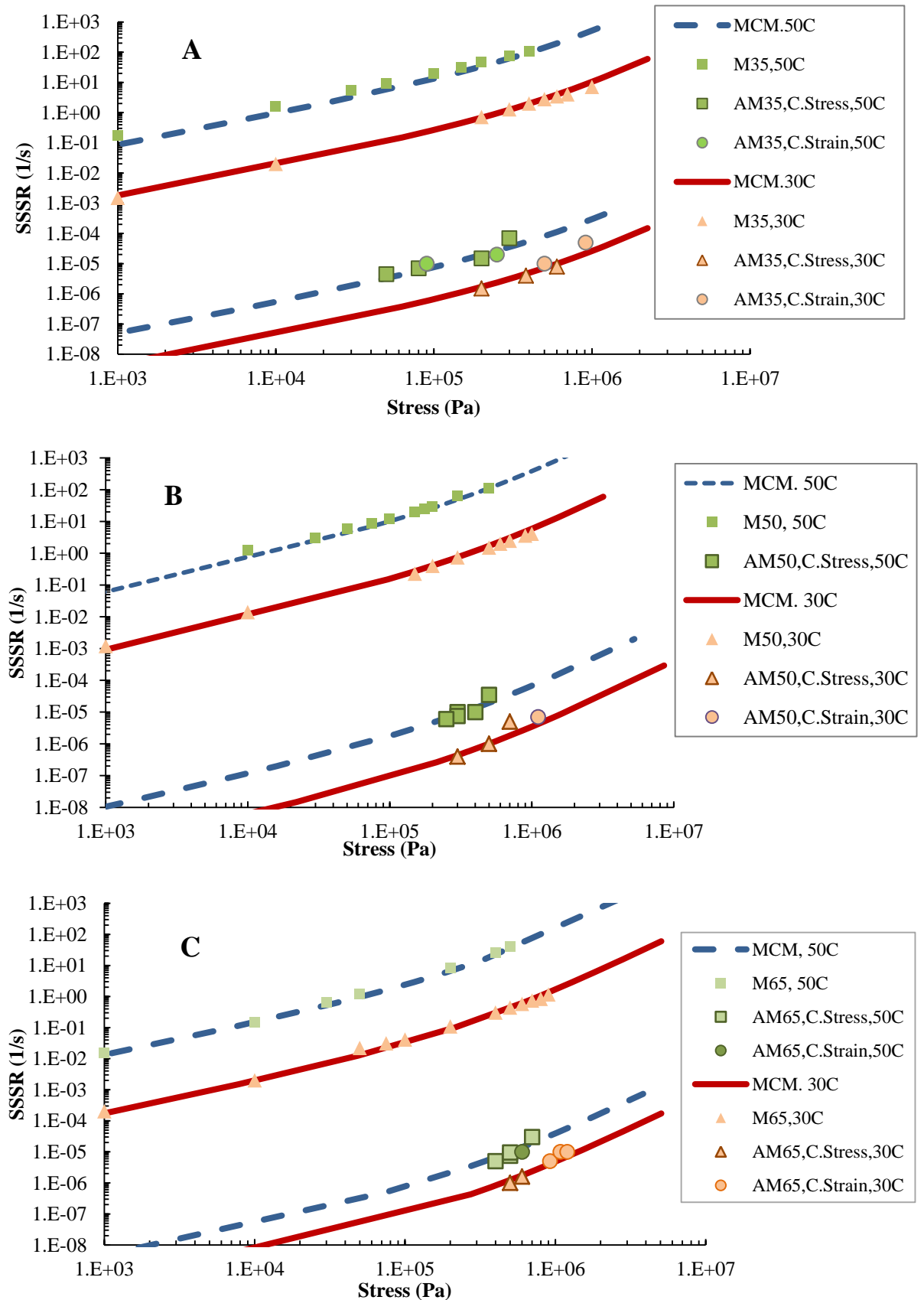
Figure 7.22 Steady state deformation and MCM of (A) M35 and AM35, (B) M50 and AM50, (C) M65 and AM65

As can be seen, the complementary nature of the two tests can be observed as the SSSR and steady state stress agree at intermediate levels of temperatures and strain rates (Deshpande *et al.*, 1999, Taherkhani, 2006). As an overall performance evaluation, mixture AM65 exhibited the maximum resistance to deformation, followed by AM50, and finally AM35. Mixture AM65 has the lowest and the highest contents of coarse aggregates and filler respectively. From this point, it is speculated that the filler and fine aggregate content plays a significant role in uniaxial deformation resistance.

7.5.3 The Stiffening Effect of Aggregates

Utilising the inclusion of stiffening factor 'S' to the MCM as detailed in Section 6.3.5, the uniaxial compression stiffening effect of coarse aggregates is measured based on the corresponding mastic resistance (Chapter 4) at 30 and 50°C. The stiffening factor is illustrated in Figure 7.23 jointly with the uniaxial compression stiffening factors of related mortars. Important observations are highlighted.

Figure 7.23 Comparison between the stiffening factors of mortars and asphalt mixtures

Although the coarse gradation of fine aggregates at mortar scale (M35-5%) significantly enhanced the resistance in comparison to the other mortars, the high air voids content at the asphalt mixture scale (AM35) reduced the stiffening of coarse aggregates to a level equal to the fine aggregate gradatio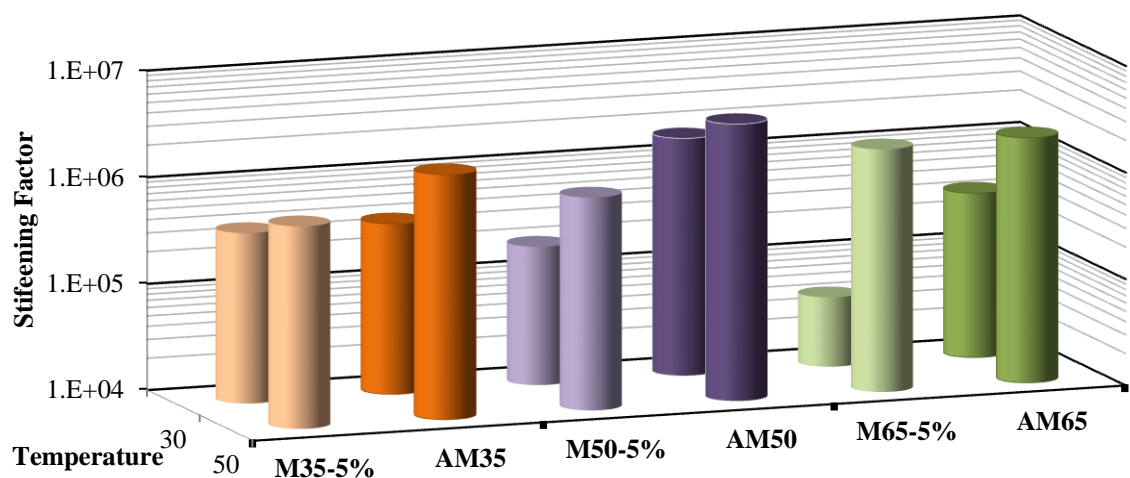n at 30°C. Similarly, the stiffening effect was not improved by the inclusion of coarse aggregates in AM65 at 50°C. Fine and coarse aggregates gradations with high and low filler content (AM65 and AM35) respectively produced approximately the same level of stiffening at 30 and 50°C. On the other hand, intermediate levels of filler content and aggregate gradation (AM50) produced the highest level of stiffening. This is a result of relatively higher filler content and lower air voids than in AM35, and larger fraction of coarse aggregates than in AM65.

7.6 X-ray of Tested Specimens

To study the change in the microstructure, samples were scanned before and after testing. Section 7.4 presented the characteristics of the mixtures in relation to the manufacturing account, and here the microstructural changes that took place after testing are investigated. Two specimens of each mixture type deformed vertically at 30°C to 0.03 prescribed axial strain level by applying 0.001 and 0.00005 constant strain rates in uniaxial testing set up. After the target strain was achieved the test was stopped and the deformed specimen was X-rayed again. Air voids properties are addressed as the main parameter to study the change.

Tested samples deformed vertically and horizontally, the height shortened and the corresponding diameter varied with height. Consequently, operating

the same slice interval (0.5 mm) in the X-ray used before testing meant that the scanned sample after testing have fewer images. To resolve this problem, the relative height is used as an alternative. For the diametrical change, the radial strain at each height can be measured through calculating the % change in the area at each slice as will be discussed later.

7.6.1 Change in AV Properties

Due to the heterogeneity of the material, the localized stress-strain relationship follows an irregular response. Asphalt specimens subjected to loading begin to fail by the nucleation of microcracks that propagate, grow, and coalesce to form macrocracks in which the AV content increases (Tashman, 2003).

Degradation can be evaluated through investigating the changes in AV properties after testing based on the 'original condition' reference state. Figure 7.24 illustrates an example of AV intensity increase after deformation. A number of studies characterised AV to provide beneficial information regarding damage evolution and its correlation to the material behaviour using the X-ray CT (Tashman *et al.*, 2004, Khan *et al.*, 2010, Masad *et al.*, 1999b, Abdul Hassan *et al.*, 2014).
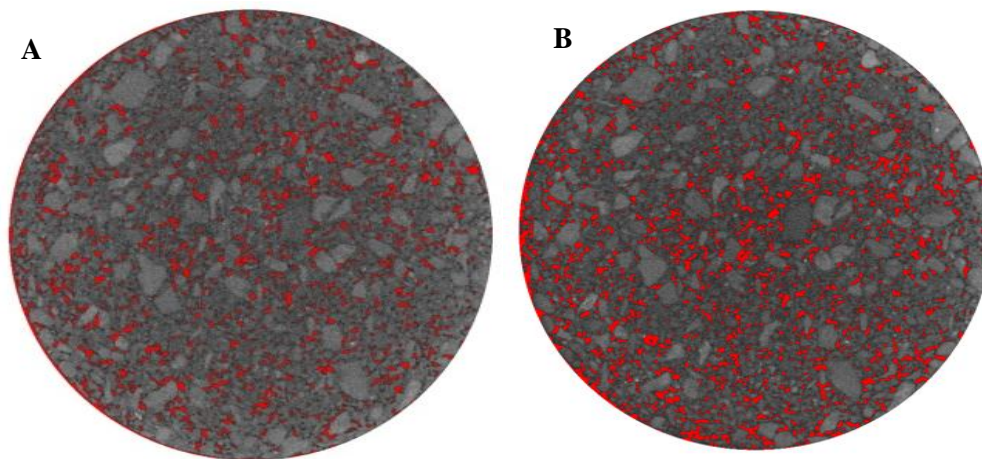
Figure 7.24 Comparison of AV intensity (A) before and (B) after deformation

In this section of the research, the objective is to observe damage evolution in different aggregate gradations (fine/coarse) as the material undergoes permanent deformation.

The characteristics of AV are studied by investigating the change in AV properties of deformed specimens. The % change in the air voids area = (final AV area-initial AV area)/(initial AV area) is presented in Figure 7.25. As can be seen, the % change in mixture AM65 is approximately uniform along the height with a slight decrease to 20% in the middle section. While mixture AM35 presents a gradual increase in the AV from bottom to the top, AM50 shows approximately a uniform distribution along the height. Thus, although the middle section in all mixtures was identified with the highest area of AV before testing within the specimen height, the maximum increase after testing was not in that region. Similarly, at 0.00005 strain rate the increase in the AV area was approximately uniform. Therefore, it can be concluded that, with some tolerance in experimental error, the uniaxial compression test is insensitive to the AV distribution along the specimen height.
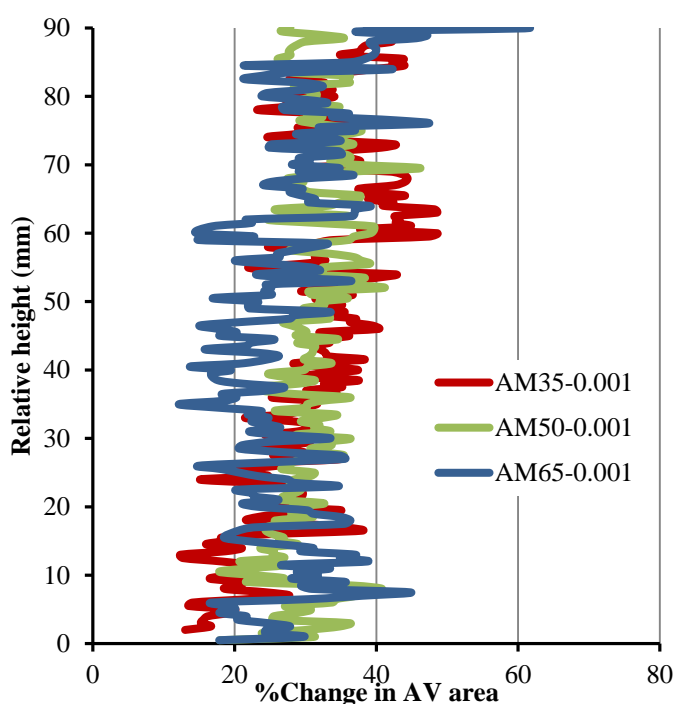
Figure 7.25 Change of AV area at 0.001 strain rate

Figure 7.26 presents the change in the properties; number, size, and circularity of AVs for the three mixtures. In all the mixtures, the top and bottom sections exhibit higher increase in number and lower growth in size, opposite to the middle section.

On the other hand, mixture of fine aggregates (AM65) exhibits more increase and lower growth in number and size of AV respectively than mixture of coarse aggregate (AM35). There is a substantial increase in the AV number of mixture AM65 if compared to AM35. This is actually because of the AV visibility limit of the X-ray. Tiny microcracks develop to detectable macrocracks after loading in which AV number is expected to grow.

For mixture AM65, locally, the section of high AV content before testing (the middle) has the minimum increase in number and maximum growth in size of AV along the height after testing. Thus, the deformed specimen of the fine

aggregate gradation has the tendency to increase the size and provide relatively lower increase in number of AV respectively at the region of high AV content, and vice versa. The regions of high AV content are speculated to widen and connect their voids, while closure of AVs (cracks) is thought to occur at regions of relatively low content.

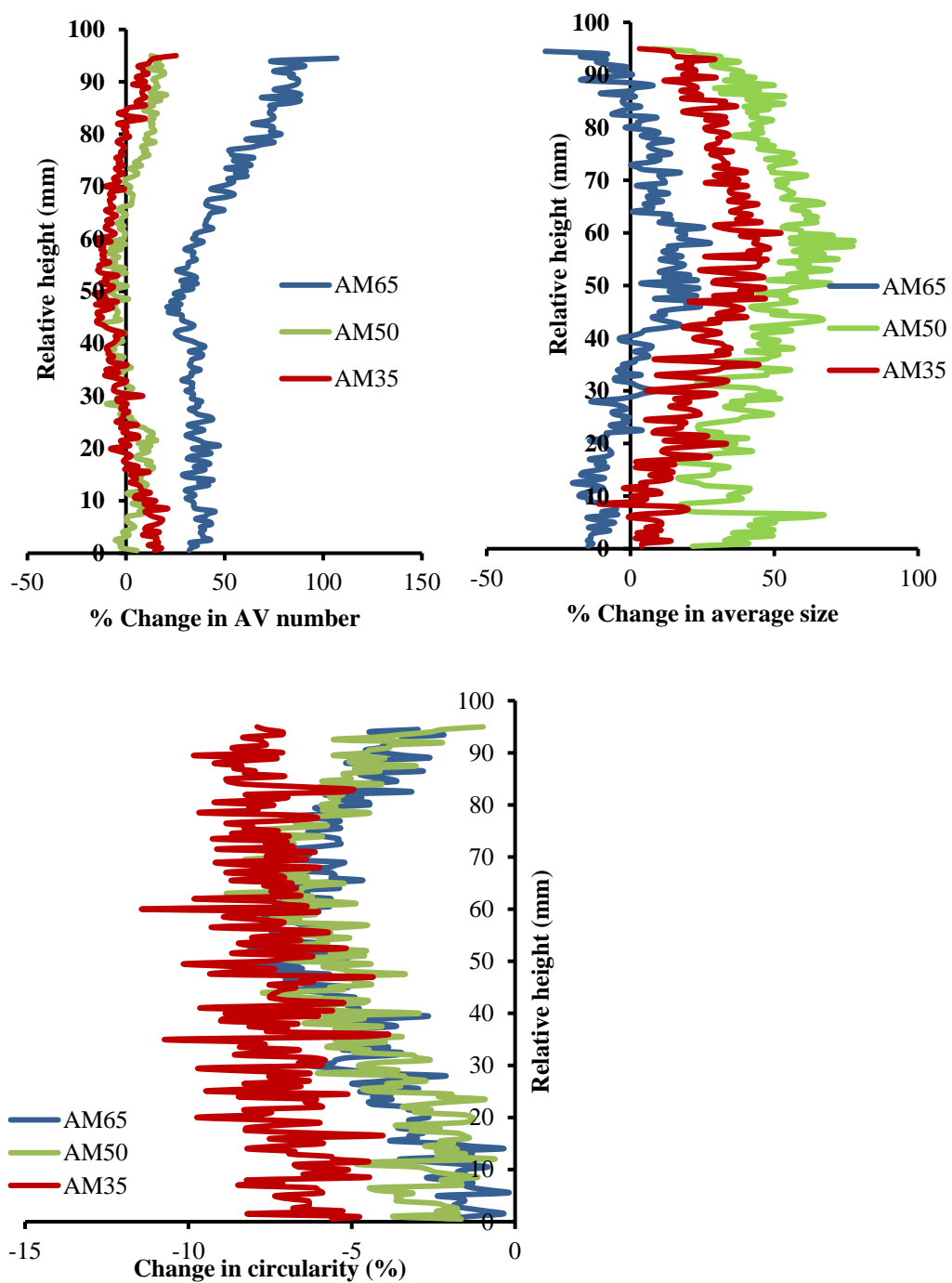**Figure 7.26 Change of AV properties at 0.00005 strain rate**

For mixture AM35, the maximum decrease in the AV number (AV closure) is within the middle section which was identified before testing as the region of high AV content. Inversely, this region provides the maximum increase in the average size of AV within the specimen height. The critical region of high air void content tends to increase the size of air voids that collate to form microcracks in preference to forming new ones. In respect to the shape, significant elongation is observed where the AV circularity reduces in both mixtures. This suggests that the increase within the AV geometry under loading is disproportional.

To compare between the strain loading rate 0.001 and 0.00005 of the three mixture types, the average % change in AV property is calculated in each section of the specimen as follows:

The % change in property = 100 x (Absolute average property value at 0.001 strain rate - Absolute average property value at 0.00005 strain rate)/ (Absolute average property at 0.00005 strain rate)

Table 7.5 compares the results between the three mixture types. The tabulated values indicate important observations. Although the final strain was equal, the higher strain rate induced a greater increase in the AV content at the three sections of all mixtures, and more within the middle section. As can be seen, the negative value in the number of air voids reveals that the lower strain rate produced higher number of air voids. On the other hand, the higher strain rate tends to widen the existing voids (cracks). In terms of circularity, the higher strain rate loading produced lower circular shape of AV than the low one.

Table 7.5 Analysis of AV properties between 0.001 and 0.00005 constant strain rate test results in the three mixtures

Specimen ID	Section	%Area	% No.	%size	%circularity
AM35	bottom	10.78	-193.78	259.14	-37.42
	mid	46.45	-76.55	2.459	-96.90
	top	27.67	-309.70	35.43	-105.65
AM50	bottom	10.99	-35.24	3.40	-51.10
	mid	31.54	306.76	14.80	-9.17
	top	46.21	-289.19	28.26	-28.66
AM65	bottom	10.42	-86.46	164.43	-50.51
	mid	59.49	-83.61	20.38	-43.21
	top	17.51	-83.53	294.90	-87.82

7.6.2 Effective Radial Strain

Specimens subjected to loading deform vertically and horizontally. Axial strain is recorded during the test and radial strain is usually measured in the middle of the specimen as an average level. In this part of the research a new procedure is introduced to measure the final radial strains along the specimen height utilising X-ray image technology.

Customarily, in the initial stage of image processing, the circumference of the specimen at each slice is approximated by a circle to remove any background noise outside the specimen. However, specimen perimeter does not follow exactly a circular path and parts of the specimen are trimmed as a consequence (Figure 7.27-A). In this research, a new technique is introduced so that the tomography of the specimen's orbit is most closely traced leaving

no part of the specimen to be neglected. This is essentially important as the accumulation of the circular approximation in a set of images builds up error in the calculation and calibration that reduce the accuracy.

The basic steps to achieve this through ImageJ is by adjusting the threshold to cover most of the features in the image (Figure 7.27-B), followed by converting the image into digital form (Figure 7.27-C), then applying 'filling holes' to close the holes without changing the border tomography (Figure 7.27-D), and finally measuring the area. The final effective strain in the material after loading (excluding the air voids both content and increase) is calculated as follows:

$$\varepsilon_r = \frac{D_2 - D_1}{D_3} \times 100$$

Where:

D_2 is the final equivalent diameter $= \sqrt{\frac{4}{\pi}(\text{final total area} - \text{initial total area})}$

D_1 is the equivalent diameter of AV increase

$$= \sqrt{\frac{4}{\pi}(final\ total\ AV\ area - initial\ total\ AV\ area)}$$

D_3 is the initial equivalent diameter without AV =

$$\sqrt{\frac{4}{\pi}(\text{initial total area} - \text{initial total AV area})}$$
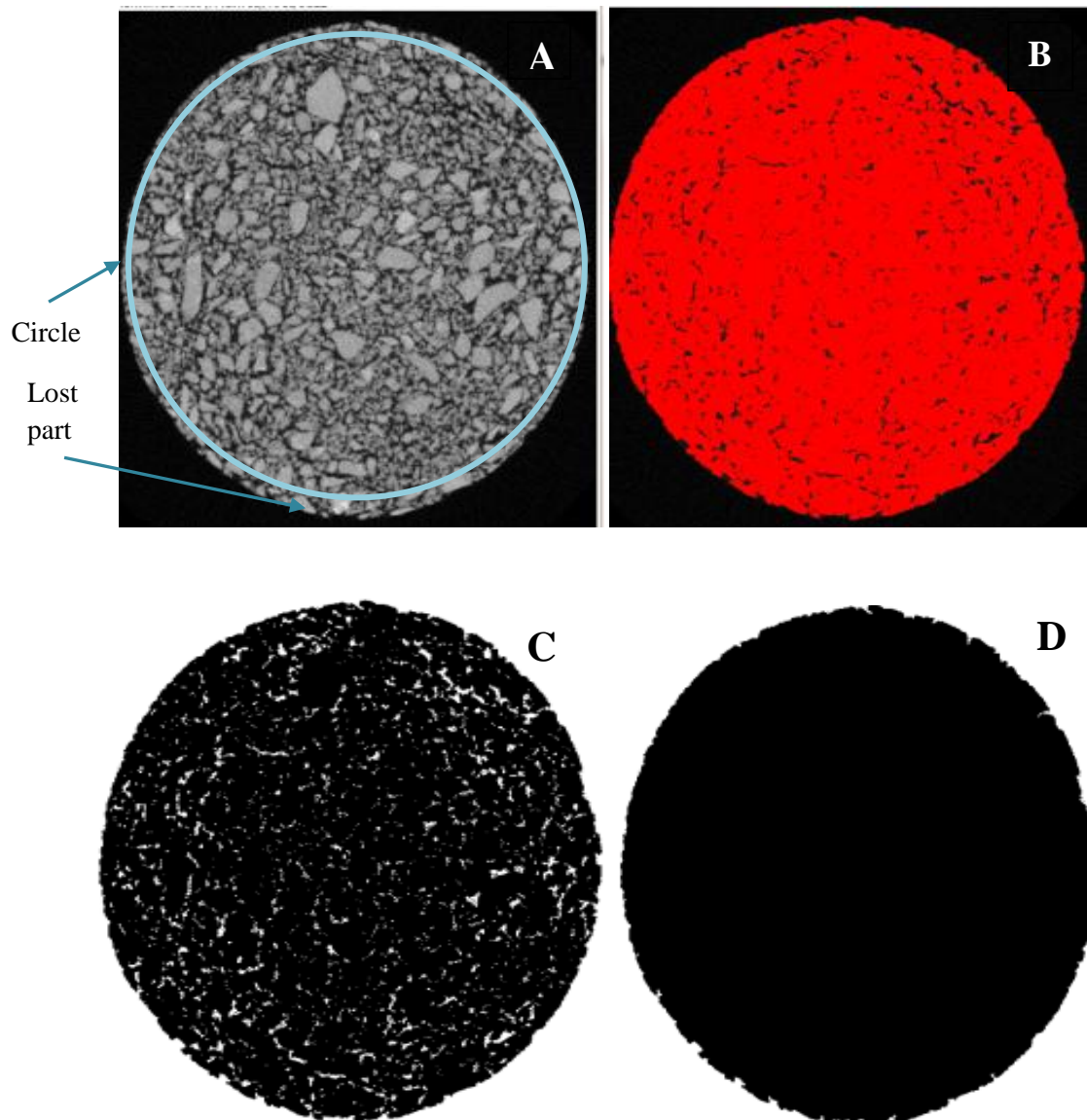
Figure 7.27 Illustration of area determination from an X-ray image

Figure 7.28 illustrates the effective strain along the height. The radial strain is non-uniform in all mixtures and exhibits positive strain (tension) in the middle and a decrease to compressive strain (negative) in the top and bottom sections. The growth in the AV size as illustrated previously in the middle section generates tensile strains while the increase in the number is indicative to compression (or low tensile strain) as in the top and bottom sections. Finally, the middle region of maximum air void content produced the maximum tensile radial strain.

Mixture AM35, which contained the maximum AV content before testing possessed the maximum tensile and compressive strains in the middle and top-bottom parts of the specimens. This indicates that the initial AV content has a significant impact in the lateral strain after testing. In addition, it should be noticed that the final lateral (radial) strain was higher than the final axial strain (3%).
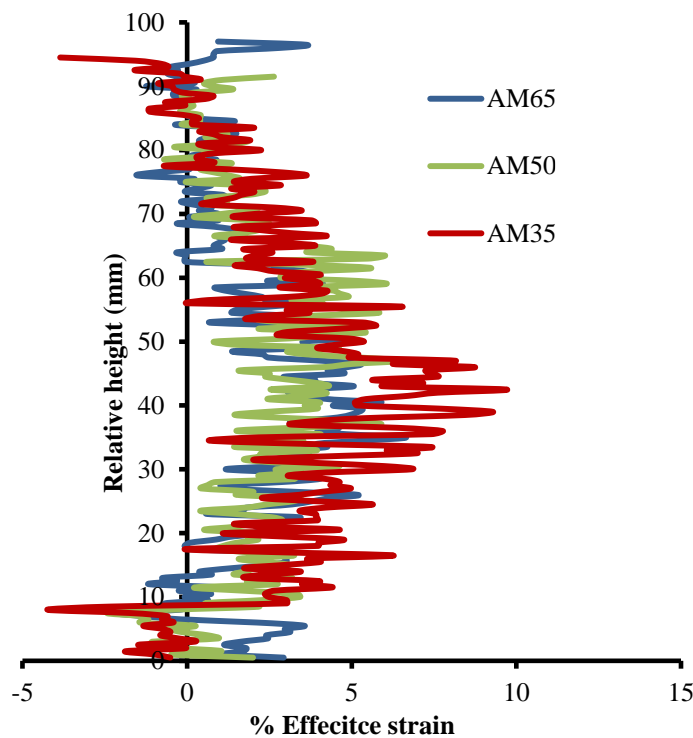
Figure 7.28 Radial effective strain distribution after testing

7.7 Conclusions

Gyratory compacted specimens revealed heterogeneous air void distribution along the height and radius, concentrated in the middle and closer to the centre. Since the gyratory force has vertical and horizontal components, it was speculated that not only the vertical transmitted energy reduces towards the centre but also the horizontal one as well. Mixtures of coarse aggregates

produced larger size and smaller number of air voids with the opposite being true to the fine aggregate gradation mixtures.

The complementary nature of the constant stress and strain rate test results at intermediate levels of temperatures and stresses agreed satisfactorily with the MCM harmonization. The stiffening effect of coarse aggregates was found to be significantly limited in the presence of high air void content. Thus, intermediate level aggregates gradation produced the highest stiffening effect in relation to the corresponding mastic. This is attributed to the relatively larger filler content and coarse aggregates in comparison respectively to the lower and upper limit aggregates gradations produced specimens.

While overall level of mortar distribution along the height was found to be uniform for all mixture types, greater segregation occurs in fine aggregate gradation mixtures both vertically and horizontally. The high viscosity of binder with high filler concentration may limit the transmission of compaction energy to distribute the coarse aggregates. In general, coarse aggregates are concentrated on the top and bottom sections and closer to the circumference.

Analysis of SSSR versus stresses indicated that the coarser the aggregate gradation, the lower the stress linearity limit. Uniaxial compression test results indicated that the test is not sensitive to air void distribution in the specimen and provides homogeneous increase in the air voids along the specimen height regardless of the mixture type and the initial regularity state of air voids.

AV analysis before the test showed that although both fine and coarse

aggregate gradations share a pattern of maximum air voids in the middle of the specimen, it was because of the higher number of AV in the former while the latter was caused by the larger sizes of AV. After testing, the maximum increase in the air void content within the specimen was not in the middle section.

Thus, locally, deformed specimens of fine and coarse aggregate gradation have the tendency to increase and decrease the size and number of AV respectively at the region of high AV content, and vice versa.

A new X-ray imaging technique was introduced to measure the final radial strain along the height. Results presented a non-uniform trend of compressive strain within the top and bottom sections while high tensile strain occurred in the middle section where initial AV content is maximum.

8. Conclusions and Recommendations

8.1 Introduction

The upper layer of flexible pavement is rutted because of permanent deformations (strains) in the asphalt mixture. The research investigated the phenomenon at four observed scales of bituminous materials with the objective to strengthening the understanding of the interrelationship and interactions between components. 10 mm DBM standard asphalt mixture type was studied as it is widely used in the UK. Mastics of filler inclusion and mortar of fine aggregates were generated from this mixture. On the binder scale, a new rutting evaluation test was developed through applying modifications to the standard multiple stress creep recovery test.

In all tested scales, at low stress levels bitumen and bituminous materials presented linear viscous behaviour, while shifted to a nonlinear viscous behaviour at higher stress levels. The steady state constitutive relationship between stresses and strains was characterised through the modified Cross model (MCM) in a satisfactory agreement with the experimental results. Moreover, through the MCM the stiffening effect of fine and coarse aggregates was measured respectively in mortar and asphalt mixture scales in relation to the corresponding mastics.

8.2 Conclusions

The main conclusions of this dissertation are summarised in three key areas in accordance to the specified objectives:

i. Binders Creep and Recovery Characteristics and the Developed MS-SCR Test

To date, most developed binder rutting evaluation procedures are predominated by testing pure or polymer modified bitumen neglecting the effect of filler as an inevitable part of the mixture. Therefore, shear creep and creep-recovery tests were performed to characterise the viscoelastic behaviour of pure bitumen and mastics over a wide range of stresses and temperatures. Based on the observation remarks a new test was designed (MS-SCR) to evaluate binders through two mechanisms; stiffening and recoverability. Two PMBs of SBS and EVA were tested as well for validation purposes. The following conclusions are withdrawn:

- The stress limit after which the behaviour transfers from linear to nonlinear was found to be temperature dependent. Increasing the temperature accelerates the trigger of nonlinearity. According to the steady state matching criterion, the stiffening effect of filler was found to be constant at low stress level and reduces nonlinearly at high levels of stresses. The more filler that is added and/or temperature is increased, the shorter is the constant stage extension. In comparison to low and intermediate filler contents, the significant stiffening effect of high filler content (65%) postulated a skeletonized structural arrangement of fillers.

- In the single creep-recovery tests, the relationship between the recovered strain (= total strain − unrecovered strain) and the total strain was found to be linear at very small total strain levels. Yet, after reaching a certain limit of total strain, the recovered strain becomes constant. This strain limit reduces to a lower level when the filler content is increased and/or the stress level is decreased, but insignificantly influenced by the temperature.

- A new method using MatLab Simulink was introduced to easily and quickly determine a single set of parameters to the mechanical Burger's model that fit both the creep and single creep recovery experimental results. In addition, the constitutive relationship between the steady state strains and stresses was captured satisfactorily by the MCM. The stiffening effect of filler inclusion and the resulted nonlinearity extension was reflected in the model by the reduction in the parameter of failure strength of structural linkage.

- Distinguishing between stiffening and recovery properties, as the MS-SCR test provided, is vital because not all binders resist rutting by the two mechanisms.

- According to the MS-SCR test, although the short recovery rate varies between different mastics of similar filler content, when the recovery lasts long enough the final recovery becomes independent of the filler type.

- PMBs exhibited significant influence by the 'delayed elastic' on both loading and unloading stages in MS-SCR test, particularly at low temperature. On the other hand, mastics with high volume of filler demonstrated a pre-interlocking stage that affects the cyclic behaviour

regardless of the temperature. Both mastics and PMBs were found to be less sensitive to temperature change than bitumen in relation to the deformation rate.

- With modified binders in the MS-SCR test, the linearity stage was found to appear between two nonlinearity phases. The initial nonlinearity at very low stresses is perceived as a stage to form the molecules networking and particle-particle full contact establishment in PMBs and mastics respectively. Following the linearity stage, the inclusion of the high normal stress to maintain the thickness in the DSR was found to transfer the binder into a second nonlinearity stage at high levels of shear stress.

ii. Mortars Shear, Uniaxial, and Triaxial Deformation Behaviour

The literature indicated that, as yet, there is a lack of knowledge on the mortar scale in terms of fine aggregates effect on permanent deformation behaviour. A new type of mortar that is developed from mastics based on a 10 mm DBM asphalt mixture was designed and manufactured. The steady state deformation behaviour of mortars with different aggregates gradations and bitumen contents was investigated. The fine aggregates stiffening effect in shear, uniaxial compression, and triaxial testing was measured through the MCM at 30 and 50°C, revealing the following major remarks:

- The resistance to shear deformation was found to be controlled by the filler content more than fine aggregate, however, fine aggregate affects more the shear stress linearity limit. On the other hand, the sensitivity of the linearity stress limit to the bitumen content is only at high temperature.

- From the single shear creep-recovery results, a trend similar to the binder was obtained between the recovered strain and total strain comprising a linear relationship followed by a constant recovered strain stage. Interestingly, the mortar attained higher recovery than mastic in the linear stage. Nevertheless, the constant recovered strain level was reached earlier in mortar than mastic in the constant stage.

- The deformation resistance and stress linearity limit increased in the state of uniaxial compression in comparison to shear, and increased more in the triaxial state with the confining condition.

- The deviation of the shear SSSR from the MCM prediction suggested that the shear nonlinearity dependency is influenced by the fine aggregates gradation.

- The dependency of the uniaxial deformation resistance on the bitumen content was found to be only valid at large filler content and high temperature conditions. When the shear test was conducted, the dependency varied based only on the filler content. Increasing the temperature increased the stiffening effect of uniaxial compression and triaxial while the shear deformation resistance was observed to increase only at high filler content.

iii. Uniaxial Deformation Behaviour of Asphalt Mixtures and the Internal Structure Through X-ray and Imaging Techniques

A preliminary investigation of the X-ray facility and available software suggested 0.5 mm scanning interval and 2 mm as the minimum detectable aggregate size for optimum scanning and data interpretation. Specimens were manufactured in three aggregate gradations that corresponded to upper

limit, lower limit, and mid-range of a 10 mm DBM asphalt mixture type. Specimens were X-rayed before and after applying uniaxial constant strain rates loading.

Scanned samples, before testing, were used to study air voids and coarse aggregates in relation to the gyratory compaction. Results from the uniaxial tests were satisfactory characterised by the MCM to measure the stiffening effect of coarse aggregates in relation to the corresponding mastics. Finally, the microstructural changes due to loading were quantified by measuring the differences between the X-ray scanned objects before and after the test. Following are the main obtained conclusions:

- Gyratory compacted specimens with fine or coarse aggregate gradation, produced higher air void content in the middle of the specimen and closer to the centre. The transmitted compaction energy not only reduces vertically but also horizontally. In addition, while a larger air void size was obtained with coarse gradation, fine gradation exhibited higher number of air voids.

- The maximum uniaxial stiffening of coarse aggregates was gained by the mid-range aggregate gradation, attributed to the higher filler content (low air void) and coarse aggregates content in comparison to the lower limit and upper limit aggregate gradations respectively.

- Prior to testing, the high air void content zone was found to be maximum in the middle and attributed to the large size and high number of air voids in the coarse and fine aggregate gradation mixtures respectively. After testing, however, the maximum increase in the air void content and

number was not in that region and the increase in the air void content was found to be approximately constant along the specimen height. The region of maximum air void content (the middle) exhibited an increase in size and decrease in number after deformation, opposite to the top and bottom sections.

- Radial strain distribution along the height after testing presented compressive modes in the top and bottom sections, and tensile strain in the middle section larger than the final applied axial strain.

8.3 Recommendations

i. Rheological Characterisation of Mastics

The dynamic shear rheometer (DSR) is a powerful piece of equipment to deliver a precise torsional loading at an accurately controlled temperature. On the other hand, with parallel plate geometry the generated stresses-strains are not uniform in the sample while 'cone and plate' geometry provides insufficient thickness for mastic samples. Further research is required to produce more mastic-suitable testing geometry with standardised sample preparation and testing protocol in the DSR taking into consideration the bond between the sample and plates.

In this research a new method to determine Burger's model parameters is explained. The advantage of using this simple method is the applicability in different creep loading configurations and easiness to switch between the time and frequency domains. It is suggested to compare between parameter values of different binders to study the change in the viscoelastic properties.

Running simulation of the model in a numerical environment is recommended to investigate the stress-strain distribution within the sample.

Although mastic rheological properties were tested at three filler concentrations (35, 50, and 60%), it is suggested to accurately determine the nonlinearity stress limit criteria in relation to filler content over a wider range of temperatures. In other words, establishment of a map that relates the filler content and temperature to the stress linearity limit is a topic for further investigation. Recent developments in X-ray technology should allow scanning of the filler distribution and structural arrangement to determine the influence of packing characteristics on the mechanical and rheological properties. Moreover, different penetration grades binders are suggested to be investigated with various types of fillers including the ageing effect to obtain a broader understanding. Polymer interaction with bitumen in a PMB form is well studied as detailed in the literature. The combination of modified polymer-filler binder is a topic that merits further study.

The developed MS-SCR test proved to establish a new procedure for evaluating binders rutting resistance. Further research is needed to standardise the test. The selected stress-strain in the test can be adjusted to improve and relate more with the realistic traffic conditions. Moreover, a similar test procedure can be adopted on larger scales of bituminous materials to evaluate the influence of added components on rutting. The effect of the normal force in the DSR should be given adequate attention.

ii.   **Mortar Permanent Deformation Behaviour**

To the best knowledge of the author, this research investigated for the first time the permanent deformation behaviour of mortars with different gradations of fine aggregates while others focused on fatigue and moisture damage. Some mortar mixtures observed high sensitivity to the confinement and further investigation is required. Burger's model identified parameter estimation procedure can be combined with the simulation in Abaqus to study the stress-strain relationship in the DSR.

The study can be extended to encompass other variables such as fine aggregates type. The effect of moisture damage can be coupled with rutting through conditioning the samples in water and then studying the influence on the stiffening effect of fine aggregates including the linearity observation.

iii.   Asphalt Mixture Deformation Behaviour

In the current research, a continuously graded mixture type (DBM) was analysed in detail at different scales. Other types of mixtures such as gap graded, with different binder contents and aggregate gradations is a topic for further study. Investigations outside the scope of tested temperatures as well as tensile stresses are recommended.

There are many successful applications of X-ray CT on asphalt mixtures including study of changes in the microstructure after testing. Introducing a non-destructive tool such as acoustic emission sensors to monitor over a long time the changes in the material behaviour during the test is proposed. It can provide a rich source of localised information for detecting cracks propagations deep inside the material. Therefore, together, they can significantly progress and increase the dimension of defect detection and

provide better linkage between the material behaviour and the microstructure.

Finally, although this study focused on permanent deformation, the multi-scale methodology developed can be utilised to assess damage due to different mechanisms such as fatigue cracking and moisture damage.

REFERENCES

Abbas, A., Masad, E., Papagiannakis, T. & Harman, T. 2007. Micromechanical modeling of the viscoelastic behavior of asphalt mixtures using the discrete-element method. *International journal of geomechanics, 7*, 131-139.

Abdul Hassan, N., Airey, G. D. & Hainin, M. R. 2014. Characterisation of micro-structural damage in asphalt mixtures using image analysis. *Construction and Building Materials, 54*, 27-38.

Airey, G. & Hunter, A. Dynamic mechanical testing of bitumen: sample preparation methods. 2003. Institution of Civil Engineers, 85-92.

Anderson, D. A., Le Hir, Y. M., Planche, J.-P., Martin, D. & Shenoy, A. 2002. Zero shear viscosity of asphalt binders. *Transportation Research Record: Journal of the Transportation Research Board, 1810*, 54-62.

Anwar Parvez, M., Al-Mehthel, M., Al-Abdul Wahhab, H. I. & Hussein, I. A. 2014. Utilization of sulfur and crumb rubber in asphalt modification. *Journal of Applied Polymer Science, 131*.

Arambula, E., Masad, E. & Martin, A. E. 2007. Influence of air void distribution on the moisture susceptibility of asphalt mixes. *Journal of materials in civil engineering, 19*, 655.

Bahia, H. U., Hanson, D., Zeng, M., Zhai, H., Khatri, M. & Anderson, R. 2001. *Characterization of modified asphalt binders in superpave mix design*.

Biro, S., Gandhi, T. & Amirkhanian, S. 2009. Determination of zero shear viscosity of warm asphalt binders. *Construction and Building Materials, 23*, 2080-2086.

Branco, C. & Franco, V. T. 2013. *A unified method for the analysis of nonlinear viscoelasticity and fatigue cracking of asphalt mixtures using the dynamic mechanical analyzer.*

Bruno, L., Parla, G. & Celauro, C. 2012. Image analysis for detecting aggregate gradation in asphalt mixture from planar images. *Construction and Building Materials,* 28**,** 21-30.

Cai, W. 2013. *Discrete Element Modelling of constant strain rate and creep tests on a graded asphalt mixture.* Tesis para la obtención del grado de Doctor. Nottingham, The University of Nottingham.

Caro, S., Masad, E., Airey, G., Bhasin, A. & Little, D. 2008. Probabilistic analysis of fracture in asphalt mixtures caused by moisture damage. *Transportation Research Record: Journal of the Transportation Research Board,* 2057**,** 28-36.

Cavalcanti De Sousa, P. 2013. *Automated Protocol for the Analysis of Dynamic Mechanical Analyzer Date from Fine Aggregate Asphalt Mixes.*

Chen, J. S. & Peng, C. H. 1998. Analyses of tensile failure properties of asphalt-mineral filler mastics. *Journal of Materials in Civil Engineering,* 10**,** 256.

Cheung, C. & Cebon, D. 1997a. Deformation mechanisms of pure bitumen. *Journal of Materials in Civil Engineering,* 9**,** 117.

Cheung, C. & Cebon, D. 1997b. Experimental study of pure bitumens in tension, compression, and shear. *Journal of rheology,* 41**,** 45.

Cheung, C. Y. 1995. *"Mechanical behaviour of bitumens and bituminous mixes",* University of Cambridge.

Coenen, A. R., Kutay, M. E., Sefidmazgi, N. R. & Bahia, H. U. 2012. Aggregate structure characterisation of asphalt mixtures using two-dimensional image analysis. *Road Materials and Pavement Design,* 13**,** 433-454.

Collop, A., Cebon, D. & Hardy, M. 1995. Viscoelastic approach to rutting in flexible pavements. *Journal of Transportation Engineering,* 121**,** 82-93.

Collop, A. C., Airey, G. D. & Khanzada, S. 2002. Creep testing of bitumens using the dynamic shear rheometer. *International Journal of Pavement Engineering,* 3**,** 107-116.

Collop, A. C. & Khanzada, S. 2001. Permanent deformation in idealised "Sand Asphalt" bituminous mixtures. *Road Materials and Pavement Design,* 2**,** 7-28.

Collop, A. C., Mcdowell, G. R. & Lee, Y. W. 2006. Modelling dilation in an idealised asphalt mixture using discrete element modelling. *Granular Matter,* 8**,** 175-184.

Cross, M. M. 1965. Rheology of non-Newtonian fluids: a new flow equation for pseudoplastic systems. *Journal of Colloid Science,* 20**,** 417-437.

Cross, S. A. & Brown, E. R. 1992. Selection of aggregate properties to minimize rutting of heavy duty pavements. *Effects of aggregates and mineral fillers on asphalt mixture performance,* 1147**,** 45.

D'angelo, J., Kluttz, R., Dongre, R. N., Stephens, K. & Zanzotto, L. 2007a. Revision of the Superpave High Temperature Binder Specification: The Multiple Stress Creep Recovery Test (With Discussion). *Journal of the Association of Asphalt Paving Technologists,* 76.

D'angelo, J. A. & Dongre, R. N. 2007b. Creep and recovery. *Public roads,* 70.

D'angelo, J. 2010. New High-Temperature Binder Specification Using Multistress Creep and Recovery. *Development in Asphalt,* 1.

Daigle, M., Fratta, D. & Wang, L. Ultrasonic and X-ray tomographic imaging of highly contrasting inclusions in concrete specimens. 2005. Citeseer.

De Sousa, P. C. 2010. *AUTOMATED PROTOCOL FOR ANALYSIS OF DYNAMIC MECHANICAL ANALYZER DATA FROM FINE AGGREGATE ASPHALT MIXES.* Texas A&M University.

De Visscher, J. & Vanelstraete, A. 2004. Practical test methods for measuring the zero shear viscosity of bituminous binders. *Materials and Structures,* 37**,** 360-364.

Delgadillo, R. & Bahia, H. U. 2010. The relationship between nonlinearity of asphalt binders and asphalt mixture permanent deformation. *Road Materials and Pavement Design,* 11**,** 653-680.

Delgadillo, R., Cho, D. W. & Bahia, H. 2006a. Part 1: Bituminous Materials: Nonlinearity of Repeated Creep and Recovery Binder Test and Relationship with Mixture Permanent Deformation. *Transportation Research Record: Journal of the Transportation Research Board,* 1962**,** 3-11.

Delgadillo, R., Nam, K. & Bahia, H. 2006b. Why do we need to change G*/sinδ and how? *Road materials and pavement design,* 7**,** 7-27.

Deshpande, V. & Cebon, D. 1999. Steady-state constitutive relationship for idealised asphalt mixes. *Mechanics of materials,* 31**,** 271-287.

Deshpande, V. & Cebon, D. 2000. Uniaxial experiments on idealized asphalt mixes. *Journal of Materials in Civil Engineering,* 12**,** 262-271.

Desmazes, C., Lecomte, M., Lesueur, D. & Phillips, M. A protocol for reliable measurement of zero-shear-viscosity in order to evaluate the anti-rutting performance of binders. 2000. 202-211.

Dhawan, A. P., Huang, H. & Kim, D. S. 2008. *Principles and advanced methods in medical imaging and image analysis*, World Scientific Pub Co Inc.

Dubois, V., Roche, C. D. L. & Burban, O. 2010. Influence of the compaction process on the air void homogeneity of asphalt mixtures samples. *Construction and Building Materials,* 24**,** 885-897.

Dunhill, S. T., Airey, G. & Collop, A. 2002. *Quasi-static characterisation of asphalt mixtures*. University of Nottingham.

Elseifi, M. A., Mohammad, L. N., Kassem, E., Ying, H. & Masad, E. 2011. Quantification of damage in the dynamic complex modulus and flow number tests using X-ray computed tomography. *Journal of Materials in Civil Engineering,* 23**,** 1687-1696.

Erkens, S. 2002. Asphalt concrete response (ACRe). *Delft University of Technology, Delft.*

Faheem, A. F. & Bahia, H. U. 2010. Modelling of Asphalt Mastic in Terms of Filler-Bitumen Interaction. *Road Materials and Pavement Design,* 11**,** 281-303.

Faheem, A. F., Wen, H., Stephenson, L. & Bahia, H. U. 2008. Effect of Mineral Filler on Damage Resistance Characteristics of Asphalt Binders (With Discussion). *Journal of the Association of Asphalt Paving Technologists,* 77.

Garba, R. 2002. Permanent deformation properties of asphalt concrete mixtures.

Gaskins, F. H., Brodnyan, J. G., Philippoff, W. & Thelen, E. 1960. The rheology of asphalt. II. Flow characteristics of asphalt. *Journal of rheology,* 4**,** 265.

Gibb, J. 1996. *Evaluation of resistance to permanent deformation in the design of bituminous paving mixtures.* The University of Nottingham

Giuliani F., M., F., Antunes I. . Creep flow behavior of asphalt rubber binder - The zero shear viscosity analysis. Proceedings of the Asphalt rubber 25th– 27th October, 2006 2006 Palm Springs, California.

Golalipour, A. 2011. *Modification of Multiple Stress Creep and Recovery Test Procedure and Usage in Specification.* UNIVERSITY OF WISCONSIN.

Gu, X., Dong, Q. & Yuan, Q. 2014. Development of an Innovative Uniaxial Compression Test to Evaluate Permanent Deformation of Asphalt Mixtures. *Journal of Materials in Civil Engineering.*

Harris, B. M. & Stuart, K. D. 1995. ANALYSIS OF MINERAL FILLERS AND MASTICS USED IN STONE MATRIX ASPHALT (WITH DISCUSSION AND CLOSURE). *Journal of the Association of Asphalt Paving Technologists,* 64.

Hassan, N. A. 2012. *Microstructural Characterisation of Rubber Modified Asphalt Mixtures* PhD, The University of Nottingham.

Hassan, N. A., Airey, G. D., Khan, R. & Collop, A. C. 2012. Nondestructive Characterization of the Effect of Asphalt Mixture Compaction on Aggregate Orientation and Segregation Using X-ray Computed Tomography. *International Journal of Pavement Research & Technology,* 5.

Hesami, E., Birgisson, B. & Kringos, N. 2014. A new protocol for measuring bituminous mastic viscosity as a function of its filler concentration. *Road Materials and Pavement Design***,** 1-14.

Hofstra, A. & Klopm, A. Permanent deformation of flexible pavements under simulated road traffic conditions. Presented at the Third International Conference on the Structural Design of Asphalt Pavements, Grosvenor House, Park Lane, London, England, Sept. 11-15, 1972., 1972.

Hunter, A. E., Airey, G. D. & Collop, A. C. 2004. Aggregate orientation and segregation in laboratory-compacted asphalt samples. *Transportation Research Record: Journal of the Transportation Research Board,* 1891**,** 8-15.

Izadi, A., Bhasin, A. & Motamed, A. 2011. Designing Fine Aggregate Mixtures to Evaluate Fatigue Crack Growth in Asphalt Mixtures. Southwest Region University Transportation Center, Center for Transportation Research, University of Texas at Austin.

Kandhal, P. S. & Mallick, R. B. 2001. Effect of mix gradation on rutting potential of dense-graded asphalt mixtures. *Transportation Research Record: Journal of the Transportation Research Board,* 1767**,** 146-151.

Kassem, E., Masad, E., Lytton, R. & Chowdhury, A. 2011. Influence of air voids on mechanical properties of asphalt mixtures. *Road Materials and Pavement Design,* 12**,** 493-524.

Kavussi, A. & Hicks, R. 1997. Properties of bituminous mixtures containing different fillers. *Journal of the Association of Asphalt Paving Technologists,* 66.

Ketcham, R. A. & Carlson, W. D. 2001. Acquisition, optimization and interpretation of X-ray computed tomographic imagery: applications to the geosciences. *Computers & Geosciences,* 27**,** 381-400.

Khan, R. 2010. *Quantification of microstructural damage in asphalt.* University of Nottingham.

Khan, R. & Collop, A. C. 2010. The use of X-ray computed tomography to characterize microdamage in asphalt. *Road Materials and Pavement Design,* 11**,** 89-109.

Khanzada, S. 2000. *Permanent Deformation in Bituominous Mixtures.* PhD PhD Thesis, Nottingham University

Kim, Y.-R., Little, D. & Lytton, R. 2003. Fatigue and healing characterization of asphalt mixtures. *Journal of Materials in Civil Engineering,* 15**,** 75-83.

Kim, Y. R., Kim, N. & Khosla, N. P. 1992. Effect of aggregate type and gradation on fatigue and permanent deformation of asphalt concrete. *Effects of aggregates and mineral fillers on asphalt mixture performance,* 1147**,** 310.

Kutay, M. E., Arambula, E., Gibson, N. & Youtcheff, J. 2010. Three-dimensional image processing methods to identify and characterise aggregates in compacted asphalt mixtures. *International Journal of Pavement Engineering,* 11**,** 511-528.

Le Hir, Y., Anderson, D., Plache, J., Martin, D. & Partl, M. Rheological characterization of bituminous binder to predict pavement rutting. Sixth International RILEM Symposium on Performance Testing and Evaluation of Bituminous Materials, 2003. RILEM Publications SARL, 117-123.

Liao, M.-C. 2007. *Small and Large Strain Rheological and Fatigue Characterisation of Bitumen-Filler Mastics.* PhD PhD Thesis, Nottingham University

Liao, M. C. & Chen, J. S. 2011. Zero Shear Viscosity of Bitumen-Filler Mastics. *Journal of Materials in Civil Engineering,* 23**,** 1672.

Lo Presti, D., Hassan, N., Khan, R. & Airey, G. 2014. Reclaimed asphalt test specimen preparation assisted by image analysis. *Journal of Materials in Civil Engineering*.

Lundy, J. R. & Sandoval-Gil, J. A. 2004. Permanent Deformation Characteristics of Oregon Mixes Using the Asphalt Pavement Analyzer.

Masad, E., Jandhyala, V., Dasgupta, N., Somadevan, N. & Shashidhar, N. 2002a. Characterization of air void distribution in asphalt mixes using X-ray computed tomography. *Journal of materials in civil engineering,* 14**,** 122-129.

Masad, E., Muhunthan, B., Shashidhar, N. & Harman, T. 1999a. Internal structure characterization of asphalt concrete using image analysis. *Journal of computing in civil engineering,* 13**,** 88.

Masad, E. & Somadevan, N. 2002b. Microstructural finite-element analysis of influence of localized strain distribution on asphalt mix properties. *Journal of engineering mechanics,* 128**,** 1105-1114.

Masad, E. A., Huang, C.-W., Dangelo, J. & Little, D. N. 2009. Characterization of asphalt binder resistance to permanent deformation based on nonlinear viscoelastic analysis of multiple stress creep recovery (MSCR) test. *Journal of the Association of Asphalt Paving Technologists,* 78.

Masad, E. A., Little, D. N., Tashman, L., Saadeh, S., Al-Rousan, T. & Sukhwani, R. 2003. Evaluation of aggregate characteristics affecting HMA concrete performance.

Morea, F., Agnusdei, J. & Zerbino, R. 2010. Comparison of methods for measuring zero shear viscosity in asphalts. *Materials and Structures,* 43**,** 499-507.

Motamed, A., Bhasin, A. & Liechti, K. M. 2012. Interaction nonlinearity in asphalt binders. *Mechanics of Time-Dependent Materials,* 16**,** 145-167.

Muraya, P. M. 2007. Permanent deformation of asphalt mixes.

Offrell, P. & Magnusson, R. 2004. In Situ Photographic Survey of Crack Propagation in Flexible Pavements. *International Journal of Pavement Engineering,* 5**,** 91-102.

Onifade, I., Jelagin, D., Guarin, A., Birgisson, B. & Kringos, N. 2013. Asphalt Internal Structure Characterization with X-Ray Computed Tomography and Digital Image Processing. *Multi-Scale Modeling and Characterization of Infrastructure Materials.* Springer.

Osman, S. 2004. *The Role of Bitumen and Bitumen/Filler Mortar in Bituminous Mixture Fatique* PhD PhD Thesis Nottignham University

Ossa, E. A. 2005. Deformation behaviour of bitumen and bituminous mixes.

Poel, V. & Der, C. 1954. A general system describing the visco-elastic properties of bitumens and its relation to routine test data. *Journal of Applied Chemistry,* 4**,** 221-236.

Qiao, Y., Flintsch, G. W., Dawson, A. R. & Parry, T. 2013. Examining Effects of Climatic Factors on Flexible Pavement Performance and Service Life. *Transportation Research Record: Journal of the Transportation Research Board,* 2349**,** 100-107.

Rahimzadeh, B. 2002. *LINEAR AND NON-LINEAR VISCOELASTIC BEHAVIOUR OF BINDERS AND ASPHALTS.* PhD PhD thesis, Nottingham University

Rahmani, E., Darabi, M. K., Abu Al-Rub, R. K., Kassem, E., Masad, E. A. & Little, D. N. 2013. Effect of confinement pressure on the nonlinear-viscoelastic response of asphalt concrete at high temperatures. *Construction and Building Materials,* 47**,** 779-788.

Razavi, M. R. 2006. *Characterization of microstructure and internal displacement field of sand using X-ray computed tomography.* WASHINGTON STATE UNIVERSITY.

Read, J. & Whiteoak, D. 2003. *The Shell bitumen handbook*, Thomas Telford.

Rigden, P. 1947. The use of fillers in bituminous road surfacings. A study of filler-binder systems in relation to filler characteristics. *Journal of the Society of Chemical Industry,* 66**,** 299-309.

Romero, P. & Masad, E. 2001. Relationship between the representative volume element and mechanical properties of asphalt concrete. *Journal of materials in civil engineering,* 13**,** 77.

Saadeh, S. a. R. 2005. *Characterization of asphalt concrete using anisotropic damage viscoelastic-viscoplastic model.* Texas A&M University.

Santagata, E., Baglieri, O., Dalmazzo, D. & Tsantilis, L. 2013. Evaluation of the anti-rutting potential of polymer-modified binders by means of creep-recovery shear tests. *Materials and structures,* 46**,** 1673-1682.

Science, R. 2014. Available: http://www.roadscience.net/services/distress-guide.

Shashidhar, N. & Romero, P. 1998. Factors affecting the stiffening potential of mineral fillers. *Transportation Research Record: Journal of the Transportation Research Board,* 1638**,** 94-100.

Shenoy, A. 2002. Estimating the Unrecovered Strain During a Creep Recovery Test from the Material's Volumetric-flow Rate. *International Journal of Pavement Engineering,* 3**,** 29-34.

Soenen, H. & Teugels, W. Rheological investigation on binder-filler interactions. Eurobitume Workshop, 1999.

Suo, Z. & Wong, W. G. 2009. Nonlinear properties analysis on rutting behaviour of bituminous materials with different air void contents. *Construction and Building materials,* 23**,** 3492-3498.

Synolakis, C. E., Zhou, Z. & Leahy, R. M. 1996. Determination of internal deformation field in asphalt cores using X-ray computer tomography. *Transportation Research Record: Journal of the Transportation Research Board,* 1526**,** 135-141.

Taherkhani, H. 2006. *Experimental Characterisation of the Compressive Permanent Deformation Behaviour in Asphaltic Mixtures*. PhD Thesis, Nottingham University

Tashman, L. 2003. *Microstructural viscoplastic continuum model for asphalt concrete*. Texas A&M University.

Tashman, L., Masad, E., D'angelo, J., Bukowski, J. & Harman, T. 2002. X-ray tomography to characterize air void distribution in superpave gyratory compacted specimens. *International Journal of Pavement Engineering,* 3**,** 19-28.

Tashman, L., Masad, E., Little, D. & Lytton, R. 2004. DAMAGE EVOLUTION IN TRIAXIAL COMPRESSION TESTS OF HMA AT HIGH TEMPERATURES (WITH DISCUSSION). *Journal of the Association of Asphalt Paving Technologists,* 73.

Tashman, L., Masad, E., Peterson, B. & Saleh, H. 2001. INTERNAL STRUCTURE ANALYSIS OF ASPHALT MIXES TO IMPROVE THE SIMULATION OF SUPERPAVE GYRATORY COMPACTION TO FIELD CONDITIONS (WITH DISCUSSION). *Journal of the Association of Asphalt Paving Technologists,* 70.

Tashman, L., Wang, L. & Thyagarajan, S. 2007. Microstructure characterization for modeling HMA behaviour using imaging technology. *Road materials and pavement design,* 8**,** 207-238.

Taylor, R. & Airey, G. 2010. Influence of surface interactions between bitumen and mineral fillers on the rheology of bitumen-filler mastics. *Efficient Transportation and Pavement Systems: Characterization, Mechanisms, Simulation, and Modeling***,** 453.

Thyagarajan, S., Tashman, L., Masad, E. & Bayomy, F. 2010. The heterogeneity and mechanical response of hot mix asphalt laboratory specimens. *International Journal of Pavement Engineering,* 11**,** 107-121.

Traxler, R., Baum, L. & Pittman, C. 1933. Experimental Determination of Void Content of Close-Packed Mineral Powders. *Industrial & Engineering Chemistry Analytical Edition,* 5, 165-168.

Traxler, R. N. a. M., J.S. 1936. Mineral Powders, Their Physical Properties and

Stabilizing Effects. *Proceedings of the Association of Asphalt Paving*

Technologies, 7.

Tsai, D.-M. 1995. A fast thresholding selection procedure for multimodal and unimodal histograms. *Pattern Recognition Letters,* 16, 653-666.

Underwood, B. S. & Kim, Y. R. 2013. Microstructural investigation of asphalt concrete for performing multiscale experimental studies. *International Journal of Pavement Engineering,* 14, 498-516.

Vlachovicova, Z., Wekumbura, C., Stastna, J. & Zanzotto, L. 2007. Creep characteristics of asphalt modified by radial styrene–butadiene–styrene copolymer. *Construction and Building Materials,* 21, 567-577.

Wang 2001. *Mechanics of asphalt,* New York, The McGraw-Hill Companies,.

Wang, H., Al-Qadi, I. L., Faheem, A. F., Bahia, H. U., Yang, S. H. & Reinke, G. H. 2011. Effect of Mineral Filler Characteristics on Asphalt Mastic and Mixture Rutting Potential. *Transportation Research Record: Journal of the Transportation Research Board,* 2208, 33-39.

Wang, L. 2010. *Mechanics of Asphalt: Microstructure and Micromechanics,* US, McGraw-Hill Professional.

Wang, L., Paul, H. S., Harman, T. & D'angelo, J. 2004. CHARACTERIZATION OF AGGREGATES AND ASPHALT CONCRETE USING X-RAY COMPUTERIZED TOMOGRAPHY-A STATE OF THE ART REPORT (WITH DISCUSSION). *Journal of the Association of Asphalt Paving Technologists,* 73.

Wasage, T., Stastna, J. & Zanzotto, L. 2011. Rheological analysis of multi-stress creep recovery (MSCR) test. *International Journal of Pavement Engineering,* 12, 561-568.

Woldekidan, M. F. 2011. *Response Modelling of Bitumen, Bituminous Mastic and Mortar*, PhD Dissertation, Delft University of Technology, The Netherlands.

Yusoff, N. I. M., Shaw, M. T. & Airey, G. D. 2011. Modelling the linear viscoelastic rheological properties of bituminous binders. *Construction and Building Materials,* 25**,** 2171-2189.

Zelelew, H., Almuntashri, A., Agaian, S. & Papagiannakis, A. 2013. An improved image processing technique for asphalt concrete X-ray CT images. *Road Materials and Pavement Design,* 14**,** 341-359.

Zelelew, H. & Papagiannakis, A. 2011. A volumetrics thresholding algorithm for processing asphalt concrete X-ray CT images. *International journal of pavement engineering,* 12**,** 543-551.

Zelelew, H. M. 2008. *Simulation of the permanent deformation of asphalt concrete mixtures using discrete element method (DEM).* Washington State University.

Zollinger, C. J. 2005. *Application of surface energy measurements to evaluate moisture susceptibility of asphalt and aggregates.* M.Sc. Thesis, Texas A&M University.

Zoorob, S., Castro-Gomes, J., Pereira Oliveira, L. & O'connell, J. 2012. Investigating the Multiple Stress Creep Recovery bitumen characterisation test. *Construction and Building Materials,* 30**,** 734-745.

Appendix A

The procedure of determining Burger's model parameters using Simulink Design Optimization (SDO) is detailed. SDO is a Matlab product that offers an easy and quick regression process to fit experimental data for simulation purposes. The creep and creep recovery experimental results of B, M35, M50, and M65 were simulated at 10, 30, and 50°c using the generalized Burger's model built into SDO. Only one set of parameters for each material is utilised to fit both the creep and creep recovery results at each temperature. Although not used, SDO can transfer between time domain and frequency domain configurations as well as different loading configurations. The followed procedural steps are:

A. Building model

1. Open Semiscape and drag the following blocks from the library:

Mass, Pulse Generator, Simulink-PS Convertor, Ideal Force Source, Mechanical Translational Reference, Ideal Translational Reference, Ideal Translational Motion Sensor, PS-Simulink Convertor, Position, Output Position, Translation Damper, Translation Spring, Solver Configuration, Mechanical Translation Reference.

2. Connect all blocks as shown in Figure 1.
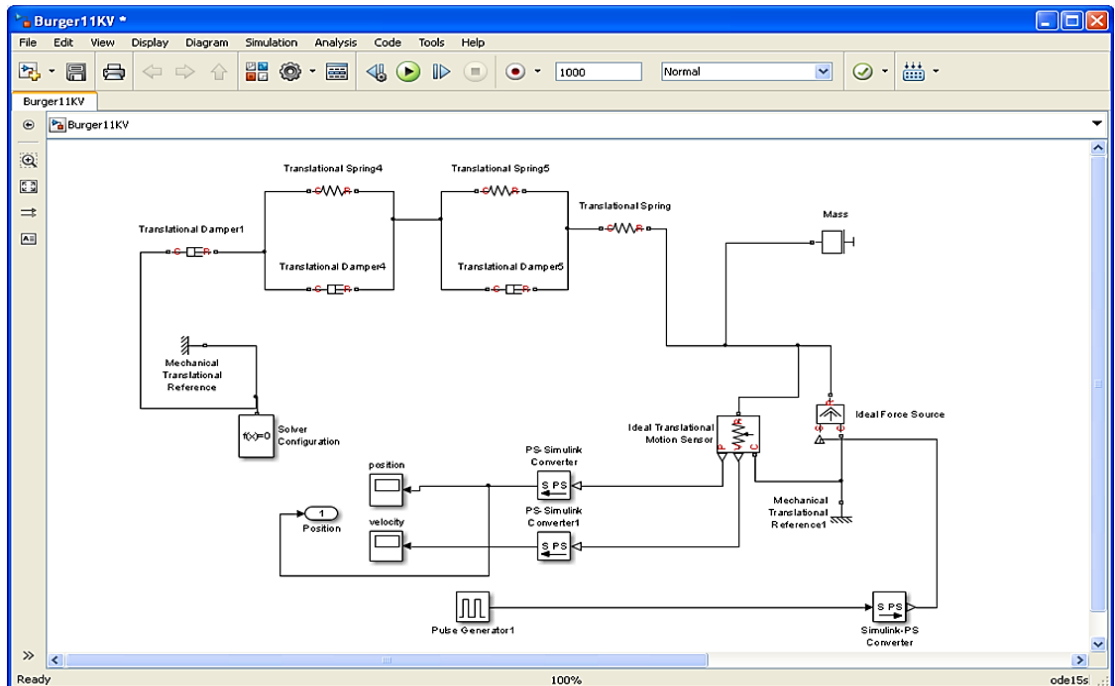
Figure 1 Assembled blocks in SDO

3. Double click on the *Translation Spring* and *Translation Damper* and insert the parameters names of the springs and damper coefficients respectively. On Matlab command prompt insert new variables and name them as previously specified.

4. Double click on the *Pulse Generator*, change time range and signal profile according to the required experimental test, as shown in Figure 2 unit signal is equivalent to 1 kPa.
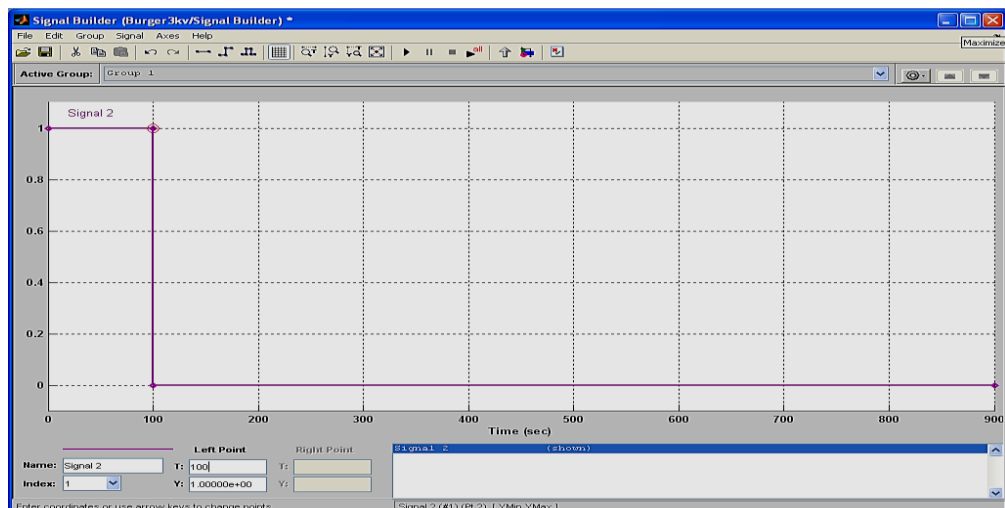
Figure 2 Signal configuration

5. To make sure the model is built correctly click ▶ and double click on *position* to display the simulation result, as displayed in Figure 3.
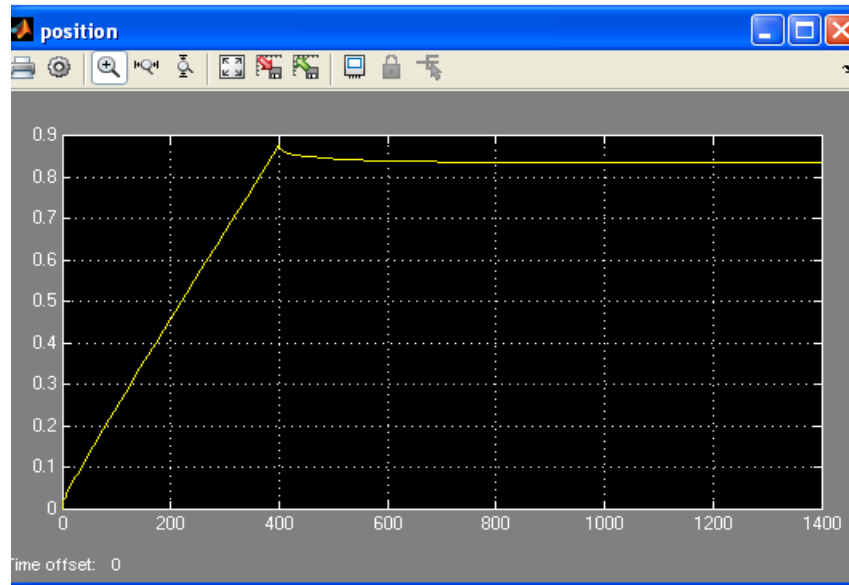
Figure 3 Signal output test

B. Import data

1. To start a new estimation project click **Analysis > Parameter Estimation** in the model window (Figure 4).
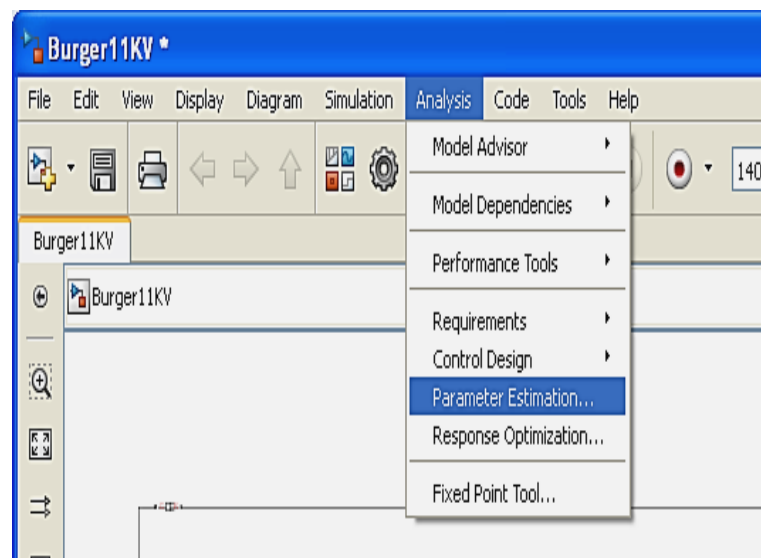
Figure 4 Starting parameter estimation

2. A new window 'Control and Estimation Tools Manager' will appear, select '**Transient Data**' and then click **New**, (Figure 5).
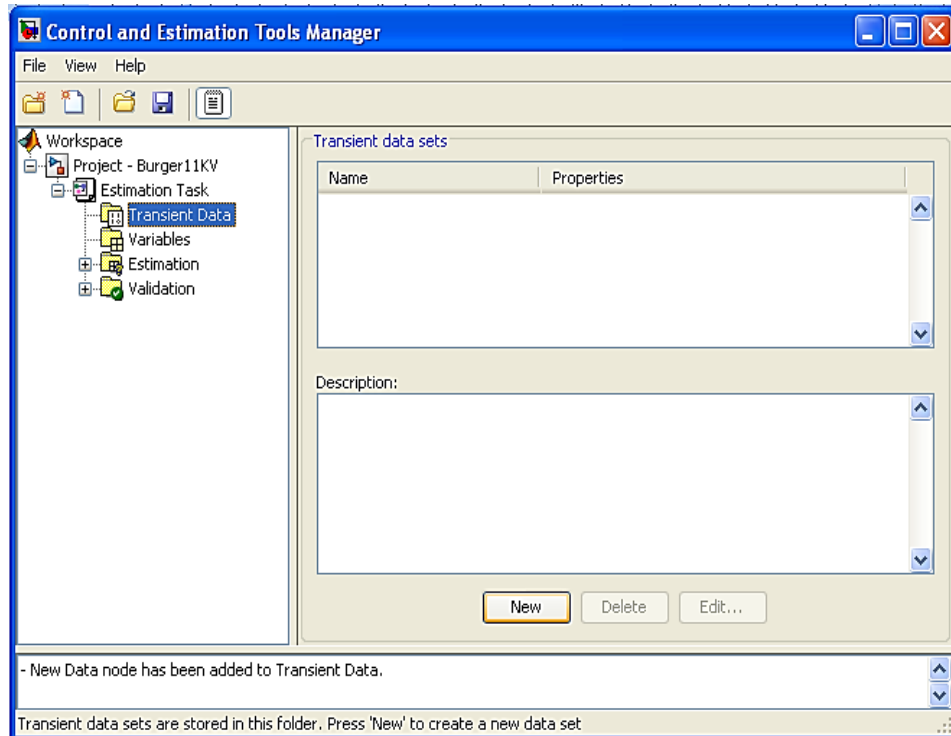
Figure 5 Opening a new estimation project

3. **New Data** icon will appear under **Transient Data**, select **Output Data** tab.

4. Right click on the **Output Data** cell and select **Import**, (Figure 6). Insert strain values in this cell. Similarly, import time data on the **Time/Ts** cell.
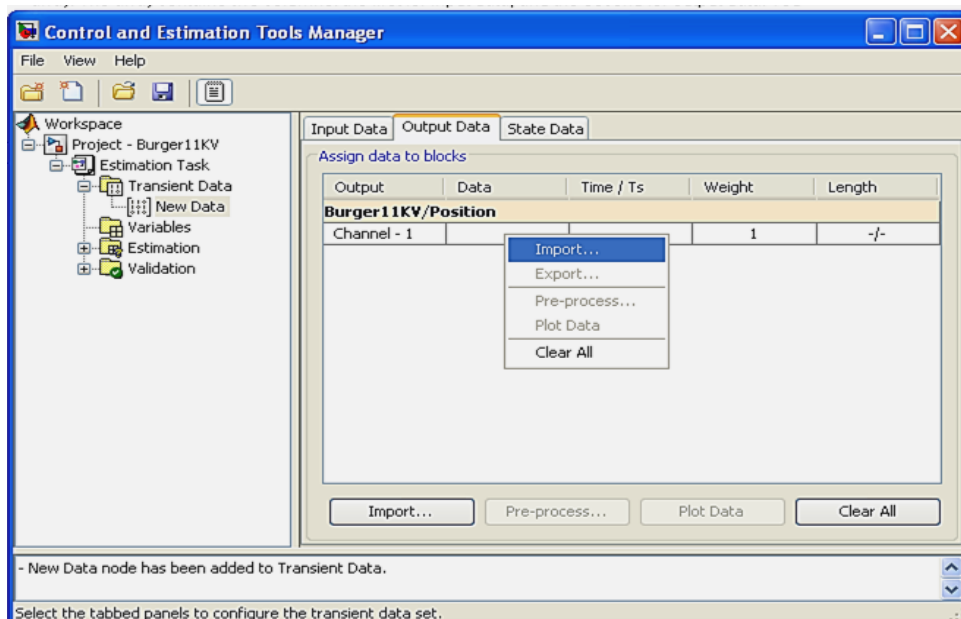
Figure 6 Importing experimental data

5. If some data require pre-processing or to check the imported data click on **Pre-processing** and **Plot Data** respectively. A plot of imported data will be displayed as shown in Figure 7.
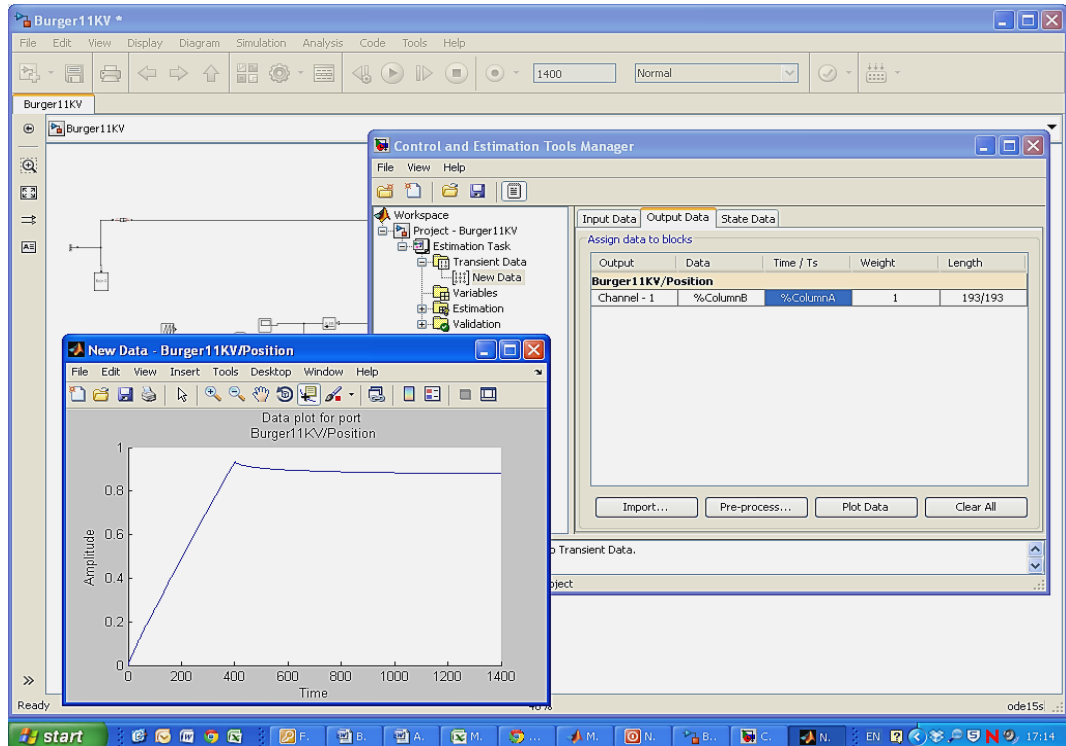
Figure 7 Plotting experimental data

6. To add the model parameters (Spring and Dashpot coefficients) select **Variables**, click **Add** button, model parameters names will appear (Figure 8). Select them all and click **Add**. To accelerate estimation enter '0' value in the **Minimum** tab under **Default** Settings for each parameter (Figure 9).
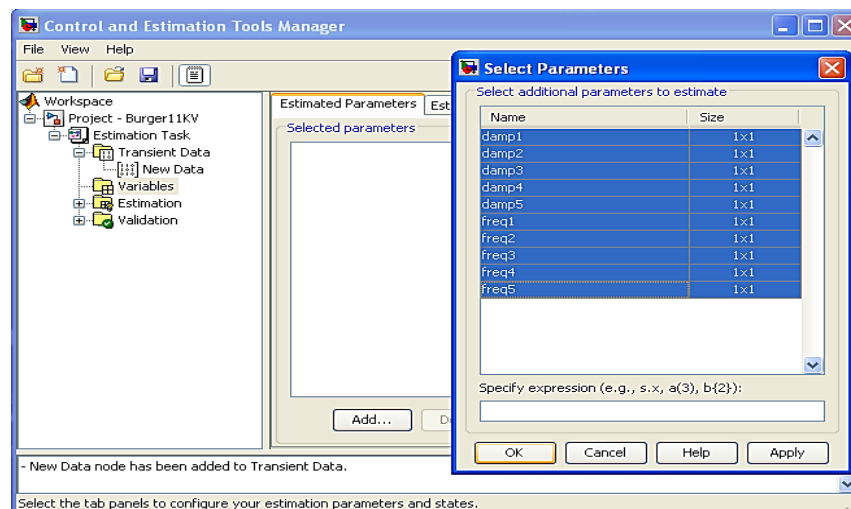
Figure 8 Selecting parameters
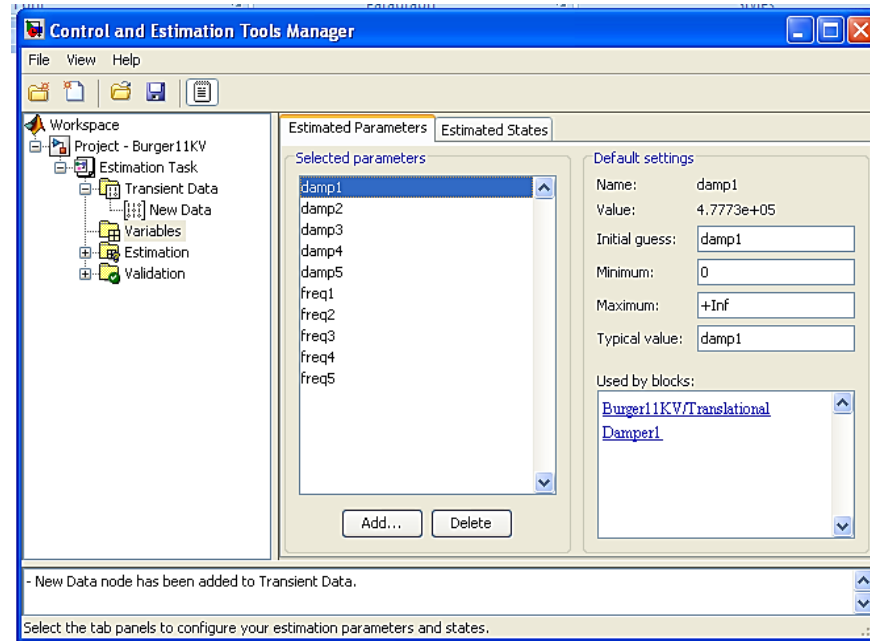
Figure 9 Specifying each parameter estimation boundary

C. Start Simulation

1. To start estimation, right-click on the **Estimation** node and click on **New** (Figure 10).
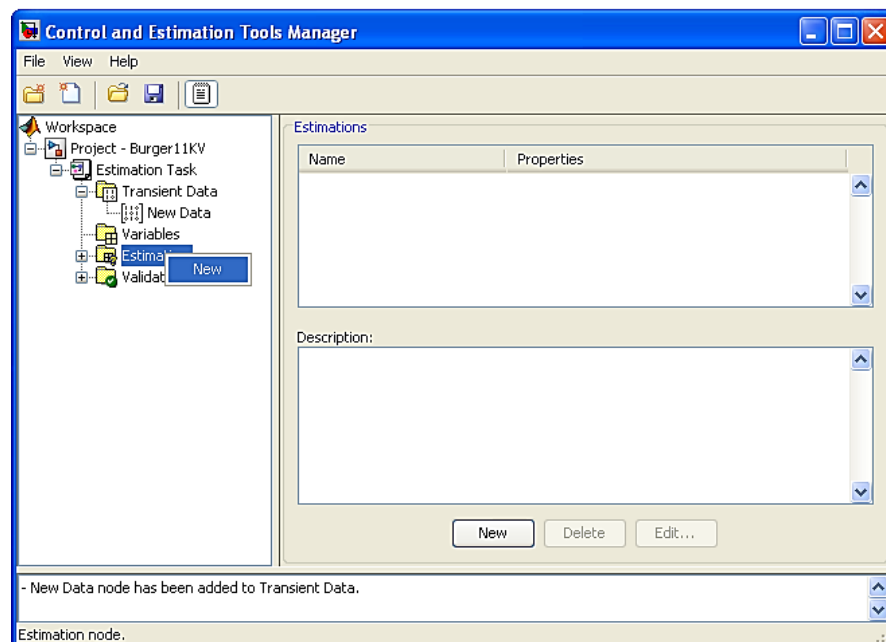
Figure 10 Opening new estimation window

2. Select the **New Estimation** node then tick on the **New Data** (Figure 10).
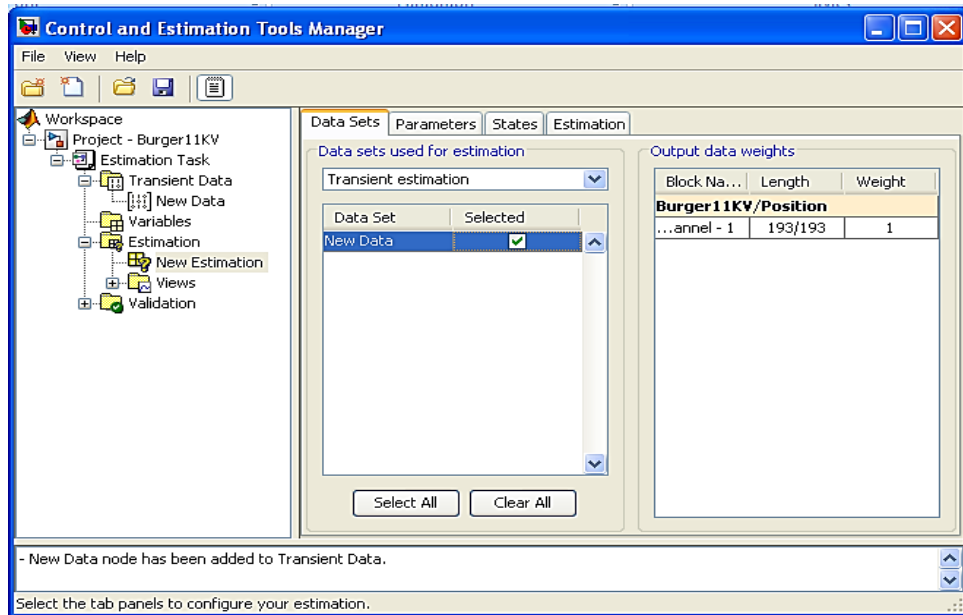
Figure 10 Selecting estimation parameter set

3. Under '**Parameter'** tab tick all boxes under (Figure 11).
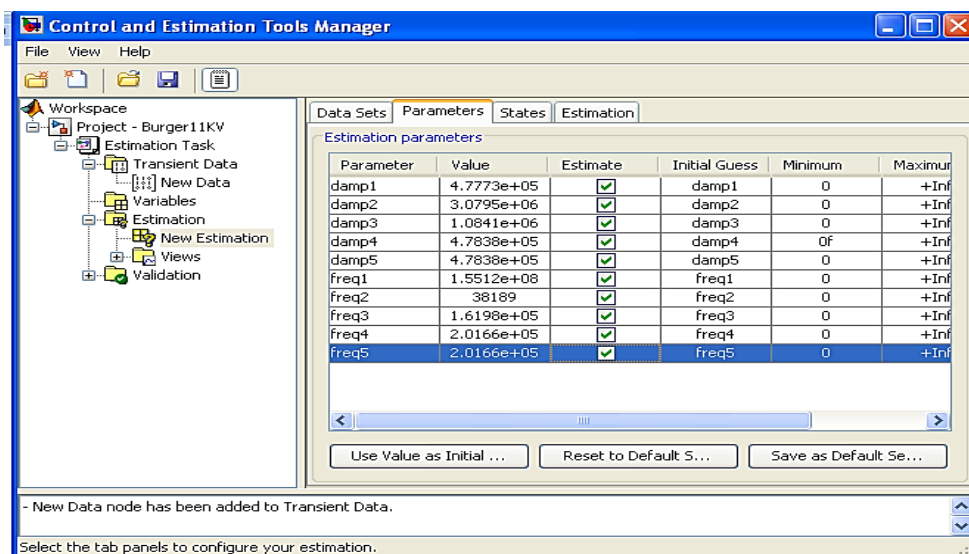
Figure 11 Selecting parameters to estimate

4. Click **Estimation option** under **Estimation** tab, and then select the required **Optimization Method** after clicking on **Optimization Options**. Reduce the **Parameter tolerance** and **function tolerance** to 0.000000001 or less to increase accuracy. Click **OK** and tick on Show progress views, then click on **Start** button to start estimation.
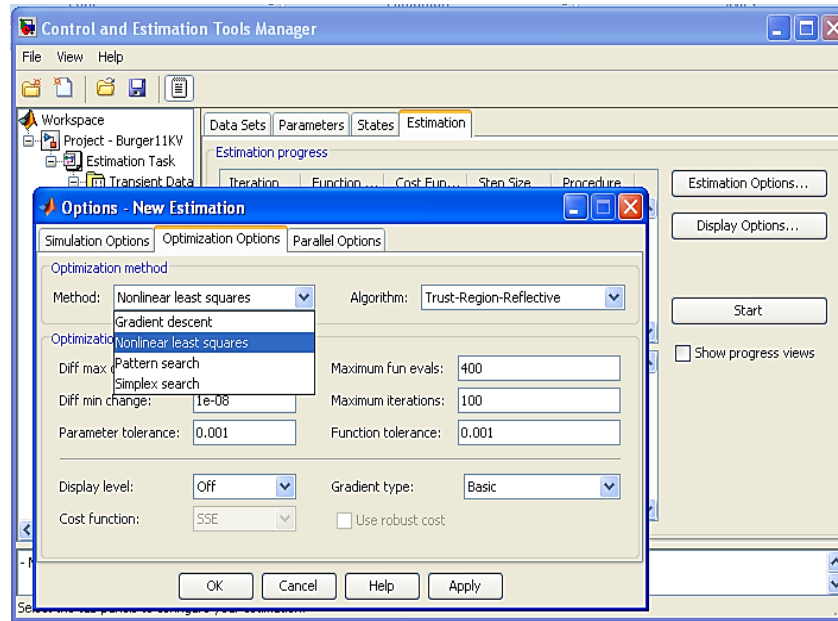
Figure 12 Optimization method selection

5. The estimation will prompt two updated graphs, one showing the **Measured and simulated** data and **the Trajectory of estimated parameter** (Figure 13).
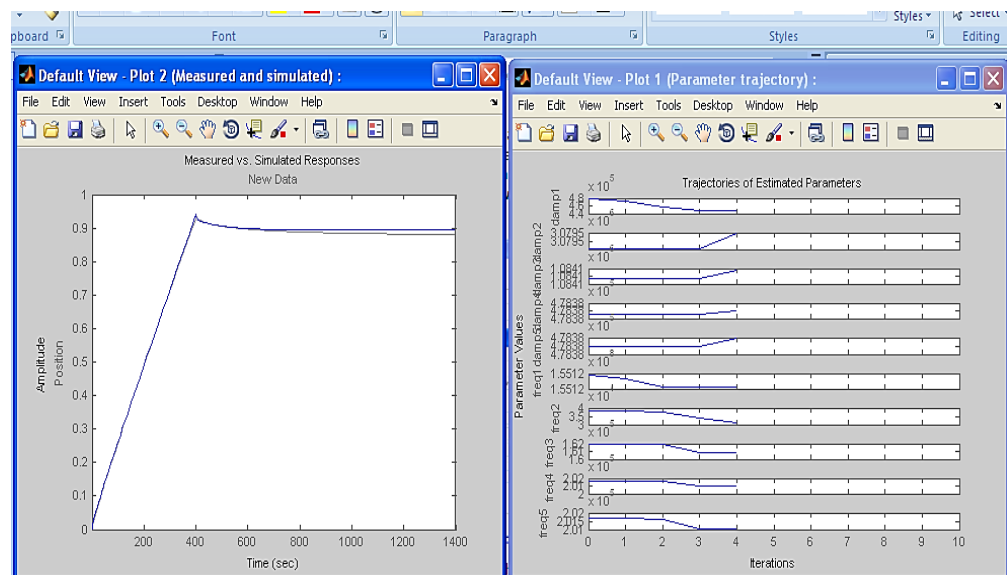
Figure 13 Plots of estimated parameters and their trajectories

6. Once the estimation is completed but was not satisfactory, either rerun the estimation by clicking **Start** button again which will use new values of parameters as initial guesses, or change the estimation method.

For a given set of experimental data comprising strain change with time, initial estimation of parameters is selected manually with a single Kelvin

model. Then by selecting 'Simple search' method the estimation with a minimum 'Zero' value of parameters is performed. To reach the required initial value, estimation options were maximised through maximizing the number of iterations and minimizing the function/parameters tolerance. The estimation is stopped when reasonable agreement is observed.

Once the optimization stopped, the estimation function was altered to 'Nonlinear least square' with parameters initial values obtained from the previous step. The 'Nonlinear least square' utilises the 'Isqnonlin' Matlab built-in function to minimize the error between the input data and model output for all time steps from 0 to t final.

For 'n' data points (t_1, ε_1) , (t_2, ε_2)... (t_n, ε_n), and with 'm' number of model parameters the model function can be identified as

$$\varepsilon = f(t, P)$$

Where t is the time, P is the vector of model parameters (damper and spring).

The objective is to find vector P of model parameters based on minimizing the sum of square error, given by:

$$min(S) = \sum_{i=1}^{n} r_i^2$$

Where $r_i = \varepsilon_i - f(t_i, P)$, is the residual error for $i = 1$ to n. The minimum is found when the gradient $\frac{dS}{dP} = 0$.

If the estimation was not enough after several trials, recognised graphically by no change in parameter values or a fixed cost function the number of Kelvin model was increased.

D. Validate estimation

After estimation is satisfactory completed a validation on another set of experimental data with the same obtained parameters values within the same temperature is performed. The validation steps involve:

1. First of all import the data set under the **Transient data** node by following same steps mentioned in importing the first set of experimental data.

2. In the **Workspace** tree add a **New Validation** by right-click on **Validation** and select **New** (Figure 14)
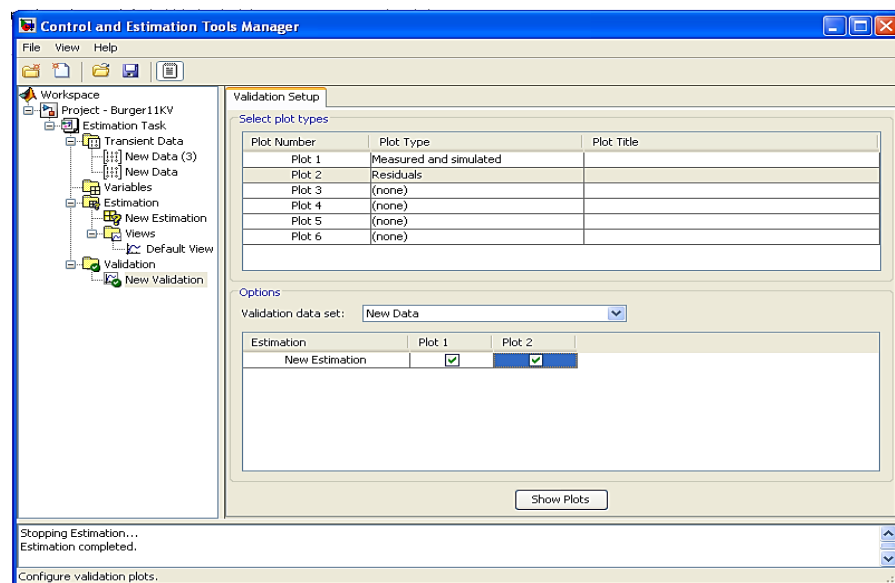
Figure 14 Opening new validation process

3. Click on **Show Plots** to compare validation data against model response, and the residual between them in two figures (Figure 15).
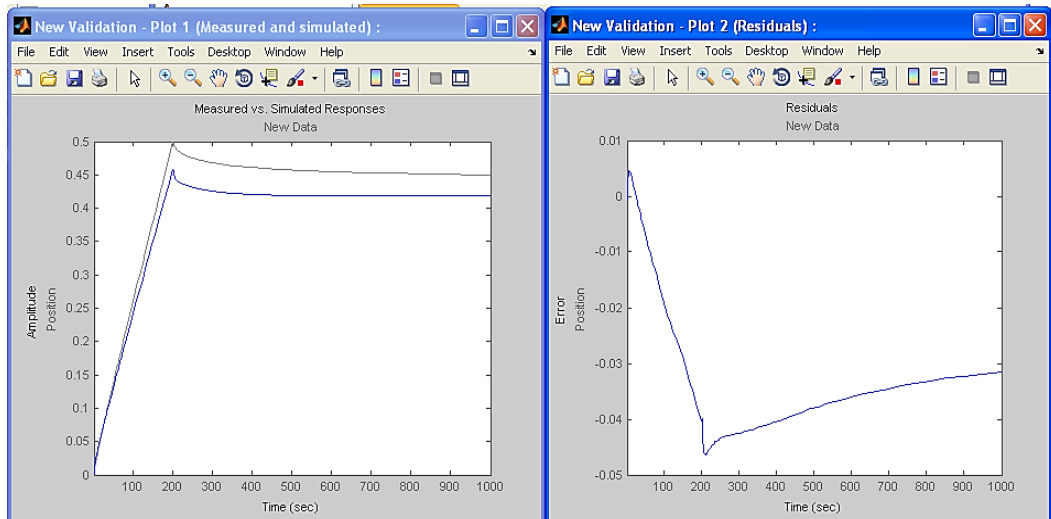
Figure 15 Plots of the validation data and the residuals

4. If the residual was considerably large, rerun the estimation again but with the new validation data set and with reducing the number of variables, i.e., allow only Kelvin model to change and fix the Maxwell parameters.

The following are illustration figures of experimental data simulation of creep and creep recovery. Experimental data are plotted by lines while the model is in dots form.
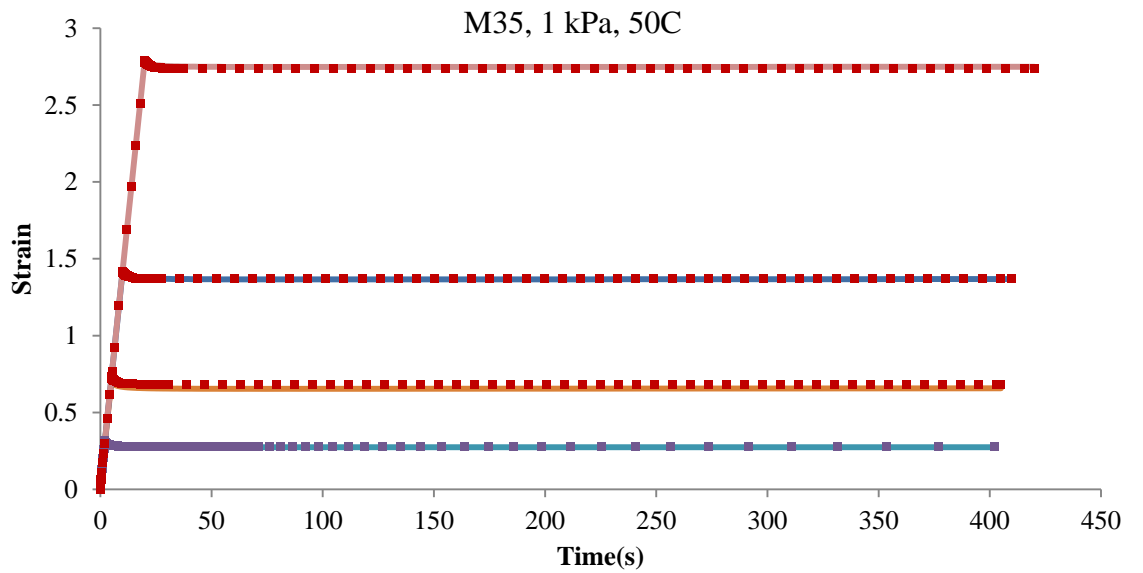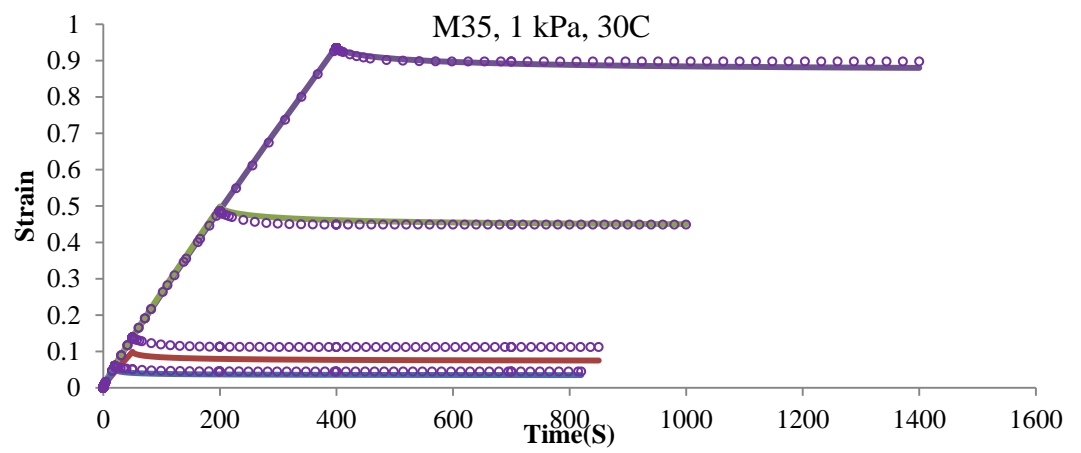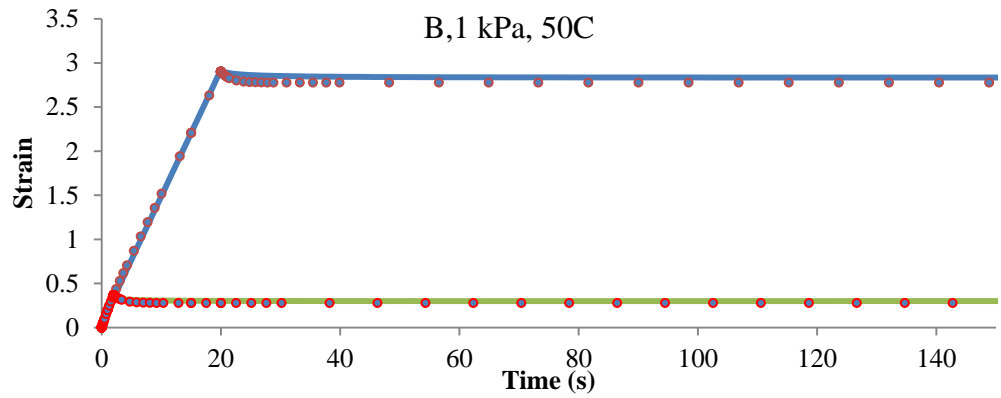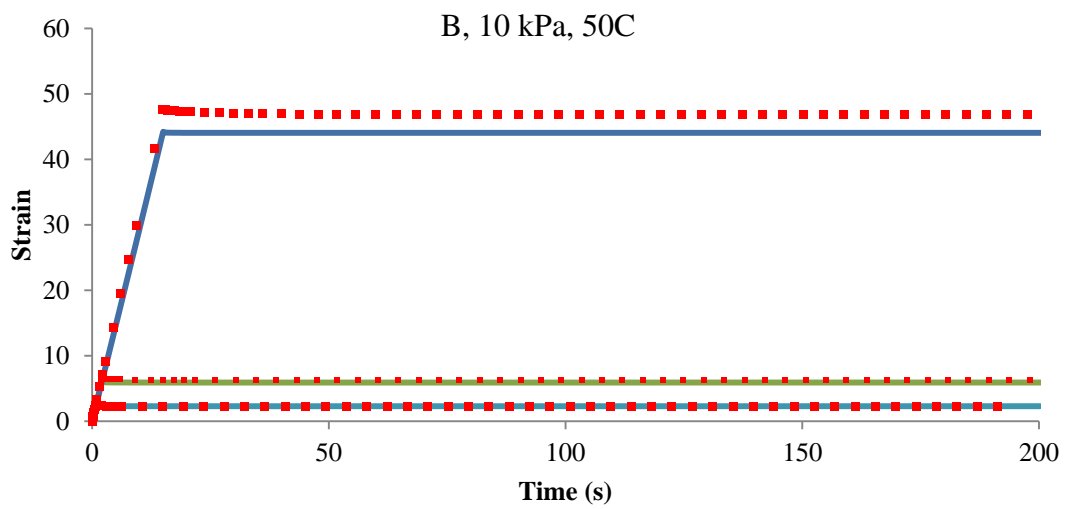
A. <u>Creep test</u>
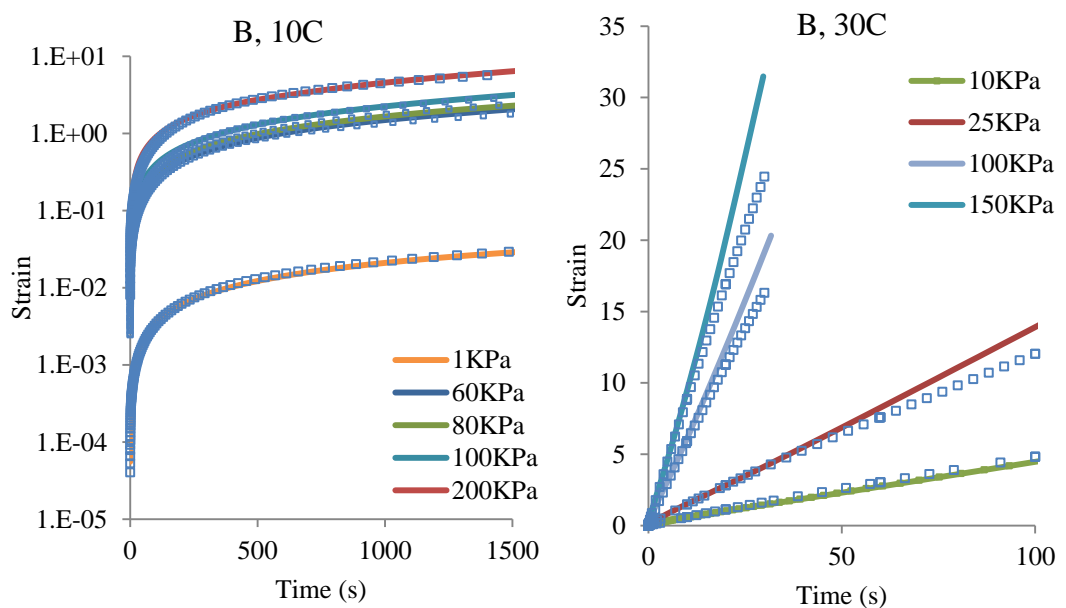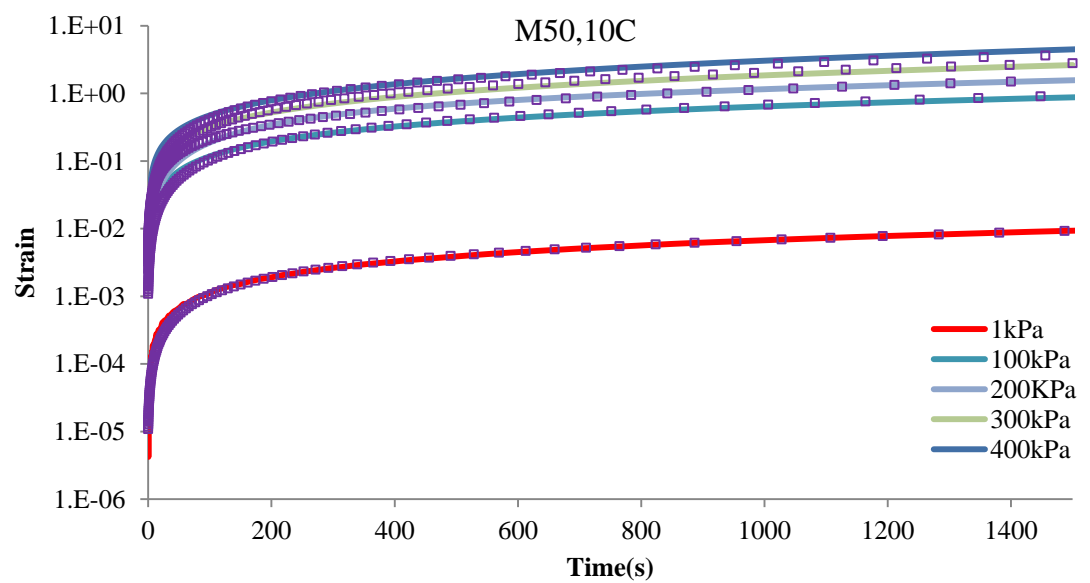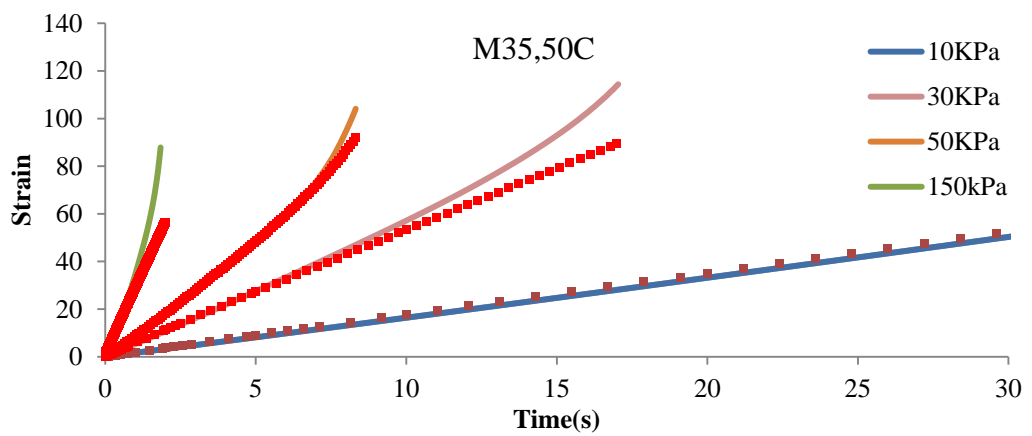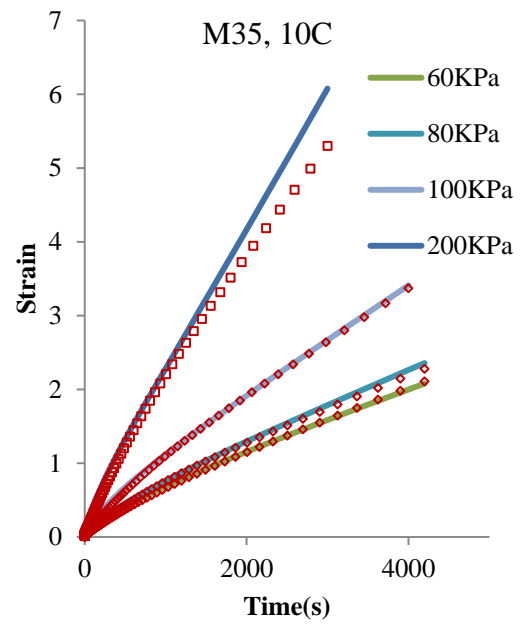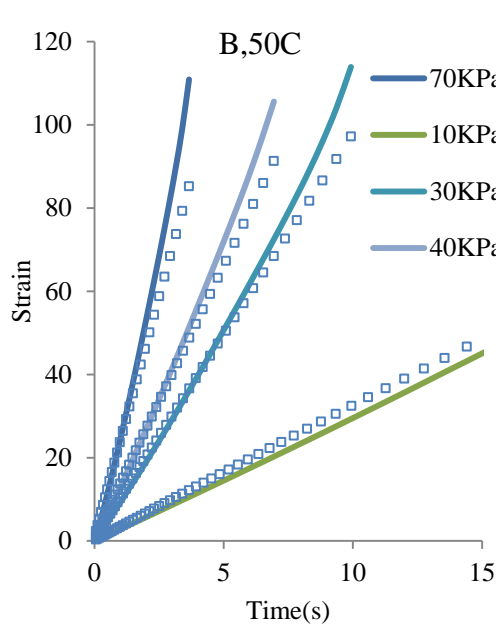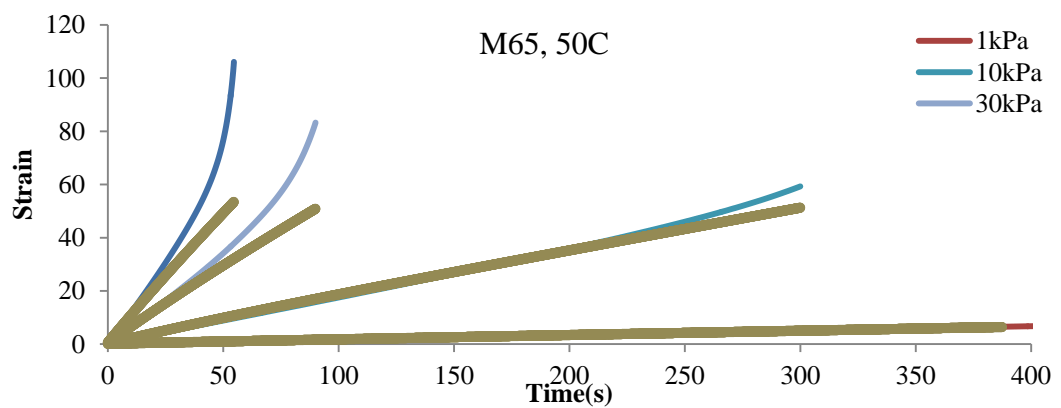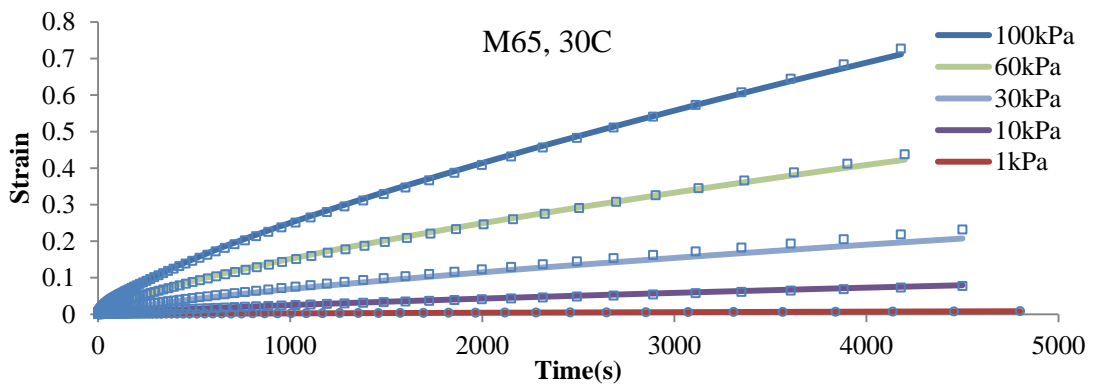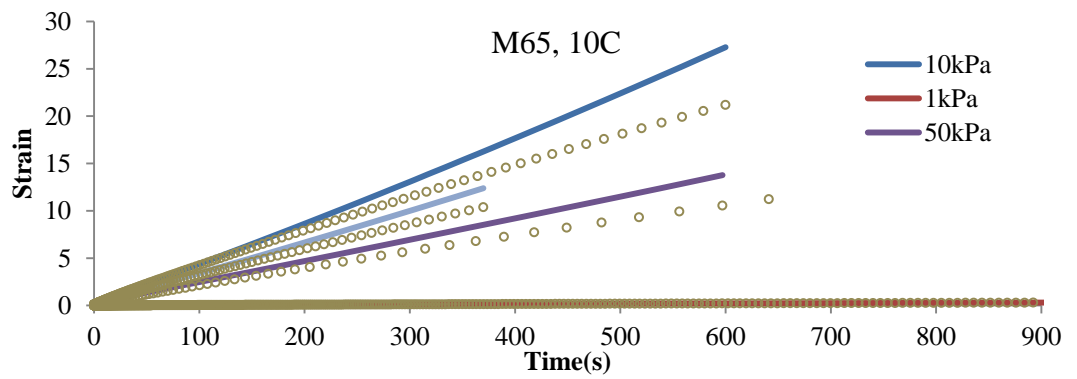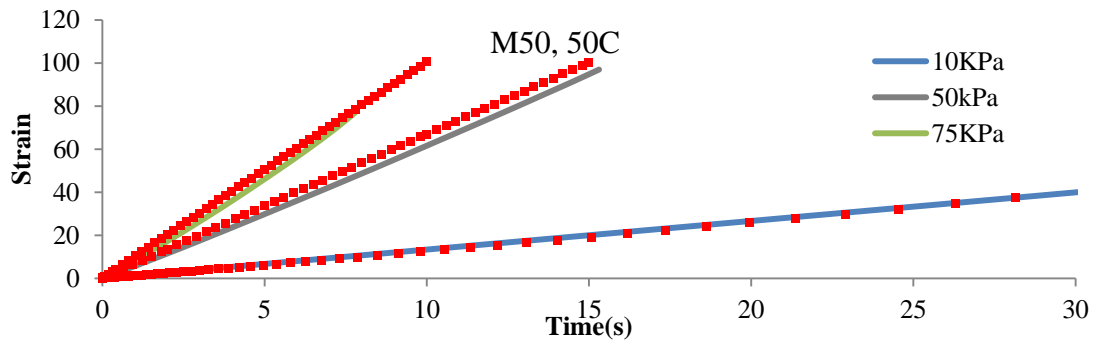
B. Single creep recovery simulation

B,1 kPa, 50C

M35, 1 kPa, 30C

M35, 1 kPa, 50C

M50, 1 kPa, 50C

M50, 1 kpa, 30C

B, 10 kPa, 50C

M35, 10 kPa, 30C

M50, 10 kPa, 30C

M35,10 kPa, 50C
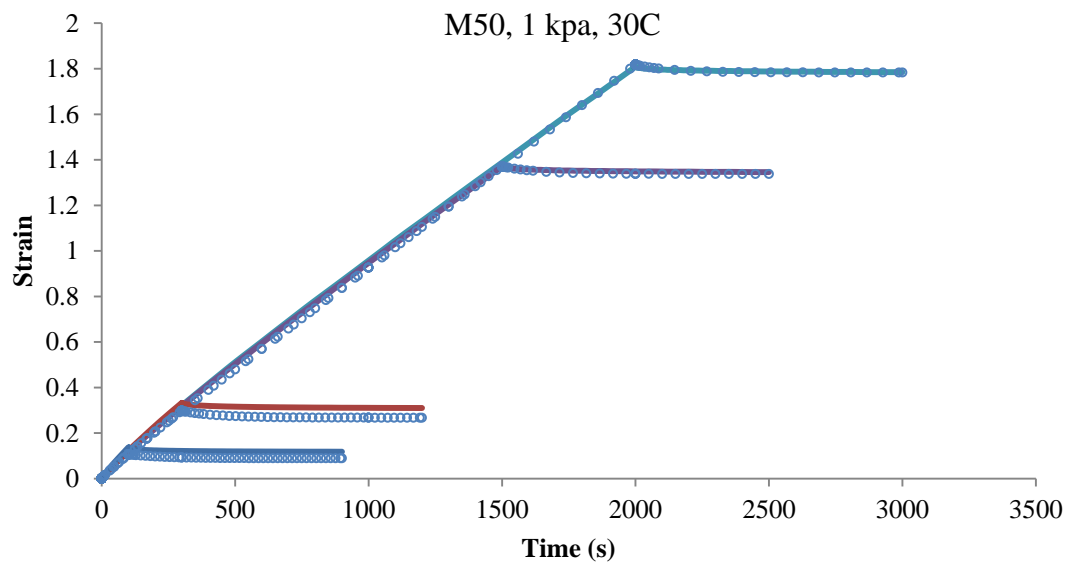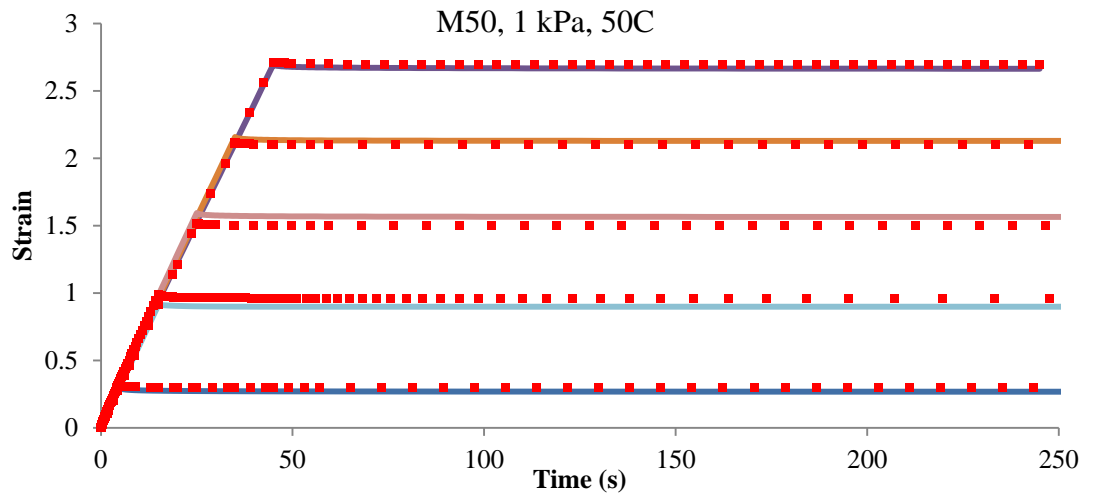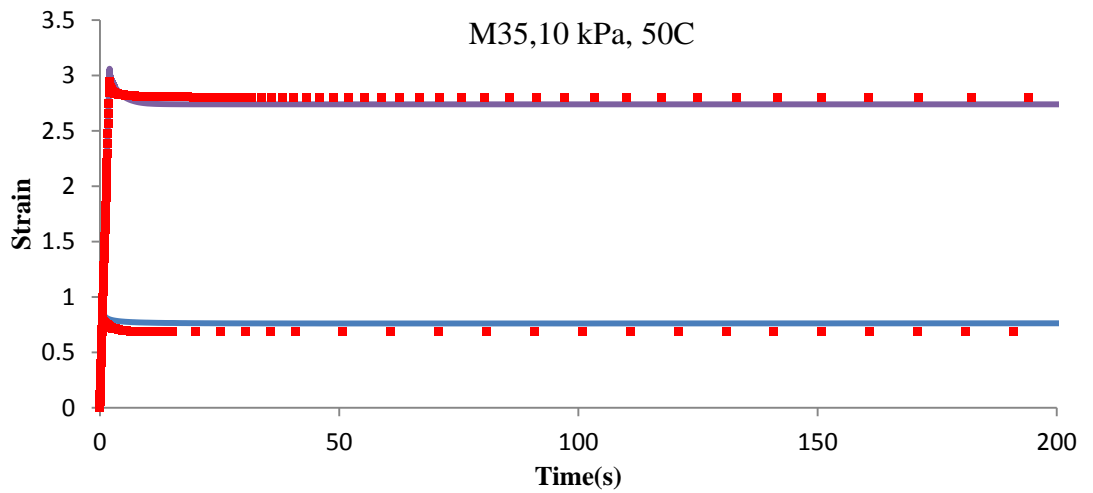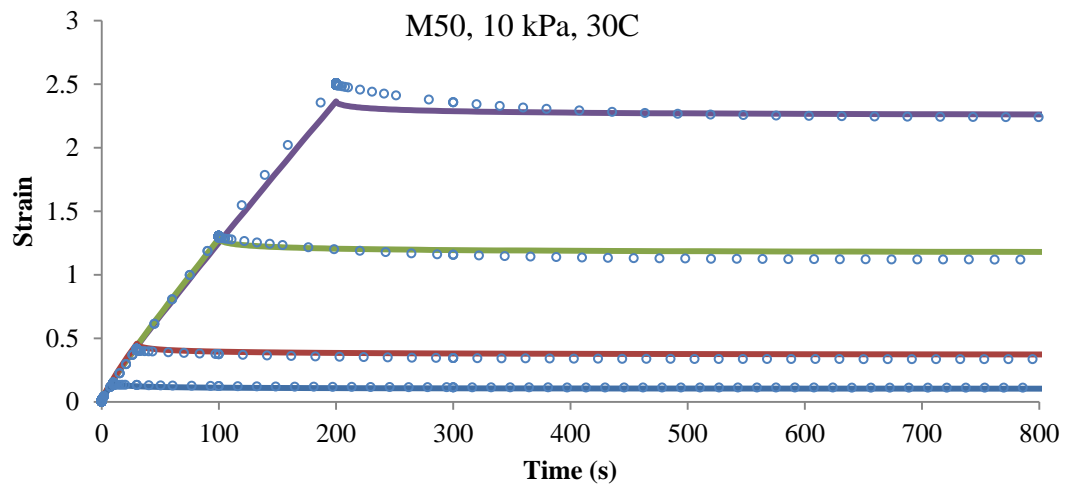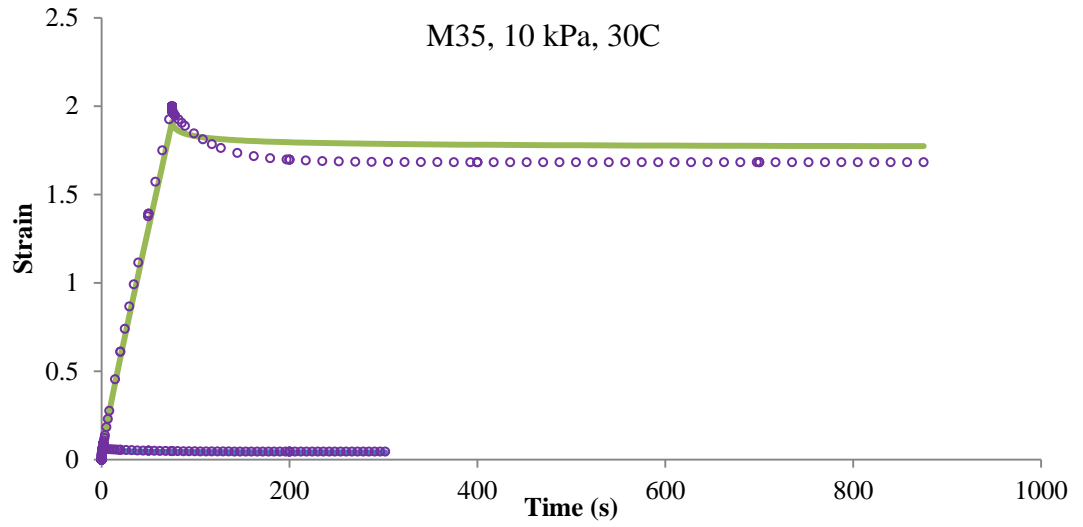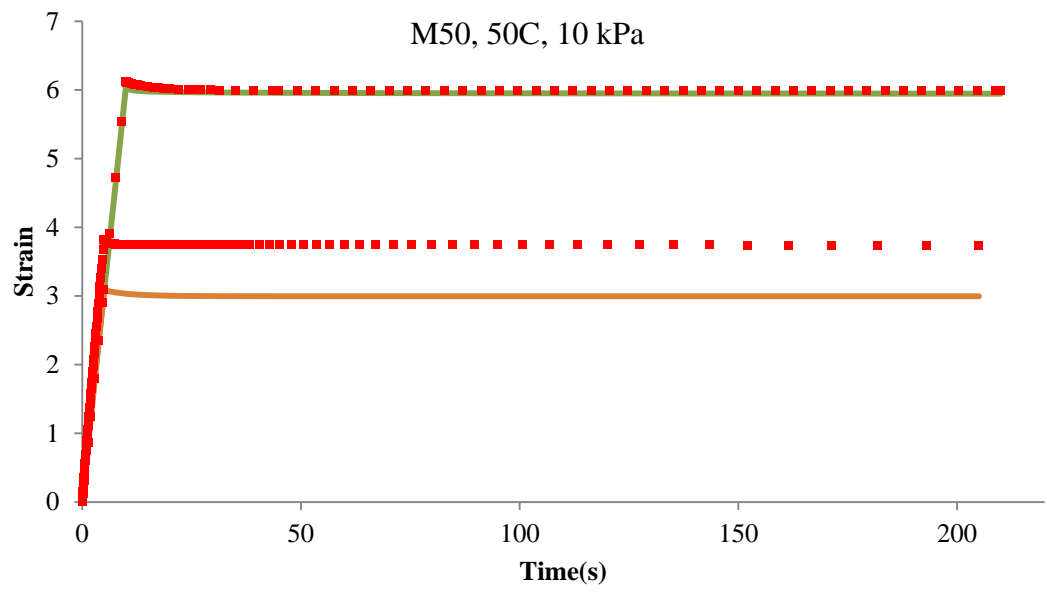
Figure 16 Experimental results and simulation of (A) Creep (B) Creep-recovery tests

Appendix B

The cylindrical mortar samples were tested in the DSR Gemini 200 after applying some modifications to the machine. An extended temperature cell (ETC) was connected to the Gemini 200 combined with a liquid nitrogen cooling system (Figure 1). An ETC utilises a regulated temperature forced gas design to ensure consistent temperature within the sample volume (minimise temperature variance). The ETC is compatible with solid fixture geometry for torsional loading. The liquid nitrogen is contained in a dewar and pressurised to supply cold gas into the cell under low temperature operations through an isolated pipe. This appendix explains in detail the procedure to prepare the mortar sample in the Gemini using the solid fixtures technique.
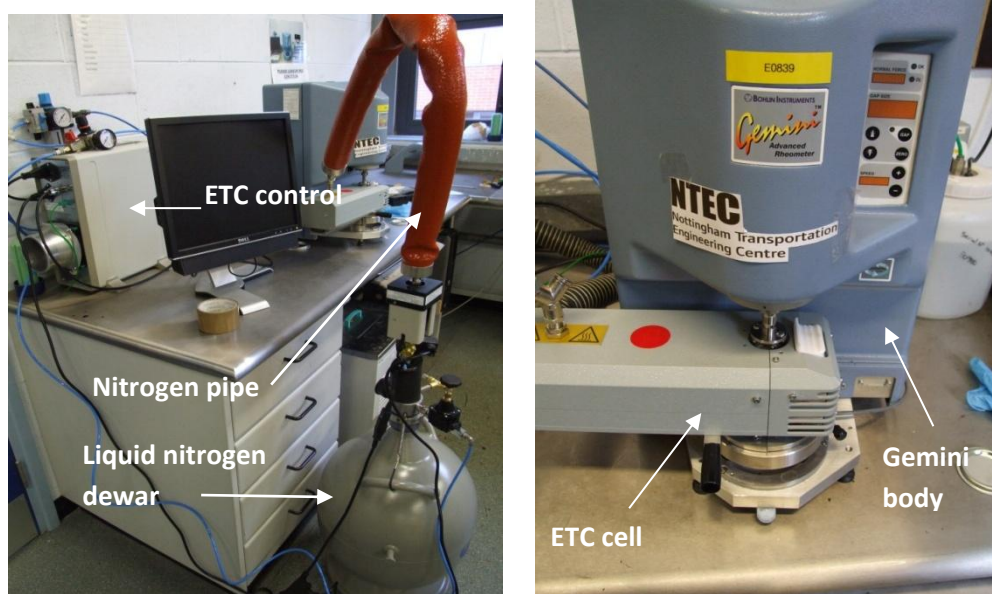

Figure 1 Gemini and ETC

Equipment

The main equipments include:

- Gemini 200 DSR

- ETC

- Dewar (Liquid Nitrogen)

- Disposable plates and glue

- Solid fixtures

Preconditioning

Sample was left in the room temperature (20°C approximately) from the store room (50°C) for an hour before conditioning to avoid sudden variation in the sample temperature. The conditioning was applied for an hour before commencing the test.

Sample Preparation

1- A sufficient amount of instant adhesive glue is to be placed on the disposable plate and sample surfaces on both sides, Figure 2. To ensure satisfactory bond additional glue is to be sited around the circumference of the sample edges and plates. Allow 10 minutes for the glue to stiffen enough.

Figure 2 Glued sample

2- Clamp the sample to the solid fixture by two bolts, Figure 3. Place the Gemini nut on the top of the solid fixture seat.

Figure 3 Fixing glued sample to solid fixture

3- Turn on the Gemini main machine simultaneously with pressing the up ◭ button on the machine. Release the button when the 'Hi' mode sign appears on the Normal Force screen.

4- Open The Bohlin software by double-clicking the icon on the desktop.

5- Software will prompt for the selection of temperature control, select ETC.

6- As soon as you select the type of test required (Creep, oscillation, or viscometry), change the **Testing configuration** to '20 mm dia and 50 mm Height' mode.

7- Open the cell and screw the clamped sample to the Gemini shaft by the nut, Figure 4.

Figure 4 Sample installation in the Gemini ETC

8- Press the ▼ 'down' button for about 5 s and the gap will automatically be lowered until the lower plate reaches the seat on the bottom solid fixture. Then screw firmly the lower plate with the two nuts.

9- Move the fixed part of ETC by the grip towards the sample and then close the chamber by closing the cell with the moveable part. The cell will start immediately after this step towards the specified temperature. The available temperature is between -150°C and +550°C with ±0.5°C accuracy.